

**Surfactant Adsorption during Collisions of Colloidal Particles: A Study
with Atomic Force Microscopy (AFM)**

William J. Lokar III

Dissertation submitted to the faculty of the Virginia Polytechnic Institute and State
University in partial fulfillment of the requirements for the degree of

Doctor of Philosophy

In

Chemistry

Dr. William. A. Ducker, Committee Chair

Dr. Mark R. Anderson

Dr. Alan R. Esker

Dr. John R. Morris

Dr. Roe-Hoan Yoon

July 19, 2004

Blacksburg, Virginia

Keywords: Surfactant, adsorption, proximal adsorption, charge regulation, surface forces,
AFM, self-consistent field theory

Copyright 2004©, William J. Lokar III

Surfactant Adsorption during Collisions of Colloidal Particles: A Study with Atomic Force Microscopy (AFM)

William J. Lokar III

Abstract

The adsorption of cationic and zwitterionic surfactants is studied in aqueous electrolyte solutions. A Maxwell relation is applied to Atomic Force Microscopy (AFM) data to obtain changes in surfactant adsorption as a function of the separation between two glass surfaces. In addition, self-consistent field theory (SCF) is used to calculate the adsorption profiles and interaction energies when two solid surfaces are brought into close proximity. Addition of surfactant is shown to affect the surface forces when lateral surfactant chain interactions are significant. The surfactant adsorbs and desorbs in response to over-lapping electric double-layers, with the adsorption being affected at larger solid–solid separations when the double-layer force is longer ranged. Furthermore, elimination of the surface charge or net surfactant charge eliminates *adsorption* with decreased solid–solid separation. The magnitude of the changes in surfactant adsorption at decreased separations is shown to scale with the chain length of the surfactant. Surfactant adsorption exceeds that required to regulate the surface charge according to the constant potential boundary condition in Poisson-Boltzmann theory. An equation of state including short-ranged (contact) tail interactions is proposed to describe both the adsorption of surfactant and the surface forces at small separations, where the double-layers overlap. Furthermore, SCF calculations show confinement–induced phase transitions when the surfactant layers on opposite surfaces merge. These phase transitions lead to further surfactant adsorption and a corresponding attractive force.

Table of Contents

Abstract.....	ii
Table of Contents.....	iii
List of Figures.....	ix
List of Tables.....	xiii
Acknowledgements.....	xiv
Chapter 1 Introduction and Literature Review.....	1
1.1 Introduction.....	1
1.2 Colloidal Forces.....	1
1.2.1 DLVO Theory.....	2
1.2.1.1 Electric Double Layer.....	2
1.2.1.2 Van der Waals Forces.....	4
1.2.2 Extended DLVO Theory.....	8
1.2.2.1 Hydration Forces.....	9
1.2.2.2 “Hydrophobic” Forces.....	11
1.2.2.3 Oscillatory Forces.....	16
1.3 Experimental Techniques for Colloidal Force Measurement.....	16
1.3.1 Disjoining Pressure.....	16
1.3.2 Surface Forces Apparatus (SFA).....	17
1.3.3 Atomic Force Microscopy (AFM).....	17
1.3.4 Additional Techniques.....	17
1.4 Surfactants in Bulk Solution.....	18
1.4.1 Surfactants.....	18
1.4.2 Surfactant Solutions.....	18
1.5 Surfactant Adsorption to Solid Surfaces.....	20
1.5.1 Adsorption Equilibrium of Cationic Surfactants.....	21
1.5.2 Dynamics of Surfactant Adsorption.....	23
1.5.3 Structure of Adsorbed Surfactant Aggregates.....	23
1.5.4 Overview of Adsorption.....	25
1.6 Proximal Adsorption.....	26

1.6.1 Theory.....	26
1.6.2 Studies of Proximal Adsorption.....	29
1.7 Cited Literature.....	32
Chapter 2 Colloidal Probe Atomic Force Microscopy.....	36
2.1 Introduction.....	36
2.2 AFM Setup and Data Analysis.....	37
2.2.1 Set-up and Measurements.....	37
2.2.2 Data Analysis.....	38
2.3 Colloidal Probe Preparation.....	42
2.3.1 Sphere Attachment.....	42
2.3.2 Spring Constant Calibration.....	44
2.4 Additional AFM Experimental Procedure.....	45
2.4.1 Reagents.....	45
2.4.2 Solid Substrates.....	46
2.4.3 Surface Forces.....	48
2.5 Cited Literature.....	49
Chapter 3 Effect of Salt Addition on Proximal Adsorption.....	51
3.1 Introduction.....	51
3.2 Experiments in Electrolyte Solution.....	53
3.2.1 Bubble Effects.....	53
3.2.2 Chemical Potential Measurements.....	54
3.2.3 Surface Forces.....	55
3.2.4 DLVO Analysis.....	58
3.3 Equation of State.....	61
3.4 Adsorption Analysis.....	62
3.5 Proximal Adsorption.....	64
3.5.1 $[C_{12}TAB] < 0.36 \text{ mM}$	64
3.5.2 $0.36 \text{ mM} < [C_{12}TAB] < 1.8 \text{ mM}$	66
3.5.3 $ccp < [C_{12}TAB] < cmc$	68
3.6 Comparison of Forces in No-Added-Salt and 20 mM KBr.....	69
3.7 Conclusions.....	71

3.8 Cited Literature.....	72
Chapter 4 Effects of Ionic Strength, pH, and Chain-length on Proximal Adsorption.....	73
4.1 Introduction.....	73
4.2 Additional Experimental.....	74
4.2.1 Solid Substrates.....	74
4.2.2 Chemical Potential Measurements.....	74
4.2.3 Zeta potential.....	75
4.3 Surface Forces.....	76
4.3.1 CPC / 10 mM KCl Solutions.....	76
4.3.2 CPC / 1 mM KCl Solutions.....	78
4.3.3 CPC Solutions at pH 1.8.....	80
4.3.4 DPC / 10 mM KCl Solutions.....	81
4.3.5 DPC / 1 mM KCl Solutions.....	82
4.3.6 Adhesion Data in Surfactant / Salt Solutions.....	83
4.4 Proximal Adsorption.....	86
4.4.1 Analysis.....	86
4.4.2 Results.....	87
4.5 Conclusions.....	93
4.6 Cited Literature.....	94
Chapter 5 The Short-range Hydrophobic Effect and Proximal Adsorption.....	95
5.1 Introduction.....	95
5.2 Additional Experimental.....	96
5.2.1 Adsorption to ‘Isolated’ Particles.....	96
5.2.2 Contact Angles.....	97
5.3 Adsorption and Contact Angles.....	97
5.4 Proximal Adsorption	98
5.4.1 Double-Layer Effects.....	98
5.4.2 Chain Effects.....	105
5.5 The Equation of State.....	108
5.6 The Mechanism of Proximal Adsorption.....	113

5.6.1	Below the Hemi-Micelle Concentration.....	113
5.6.2	$hmc < [\text{Surfactant}] < ccp$	113
5.6.3	$ccp < [\text{Surfactant}] < cmc$	115
5.6.4	<i>Proximal Sorption in 'Contact'</i>	116
5.7	Conclusions.....	117
5.8	Cited Literature.....	118
Chapter 6	Proximal Adsorption in Mixed Cationic-Zwitterionic Surfactants.....	119
6.1	Introduction.....	119
6.2	Additional Experimental.....	122
6.2.1	Reagents.....	122
6.2.2	Adsorption to 'Isolated' Surfaces.....	123
6.3	Interactions in DDAPS Solutions.....	126
6.4	Interactions in Mixed DDAPS/DPC Solutions.....	129
6.4.1	Constant DPC Concentration.....	129
6.4.2	Constant DDAPS Concentration.....	135
6.5	Total Proximal Adsorption for DDAPS/ DPC/ KCl.....	137
6.6	Conclusions.....	139
6.7	Cited Literature.....	139
Chapter 7	Self-Consistent Field Theory: Methods and Applications to Surfactants in Bulk Solution.....	141
7.1	Introduction.....	141
7.2	The Theory.....	142
7.2.1	Lattice.....	141
7.2.2	Potential Energy.....	144
7.2.3	Extension to Chain Molecules.....	146
7.3	Bulk Surfactant Behavior.....	152
7.3.1	Cmc Determination.....	152
7.3.2	Parameters.....	153
7.4	Conclusions.....	159
7.5	Cited Literature.....	159

Chapter 8	SCFA Calculations of Adsorption between Neutral Surfaces.....	161
8.1	Introduction.....	161
8.2	Additional Theoretical Detail.....	161
8.3	Adsorption at Large Separations.....	164
	8.3.1 (420) Surface.....	164
	8.3.2 (031) Surface.....	166
8.4	Adsorption between Confined Surfaces.....	169
	8.4.1 (420) Surfaces.....	169
	8.4.2 (031) Surfaces.....	170
8.5	Interaction between Surfaces.....	172
	8.5.1 (420) Surfaces.....	172
	8.5.2 (031) Surfaces.....	177
8.6	Adsorbed Surfactant Layer Thickness.....	179
	8.6.1 Analysis.....	179
	8.6.2 Experimental Consequences.....	180
8.7	Electrolyte Adsorption/Desorption Behavior.....	181
8.8	Conclusions.....	183
8.9	Cited Literature.....	183
Chapter 9	SCFA Calculations of Adsorption between Charged Surfaces.....	185
9.1	Introduction.....	185
9.2	Adsorption to Constant Charge Solids at Large Separation.....	185
9.3	Effect of Surface Charge on Solid-Solid Interactions.....	187
9.4	Adsorption and Phase Transitions in Confined Films.....	191
9.5	Electric Potential versus Separation.....	196
9.6	Regulation of the Surfactant Layer Thicknesses.....	197
9.7	Proximal Adsorption of Salt.....	198
9.8	Effect of Surfactant Chain Length.....	200
9.9	Conclusions.....	201
9.10	Cited Literature.....	202
Chapter 10	Summary and Future Work.....	203
10.1	Introduction.....	203

10.2 Predicting Interactions from Adsorption Isotherms.....	203
10.2.1 Region (1): [Surfactant] < <i>hmc</i>	204
10.2.2 Region (2): <i>hmc</i> < [Surfactant] < <i>ccp</i>	205
10.2.3 Region (3) <i>ccp</i> < [Surfactant] < <i>cmc</i>	206
10.2.4 Region (4) [Surfactant] > <i>cmc</i>	206
10.3 Prediction of Adsorption between Confined Surfaces.....	207
10.3.1 Region (1): [Surfactant] < <i>hmc</i>	207
10.3.2 Region (2): <i>hmc</i> < [Surfactant] < <i>ccp</i>	207
10.3.3 Region (3) <i>ccp</i> < [Surfactant] < <i>cmc</i>	208
10.4 Conclusions	209
10.5 Future Work.....	209
10.6 Cited Literature.....	210
VITA	211

List of Figures

Figure	Title	Page
1.1	Depiction of electric potential and ion distributions.....	3
1.2	Potential energy of interaction vs. separation (DLVO).....	7
1.3	Illustration of two surfactants.....	18
1.4	Physical properties of surfactants solutions near the <i>cmc</i>	19
1.5	General adsorption isotherm and representative surfactant structures.....	25
1.6	Derivation of proximal adsorption Maxwell relation.....	26
1.7	Schematic of proximal adsorption.....	29
2.1	Photograph of Digital Instruments AFM Module.....	37
2.2	Schematic of AFM force measurement.....	38
2.3	Plot of cantilever tip deflection as a function of piezo displacement.....	39
2.4	Example of typical force versus separation data obtained by AFM.....	41
2.5	Photograph of the apparatus used for mounting colloidal spheres.....	42
2.6	Photograph of a glass sphere attached to AFM cantilever.....	43
2.7	Calibration plot for determination of cantilever spring constants.....	44
2.8	AFM height image of a borosilicate glass plate.....	47
2.9	AFM height image of a borosilicate glass sphere (large scale).....	47
2.10	AFM height image of a borosilicate glass sphere (zoom).....	48
3.1	Dodecyltrimethylammonium bromide (C ₁₂ TAB).....	51
3.2	Interaction energies between silica surfaces in C ₁₂ TAB solutions.....	51
3.3	Interaction energies and C ₁₂ TAB proximal adsorption in no salt.....	52
3.4	Forces in 1.4 mM C ₁₂ TAB at various KBr concentrations.....	54
3.5	C ₁₂ TA ⁺ -selective electrode potential vs C ₁₂ TAB concentration.....	55
3.6	Forces in low concentration C ₁₂ TAB / 20 mM KBr solutions.....	55
3.7	Forces in high concentration C ₁₂ TAB / 20 mM KBr solutions.....	56
3.8	Zeta potential of glass particles in C ₁₂ TAB / 20 mM KBr solutions.....	57
3.9	Adhesion data in C ₁₂ TAB / 20 mM KBr solutions.....	58
3.10	Comparison of measured forces to DLVO Theory.....	60
3.11	Interaction energy versus C ₁₂ TAB chemical potential in 20 mM KBr.....	64
3.12	Proximal adsorption and comparison to charge behavior in 20 mM KBr.....	65

3.13	Proximal adsorption above the charge compensation point in 20 mM KBr...	69
3.14	Analysis of attractive forces.....	71
4.1	CPC and DPC.....	73
4.2	Surfactant selective electrode data for CPC and DPC.....	75
4.3	Forces between glass surfaces in CPC / 10 mM KCl solutions.....	77
4.4	Zeta-potential of glass spheres in CPC / 10 mM KCl solutions.....	78
4.5	Forces between glass surfaces in CPC / 1 mM KCl solutions.....	79
4.6	Forces between glass surfaces in CPC solutions at pH 1.8.....	80
4.7	Forces between glass surfaces in DPC / 10 mM KCl solutions.....	81
4.8	Forces between glass surfaces in DPC / 1 mM KCl solutions.....	82
4.9	Comparison of forces on approach and retraction.....	83
4.10	Adhesion in CPC / 10 mM KCl at different scan rates.....	84
4.11	Adhesion versus concentration in various surfactant solutions.....	85
4.12	Interpolations of experimental data.....	87
4.13	Proximal adsorption of CP^+ versus separation in CPC / 10 mM KCl.....	88
4.14	Proximal adsorption of CP^+ versus separation in CPC / 1 mM KCl.....	89
4.15	Proximal adsorption of CP^+ versus separation in CPC at pH 1.8.....	90
4.16	Proximal adsorption of DP^+ versus separation in DPC / 10 mM KCl.....	90
4.17	Proximal adsorption of DP^+ versus separation in DPC / 1 mM KCl.....	91
4.18	Proximal adsorption versus chemical potential at ($s=s_0$).....	93
5.1	Adsorption isotherm of CPC on glass in 10 mM KCl.....	97
5.2	Receding contact angles on glass for CPC solution droplets.....	98
5.3	Changes in surface excess vs separation on a semi-logarithmic scale.....	99
5.4	Comparison of proximal adsorption decay lengths to Debye-lengths.....	100
5.5	Representation of the shift in charge plane.....	101
5.6	Constant Potential DLVO fits to experimental force data.....	102
5.7	Fitted DLVO potentials versus surfactant concentrations.....	105
5.8	Comparison of $\Delta\Gamma$ to $\Delta\sigma$ from Poisson-Boltzmann theory (DLVO).....	106
5.9	Deviations from Poisson-Boltzmann theory.....	107
5.10	Adsorption isotherms for CPC at different separations in 10 mM KCl.....	109
5.11	$A(\theta)$ and electrostatic potentials versus θ for CPC in 10 mM KCl.....	111

5.12	Fitted $A(\theta)$ and isotherms for CPC in 10 mM KCl.....	112
5.13	Depiction of regulation below the hemi-micelle concentration.....	113
5.14	Depiction of regulation for $hmc < [\text{surfactant}] < ccp$	114
5.15	Depiction of regulation for $ccp < [\text{surfactant}] < cmc$	116
6.1	DDAPS and DPC.....	119
6.2	Schematic of ATR-IR experimental set-up.....	123
6.3	Sample ATR-IR Spectra.....	124
6.4	Adsorption of DDAPS and DPC on an oxidized silicon ATR crystal.....	126
6.5	Forces between glass surfaces in 1 mM KCl and $[\text{DDAPS}] < 2\text{mM}$	127
6.6	Forces between glass surfaces in 1 mM KCl and $[\text{DDAPS}] > 2\text{mM}$	128
6.7	Forces between glass surfaces in DPC and 1 mM KCl	129
6.8	Adsorption of DDAPS and DPC in 0.05 mM DPC and 1 mM KCl.....	130
6.9	Forces between glass surfaces in DDAPS, 0.05 mM DPC, and 1 mM KCl .	132
6.10	Proximal adsorption of DDAPS in 0.05 mM DPC and 1 mM KCl.....	133
6.11	Comparison of forces in DDAPS with and without 0.05 mM DPC.....	134
6.12	Forces between glass surfaces in DPC, 0.75 mM DDAPS, and 1 mM KCl.	135
6.13	Adsorption of DDAPS and DPC in 0.75 mM DDAPS and 1 mM KCl.....	136
6.14	Proximal adsorption of DPC in 0.75 mM DDAPS and 1 mM KCl.....	137
6.15	Comparison of proximal adsorption at different conditions.....	138
6.16	Schematic of proximal adsorption in a mixed surfactant system.....	138
7.1	Schematic of a one-dimensional SCFA lattice.....	143
7.2	Depiction of the structure and ranking numbers for $\text{C}_{16}\text{P}_3^+$	147
7.3	Schematic of two possible conformations of A_4B_4	150
7.4	Cmc determination from SCFA calculations (spherical micelles).....	152
7.5	Cmc versus chain length for C_nP_3^+ in various electrolyte concentrations....	154
7.6	Chemical potential of $\text{C}_{16}\text{P}_3^+$ versus salt concentration (various shapes)....	156
7.7	Radial segment distribution for spherical $\text{C}_{16}\text{P}_3^+$ micelles.....	157
7.8	Electrical potential around a spherical $\text{C}_{16}\text{P}_3^+$ micelle.....	158
8.1	Depiction of the lattice arrangement for SCFA of interacting surfaces.....	163
8.2	Adsorption isotherms at various electrolyte concentrations (420).....	165
8.3	Segment distributions near an isolated (420) surface.....	166

8.4	Adsorption isotherm for $C_{16}P_3^+$ on a neutral (031) surface.....	167
8.5	Adsorption isotherms at various electrolyte concentrations (031).....	167
8.6	Comparison of (420) and (031) adsorption isotherms.....	168
8.7	Adsorption isotherms at various separations (420) in 10 mM salt.....	169
8.8	Adsorption isotherms at various separations (420) in 100 mM salt.....	170
8.9	Adsorption isotherms at various separations (031) in 10 mM salt.....	171
8.10	Interaction energies for (420) surfaces in $C_{16}P_3^+$ and 10 mM salt.....	172
8.11	Electrical potential as a function of separation.....	173
8.12	Density profiles and adsorption isotherms for (420) surfaces.....	174
8.13	Schematic of confinement-induced phase transition.....	175
8.14	$\Delta\Gamma$ as a function of separation between (420) surfaces.....	177
8.15	Interaction energy and $\Delta\Gamma$ for (031) surfaces.....	178
8.16	Fractional thickness of the surfactant layer vs separation (420).....	180
8.17	Electrolyte proximal adsorption for (420) surfaces.....	182
9.1	Adsorption isotherms as a function of surface charge density.....	186
9.2	Segment distributions near an isolated (420) constant charge surface.....	187
9.3	Interaction energies vs separation for various surface charges.....	188
9.4	Schematic of surface charge effect on adsorption above the <i>ccp</i>	189
9.5	Adsorption isotherms at various separations for a constant charge surface..	192
9.6	Density profiles and schematic of confinement-induced phase transition...	194
9.7	Interaction energies and $\Delta\Gamma$ as a function of separation.....	195
9.8	Electrostatic potential vs separation for a constant charge surface.....	196
9.9	Thickness of surfactant layers as a function of separation.....	198
9.10	Density profiles for K near a (420) surface at different separations.....	199
9.11	$\Delta\Gamma$ and interaction energies as a function surfactant chain length.....	200
10.1	General adsorption isotherm of ionic surfactant.....	204

List of Tables

Table	Title	Page
1.1	Hamaker Constants for Common Materials.....	6
3.1	Fitted DLVO Parameters for C ₁₂ TAB Experiments.....	60
4.1	Cmc values for CPC and DPC at various solution conditions.....	75
5.1	Fitted DLVO Parameters for CPC Experiments.....	103
5.2	Fitted DLVO Parameters for DPC Experiments.....	104
6.1	Extinction coefficients and penetration depths for ATR-IR spectra.....	125
6.2	Fitted Surface Potential and Charge for DDAPS in DPC/ KCl.....	131
7.1	Bulk Chi parameters.....	154
7.2	Cmc of C ₁₆ P ₃ ⁺ from SCFA at various monovalent salt concentrations.....	156
8.1	Chi parameters for the (420) and (031) surfaces.....	164
8.2	Electric Potentials at the Mid-Plane between (420) surfaces.....	173
9.1	Electrostatic potentials at different charge densities.....	190

Acknowledgements

This work is based on research supported by the National Science Foundation Grant CHE-0203987 and the Thomas F. Jeffress and Kate Miller Jeffress Memorial Trust (J-472). In addition, I would like to thank the Graduate School at Virginia Tech for support in the form of a Cunningham Fellowship. In addition, a special acknowledgement goes to Dr. T. C. Ward for use of the IR spectrometer, Dr. Matthew Eick at Virginia Tech for the BET analysis of our glass spheres, and Dr. Mark Edwards for use of the Zeta Meter.

I would like to extend a special thanks to the faculty and staff at Wageningen University in the Netherlands for their hospitality during the theoretical portion of this project. In particular, I would like to acknowledge Luuk Koopal and Frans Leermakers for their guidance and discussions.

I would like to acknowledge the members of my committee Dr. Alan Esker, Dr. John Morris, Dr. Mark Anderson, and Dr. Roe-Hoan Yoon for encouragement, helpful suggestions, and constructive criticism.

I would like to thank the members of the Ducker Group for supplying an outstanding working environment for the last five years. Without all of you, it would not have been possible. In particular, Aysen Tulpar for being beside me through it all, Clayton McKee for lightening the mood when it needed it, and Spencer Clark all his help with the infrared spectroscopy. Furthermore, I would like to thank Vivek Subramanian for his guidance in teaching me AFM.

I would like to thank William Ducker for all of his help and teachings over the years. I could not have asked for a better advisor.

I would like to thank Amanda Willis for her encouragement throughout the final months and for making Blacksburg a worthwhile place to be.

Finally, I would like to especially thank my parents for their years of encouragement and for making me what I am today.

Surfactant Adsorption during Collisions of Colloidal Particles: A Study with Atomic Force Microscopy (AFM)

Chapter 1

Introduction and Literature Review

1.1 Introduction

Colloidal particles are small particles, whose sizes range in one dimension from 1 nm to 1 μm . These particles have the unique property that they are small enough that gravitational forces do not significantly contribute to their behavior. They are, however, large enough that they do not behave as quantum particles. A dispersion of colloidal particles in a liquid medium (colloidal dispersion or suspension) is governed by the inter-surface forces acting between the particles.

Colloidal suspensions are important in many industrial applications. Colloidal particles can be found in paints, ceramics, soils, foams, aerosols, and milk, to name a few. For example, latex paint is composed largely of polymeric latex particles dispersed in an aqueous medium. Milk, on the other hand, is an example of a biological colloidal dispersion in which fat particles are dispersed in an aqueous solution. A colloidal suspension can be stabilized by the presence of a repulsive force acting between the colloidal particles. An attractive force, on the other hand, can lead to aggregation of particles, causing a destabilization of the suspension. An example of the destabilization of a colloidal suspension includes the clumping that occurs in soured milk.

Commonly, colloidal stability is controlled through the adsorption of polymers, proteins, or surfactants to the particles of interest. The work presented in this thesis will focus upon the role of surfactants in altering the surface forces. In particular, attention will be given to the interplay between surfactant adsorption and the interaction energies between colliding particles.

1.2 Colloidal Forces

First, forces arising in colloidal systems and the theories behind their manipulation will be discussed. As a starting point, classic DLVO theory and its constituent

electrostatic double-layer and van der Waals contributions will be presented, followed by extensions to DLVO theory that include hydration, “hydrophobic”, and oscillatory forces.

1.2.1 DLVO Theory

Colloidal stability was studied by Hamaker in terms of electrostatic and van der Waals interactions in the mid-1930's.^{1,2} This theory, however, was more qualitative than quantitative. In the 1940's the classical standard for interaction forces between colloidal particles was developed.³⁻⁵ Named for its originators, Derjaguin, Landau, Verwey, and Overbeek, DLVO theory states that surface forces can be considered to be the sum of electrical double-layer forces and van der Waals interactions.

1.2.1.1 Electric Double-Layer

When a solid containing ionic species is placed in a liquid, the ionic groups on the surface can dissociate and dissolve in the liquid. This process creates a charge on the solid called the surface charge, σ_0 . Due to the separation of charge, an electric potential, ψ , develops, which decays perpendicular to the surface (z -direction). The potential created follows from the Poisson equation.

$$\frac{\partial^2 \psi}{\partial z^2} = -\frac{\rho(z)}{\epsilon} \quad (1.1)$$

where $\rho = \sum_i v_i c_i e$ is the charge density, ϵ is the dielectric permittivity of the solvent, v_i is the valence of ion i , c_i is the concentration of ion i , and e is the elementary charge. The concentration of each ion can be calculated from the electrical potential according to the Boltzmann distribution.

$$c_i(z) = c_i^b \exp\left(-\frac{v_i e \psi(z)}{k_B T}\right) \quad (1.2)$$

where b indicates the bulk, k_B is Boltzmann's constant, and T is the absolute temperature.

Ions of opposite sign to that of the surface potential are attracted to the region near the surface, while ions with the same sign as the surface charge are repelled from the surface. In the case of ions that have no specific interaction with the surface, this profile can be considered to be continuous away from the solid. If, however, the ions have specific

interactions, they can be strongly bound to the solid and significantly affect the potential. These types of ions are called potential determining ions. Such examples include, protons on surfaces with dissociable hydroxyl groups such as silica, molecules from a crystal lattice such as Ag^+ and I^- for AgI , and also other surface-active molecules (i.e. surfactants).

A model developed by Stern,⁶ considers a layer of tightly bound ions to the surface and a potential that decays away from the outer plane of this layer (Stern plane). This model is depicted in Fig. 1.1. The molecules and ions within the Stern plane comprise the Stern layer and dictate the potential that governs the distribution of ions in solution. Often, there is a distinction made between the surface potential (on the actual solid) and the Stern potential (at the Stern plane). Experimentally, it is difficult to distinguish between the surface and Stern layer potentials. Therefore, in all experimental work presented here, the surface potential and surface charge mentioned will be that at the Stern plane.

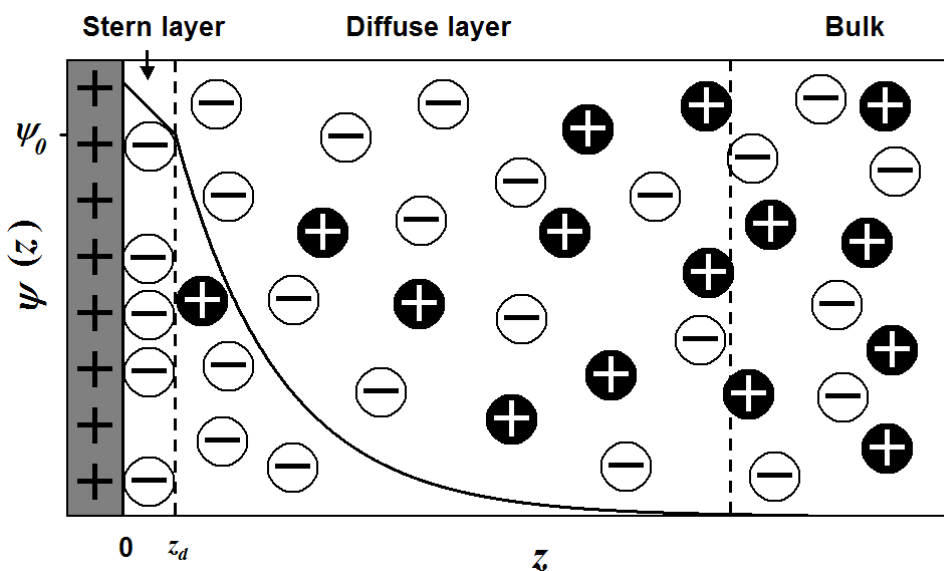


Figure 1.1 Depiction of the electric potential and ion distribution away from a charged, solid surface. Ions of opposite charge to the surface are more concentrated near the surface.

The electric double-layer consists of two layers: the Stern layer and a diffuse layer of ions. This diffuse layer is more concentrated in ions of opposite sign to the surface potential, while the ions of the same charge as the surface are depleted from the double-layer. The potential can be determined within the diffuse layer by combination of eqs. 1.1 and 1.2, known as the Poisson-Boltzmann equation (valid for infinite flat surfaces and point ions).

$$\frac{\partial^2 \psi}{\partial z^2} = -\frac{e}{\varepsilon} \sum_i v_i c_i^b \exp\left(\frac{-v_i e \psi(z)}{k_B T}\right) \quad (1.3)$$

Exact analytical solutions of the Poisson-Boltzmann equation are not available; therefore, eq. 1.3 must be solved numerically. By applying several simple, yet valid assumptions, analytical solutions can be obtained.

For small surface potentials (i.e. when $\psi_0 \leq 25$ mV for a 1:1 electrolyte) the Poisson-Boltzmann equation reduces to

$$\frac{\partial^2 \psi}{\partial z^2} = \kappa^2 \psi(z) \quad (1.4)$$

where

$$\kappa^{-1} = \sqrt{\frac{\varepsilon k_B T}{e^2 \sum_i c_i^b v_i^2}} \quad (1.5)$$

The solution to eq. 1.4 is:

$$\psi(z) = \psi_0 \exp(-\kappa(z - z_d)) \quad (1.6)$$

where κ^{-1} , which is related to the thickness of the diffuse part of the double-layer, is the characteristic decay length or Debye-length of the double-layer force.

1.2.1.2 Van der Waals Forces

The second force considered in DLVO theory is the van der Waals interaction. This force arises from electromagnetic fields due to electrons in matter. Attractive energies between molecules result from dipole-induced dipole interactions that decay with distance as r^{-6} . The van der Waals force between two condensed phases in a vacuum is more complex. The simplest approach assumes that the van der Waals force is a sum of all pair-wise molecular interactions through a continuous media (Hamaker theory).⁵ The attractive potential can be determined between two large parallel plates, and for the

specific case where the plate separation, s , is much smaller than the plate thickness, d , yielding the following expression:

$$E_{vdW} = -\frac{A}{12\pi s^2} \text{ for parallel plates when } s \ll d \quad (1.7)$$

where A is the Hamaker constant, which is characteristic of the plates and the intervening medium. The Hamaker constant is proportional to the square of both the density of atoms and the atomic polarizability of the material.

When a third medium is placed between the plates, the intervening medium will absorb electromagnetic radiation that is being passed from one plate to the other. Consequently, the electromagnetic interaction between the plates will be reduced across this intervening medium and the Hamaker constant will become smaller in magnitude. For two different materials interacting through a third different medium, the Hamaker constant is approximated by eq. 1.8.⁷

$$A_{132} = \left(\sqrt{A_{33}} - \sqrt{A_{11}}\right)\left(\sqrt{A_{33}} - \sqrt{A_{22}}\right) \quad (1.8)$$

If the particles are similar then $A_{11}=A_{22}$ and eq. 1.8 simplifies to

$$A_{131} = \left(\sqrt{A_{33}} - \sqrt{A_{11}}\right)^2 \quad (1.9)$$

Using these equations, the Hamaker constant for two particles interacting through a medium can be developed from knowledge of how the atoms of one substance interact with themselves.

Work by Lifshitz et al,⁸ using detailed quantum-field theory, brought new light to the theory of the van der Waals attractive force. Lifshitz theory, like Hamaker theory, states that the attractive force between particles is a result of the overlap of fluctuating electromagnetic fields around the atoms or particles. The difference between the two theories is that Lifshitz accounts for many-body interactions, as well as pair-wise interactions. An analytical solution to the many-body problem is impractical, however, many-body interactions can be incorporated through the use of spectroscopic data. The wavelength of electromagnetic radiation that most affects the attractive forces is that of the same order of magnitude as the separation between particles.

For two similar materials, ε_1 , interacting through a medium, ε_2 , the Hamaker constant is approximated by eq. 1.10, where ε_i are the frequency dependent dielectric permittivities and \hbar is Planck's constant divided by 2π .⁷

$$A_{121} = \frac{3kT}{4} \left[\frac{\varepsilon_1(0) - \varepsilon_2(0)}{\varepsilon_1(0) + \varepsilon_2(0)} \right]^2 + \frac{3\hbar}{4\pi} \int_0^\infty \frac{kT}{\hbar} \left[\frac{\varepsilon_1(i\omega) - \varepsilon_2(i\omega)}{\varepsilon_1(i\omega) + \varepsilon_2(i\omega)} \right]^2 d\omega \quad (1.10)$$

A list of Hamaker constants for different materials interacting through air and water is given in Table 1.1.

Table 1.1. Hamaker Constants for Common Materials, M ($\times 10^{20} \text{ J}^{-1}$)

Material	M Air M	M Water M	M Water Air	M Air Water
Water	3.7	0.0	0.0	3.7
Teflon	3.8	0.3	0.1	3.7
Hexadecane	5.2	0.5	-0.5	4.3
Fused quartz	6.5	0.8	-1.0	4.8
Fused silica	6.6	0.8	-1.0	4.8
Polystyrene	6.6	1.0	-1.1	4.8
Mica (green)	10.0	2.1	-	-
Sapphire	16.0	5.0	-3.8	7.4

Adapted from Evans, D. F.; Wennerström, H. *The Colloidal Domain: Where Physics, Chemistry, Biology, and Technology Meet*; 2nd ed.; Wiley-VCH: New York, 1999.

It is assumed in DLVO theory that both the double-layer and van der Waals components are independent and can be summed to obtain the total interaction energy. For flat surfaces, eqs. 1.11 and 1.12 provide a method of calculating the DLVO interaction per unit area of one flat surface interacting with another flat surface, E_a . Eq. 1.11 is valid for 1:1 electrolytes in the limit that the double-layers overlap weakly ($\kappa s > 1$). Eq. 1.12 is valid in the limit of low potentials and follows from the use of eq. 1.6 for the potential.

$$E_a = -\frac{A}{12\pi s^2} + \frac{64k_B T c^b}{\kappa} \left(\tanh \left(\frac{ze\psi_0}{4k_B T} \right) \right)^2 \exp(-\kappa s) \quad (\text{weak overlap approx.}) \quad (1.11)$$

$$E_a = \frac{-A}{12\pi\kappa^2} + 2\varepsilon\kappa\psi_0^2 \exp(-\kappa s) \quad (\text{for flats at low potential}) \quad (1.12)$$

Since experimental systems often consist of non-planar colloids, Derjaguin related the force to the energy per unit area (E_a) for the flat-flat case.⁹ Derjaguin's approximations, given below, are valid for cases where the particle radius, R , is much greater than the range of the force. Eq. 1.13 provides a useful link between theory and experiment.

$$E_{a_{\text{flat-flat}}} = \frac{F_{\text{sphere-sphere}}}{\pi R} = \frac{F_{\text{sphere-flat}}}{2\pi R} = \frac{F_{\text{cylinder-cylinder}}}{2\pi R} \quad (1.13)$$

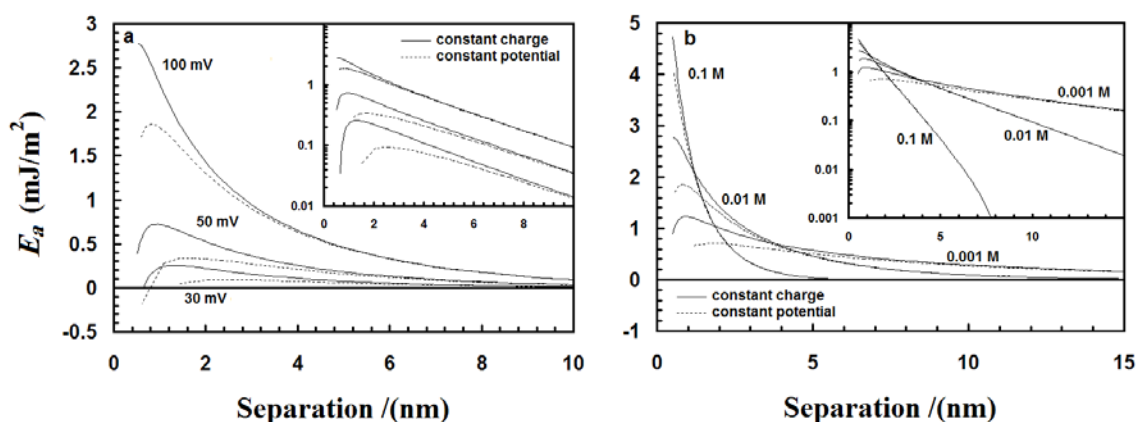


Figure 1.2 Plots of the potential energy of interaction vs. separation between two flat, charged surfaces as a function of **a)** surface potential at an ionic strength of 0.01 M and **b)** ionic strength at a surface potential of 100 mV. Curves are obtained from DLVO theory using a complete numerical solution of the Poisson-Boltzmann equation and a Hamaker constant of 0.8×10^{-20} J. The insets show the data on a log-lin scale. The solid lines are calculated at constant surface charge and the dashed lines are calculated at constant surface potential.

Colloid scientists often use knowledge of DLVO theory to control colloid stability by regulating the repulsive double-layer contribution. This is done in two basic ways. The surface potential can be altered by adsorption of potential determining ions at the particle-solution interface. Adsorption of oppositely charged ions leads to a decrease in the magnitude of the surface potential and hence a decrease in the repulsive force, thus destabilizing the colloids. A second means of changing stability is by altering the bulk

electrolyte concentration. An increase in electrolyte leads to a decrease in the decay length of the double layer repulsion as given by eq. 1.5. As a result, the barrier to coagulation decreases and shifts to smaller separations. The effects of surface potential and electrolyte concentration on DLVO energies are given in Fig. 1.2.

In addition, two basic cases or boundary conditions are explored; constant surface potential and constant surface charge. It is assumed in the calculations that as the surfaces approach, one of these two conditions holds. At constant charge, the potential increases as the separation decreases, and the gradient of the interaction energy increases more with decreasing separation than at constant surface potential. At small separations, most experimental cases fall between these two boundary conditions. At larger separations the two solutions converge and are relatively independent of separation.¹⁰

In 1971 Ninham and Parsegian solved the Poisson-Boltzmann equation for conditions between constant charge and constant potential by considering the surface to have ionizable groups that contribute to the surface potential and charge.¹⁰ For surface force measurements, where there is a large reservoir of electrolyte, a more appropriate condition may be that of constant chemical potential. This will be discussed in more detail in the following chapters.

1.2.2 Extended DLVO Theory

It is apparent from assumptions made in DLVO theory that additional considerations should be made for forces other than van der Waals and electrostatic double-layer forces. First, DLVO is a theory of the stability of lyophobic (liquid-fearing) particles. Lyophilic (liquid-loving) particles will require special consideration. In addition, it has been mentioned by Verwey and Overbeek that strongly hydrophobic particles also deviate from DLVO theory.⁵ Possible extensions to DLVO theory stem from the assumption in DLVO that the intervening medium is continuous up to the interface and that the surfaces are smooth and lyophobic. Therefore, these assumptions do not consider the effects of surface heterogeneity or solvent structure.

Derjaguin and Churaev¹¹ mentioned the presence of an additional force between quartz and mica surfaces, however, the theory to that point was uncertain. They later came up with a general rule for DLVO theory governing the lyophilicity and lyophobicity

of particles: DLVO holds only for partially wetted materials, that is, when the advancing contact angle of water on the surface lies between 15° and 64° .¹² Below $\theta_A=15^\circ$, the substrate is too hydrophilic and above $\theta_A = 64^\circ$ the substrate is too hydrophobic to apply DLVO theory without modification. Improvements to DLVO theory have been made by the adoption of more realistic assumptions and by considering additional forces.

1.2.2.1 Hydration Forces

Early work by Israelachvili and Adams¹³ showed an additional (compared to DLVO theory) repulsion between mica surfaces in the presence of potassium nitrate solutions. Their study stated that the additional repulsion was independent of salt concentration. The work also proposed that this force might be independent of electrolyte type.

Later experimental work by Pashley¹⁴ also revealed repulsive forces between mica surfaces in excess of DLVO theory, but with a different conclusion. Experiments conducted in sodium and potassium salt solutions showed an additional repulsion at salt concentrations greater than 10^{-4} M, and several key conclusions were drawn. The additional repulsion was present at high, negative surface potentials when the substrate had no ability to hydrogen bond. In addition, these repulsive forces were absent when H^+ was the most abundant surface counter-ion. Subtraction of DLVO theory from the experimental forces gave a repulsive force with an exponential decay length of about 0.9 nm. This repulsion was determined to be the result of overlap of hydration shells of ions between the two interacting surfaces. As the surfaces come closer, the hydrating water molecules must be lost to accommodate this decreased volume. Work must be done to remove the water of hydration, which leads to the repulsive force.

Further work has shown that, while this repulsion is the result of hydration effects, it is slightly more complicated.¹⁵ On mica it was determined that ion exchange at the surface plays an important role. In electrolyte solutions, protons are displaced from the mica surface and replaced by cations from solution. This would explain the absence of hydration repulsions in the presence of acid, where the protons are the cations. Furthermore, it was found that K^+ ions cause hydration effects at 10% surface coverage where Li^+ , Na^+ , and Cs^+ do not produce such effects until a coverage of 30%. This discrepancy is due to the natural occurrence of K^+ on mica surfaces. Thus, K^+ fits the

lattice sites of mica better than the other cations. Pashley also suggested that the exact nature of this hydration force is difficult to determine by comparison to DLVO theory because the Hamaker constant for the van der Waals attraction will differ in the region of highly concentrated salt between the surfaces. Pashley concluded that since the hydration force was only present at higher electrolyte concentrations, the hydration force is dependent upon the state of the hydrated ions between the surfaces. If the adsorbed hydrated ions can exchange with protons, then they can leave the region from between the surfaces and be replaced by protons from solution. If this occurs, there is no hydration force. On the other hand, if the hydrated ions are prevented from desorbing, then a decrease in separation is affected by removing the water of hydration. Pashley later showed that this net hydration force followed a double-exponential decay.¹⁶ The double-exponential is due to a primary (surface hydration) and secondary (hydration of adsorbed ions) hydration force. For the cases of lithium, sodium, potassium, and cesium salts, the second decay length was on the order of 1 nm, while the first decay length was 0.3nm for Li^+ and Na^+ , but 0.17nm for K^+ and Cs^+ . Parsegian reported that hydration repulsions between surfactant bilayers had larger decay lengths (2.7-3.3 nm).¹⁷

In the early 1980's Rabinovich and co-workers¹⁸ reported structural forces between glass threads in KCl solutions, however, they have not elaborated on the nature of these forces. In separate studies, Yoon and Yotsumoto studied the hydration force on rutile (TiO_2)¹⁹ and silica.²⁰ For rutile, no additional hydration force was present in the absence of salt. In the presence of NaCl above 20 mM, hydration forces were observed and fit a double exponential as suggested by Pashley.²¹ For silica, a hydration force is observed in the absence of salt. This additional repulsion between silica surfaces has also been seen by Ducker et al²² and is attributed to a primary hydration force as mentioned earlier.

Later work by Yoon and Subramanian²³ on fully hydroxylated silica showed hydration forces below 15 nm separations in the water. These hydration forces were not observed in the presence of 15% methanol and were decreased in 10-20% ethanol. They suggested that this result is due to the disruption of the water structure by alcohol at the silica-water interface. Hydration forces in this study were unaffected by pyridine or trifluoroethanol, suggesting that these molecules cannot displace water from the silica surface.

Experimental observations of hydration repulsions stem from the energy required to remove the water adsorbed to hydrophilic surfaces (primary) or due to the removal of hydration shells of adsorbed hydrated ions (secondary). If the hydrated ion can exchange with an unhydrated ion or can simply desorb, then no hydration force is observed.

Monte Carlo simulations and density fluctuation theory (DFT) studies of hydration forces by Forsman et al²⁴ for two flat planar surfaces separated by water showed that when the Debye-length (κ^{-1}) is larger than half a molecular diameter a strong repulsion in addition to DLVO is apparent. DFT studies were conducted with non-polar liquids as the intervening medium. Similar solvation forces were apparent in non-polar solvents for substrates, which were sufficiently solvophilic.

Theoretical studies by Burak and Andelman²⁵ have shown an attractive component to the hydration force. Their work predicts a less repulsive force at high surface charge. The authors failed to mention whether their comparison was to that of the constant charge or constant potential form of Poisson-Boltzmann. It could be that their results are simply one of the intermediate cases between constant charge and constant potential although it has been mentioned in the literature that the hydration interaction is actually attractive or oscillatory.²⁶ Israelachvili and Wennerström²⁶ have mentioned that it is the entropy loss of counter-ions as the surfaces approach that leads to the repulsion.

1.2.2.2 “Hydrophobic” Forces

Some surface force measurements reveal forces that are more attractive than predicted by DLVO Theory. These forces often occur between two surfaces with high water contact angles, and therefore are called “hydrophobic” forces. The mechanism for this large attraction continues to be a source of great debate. Furthermore, there are surfaces that are innately hydrophobic and those made hydrophobic by the addition of surfactant.

Three possible explanations have arisen in the literature to explain “hydrophobic” forces. (1) One school of thought is that these forces arise due to an increase in chemical potential of water molecules between the surfaces than in the bulk. To maintain equilibrium, the water molecules leave the volume between the surfaces and move to the bulk where they can readily hydrogen bond. (2) Another belief is that these strongly

attractive forces are brought about by cavitation of small bubbles between the surfaces.

(3) The possibility of an induced dipolar attraction has also been proposed. Below several studies involving these extraordinarily long-ranged attractive forces are outlined.

(1) Isrealachvili and Pashley²¹ studied the effects of the adsorption of cetyltrimethylammonium bromide (C₁₆TAB) onto negatively charged mica surfaces. They note that just below the critical micelle concentration (*cmc*) of C₁₆TAB, the surfaces go from negatively charged to neutral hydrophobic surfaces as the positive charged surfactant adsorbs. Comparison of force plots to DLVO theory showed an additional attractive component in excess of van der Waals attractions. They reported a decay length of 1.0 nm for this additional attractive force and state that the strength of this force is independent of electrolyte and pH. Claesson and co-workers²⁷ showed a similar short-range decay of 1.2 nm between surfaces made hydrophobic by surfactant.

Pashley et al²⁸ showed that adsorption of dihexadecyl dimethylammonium acetate (DHDAA) on mica surfaces leads to the formation of a hydrophobic surface. When these surfaces are brought within close proximity (less than 15 nm), attractive forces are observed on the order of one to two orders of magnitude greater than those for simple van der Waals attractions. The decay length reported in the presence of DHDAA is 1.4 nm compared to 1.0 nm reported previously for C₁₆TAB. Despite the fact that cavitation is known to occur in the presence of strongly hydrophobic surfaces, the authors report the absence of such cavitation in adsorption studies with C₁₆TAB, but mention the formation of a bridging bubble when the DHDAA/mica surfaces are separated.

Yoon and co-workers²⁹⁻³¹ conducted several studies of the “hydrophobic” force produced by adsorption of dodecylammonium chloride surfactant. They fit the hydrophobic force to a power law like that of the van der Waals force. Comparison of the hydrophobic force constant to the Hamaker constant from the dispersion interaction gives a comparison of the magnitude of the forces. It was found that the hydrophobic force constant is about an order of magnitude larger than the Hamaker constant.³¹ In studies done on mica, short-range “hydrophobic” forces were apparent in surfactant at pH 5.7. The decay length of this force was 1.3 nm, similar to those found in other surfactants by Pashley.^{21,28} At pH 9.5, a longer-ranged force was present with an exponential decay

length of 5.5nm. A similar decay length of 5.6 nm has been found by Parker et al³² for the attraction between silanated glass surfaces.

In the presence of decanol, Yoon²⁹ found a decay length of 9 nm. These longer ranged forces were attributed to co-adsorption of ionic and neutral molecules contributing to a larger packing density of hydrophobic chains on the surface. Furthermore, 0.1 mM KCl was found to reduce the jump-in distance and long-range attraction in the surfactant/mica systems.

Claesson et al^{27,33} suggest that the hydrophobic attraction is a result of surface induced water structure. They reported decay lengths of 15.8 nm for long-range attractive forces in double-chain cationic surfactant solutions. They suggested that hydrogen bond propagated ordering effects are a large contributor, however, they did not explain the extension of such forces out to 90 nm separations. This surface induced water structure was shown in simulations by Derjaguin, where the dipoles of water were shown approximately perpendicular to hydrophilic and parallel to hydrophobic surfaces.¹²

The hydrophobic interaction is often reported as a strong long-ranged attraction in excess of Hamaker-Lifshitz forces.^{34,35} Yaminsky and Ninham report that hydrophobic attractions take place as a result of density fluctuations between surfaces in poorly wetting liquids.³⁴ This result is further supported by density functional theory calculations and Monte Carlo simulations by Forsman and co-workers.³⁵ They show that a liquid density depression between hydrophobic surfaces leads to a strong attraction in excess of DLVO. They find that this density depression and subsequent attractive force occurs even in the absence of vapor nucleation between surfaces.³⁵ Earlier studies by Forsman et al³⁶ show agreement with experimental results at smaller separations and show no evidence of cavitation.

(2) In other studies, it has been suggested that hydrophobic attractions of larger ranges (on the order on 100nm) are caused by a bridging bubble mechanism.³⁶ Experimental evidence of these bridging bubbles has been given by Carambassis et al.³⁷ The range in which these bridging bubbles were apparent on hydrophobized silica was 20-200nm. A thermodynamic analysis by Attard,³⁸ suggests the stability of microscopic bubbles between hydrophobic surfaces at separations less than 50 nm. Furthermore, he

reports that the bubbles are convex when the contact angle is below 90° and concave when the contact angle is above 90° .

Recent work by Butt et al³⁹ showed large jumps in attractive curves between hydrophobic surfaces in the absence of surfactant and suggests bridging bubbles as the mechanism. Higashitani et al⁴⁰ showed that degassing solutions of trimethylammonium surfactants leads to a reduction in the attractive force. Furthermore, degassing led to a loss of discontinuous jumps that are observed in gassed solutions. They attributed these jumps to the presence of bubbles. Work by Ducker et al⁴¹ suggests that a large portion of the reduction in attraction caused by degassing solutions is the result of a shift in the point of zero charge (pzc) brought about by changing the pH.

Craig et al⁴² showed that the hydrophobic interaction between silica surfaces coated with cetylpyridinium chloride (CPC) surfactant was independent of added electrolyte up to 100 mM. They also reported that smaller ranges for the hydrophobic force may be the result of a decreased interaction of the surfaces with dissolved gases.⁴² This also supports a bridging bubble mechanism in the case of the longer ranged attraction.

In addition, the long-range attraction was found only when the advancing contact angle on the surface was greater than 90° .²⁹ Yoon²⁹ has suggested that cavitation effects above this critical contact angle allow for the extended range of the hydrophobic force. Studies of hydrophobic surfaces in argon-saturated water show an increased attraction, further supporting the cavitation theory.⁴³ In addition, the force increased rapidly as the advancing contact angle exceeded 95° .

The effect of salt on the hydrophobic force has been debated. Addition of salt has been reported to reduce attraction,^{29,44} while other work has deemed the hydrophobic attraction to be weakly salt dependent.²⁷

Mention of cavitation and bubble bridging as a mechanism for the hydrophobic force, coupled with discrepancies in the literature as to the effect of salt on the hydrophobic force, leads to the following discussion of bubbles, electrolytes and the link between them.

Considine⁴⁵ showed a large attractive jump between latex spheres in aqueous solutions. In the absence of surfactants, these attractions were independent of electrolyte concentration and the range was highly dependent on dissolved gases in the solution.

They proposed coalescence of small bubbles attached to the approaching hydrophobic surfaces as a possible mechanism. By passing degassed solutions through the AFM flow cell, they obtained force-distance profiles with a significantly reduced 'jump-in'. This bubble coalescence model has been proposed by Ishida et al.⁴⁶ on the basis of force measurements coupled with AFM imaging of bubbles attached to a silanated silica surface and by studies of the change in force profiles at first contact and subsequent interactions.⁴⁷ They found short-ranged hydrophobic forces at first contact and a significantly increased range on subsequent encounters. Despite this effect, they reported that dissolved gas does not affect the force curves. Instead, they postulate that exposure to air causes nano-bubbles on the hydrophobic surface. Yakubov⁴⁸ showed a considerable 'jump-in' between hydrophobic surfaces that also depended upon subsequent contacts, similar to the results of Ishida mentioned above. This also supports the theory of a bridging bubble leading to the long-range hydrophobic interaction.

Craig et al.⁴⁹ also studied dissolved gas effects of force profiles. They studied the forces between silica surfaces in the presence of C₁₆TAB and also CPC in 100 mM NaCl. In both cases, a reduction in the range of the attractive force was obtained when the samples were degassed. To further study the effects of cavitation, they looked at neutron irradiation of the samples, which is known to increase cavitation.⁵⁰ The neutron irradiated samples showed an increased attractive force, thereby supporting the hypothesis that cavitation affects the hydrophobic attraction. Ultimately, their results are consistent with a proposed mechanism that the hydrophobic attractions are caused by the meta-stability of the intervening aqueous layer between hydrophobic surfaces.

The direct measurement of the interaction between a bubble and a hydrophobic silanated silica surface has been measured.^{47,51,52} Ducker⁵² and Ishida⁴⁷ both show no repulsion and a strong attractive 'jump-in' for this interaction, while Fielden and co-workers⁵¹ report a monotonic repulsion. The reason for this discrepancy is unknown.

Craig and co-workers⁵³ have conducted an extensive study on the effects of different salts on the coalescence of bubbles. They reported that HCl and H₂SO₄ have no effect on bubble coalescence. Given the proposed bubble effects on the hydrophobic force, they postulated that only salts that reduce bubble coalescence could reduce the hydrophobic attraction. This hypothesis could explain the discrepancies mentioned previously.

(3) Additional work suggests that the long-range attraction could be the result of reordering of adsorbed molecules to cause an induced electrostatic attraction between surfaces. Experimental observations by Tsao et al⁵⁴ showed forces in double-chain surfactants that were larger than the van der Waals force. They proposed that the attraction is due to polarized domains of surfactant on the surface and presented AFM images showing patches of varying height. They used a model including the idea of correlations between domains to explain their data.

Using a charge regulation primitive model, Spalla et al^{55,56} have shown that attractive forces can occur between net neutral surfaces that are coated in adsorbed ions. This attraction occurs as the result of ion-ion correlations. Furthermore, they have shown reasonable agreement with experimental work on C₁₆TAB coated glass surfaces.⁴⁴ In addition, Miklavic et al⁵⁷ have used double-layer theory to show that attractive forces can occur between net neutral surfaces interacting at the constant potential boundary or when the ions on the surfaces are free to migrate. They report decay lengths that are dependent upon charge inhomogeneities and the Debye-length. Ion-ion correlations seem like a plausible explanation for the longer ranged attractions found in surfactant solutions, since the attractions are often found at concentrations where the surface charge is expected to be net-neutral.

1.2.2.3 Oscillatory Forces

Oscillatory forces arising from the displacement of molecules from the intervening liquid layer between particles have also been reported in the literature.^{7,26} The periodicity of the oscillatory force corresponds to the molecular diameter of the molecules being excluded. These oscillations are often not apparent in force measurements due to surface roughness effects and low concentrations of excluded species.

1.3 Experimental Techniques for Colloidal Force Measurement

1.3.1 Disjoining Pressure

The first methods of determining the forces between surfaces were the measurement of the disjoining pressures between a bubble and a solid surface⁴ and the measurement of forces between a flat solid and an optical lens by Derjaguin.^{58,59} In the first method the

liquid film thickness was measured optically, while the internal pressure of the bubble was monitored by the Laplace equation. In the second technique, the separation between the solids was determined optically by measuring Newton's rings. The force was measured from the electric current required to balance the surface forces with a microbalance. Additional details are given elsewhere.⁵⁹ A series of measurements at different separations can provide a force versus separation curve.

1.3.2 Surface Forces Apparatus (SFA)

Disjoining pressure measurements were the preferred means of studying interfacial forces until the development of the SFA in 1978. Developed by Israelachvili, the SFA was specifically designed to measure forces between perpendicular cylinders covered in a thin mica layer.¹³ The force between two crossed cylinders is measured by the deflection of a double cantilever spring of known spring constant. The separation between the rods is measured by analyzing fringes of equal chromatic order using interferometry. The use of the SFA revolutionized the measurement of surface forces for the next decade.

1.3.3 Atomic Force Microscopy (AFM)

In 1986 Binnig et al developed AFM.⁶⁰ AFM was originally designed to image solid substrates, using the surface forces as the contrast mechanism. Several years later, Ducker et al.^{22,61} began using an atomic force microscope (AFM) to measure inter-particle forces in liquids. This was done by attaching a micron-sized particle to a commercially available AFM cantilever by means of an epoxy resin. Analysis of cantilever deflection-distance profiles, as well as knowledge of the spring constant of the cantilever, allows for the determination of a force versus separation curve. Due to its simplicity, AFM has become a very prominent means of measuring inter-particle forces and will be the method of choice in this work. Additional information will be given in chapter 2.

1.3.4 Additional Techniques

Osmotic pressure has also been used as a means for determining inter-particle forces in aqueous dispersions of particles.⁶²⁻⁶⁴ Yet another method in the literature for

measuring forces between particles is differential electrophoresis.⁶⁵ While this method appears to have limitations in determining forces as a function of separation, it does appear to provide accurate values for forces between particles at their equilibrium separation. Other methods of force measurement that can be found in the literature include total internal reflection microscopy (TIRM),⁶⁶ force balance,⁵⁹ and Interfacial Gauge.⁶⁷

1.4 Surfactants in Bulk Solution

1.4.1 Surfactants

As a prelude to a discussion of surfactant adsorption on solid surfaces, the behavior of surfactants in bulk solution will be discussed. Surfactants are the primary ingredient in soaps and detergents and, as mentioned above, they are used as a means to stabilize colloidal particles. A surfactant consists of a hydrophilic head group (either charged or uncharged) and a hydrophobic tail. Fig. 1.3 shows the structure of two surfactants used in this work. The hydrophobic tails are insoluble in polar solvents, while the head-groups are often very soluble in polar solvents. As a consequence of this “dual-identity”, surfactants have the unique ability to spontaneously self-assemble into larger aggregates in solution.

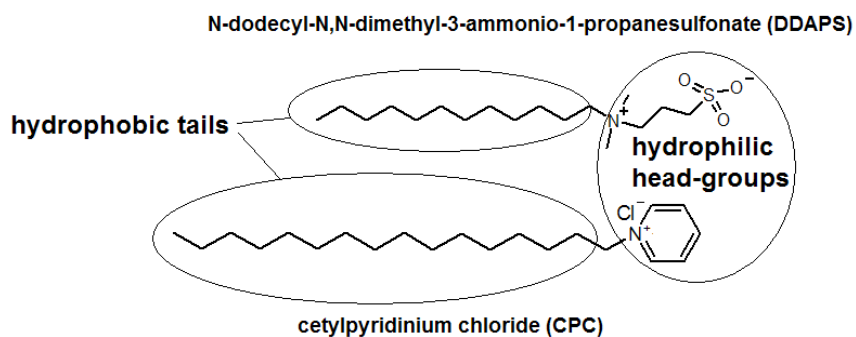


Figure 1.3 Illustration of two surfactants.

1.4.2 Surfactant Solutions

In this thesis, the forces between solid surfaces coated in surfactant are discussed. These force measurements are performed such that the surfaces are in equilibrium with a large reservoir of bulk surfactant solution. Therefore, the behavior of surfactants in bulk

solution should be discussed. As mentioned, surfactants can aggregate in solution. This aggregation occurs above a critical temperature and concentration. The critical temperature or Krafft temperature is the minimum temperature required to form micelles in solution. The critical concentration at which micelles form, is known as the critical micelle concentration (*cmc*).

The *cmc* can be determined by measurement of surface tension, conductance, osmotic pressure, turbidity, and by selective-electrode potentials.⁷ Fig. 1.4 shows how some of the physical properties of surfactant solutions change near the *cmc*. Different measurements yield slightly different *cmc* values depending upon the technique used because the formation of micelles occurs over a small concentration range. Different techniques are sensitive to different concentrations in this range.

Micellization occurs rather than precipitation due to a competition between repulsive and attractive forces. This results in a minimum in the chemical potential as a function of aggregation number and allows formation of a thermodynamically stable aggregate of a defined size. The competing forces causing micellization include the attractive hydrophobic chain interaction (short-range hydrophobic effect) and the repulsion between head groups. For nonionic surfactants, the head group repulsion is reduced (no electrostatic component), leading to a lower *cmc*. Furthermore, the aggregation numbers for nonionics are higher than for ionic surfactants.

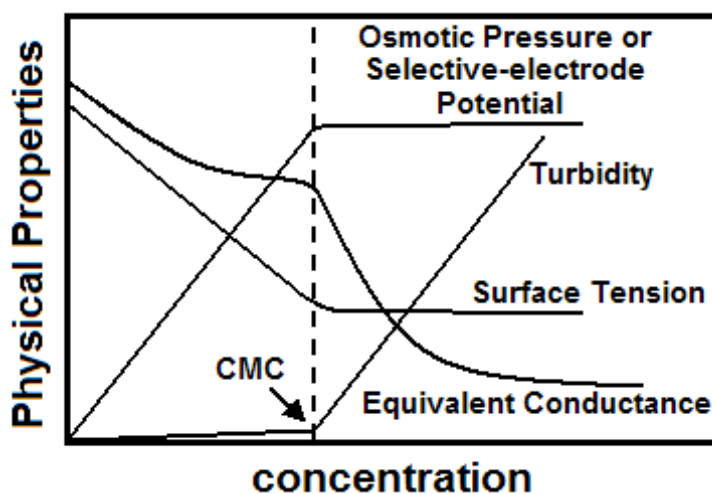


Figure 1.4 Physical properties of surfactants solutions near the *cmc*. All properties shown show a change in slope near the *cmc*.

Here the effects of temperature, chain length, and salt concentration on the *cmc* in bulk solution are discussed.⁷ As the temperature of the solution is increased, the *cmc* increases and the aggregation number decreases as a result of the increased surfactant solubility (decreased short-range hydrophobic effect). Increasing the hydrophobic chain length, leads to aggregation at lower concentrations. As a consequence, the *cmc* decreases and the aggregation number increases as the chain length increases.

A detailed theory of micellar shapes has been devised by Israelachvili et al⁶⁸ This theory introduces a surfactant packing parameter, N_s . Eq. 1.14 relates the packing parameter to the effective head group area, a_o , the volume of the hydrophobic tail, v , and the length of the hydrophobic chain, l .

$$N_s = \frac{v}{la_o} \quad (1.14)$$

The value of N_s determines the shape of the micelles in solution. For values of $N_s \leq \frac{1}{3}$, spherical micelles form in solution. For $\frac{1}{3} < N_s < \frac{1}{2}$ the shape is cylinders. For $\frac{1}{2} < N_s < 1$ bilayer structures are formed. When N_s exceeds 1, inverted micelles or vesicles are formed.

Electrolyte concentration is another factor that influences micellar properties. Increasing the ionic strength of the solution leads to a decrease in the *cmc* due to the increased shielding of the electrostatic repulsions between head groups, and thus a decreased effective head group area, a_o .

1.5 Surfactant Adsorption to Solid Surfaces

This section discusses how surfactants adsorb at the solid-liquid interface, with particular emphasis on adsorption of cationic surfactants at the silica-water interface. Adsorption will be discussed in relationship to surfactant structure, substrate effects, and added electrolyte.

The discussion will begin with the thermodynamic driving forces both for and against adsorption. The more polar portion of a surfactant tends to adsorb to the more polar portion of a surface, whereas the hydrophobic tails tends to adsorb to the more hydrophobic regions of a surface.⁶⁹ There are several competing enthalpic, as well as entropic effects that govern adsorption. For a hydrophilic surface, there is a competition

between the polar surfactant head and the water at the surface. It costs energy to remove the water of hydration, however, a more hydrated surfactant can minimize this enthalpic loss. In addition, the hydrophobic chain prefers to be at the surface rather than aqueous solution. This process is much more favorable, when the surface is hydrophobic. In addition, if the surface possesses charge, a Coulombic attraction or repulsion may also be present. High densities of charged surfactant at an interface can also lead to lateral Coulombic forces between adjacent adsorbed surfactant molecules. Entropic factors are also present. Molecules adsorbed to a surface lose entropy compared to the bulk. Desorption of water or other ions from a surface as the surfactant adsorbs will contribute a favorable entropic contribution to the overall adsorption process.

The amount of adsorbed surfactant as a function of equilibrium surfactant concentration at constant temperature (the adsorption isotherm) is one key to understanding surfactant adsorption. One of the most prevalent means of producing an adsorption isotherm is by a solution depletion method, whereby particles are equilibrated with surfactant solution and the concentration change is measured. The concentration change multiplied by the solution volume gives the adsorbed amount. This method requires an accurate method for determining the concentration of a surfactant in solution. The concentration of surfactant can be measured from two-phase titrations,^{70,71} one-phase titrations,^{72,73} photometric titrations,⁷⁴ electrochemical methods,⁷⁵⁻⁸¹ several precipitation methods,^{82,83} and EPR.^{84,85} UV spectroscopy can also be used if the surfactant contains a UV chromophore.^{86,87} Other methods found in recent literature for determining adsorption isotherms include optical reflectometry,⁸⁸⁻⁹⁰ *in situ* ellipsometry,^{91,92} and attenuated total reflectance infrared spectroscopy (ATR-IR).^{93,94} The latter three techniques are surface specific and give a direct measurement of the surface excess concentration.

1.5.1 Adsorption Equilibrium of Cationic Surfactants

Koopal et al^{86,95} studied the effects of dodecyl pyridinium chloride (DPC) and cetyl pyridinium chloride (CPC) adsorption on silica. Contact angles, flotation recovery, and colloid instability all reached a maximum at the charge compensation point (*ccp*). The *ccp* is when the amount of surfactant adsorbed is sufficient to neutralize the surface

charge. Koopal et al found an inverse relationship between the magnitude of the surface charge and the contact angle of water. This is consistent with the adsorption of surfactant both neutralizing the surface charge and simultaneously increasing the surface hydrophobicity as a result of the hydrocarbon tails. They found that both DPC and CPC adsorbed similarly in the first layer, however, CPC adsorbed in larger amounts in the second layer, and the adsorption isotherm showed a steeper rise in the region between steps. They attributed the steeper rise to increased interactions between the longer chains of CPC. Furthermore, they also attributed this longer chain length to the fact that the hydrophobicity (given by the contact angle with water) showed a sharper maximum in CPC than in DPC.

In the presence of salt, the adsorption isotherm of $C_{16}TAB$ on silica changes from a stepped isotherm to a more “S-shaped” isotherm.⁸⁹ This was also shown for DPC and CPC.^{86,87} Atkin et al⁸⁹ showed that pH has little effect on $C_{16}TAB$ adsorption kinetics in the absence of salt. Below the *cmc* in salt, an increase in pH increases the sticking ratio, which is the ratio of the observed kinetics to the theoretical diffusion-limited kinetics. The increase in sticking ratio leads to increased adsorption below the *cmc*. In the presence of salt, Koopal et al⁸⁶ showed that the adsorption plateau above the *cmc* increases as pH is increased. This effect was also reported by Szekeres et al⁹⁶ In addition, Koopal found that all adsorption isotherms in salt had a common intersection point corresponding to the point of zero charge. This point depended upon pH, surface charge and surface potential.

Several papers have reported this common intersection point in adsorption isotherms of cationic surfactants on silica.^{86,87,91,96-98} It has been found that below this point, the addition of salt decreases adsorption, while above this point, the addition of salt increases adsorption. The adsorption suppression below the *ccp* is considered to be a result of the shielding of surface charge, in turn decreasing the Coulombic attraction between the surfactant and the surface. Above the *ccp*, the enhanced adsorption results from screening of the charged head-groups, allowing a more tightly packed second layer. This is consistent with experimental work done by Velegol et al⁸⁸ and with theoretical studies by Hall.⁹⁹

Wangnerud⁹¹ showed by *in situ* ellipsometry that the extent of dissociation of silanol groups on silica is dependent on both pH and the surface excess of $C_{16}TA^+$. This has also been shown through surface titrations by Koopal et al,⁸⁷ who reported an increase in negative surface charge as surfactants adsorb at low concentrations. Studies conducted in 10 mM salt showed that the adsorption of $C_{16}TA^+$ increased as pH is increased.⁹¹ This was attributed to an increase in charge density as protons are removed from the silanol groups on silica. It is apparent that the charge on the surface plays a critical role in surfactant adsorption. Experimental work on surfactant adsorption on constant charge self-assembled monolayers on gold by Tulpar and Ducker,¹⁰⁰ has shown that the adsorbed amount at the first plateau scales with the charge on the surface. It was also shown that the adsorption in the second layer increased with an increase in the surface charge.

1.5.2 Dynamics of Surfactant Adsorption

Important for the work conducted in this thesis is the kinetics of adsorption and the rearrangement of adsorbed layers. Optical reflectometry work by Atkin et al, show that the initial rate of adsorption is enhanced by a longer aliphatic chain on trimethylammonium surfactants.¹⁰¹ Furthermore, the slow adsorption regime reported in the absence of electrolyte is seen to disappear for adsorption of cetylpyridinium bromide surfactants on silica in 10 mM KBr.¹⁰² Pagac et al¹⁰³ studied adsorption and desorption of $C_{16}TAB$ and found that adsorption occurred slower on the first adsorption. When the layer was partially desorbed and re-adsorbed, the second adsorption occurred faster over the same range of surface excesses. Pagac attributed this to a restructuring of the initial layers with time. Recent spectroscopic studies by Clark and Ducker,⁹⁴ showed that the exchange of tetradecyltrimethylammonium surfactants in and out of an adsorbed layer is very rapid even in the absence of added electrolyte.

1.5.3 Structure of Adsorbed Surfactant Aggregates

Several studies have been done using AFM to image adsorbed surfactant structures *in situ*. These studies will now be discussed, however, as will be shown in this thesis, the force used as the feed back mechanism in AFM, may have the ability to change the aggregates. Early studies of adsorbed surfactant structures were done by Manne et

al.^{104,105} They showed that quaternary ammonium surfactants (mainly C₁₄TAB) formed surface aggregates at concentrations twice the *cmc*. Aggregate structures varied according to substrate. Spherical aggregates were reported on silica, cylindrical aggregates were found on mica, and for graphite and MoS₂ surfaces hemi-cylinders were reported.¹⁰⁵ It must be noted that AFM does not provide the ability to discriminate hemispheres or hemi-cylinders from full spheres or cylinders.

Ducker and co-workers¹⁰⁶⁻¹¹⁰ have done extensive studies relating the effect of surface, counter-ion, and added electrolyte composition on the structure of adsorbed aggregates. They found a decrease in the adsorbed aggregate curvature as the surface hydrophobicity increases in zwitterionic systems.¹⁰⁷ This was attributed to a favorable decrease in the contact between the hydrophobic portion of the surfactant and water. Lamont and Ducker¹⁰⁹ also studied the effect of added salt on the organization of C₁₆TAB adsorbed to mica. They found that added salt increases the curvature of the aggregate, and that the effect increases along the order Li⁺, K⁺, Cs⁺. The more polarizable co-ion in this case increases curvature. This is in contrast to the effect of surfactant counter-ions, which decrease the curvature as the polarizability increases.¹⁰⁶ The cation effect is due to the adsorption of these co-ions to the solution-mica interface.

Subramanian and Ducker¹⁰⁶ have postulated that the “hard” or “soft” nature of the counter-ion dictates the curvature of the adsorbed structure. “Soft” ions are more polarizable and can more effectively shield head groups leading to a less curved structure. “Hard” ions on the other hand, are highly hydrated and cannot approach the head groups as closely. This leads to a less shielded repulsion between head groups and therefore more curved aggregates.

Velegol et al⁸⁸ have also studied the effect of counter-ions and added electrolyte on surfactant adsorption to silica. They showed that changing the counter-ion from Br⁻ to Cl⁻ decreases the maximum adsorption by 60% and changes the structure of the adsorbed species from cylinders to spheres above the *cmc*. These structural changes are consistent with the “hard”/ “soft” theory mentioned above.

At low salt and surfactant concentrations, Koopal^{86,87} proposed that the initial adsorption of DPC and CPC occurs parallel to the surface. This occurs on a pyrogenic silica, which is more hydrophobic than a fully hydroxylated silica.⁸⁹ This effect was also

seen by Zajac et al.¹¹¹ for benzyldimethyl ammonium bromide on a hydroxylated silica in the absence of salt. At high salt (100 mM), however, chains were not parallel to the surface. Their study did not include intermediate salt concentrations. EPR studies have shown that a spin-labeled version of C₁₆TAB also adsorbs flat at low surfactant concentrations and low pH.⁸⁴

As the surface excess increases, the surfactant-chains can interact with each other more favorably than with water (short-range hydrophobic effect). When this occurs the adsorption rises. The concentration where this tail association begins has been called the hemi-micelle concentration, *hmc*.¹¹² Neutron reflectivity studies of C₁₆TAB adsorbed to amorphous silica, suggest that a defective bilayer of flattened micelles exist between $\frac{1}{2}$ and $\frac{2}{3}$ *cmc*.^{113,114}

1.5.4 Overview of Adsorption

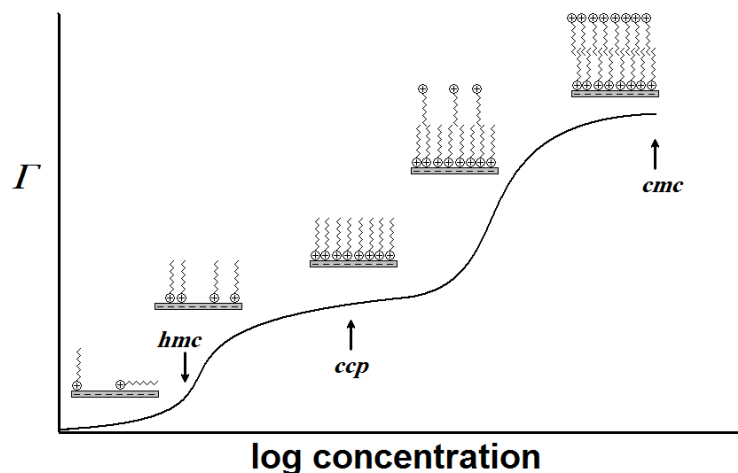


Figure 1.5 General adsorption isotherm and representative surfactant structures on the surface.

In summary, for the negatively charged surfaces discussed in this work, a general adsorption isotherm and corresponding surfactant structure is presented in Fig. 1.5. At low concentrations the surfactant adsorbs relatively flat and gradually extends away from the surface allowing for more tail-tail interactions. After the charge on the surface has been compensated, the additional surfactant changes orientation and adsorbs with its head away from the surface. As the *cmc* is approached, a bilayer-like structure forms.

Depending upon the actual system, other structures can form. In our particular systems, it is more likely that spherical or hemi-spherical structures are present near the *cmc*.

1.6 Proximal Adsorption

1.6.1 Theory

In the section about colloidal forces, the work of Ninham and Parsegian regarding surfaces with ionizable groups was discussed.¹⁰ As these types of surfaces interact the degree of ionization can decrease (counter-ion adsorption) to minimize the electrostatic double-layer repulsion. This concept is known as charge regulation and can be extended to all ions in solution. Flux of ions in and out of the double-layer can help to reduce the repulsive double-layer and regulate the interaction. A general thermodynamic relationship for the regulation of adsorption of all ions was derived by Hall¹¹⁵ and a year later by Ash et al.¹¹⁶ This equation relates changes in adsorption, Γ as a function of separation, s , to changes in E_a as a function of chemical potential, μ .

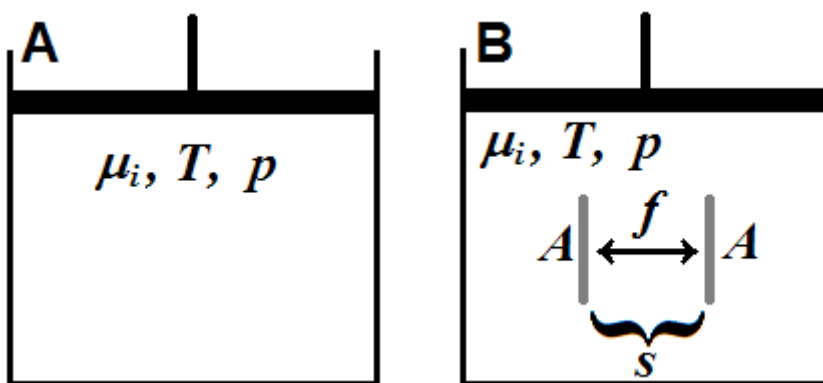


Figure 1.6 Two containers A and B containing solutions of molecules i . The chemical potentials of molecules i , the temperature, and the pressure are held constant in both systems. In container B, two surfaces each of area A are immersed having a separation, s and a force per unit area, f between them.

First, consider two containers A and B in Fig. 1.6, both of which are held at fixed chemical potential of all species i , and constant pressure and temperature. Immersed in container B are two surfaces of area A with separation, s , and inter-surface force per unit

area, f . The outer side of each surface is neglected because it has no interaction with the other surface. The differential Gibbs' free energy of each container is given by

$$dG^A = -S^A dT + V^A dp + \sum_i \mu_i dn_i^A \quad (1.15a)$$

$$dG^B = -S^B dT + V^B dp + \sum_i \mu_i dn_i^B + 2\gamma dA - AfdS \quad (1.15b)$$

where n_i is the number of molecules of i in the system, and γ is the surface free energy for each surface. Subtraction of eq. 1.15b from eq. 1.15a results in

$$d(G^A - G^B) = -(S^A - S^B)dT + (V^A - V^B)dp + \sum_i \mu_i d(n_i^A - n_i^B) - 2\gamma dA + AfdS \quad (1.16)$$

Integration at constant T , μ_i , p , and s yields,

$$(G^A - G^B) = \sum_i \mu_i (n_i^A - n_i^B) - 2\gamma A \quad (1.17)$$

Differentiation of eq. 1.17 yields,

$$d(G^A - G^B) = \sum_i \mu_i d(n_i^A - n_i^B) + \sum_i (n_i^A - n_i^B) d\mu_i - 2\gamma dA - 2Ad\gamma \quad (1.18)$$

Now subtracting eq. 1.16 from eq. 1.18 yields,

$$0 = (S^A - S^B)dT - (V^A - V^B)dp + \sum_i (n_i^A - n_i^B) d\mu_i - 2Ad\gamma - AfdS \quad (1.19)$$

Considering the case of constant T and p ,

$$2Ad\gamma = \sum_i (n_i^A - n_i^B) d\mu_i - AfdS \quad (1.20)$$

The difference in number of molecules in container B versus A, $(n_i^B - n_i^A)$ is simply the number of molecules adsorbed onto the two surfaces. Therefore, we can divide through by the total plate area, $2A$ and get,

$$-d\gamma = \sum_i \Gamma_i d\mu_i + \frac{1}{2} f dS \quad (1.21)$$

where Γ_i is the adsorbed amount of i per unit area.

Since eq. 1.21 is an exact differential, holding the chemical potential of all other species j constant, yields a Maxwell relation

$$\left(\frac{\partial \Gamma_i}{\partial S} \right)_{T, p, \mu_i, \mu_j} = \frac{1}{2} \left(\frac{\partial f}{\partial \mu_i} \right)_{T, p, S, \mu_j} \quad (1.22)$$

Integrating eq. 1.22 with respect to s from infinity down to some separation s , and remembering that $f = -\left(\frac{\partial E_a}{\partial s}\right)$, gives

$$\Gamma_i(s) - \Gamma_i(\infty) = -\frac{1}{2} \left(\frac{\partial E_a}{\partial \mu_i} \right)_{T,p,s,\mu_j} \quad (1.23)$$

In the case of an ionic surfactant adsorbing in the presence of excess electrolyte containing a common counter-ion, the chemical potential of the counter-ion is essentially unchanged and eq. 1.23 can be used. In the absence of a large reservoir of excess electrolyte, the cation and anion are linked. Often for a $Z:Z$ electrolyte it is convenient to consider the mean chemical potential $\mu_{\pm} = \frac{\mu_+ + \mu_-}{2}$. In this case eq. 1.22 becomes

$$\left(\frac{\partial(\Gamma_+ + \Gamma_-)}{\partial s} \right)_{T,p,\mu_i,\mu_j} = \frac{1}{2} \left(\frac{\partial f}{\partial \mu_{\pm}} \right)_{T,p,s,\mu_j} \quad (1.24)$$

Here, only the change in the sum of the surfaces excesses of both species can be calculated. In the case where the electrolyte adsorbs as a net neutral unit, then $\Gamma_+ = \Gamma_- = \Gamma_{\pm}$, and eq. 1.24 becomes

$$\left(\frac{\partial(\Gamma_{\pm})}{\partial s} \right)_{T,p,\mu_i,\mu_j} = \frac{1}{4} \left(\frac{\partial f}{\partial \mu_{\pm}} \right)_{T,p,s,\mu_j} \quad (1.25)$$

and the corresponding integration gives

$$\Gamma_{\pm}(s) - \Gamma_{\pm}(\infty) = -\frac{1}{4} \left(\frac{\partial E_a}{\partial \mu_{\pm}} \right)_{T,p,s,\mu_j} \quad (1.26)$$

Eq. 1.26 can be viewed as a sort of limiting case, although the true behavior can be much more complicated because on a charged surface, the surface excess of cations and anions will have opposite signs. This means that the total surface excess could change by +4 molecules by adsorbing 4 cations and desorbing no anions or by adsorbing 2 of each ion. Therefore, the adsorption of each species remains unattainable by this procedure.

The beauty of eq. 1.22 is that it is valid for all forces and is true for all substrate shapes and types as shown by Hall.¹¹⁵ Another advantage to using this Maxwell relation approach to studying forces and adsorption is that it is independent of the type of force present. Knowledge of the forces mentioned in the previous section is not required for

the quantitative determination of surface excesses with eq. 1.22. Knowledge of these forces is, however, important in determining the mechanisms for such adsorption processes.

One major stipulation for this analysis is that the system be at adsorption equilibrium. If the separation between particles changes too rapidly compared to the kinetics of adsorption, then the adsorption will not be at equilibrium and eq. 1.23 is no longer valid. Hall reports that at non-equilibrium conditions, a smaller force will be measured upon separation of the colloids, while a larger force will be present while bringing the particles together. Therefore, care must be taken to ensure that equilibrium is maintained in order for the proximal adsorption analysis to provide accurate results.

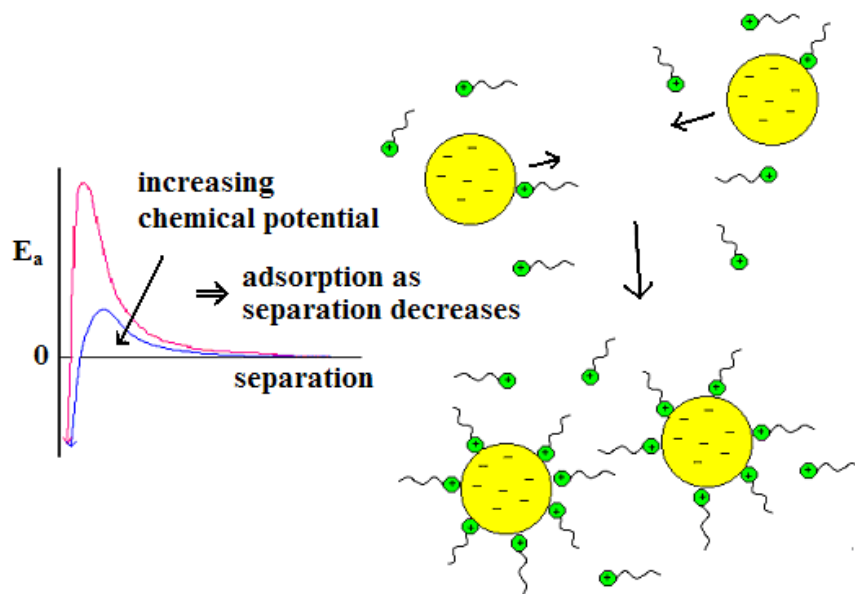


Figure 1.7 Schematic of proximal adsorption. Changes in adsorption change the interaction energies as a function of separation.

1.6.2 Studies of Proximal Adsorption

Ash et al¹¹⁶ utilized this Maxwell relation in the study of gas adsorption to solid surfaces. At high gas pressures the repulsive force between two plates increased as the pressure was increased. Utilizing an equation similar to eq. 1.22, they showed a positive

value for $\left(\frac{\partial \Gamma_i}{\partial s}\right)_{\mu_i, \mu_j, T, p}$ at high pressures. Therefore, the gas is desorbing from the surfaces as the separation decreases.

Pethica¹¹⁷ reported that small changes in adsorption result in large force changes. He showed that for free energy change of $25k_B T$ and a concentration change of 10%, an adsorption change of only 0.1% was present at a given separation relative to infinite separation. Yaminsky and co-workers¹¹⁸ showed that for C₁₆TAB adsorption to silica, similar small adsorption changes were present from infinite separation down to 20nm. Near the *ccp* (4.5×10^{-5} M), they found an increase in adsorption of approximately 1% down to 20 nm. Reducing the separation from 20 nm down to contact, however, resulted in an increase in adsorption of 300-400%. This separation range is similar to those reported for hydrophobic forces. Interestingly, they report that the *ccp* decreases as separation decreases. This is not surprising in that surfactant adsorbs to neutralize unfavorable repulsions at small separations.

Other studies of proximal adsorption are reported in the literature.¹¹⁹⁻¹²¹ Christensen and Yaminsky¹¹⁹ studied interactions on hydrophobic surfaces that were made hydrophobic by adsorption of cationic surfactants to mica. Podornik and Parsegiiian¹²⁰ and Pethica¹²¹ analyzed data from the literature in terms of the proximal adsorption analysis. In addition, Pethica used the proximal adsorption concept to analyze data from Kékicheff et al¹²² Notice that at low concentrations the surfactants adsorb as the separation is decreased. Above the *ccp*, the surfactants show desorption as the separation is decreased. This is consistent with the formation of a bilayer above the *ccp*. This desorption above the *ccp* occurs to reduce the electrostatic repulsion between positively charged surfaces (resulting from surfactant head groups extending from the surface).

Rutland and Parker¹²³ performed an extensive study of surface forces between glass surfaces in C₁₆TAB solutions, however, an analysis based upon eq. 1.23 was not performed. In these solutions, equilibrium may not be fully established due to the slow adsorption shown later by Atkin et al.⁸⁹ Nonetheless, Rutland and Parker found that the forces agreed best with the constant charge boundary condition of DLVO theory and that the plane of charge had to be shifted toward bulk solution to fit data at higher surfactant concentrations. Furthermore, they report attractive forces at concentrations well below

the expected *ccp*. They also showed that leaving the surfaces in contact at sufficiently low surfactant concentrations leads to a change in force and condensation of surfactant between the surfaces.¹²⁴

Recently, Subramanian and Ducker¹²⁵ studied the adsorption of dodecyltrimethylammonium bromide (C₁₂TAB) on glass/silica surfaces using AFM. At low surfactant concentrations ($< \frac{cmc}{10}$), the force curves go from monotonically repulsive to monotonically attractive over a range of two orders of magnitude in concentration. The proximal adsorption analysis shows that at separations smaller than 60 nm, surfactant adsorbs as the separation is decreased until the maximum attraction is achieved. At this maximum attraction, the adsorption remains constant within experimental error. As the surfactant concentrations are increased above $\frac{cmc}{10}$, the force curves become increasingly repulsive. This is indicative of desorption of surfactants as the separation is decreased. This is similar to the results found by Pethica. The explanation for this desorption is the same as presented earlier for Pethica's study. The energy of interaction becomes more repulsive as separation is decreased, and surfactant desorbs as the separation is decreased. In addition, in this regime, the amount of adsorption change is affected little from concentration to concentration.

In highly concentrated micellar solutions (~10–40 times the *cmc*), repulsion is decreased between 3 and 7 nm separations. This means that a large adsorption is occurring even in the presence of a steep repulsion due to surfactant head groups facing the solution. They attribute this adsorption to the overlap of depletion layers around adsorbed micelles.

The work of Subramanian and Ducker was indeed a big step forward in the study of proximal adsorption, in that it was the first study to specifically look at proximal adsorption over large concentration ranges. Like most of the studies above, the absence of a reservoir of electrolyte means that the analysis is complicated by the adsorption–desorption behavior of the counter-ion described with eqs. 1.25 and 1.26.

In this work the understanding of proximal adsorption will be improved by looking at systems where the proximal adsorption of the surfactant ion alone can be deduced.

Furthermore, the effects of ionic strength, pH, chain length, and the presence of other surfactants are examined. The inclusion of a Frumkin-style interaction term in the equation of state will be discussed as a means to improve the understanding of charge regulation in solutions of chain molecules.

1.7 Cited Literature

- (1) Hamaker, H. C. *Rec. Trav. Chim.* **1936**, *55*, 1015.
- (2) Hamaker, H. C. *Rec. Trav. Chim.* **1937**, *56*, 727.
- (3) Derjaguin, B. V.; Landau, L. D. *Acta Phys.-Chim URSS* **1941**, *14*, 633.
- (4) Derjaguin, B. V. *Trans. Faraday. Soc.* **1940**, *36*, 203.
- (5) Verwey, E. J.; Overbeek, J. T. G. *Theory of the Stability of Lyophobic Colloids*; Elsevier: Amsterdam, 1948.
- (6) Stern, O. *Z. Electrochem.* **1924**, *30*, 508.
- (7) Evans, D. F.; Wennerström, H. *The Colloidal Domain: Where Physics, Chemistry, Biology, and Technology Meet*, 2nd ed.; Wiley-VCH: New York, 1999.
- (8) Dzyaloshinskii, I. E.; Lifshitz, E. M.; Pitaevskii, L. P. *Adv. Phys.* **1961**, *10*, 165.
- (9) Derjaguin, B. V. *Kolloid-Zeitschrift* **1934**, *69*, 155.
- (10) Ninham, B. W.; Parsegian, V. A. *J. Theor. Biol.* **1971**, *31*, 405.
- (11) Derjaguin, B. V.; Churaev, N. V. *J. Colloid Interface Sci.* **1974**, *49*, 249.
- (12) Derjaguin, B. V.; Churaev, N. V. *Colloids and Surfaces* **1989**, *41*, 223.
- (13) Israelachvili, J. N.; Adams, G. E. *J. Chem. Soc. Faraday Trans. I* **1978**, *74*, 975.
- (14) Pashley, R. M. *J. Colloid Interface Sci.* **1981**, *80*, 153.
- (15) Pashley, R. M. *J. Colloid Interface Sci.* **1981**, *83*, 531.
- (16) Pashley, R. M. *Adv. Coll. Inter. Sci.* **1982**, *16*, 57.
- (17) Parsegian, V. A.; Rand, R. P.; Fuller, N. L. *J. Phys. Chem* **1991**, *95*, 4777.
- (18) Rabinovich, Y. I.; Derjaguin, B. V.; Churaev, N. V. *Adv. Coll. Inter. Sci.* **1982**, *16*, 63.
- (19) Yotsumoto, H.; Yoon, R. H. *J. Colloid Interface Sci.* **1993**, *157*, 426.
- (20) Yotsumoto, H.; Yoon, R. H. *J. Colloid Interface Sci.* **1993**, *157*, 434.
- (21) Israelachvili, J.; Pashley, R. *Nature* **1982**, *300*, 341.
- (22) Ducker, W. A.; Senden, T. J.; Pashley, R. M. *Langmuir* **1992**, *8*, 1831.
- (23) Yoon, R. H.; Subramanian, V. *J. Colloid Interface Sci.* **1998**, *204*, 179.
- (24) Forsman, J.; Woodward, C. E.; Jönsson, B. *Langmuir* **1997**, *13*, 5459.
- (25) Burak, Y.; Andelman, D. *J. Chem. Phys.* **2001**, *114*, 3271.
- (26) Israelachvili, J. N.; Wennerström, H. *Nature* **1996**, *379*, 219.
- (27) Claesson, P. M.; Blom, C. E.; Herder, P. C.; Ninham, B. W. *J. Colloid Interface Sci.* **1986**, *114*, 234.
- (28) Pashley, R. M.; McGuiggan, P. M.; Ninham, B. W.; Evans, D. F. *Science* **1985**, *229*, 1088.
- (29) Yoon, R. H.; Ravishankar, S. A. *J. Colloid Interface Sci.* **1996**, *179*, 391.
- (30) Yoon, R. H.; Ravishankar, S. A. *J. Colloid Interface Sci.* **1996**, *179*, 403.
- (31) Yoon, R. H.; Aksoy, B. S. *J. Colloid Interface Sci.* **1999**, *211*, 1.
- (32) Parker, J. L.; Claesson, P. M. *Langmuir* **1994**, *10*, 635.

- (33) Eriksson, J. C.; Ljunggren, S.; Claesson, P. M. *J. Chem. Soc. Faraday Trans. 2* **1989**, *85*, 163.
- (34) Yaminsky, V. V.; Ninham, B. W. *Langmuir* **1993**, *9*, 3618.
- (35) Forsman, J.; Jönsson, B.; Woodward, C. E.; Wennerström, H. *J. Phys. Chem. B* **1997**, *101*, 4253.
- (36) Forsman, J.; Jönsson, B.; Woodward, C. E. *J. Phys. Chem* **1996**, *100*, 15005.
- (37) Carambassis, A.; Jonker, L. C.; Attard, P.; Rutland, M. W. *Phys. Rev. Lett.* **1998**, *80*, 5357.
- (38) Attard, P. *Langmuir* **2000**, *16*, 4455.
- (39) Nguyen, A. V.; Nalaskowski, J.; Miller, J. D.; Butt, H.-J. *Int. J. Miner. Process.* **2003**, *72*, 215.
- (40) Sakamoto, M.; Kanda, Y.; Miyahara, M.; Higashitani, K. *Langmuir* **2002**, *18*, 5713.
- (41) Zhang, J.; Ducker, W. A. *in preparation*.
- (42) Craig, V. S. J.; Ninham, B. W.; Pashley, R. M. *Langmuir* **1998**, *14*, 3326.
- (43) Rabinovich, Y. I.; Yoon, R. H. *Colloids and Surfaces A* **1994**, *93*, 263.
- (44) Kékicheff, P.; Spalla, O. *Phys. Rev. Lett.* **1995**, *75*, 1851.
- (45) Considine, R. F.; Hayes, R. A.; Horn, R. G. *Langmuir* **1999**, *15*, 1657.
- (46) Ishida, N.; Inoue, T.; Miyahara, M.; Higashitani, K. *Langmuir* **2000**, *16*, 6377.
- (47) Ishida, N.; Sakamoto, M.; Miyahara, M.; Higashitani, K. *Langmuir* **2000**, *16*, 5681.
- (48) Yakubov, G. E.; Butt, H.-J.; Vinogradova, O. I. *J. Phys. Chem. B* **2000**, *104*, 3407.
- (49) Craig, V. S. J.; Ninham, B. W.; Pashley, R. M. *Langmuir* **1999**, *15*, 1562.
- (50) Sette, D.; Wanderlingh, F. *Phys. Rev.* **1962**, *125*, 409.
- (51) Fielden, M. L.; Hayes, R. A.; Ralston, J. *Langmuir* **1996**, *12*, 3721.
- (52) Ducker, W. A.; Xu, Z.; Israelachvili, J. N. *Langmuir* **1994**, *10*, 3279.
- (53) Craig, V. S. J.; Ninham, B. W.; Pashley, R. M. *J. Phys. Chem.* **1993**, *97*, 10192.
- (54) Tsao, Y.-H.; Evans, D. F.; Wennerström, H. *Science* **1993**, *262*, 547.
- (55) Belloni, L.; Spalla, O. *J. Chem. Phys.* **1997**, *107*, 465.
- (56) Spalla, O.; Belloni, L. *Phys. Rev. Lett.* **1995**, *74*, 2515.
- (57) Miklavic, S. J.; Chan, D. Y. C.; White, L. R.; Healy, T. W. *J. Phys. Chem.* **1994**, *98*, 9022.
- (58) Derjaguin, B. V.; Abrikosova, I. I.; Leib, E. *Vestnik AN SSSR* **1951**, *6*, 125.
- (59) Derjaguin, B. V.; Rabinovich, Y. I.; Churaev, N. V. *Nature* **1978**, *272*, 313.
- (60) Binnig, G.; Quate, C.; Gerber, G. *Phys. Rev. Lett.* **1986**, *56*, 930.
- (61) Ducker, W. A.; Senden, T. J.; Pashley, R. M. *Nature* **1991**, *353*, 239.
- (62) Barclay, L.; Harrington, A.; Ottewill, R. H. *Kolloid-Zeitschrift* **1971**, 655.
- (63) Barclay, L. M.; Ottewill, R. H. *Spec. Disc. Faraday Soc.* **1970**, *1*, 138.
- (64) Amos, D. A.; Markels, J. H.; Lynn, S.; Radke, C. *J. Phys. Chem. B* **1998**, *102*, 2739.
- (65) Velegol, D.; Anderson, J. L.; Garoff, S. *Langmuir* **1996**, *12*, 4103.
- (66) Walz, J. Y.; Prieve, D. C. *Langmuir* **1992**, *8*, 3073.
- (67) Yaminsky, V. V.; Ninham, B. W.; Stewart, A. M. *Langmuir* **1996**, *12*, 836.
- (68) Israelachvili, J.; Mitchell, D. J.; Ninham, B. W. *J. Chem. Soc. Faraday Trans.* **1976**, *72*, 1525.

- (69) Adamson, A. W.; Gast, A. P. *Physical Chemistry of Surfaces*, 6th ed.; John Wiley & Sons, Inc.: New York, 1997.
- (70) Tsubouchi, M.; Yamamoto, Y. *Anal. Chem.* **1983**, *55*, 583.
- (71) Tsubouchi, M.; Mitsushio, H.; Yamasaki, N. *Anal. Chem.* **1981**, *53*, 1957.
- (72) Cross, J. T. *Analyst* **1965**, *90*, 315.
- (73) Metcalfe, L. D.; Martin, R. J.; Schmitz, A. A. *J. Am. Oil Chem. Soc.* **1966**, *43*, 355.
- (74) Motomizu, S.; Gao, Y.; Uemura, K.; Ishihara, S. *Analyst* **1994**, *119*, 473.
- (75) Cutler, S. G.; Meares, P.; Hall, D. G. *J. Electroanal. Chem.* **1977**, *85*, 145.
- (76) Cutler, S. G.; Meares, P.; Hall, D. G. *J. Chem. Soc. Faraday Trans. 1* **1978**, *74*, 1758.
- (77) Kale, K. M.; Cussler, e. L.; Evans, D. F. *J. Phys. Chem* **1980**, *84*, 593.
- (78) Gharibi, H.; Bloor, D. M.; Hall, D. G.; Wyn-Jones, E. *Langmuir* **1992**, *8*, 782.
- (79) Gharibi, H.; Palepu, R.; Tiddy, G. J. T.; Hall, D. G.; Wyn-Jones, E. *J. Chem. Soc., Chem. Commun.* **1990**, 115.
- (80) Gharibi, H.; Razavizadeh, B. M.; Rafati, A. A. *Colloids and Surfaces A* **1998**, *136*, 123.
- (81) Gharibi, H.; Takisawa, N.; Brown, P.; Thomason, M. A.; Painter, D. M.; Bloor, D. M.; Hall, D. G.; Wyn-Jones, E. *J. Chem. Soc. Faraday Trans.* **1991**, *87*, 707.
- (82) Lincoln, P. A.; Chinnick, C. C. T. *Analyst* **1956**, *81*, 100.
- (83) Banick, W. M.; Valentine, J. R. *Analyst* **1964**, *89*, 435.
- (84) Bakker, M. G.; Turner, G. L.; Treiner, C. *Langmuir* **1999**, *15*, 3078.
- (85) Esumi, K.; Matoba, M.; Yamanaka, Y. *Langmuir* **1996**, *12*, 2130.
- (86) Goloub, T. P.; Koopal, L. K. *Langmuir* **1997**, *13*, 673.
- (87) Goloub, T. P.; Koopal, L. K.; Bijsterbosch, B. H.; Sidorova, M. P. *Langmuir* **1996**, *12*, 3188.
- (88) Velegol, S. B.; Fleming, B. D.; Biggs, S.; Wanless, E. J.; Tilton, R. D. *Langmuir* **2000**, *16*, 2548.
- (89) Atkin, R.; Craig, V. S. J.; Biggs, S. *Langmuir* **2000**, *16*, 9374.
- (90) Furst, E. M.; Pagac, E. S.; Tilton, R. D. *Ind. Eng. Chem. Res.* **1996**, *35*, 1566.
- (91) Wängnerud, P.; Olofsson, G. *J. Colloid Interface Sci.* **1992**, *153*, 392.
- (92) Arnebrant, T.; Bäckström, K.; Jönsson, B.; Nylander, T. *J. Colloid Interface Sci.* **1989**, *128*, 303.
- (93) Neivandt, D. J.; Gee, M. L.; Tripp, C. P.; Hair, M. L. *Langmuir* **1997**, *13*, 2519.
- (94) Clark, S.; Ducker, W. A. *J. Phys. Chem. B* **2003**, *107*, 9011.
- (95) Koopal, L. K.; Goloub, T. P.; de Keizer, A.; Sidorova, M. P. *Colloids and Surfaces A* **1999**, *151*, 15.
- (96) Szekeres, M.; Dékány, I.; de Keizer, A. *Colloids and Surfaces A* **1998**, *141*, 327.
- (97) Lee, E. M.; Koopal, L. K. *J. Colloid Interface Sci.* **1996**, *177*, 478.
- (98) Böhmer, M. R.; Koopal, L. K. *Langmuir* **1992**, *8*, 2649.
- (99) Hall, D. G. *Colloids and Surfaces A* **1994**, *90*, 285.
- (100) Tulpar, A.; Ducker, W. *J. Phys. Chem. B* **2004**, *108*, 1667.
- (101) Atkin, R.; Craig, V. S. J.; Wanless, E. J.; Biggs, S. *J. Colloid Interface Sci.* **2003**, *266*, 236.
- (102) Atkin, R.; Craig, V. S. J.; Biggs, S. *Langmuir* **2001**, *17*, 6155.
- (103) Pagac, E. S.; Prieve, D. C.; Tilton, R. D. *Langmuir* **1998**, *14*, 2333.

- (104) Manne, S.; Cleveland, J. P.; Gaub, H. E.; Stucky, G. D.; Hansma, P. K. *Langmuir* **1994**, *10*, 4409.
- (105) Manne, S.; Gaub, H. E. *Science* **1995**, *270*, 1480.
- (106) Subramanian, V.; Ducker, W. *Langmuir* **2000**, *16*, 4447.
- (107) Ducker, W. A.; Grant, L. M. *J. Phys. Chem. B* **1996**, *100*, 11507.
- (108) Wanless, E. J.; Davey, T. W.; Ducker, W. A. *Langmuir* **1997**, *13*, 4223.
- (109) Lamont, R. E.; Ducker, W. A. *J. Am. Chem. Soc.* **1998**, *120*, 7602.
- (110) Liu, J.-F.; Ducker, W. A. *J. Phys. Chem. B* **1999**, *103*, 8558.
- (111) Zajac, J.; Trompette, J. L.; Partyka, S. *Langmuir* **1996**, *12*, 1357.
- (112) Somasundaran, P.; Fuerstenau, D. W. *J. Phys. Chem.* **1966**, *70*, 90.
- (113) Rennie, A. R.; Lee, E. M.; Simister, E. A.; Thomas, R. K. *Langmuir* **1990**, *6*, 1031.
- (114) McDermott, D. C.; McCarney, J.; Thomas, R. K.; Rennie, A. R. *J. Colloid Interface Sci.* **1994**, *162*, 304.
- (115) Hall, D. G. *J. Chem. Soc. Faraday Trans. 2* **1972**, *68*, 2169.
- (116) Ash, S. G.; Everett, D. H.; Radke, C. J. *J. Chem. Soc. Faraday Trans. 2* **1973**, *69*, 1256.
- (117) Pethica, B. A. *Colloids and Surfaces A* **1986**, *20*, 151.
- (118) Yaminsky, V. V.; Ninham, B. W.; Christenson, H. K.; Pashley, R. M. *Langmuir* **1996**, *12*, 1936.
- (119) Christenson, H. K.; Yaminsky, V. V. *Colloids and Surfaces A* **1997**, *129-130*, 67.
- (120) Podgornik, R.; Parsegian, V. A. *J. Phys. Chem.* **1995**, *99*, 9491.
- (121) Pethica, B. A. *Colloids and Surfaces A* **1995**, *105*, 257.
- (122) Kékicheff, P.; Christenson, H. K.; Ninham, B. W. *Colloids and Surfaces* **1989**, *40*, 31.
- (123) Rutland, M. W.; Parker, J. L. *Langmuir* **1994**, *10*, 1110.
- (124) Parker, J. L.; Rutland, M. W. *Langmuir* **1993**, *9*, 1965.
- (125) Subramanian, V.; Ducker, W. *J. Phys. Chem. B* **2001**, *105*, 1389.

Chapter 2

Colloidal Probe Atomic Force Microscopy

2.1 Introduction

Atomic Force Microscopy (AFM) was invented in 1986 by Binnig et al¹ as a technique to image solid substrates. Imaging with AFM provided a distinct advantage over another popular surface microscopy, scanning tunneling microscopy (STM).²⁻⁴ In contrast to STM, AFM could image non-conducting surfaces. AFM utilizes the force between a sharp tip and the molecules on the surface as its contrast mechanism. The tip is attached to a cantilever spring, which deflects as a result of a force between tip and sample. The deflection is measured by laser reflection off of the cantilever. Images can be obtained by scanning an area of the surface while monitoring either the deflection of the cantilever or the movement of the tip required to maintain a constant deflection. If the tip is in contact with the surface, the deflection of the tip maps the topography of the surface so long as the solid surface is not deformed by the interaction with the tip.

In 1991, Ducker et al^{5,6} pioneered the use of AFM to study the forces acting on a colloidal particle when it is brought near a flat surface. This was done by attaching a colloidal particle to an AFM cantilever. At the time of this advance, the principle force measuring technique was the Surface Forces Apparatus (SFA).⁷ AFM provided a distinct advantage over SFA in that AFM enabled the study of forces between a much larger selection of substrates. This is because SFA requires transparent substrates so that interferometry can be performed to obtain the surface-surface separation. In addition, SFA uses more macroscopic surfaces in a crossed-cylinder geometry, whereas AFM can be used with a wide variety of shapes and sizes. Furthermore, the actual AFM experiments are more economical due to smaller sample volumes and most important, easier to obtain a clean environment for experimentation.

In this chapter the experimental set-up of the AFM experiment will be discussed along with how the AFM data is converted to a force versus separation curve. In addition, the preparation and calibration of colloidal probe cantilever tips will be discussed.

2.2 AFM Setup and Data Analysis

2.2.1 Set-up and Measurements

The set-up of the Digital Instruments AFM is shown in Fig. 2.1. The AFM cantilever is anchored into a liquid cell by means of a small, spring-loaded clip. The liquid cell is mounted in the AFM head, which is secured to the scanner.



Figure 2.1 Digital Instruments Nanoscope III AFM. This particular photograph shows a J-scanner and contact mode liquid cell. The AFM is isolated from vibrations by employing a large concrete slab hanging from the ceiling by bungee cords.

The force is measured by monitoring the deflection of the cantilever as a function of the movement of a piezo-electric crystal. A schematic of this process is shown in Fig. 2.2. The measurement of the cantilever deflection is achieved by reflecting a laser off of the backside of the cantilever and collecting the signal with a photodiode detector. The photodiode converts the intensity of the light to an electrical signal, which is monitored by a computer. The tip and solid sample are brought into close proximity by use of the mechanical drive and the piezo-electric crystal (contained in the scanner). Crude motion in the direction perpendicular to the surface is achieved by the mechanical drive, while fine movements are achieved by applying a known voltage to the piezo-electric crystal.

Application of such a voltage causes the crystal to expand or contract. This motion is calibrated by imaging a calibration grating and comparing measured and known distances in 3 dimensions. (Note: Only the z-dimension is required for force measurements.)

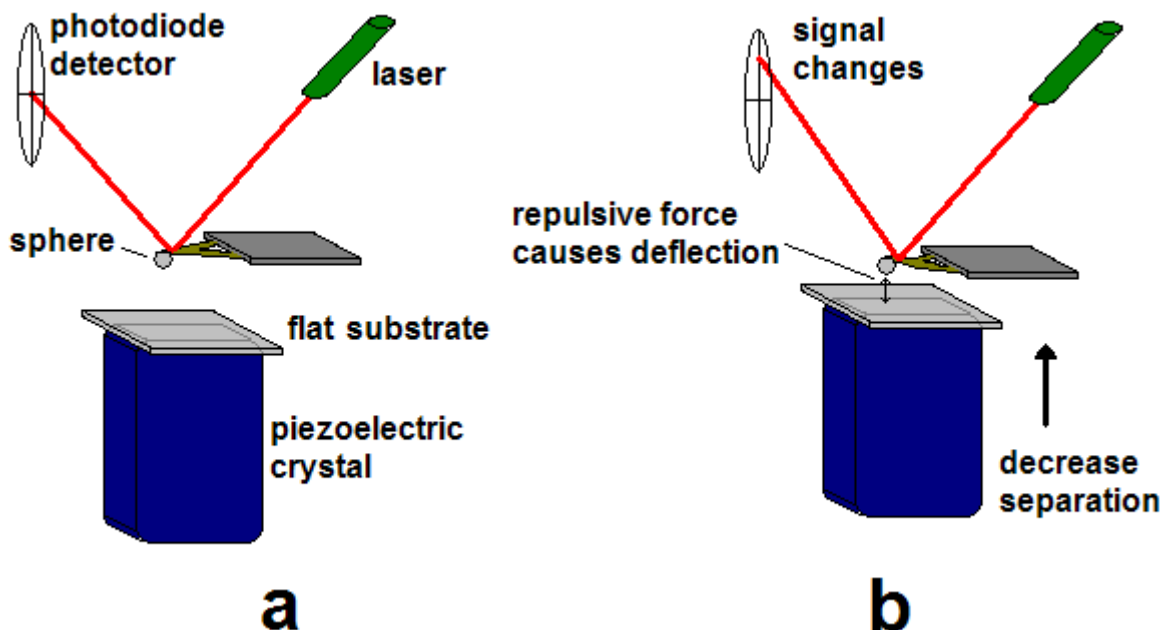


Figure 2.2 Schematic of AFM force measurement. **a)** A laser beam is reflected off of the AFM cantilever to a photodiode detector. **b)** At a smaller separation there is a different force between the sphere and the flat substrate. The force between substrates causes a deflection of the cantilever and a resulting change in voltage output from the photodiode.

2.2.2 Data Analysis

The data produced by the AFM is a plot of the cantilever deflection versus movement of the piezo. In order to obtain the actual interaction force as a function of inter-surface separation, a bit of manipulation is required. The conversion of the raw data to a force-separation plot will now be discussed. Fig. 2.3 shows a typical deflection-piezo displacement plot obtained with AFM.

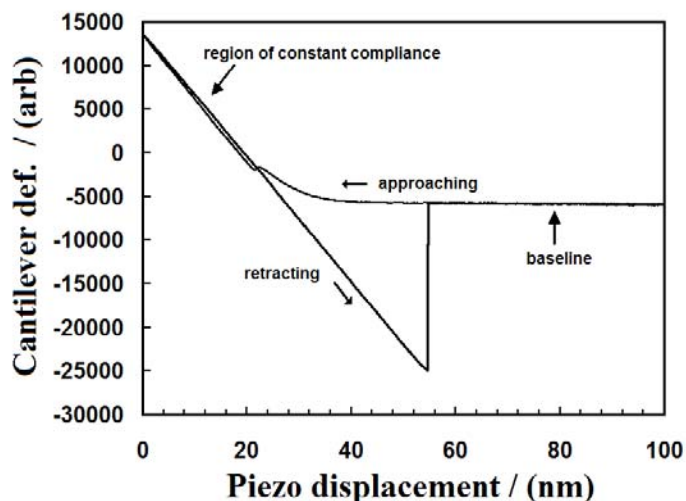


Figure 2.3 Plot of cantilever deflection as a function of piezo displacement. The approaching and retracting curves are different due to a non-equilibrium adhesion between the two surfaces.

In order to determine the force-separation profile for two surfaces, two crucial bits of information are required. First is the linear region of the curve at small piezo displacements (the region of constant compliance). Here it is assumed that the tip and solid substrate are in molecular contact and the tip moves with the piezo (i.e. all deflection is due to the piezo movement). The slope of the constant compliance regime provides a means of converting the arbitrary deflection values to deflection in nanometers.

$$\frac{\text{deflection (arb)}}{\text{slope} \left(\frac{\text{arb}}{\text{nm}} \right)} = \text{deflection (nm)} \quad (2.1)$$

Care must be taken when analyzing the constant compliance regime. When dealing with pliable substrates or soft adsorbate films, it is possible that the constant compliance slope will change as these materials are compressed. Therefore, a large amount of constant compliance should be obtained to get a slope that corresponds to molecular contact.

With the deflection in units of nanometers, the separation between the surfaces can be determined. This is first done by calculating a change in separation, Δs relative to some

arbitrary separation. This value is the sum of the piezo movement and the cantilever deflection since a positive deflection moves the tip further from the solid substrate (Fig. 2.2).

$$\Delta s \text{ (nm)} = \text{piezo distance (nm)} + \text{deflection (nm)} \quad (2.2)$$

The absolute separation is now determined by equating the average Δs over the constant compliance regime to zero (i.e. the separation does not change in contact). By doing so, all values for Δs now represent the separation relative to some zero separation, s_0 , given by the constant compliance regime. All inter-surface separations discussed for AFM work will therefore be denoted as $s-s_0$. In the case of adsorbates on the solid surfaces, it is possible that some adsorbate remains trapped between the solid surfaces at “contact”, therefore s_0 may differ slightly from the actual zero separation of the two solids. This will be discussed in the context of our measurements in later chapters.

The cantilever deflection must be converted to an actual force. The baseline is first determined (e.g. the flat region at large piezo displacements in Fig. 2.3). In this region there is no interaction between the substrates and the absolute force in this region is set equal to zero. The actual piezo displacements, where the baseline occurs is dependent upon the range of the force, which is dictated by several system parameters, such as those discussed in chapter 1.

The force relative to the baseline is obtained by multiplying the deflection by the known spring constant of the cantilever. The nominal value of the spring constant is often quoted by the manufacturer, however, the value can differ by up to 33% from the quoted value. Therefore, each cantilever has been calibrated in this work. The calibration procedure will be discussed in the next section.

Since the deflection is measured by the photodiode output voltage, a zero voltage does not correspond to zero deflection (Fig. 2.3). To obtain the absolute force, the force at large separation (where no deflection occurs) is set equal to zero (baseline). The plot of force versus separation obtained from the raw data in Fig. 2.3 is shown in Fig. 2.4 for comparison.

There are two interesting features in Fig. 2.4 that should be mentioned as they have particular importance throughout this work. The first is the sharp reduction in force at $2 \text{ nm} < s-s_0 < 4 \text{ nm}$. Such a sharp, discontinuous movement of the tip is brought about by

an attractive force, whose gradient exceeds the cantilever spring constant. This jump into contact of the tip is often referred to as a ‘jump-in’ and will be mentioned in subsequent chapters. Some possible explanations for this ‘jump-in’ include the increased contribution of the van der Waals force to the overall force law⁸⁻¹⁰ and the depletion of surfactant as the tip pushes through a surfactant layer.¹¹⁻¹⁵ Other possible mechanisms will be discussed in the following chapters.

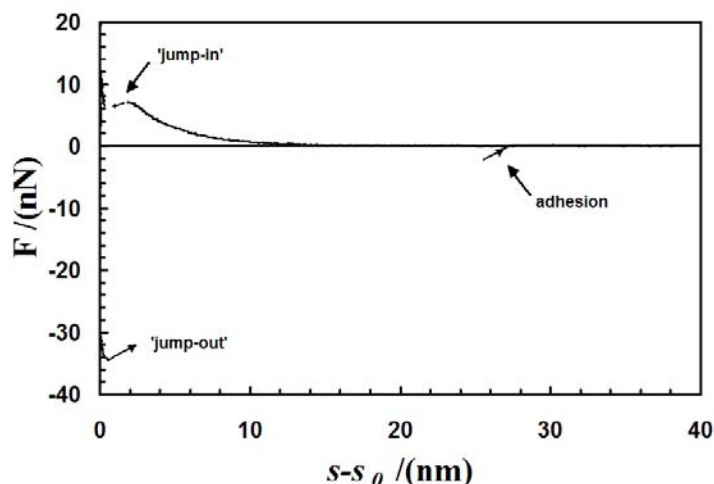


Figure 2.4. Example of typical force versus separation data obtained by AFM. This particular force curve is obtained from the raw data in Fig. 2.3 and is typical of cationic surfactants on glass surfaces at concentrations between the hemi-micelle concentration and the cmc of the surfactant.

The second feature of interest in Fig. 2.4 is the discontinuous ‘jump-out’ as the tip is retracted from the surface. Such a jump occurs as the result of a non-equilibrium adhesive contact between the tip and the solid substrate. As the tip is retracted, the tip is stuck to the surface until the negative deflection of the cantilever equals that of the adhesive force, at which point, the cantilever snaps back to its equilibrium position. The adhesive force can be calculated by multiplying the equilibrium separation after the jump by the spring constant of the cantilever. This is because as long as the tip and surface are in contact all piezo movement results in cantilever deflection.

The AFM data in this thesis is representative of the surface forces. The surface force, however, is only equal to the spring force under quasi-static conditions. In other words,

when there is negligible acceleration of the colloidal probe. Acceleration can easily be noted by increased spacing in the data points. Under conditions where the probe accelerates (during jumps), mechanical equilibrium is not maintained, and the deflection does not correspond to a surface force. In these regions data points are not shown, but rather an arrow is shown to indicate the jump.

2.3 Colloidal Probe Preparation

2.3.1 Sphere Attachment

As mentioned above, the colloidal probe technique involves attachment of a sphere to the cantilever. In this thesis, the geometry chosen is a sphere interacting with a flat solid surface. This geometry is chosen due to the ease of alignment over a sphere-sphere geometry. A colloidal particle is attached to the AFM cantilever as was originally done by Ducker et al.^{5,6} Attachment of a micron-sized sphere is achieved through manipulation with a three-dimensional translation stage. The set-up is shown in Fig. 2.5.

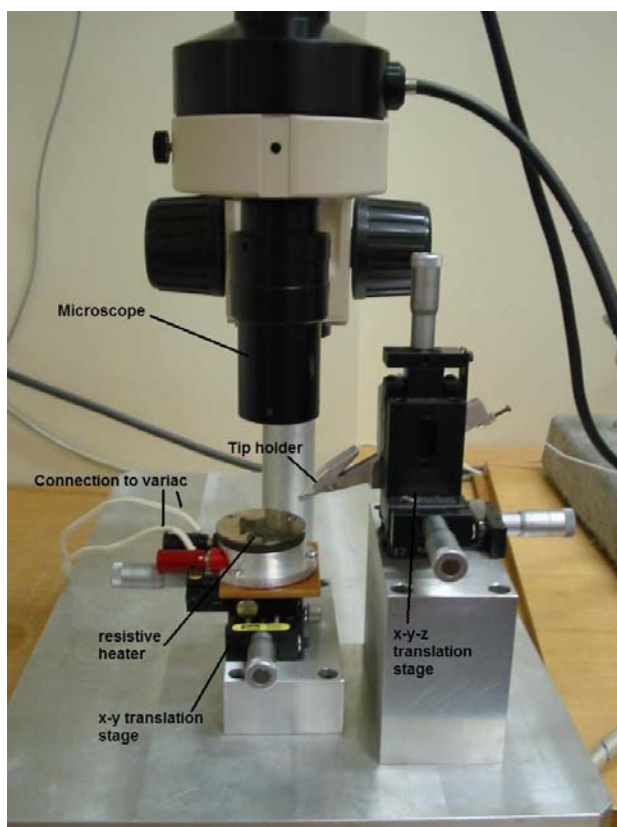


Figure 2.5 Photograph of the apparatus used for mounting colloidal spheres. The set-up shown is with the 10X microscope, which was primarily used for glue application. A 50X lense was used for mounting and measurement of the spheres. The microscope was connected to a video display for easy viewing. Glue was melted by heating on a sample stage. The temperature was controlled by a variable voltage supply (variac) with a resistive heating element under the stage.

Epon 1004 epoxy is placed on a freshly cleaved mica sheet and melted on the heating stage, which is connected to a variac. The voltage is regulated to change the temperature and melt the epoxy. The epoxy needs to be just hot enough to melt, yet not too liquid-like. A commercial AFM cantilever with an integrated tip is mounted in the tip holder and brought down to the surface and pressed softly into the molten glue. The tip is then brought into contact with an epoxy free region of the mica several times to removed excess epoxy from the tip. The tip is then retracted using the micrometer set-up, and the glue is replaced by a cleaved mica sheet containing the particles of interest (the particles are UV treated for 30 minutes before attachment). The micrometers are adjusted until a sphere of suitable characteristics (spherical shape and proper size) is found. The tip is then lowered to the surface, adjusting the microscope periodically to avoid crashing the tip into the surface. The spheres will be hot and will remelt the epoxy when the tip is brought into contact with the sphere. The temperature is especially crucial during this step. If the temperature is too high then the glue will melt quickly and run off of the tip and onto the particles. After contact between the tip and sphere (usually only a second or two to remelt the epoxy), the tip is retracted and viewed under a microscope to make sure that the sphere is centered properly on the tip. Fig. 2.6 shows a photograph of a colloidal silica particle attached to an AFM cantilever.



Figure 2.6 Photograph of a glass sphere attached to an AFM cantilever.

2.3.2 Spring Constant Calibration

In order to accurately measure the forces, the spring constant of the cantilever must be determined. In this work each individual cantilever has been calibrated by the method of Cleveland et al.¹⁶ The Cleveland method involves attachment of small end masses to the tip of the cantilever and then measuring the resonant frequency (ν_{res}) with the auto tune feature of the AFM. The relationship between the resonant frequency of the cantilever and the spring constant, k , is given as

$$\nu_{res} = \frac{1}{2\pi} \sqrt{\frac{k}{M+m}} \quad (2.3)$$

where m is the effective mass of the cantilever and M is the end mass. Rearrangement of equation 2.3 yields

$$M = \frac{k}{(2\pi\nu_{res})^2} - m \quad (2.4)$$

By measuring the resonant frequencies as a function of several different end masses, the spring constant can be determined from the slope of a plot of M versus $\frac{1}{(2\pi\nu_{res})^2}$.

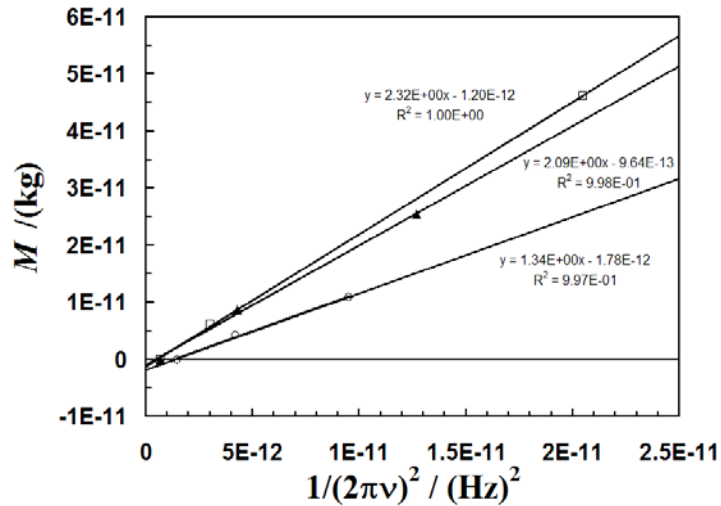


Figure 2.7 Calibration plot for determination of cantilever spring constants. The slopes of the fits give the spring constant for the three cantilevers shown.

Large tungsten spheres of varying size are mounted on the AFM cantilever by the same method mentioned above. Tungsten is chosen both for its availability and density.

In Cleveland's original set-up, capillary forces were used to attach the tungsten spheres to the tip. In this work, consistent attachment with capillary forces was unsuccessful, therefore a small amount of epoxy was used. Unlike, for the force measurements the tungsten spheres only need to stay attached long enough for the resonant frequency to be measured. Therefore, a comparatively small amount of epoxy is used for the spring constant calibration. This small amount of epoxy is negligible in mass compared to the added mass and can be neglected. This is confirmed by the fact that the $M = 0$ does not differ significantly from the fit in Fig. 2.7. After attachment of the tungsten sphere, the tip is oscillated by the auto tune feature of the AFM and the resonant frequency is obtained for cantilever-sphere couple. The spheres are then removed by dipping in chloroform, which dissolves the epoxy. A sample plot of for a selection of cantilevers is shown in Fig. 2.7

The radii of the individual spheres are measured with a video caliper calibrated using the AFM calibration gratings.

2.4 Additional AFM Experimental Procedure

In addition to the discussion above, the following section gives experimental detail regarding the AFM experiments performed in this work. This procedure holds for all AFM work in this thesis, unless otherwise noted in the subsequent text.

2.4.1 Reagents

Dodecyltrimethylammonium bromide (Aldrich, Milwaukee, WI) was recrystallized three times from a distilled ethanol/water mixture. Cetylpyridinium chloride and dodecylpyridinium chloride (Aldrich, Milwaukee, WI) were recrystallized three times from a 10:1 mixture of HPLC-grade acetone and methanol. N-dodecyl-N,N-dimethyl-3-ammonio-1-propanesulfonate (Sigma, St. Louis, MO) was recrystallized three times from isopropanol (HPLC grade). There was no minimum in a plot of surface tension vs. concentration for either surfactant. Water was prepared by an EASYpure UV system (model D7401, Barnstead Thermolyne Co., Dubuque, IA). The water had a conductivity of 18.3 M Ω /cm at 25 °C and a surface tension of 72.3 mN/m at 22.5 °C. By the time that preparation of the solutions was finished, CO₂ from the air had equilibrated in the

solution, so all experiments were at $\text{pH} \approx 6$, unless otherwise noted. NaOH (Fischer Scientific, Pittsburgh, PA), KCl (Aldrich, Milwaukee, WI) and KBr (Aldrich, Milwaukee, WI) were each roasted in air at $300\text{ }^\circ\text{C}$ to decompose organic impurities. HCl (EM Science, Gibbstown, NJ) was used as received.

2.4.2 Solid Substrates

In the experiments in Chapter 3 for dodecyltrimethylammonium bromide, fused silica plates (Alfa Aesar, Ward Hill, MA) were cleaned by boiling in concentrated sulfuric acid (95.7%, analytical grade; Baker, USA) for at least 12 h. The plates were then rinsed thoroughly with water and dried under a stream of high purity nitrogen. Plates were completely wet by water after the cleaning procedure. The glass spheres used were a soda-lime glass (Polysciences Inc., Warrington, PA) and were subjected to UV radiation for 30 minutes prior to use to burn off organic impurities. These substrates were chosen for comparison of the results to previous work.¹⁷ For all other AFM measurements, a borosilicate glass sphere (Duke Scientific, Palo Alto, CA) and a borosilicate glass plate (Fischer Sci., Pittsburgh, PA) were used. Both had an r.m.s. roughness of approximately 0.3 nm over $(400\text{ nm})^2$. Images of our substrates are shown in Figs. 2.8-2.10. The images of the flat surfaces were obtained by imaging at a scan rate of 1 Hz with a sharp, low spring constant silicon cantilever. The images of the sphere were obtained by imaging an ultrasharp grating (TGT01, Silicon-MDT Ltd., Moscow, Russia) with a colloidal probe tip at different scan rates. The borosilicate plates are more fragile and a different cleaning procedure was used. The plate and the cantilever-mounted sphere were cleaned with an argon/water cold plasma (March Instruments, Concord, CA) at 20 watts and 1 mTorr for 4 minutes. The plates were completely wet by water after the cleaning procedure. Furthermore, this procedure is less time consuming than the sulfuric acid treatment and also allows for the same pretreatment of both sphere and flat surface.

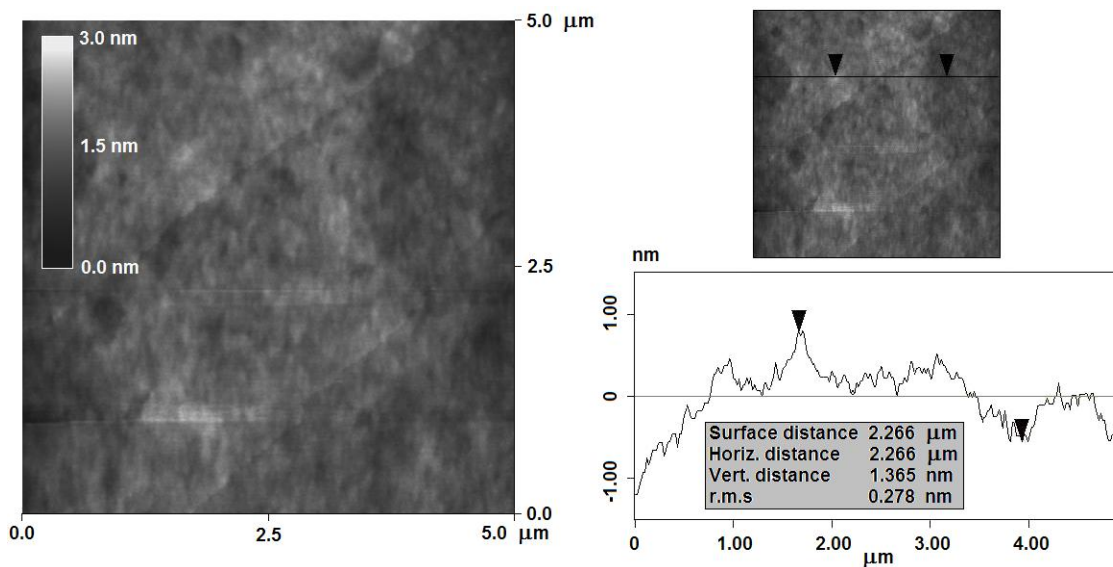


Figure 2.8 AFM height image of a borosilicate glass plate (left). This image was taken over a $25 \mu\text{m}^2$ region at a scan rate of 1 Hz. Over this image, the r.m.s. roughness was 0.297 nm. In addition, individual asperities can be analyzed (right). The r.m.s. roughness along the cross-section shown is 0.278 nm.

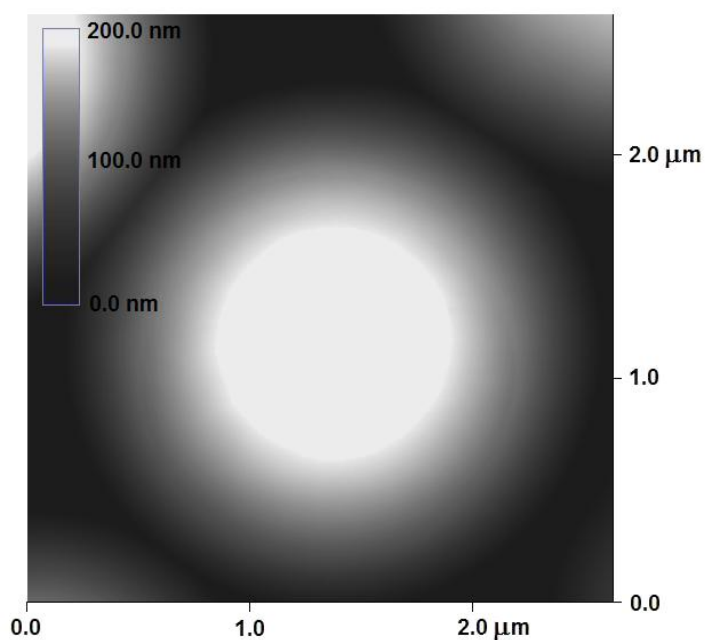


Figure 2.9 AFM height image of a borosilicate glass sphere. This image was taken over a $6.9 \mu\text{m}^2$ region at a scan rate of 5 Hz.

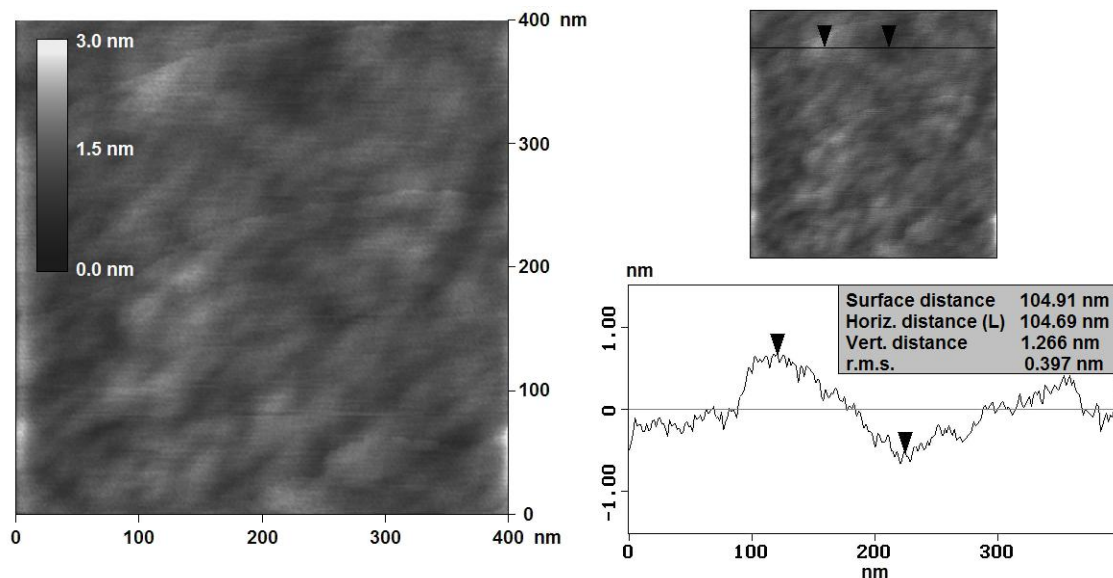


Figure 2.10 AFM height image of a borosilicate glass sphere (left). This image was taken over a $0.16 \mu\text{m}^2$ region at a scan rate of 2 Hz. Over this image, the r.m.s. roughness was 0.249 nm. In addition, individual asperities can be analyzed (right). The r.m.s. roughness noted in the figure is that over the cross-section shown.

2.4.3 Surface Forces

Surface force measurements were conducted with a Digital Instruments Nanoscope III AFM at $25 \pm 1 \text{ }^\circ\text{C}$ at a scan rate of 1 Hz ($0.1\sim 0.5 \mu\text{m s}^{-1}$).^{5,6} Forces were measured using triangular silicon cantilevers ($k \sim 1.4 \text{ N/m}$, Park Scientific, Sunnyvale, CA). A sphere was glued to the cantilever using Epon 1004 resin (Shell Chemical Co.). The diameter of individual spheres was measured with $\pm 0.5 \mu\text{m}$ error using an Olympus BH-2 light microscope with a video caliper. In our experiments $2 \mu\text{m} < R < 4 \mu\text{m}$ and the forces are non-zero for $s < 30 \text{ nm}$, so the Derjaguin approximation is appropriate when the sphere remains undeformed. Changes to the shape of the adsorbed layer are generally more facile than changes to the glass support and these may change the geometry during the interaction. The error in the spring constant was $\pm 7\%$, giving a total systematic error of about 13% in $F/2\pi R$.

At the start of each experiment, the AFM cell was flushed thoroughly with water. If a monotonic repulsion was not obtained, 40 mM NaOH solution was injected into the flow cell and equilibrated for 5–10 min. The cell was then flushed with water until a

monotonic repulsion appeared. NaOH probably dissolves the first few layers from both the plate and sphere, resulting in fresh, clean surfaces for subsequent experimentation. The absence of an attractive minimum in the force between the sphere and plate in water was used as a test for a hydrophilic surface. This is because the repulsive hydration force largely cancels the attractive van der Waals force, which is small due to a small silica/water/silica Hamaker constant. Surfaces were only used when there was no attractive minimum.

Since an equilibrium model is used to interpret our data, it was important to establish that the measurements were at adsorption equilibrium. This was determined by noting that the forces were (a) the same when the concentration was increased and decreased (b) the same on approach and separation and (c) the same when the speed was increased or decreased by a factor of 10. There were three circumstances when the results did not meet these criteria. (1) The forces were not reversible during mechanical instabilities of the cantilever. (2) The force for concentrated surfactant solutions was speed dependent at 10 Hz just before the mechanical instability. (3) Most important, the force was not reproducible when the concentration was decreased from above the force minimum (near the *ccp*) in large increments. This suggests that there may be a slow adsorption or rearrangement on a longer time-scale.

Finally, obtaining a flat baseline for AFM force measurements in liquids is often complicated by the presence of an interference pattern produced by stray laser light that reflects off of the solid substrate and is collected by the detector. In this work, this problem has been essentially eliminated by simply placing a piece of black tape between the stainless steel sample plate and the flat, solid substrate. It appears as though this black tape absorbs a majority of the stray light and keeps it from reflecting back to the photodiode.

2.5 Cited Literature

- (1) Binnig, G.; Quate, C.; Gerber, G. *Phys. Rev. Lett.* **1986**, *56*, 930.
- (2) Binnig, G.; Rohrer, H.; Gerber, C.; Weibel, E. *Phys. Rev. Lett.* **1982**, *49*, 57.
- (3) Binnig, G.; Rohrer, H. *Helv. Phys. Acta.* **1982**, *55*, 726.
- (4) Hansma, P. K.; Tersoff, J. *J. Appl. Phys.* **1987**, *61*, R1.
- (5) Ducker, W. A.; Senden, T. J.; Pashley, R. M. *Nature* **1991**, *353*, 239.
- (6) Ducker, W. A.; Senden, T. J.; Pashley, R. M. *Langmuir* **1992**, *8*, 1831.

- (7) Israelachvili, J. N.; Adams, G. E. *J. Chem. Soc. Faraday Trans. I* **1978**, *74*, 975.
- (8) Derjaguin, B. V.; Landau, L. D. *Acta Phys.-Chim URSS* **1941**, *14*, 633.
- (9) Derjaguin, B. V. *Trans. Faraday. Soc.* **1940**, *36*, 203.
- (10) Verwey, E. J.; Overbeek, J. T. G. *Theory of the Stability of Lyophobic Colloids*; Elsevier: Amsterdam, 1948.
- (11) Pashley, R. M.; Israelachvili, J. N. *Colloids and Surfaces* **1981**, *2*, 169.
- (12) Kékicheff, P.; Christenson, H. K.; Ninham, B. W. *Colloids and Surfaces* **1989**, *40*, 31.
- (13) Patrick, H. N.; Warr, G. G.; Manne, S.; Aksay, I. A. *Langmuir* **1999**, *15*, 1685.
- (14) Wanless, E. J.; Ducker, W. A. *Langmuir* **1997**, *13*, 1463.
- (15) Wanless, E. J.; Ducker, W. A. *J. Phys. Chem.* **1996**, *100*, 3207.
- (16) Cleveland, J. P.; Manne, S.; Bocek, D.; Hansma, P. K. *Rev. Sci. Instrum.* **1993**, *64*, 403.
- (17) Subramanian, V.; Ducker, W. *J. Phys. Chem. B* **2001**, *105*, 1389.

Chapter 3

Proximal Adsorption in Electrolyte Solution:
Comparison to Results in the Absence of Salt

3.1 Introduction

The first systematic study of the behavior of surfactants between two interacting colloidal surfaces was conducted by Subramanian and Ducker.¹ In their work they applied the Maxwell relation derived in chapter 1 (eq. 1.22) to AFM measurements of the interaction between a silica plate and a soda-lime glass sphere. Interaction forces were measured as a function of dodecyltrimethylammonium bromide ($C_{12}TAB$, Fig. 3.1) concentration in the absence of other electrolyte (excluding small amounts of H^+ , OH^- , CO_3^{2-}).

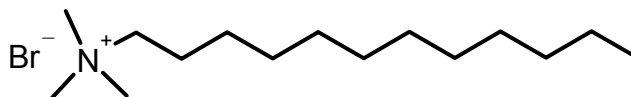


Figure 3.1 Dodecyltrimethylammonium bromide ($C_{12}TAB$)

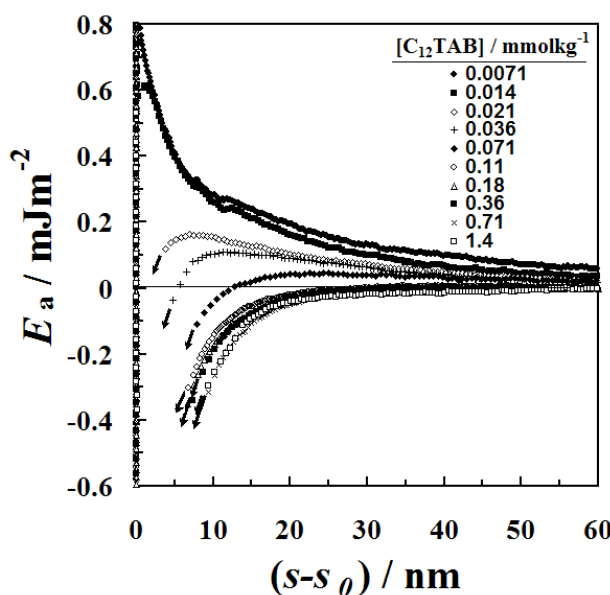


Figure 3.2 Interaction energy per unit area of two interacting flat silica-like surfaces as a function of separation at various $C_{12}TAB$ concentrations. The forces decrease as the concentration is increased. Reprinted in part with permission from Subramanian, V.; Ducker, W. J. *Phys. Chem. B* **2001**, 105 1389-1402. Copyright 2001 American Chemical Society.

Fig. 3.2 shows force data from their experiments. The interaction per unit area between two flat surfaces, E_a is calculated from the force data by applying the Derjaguin

approximation discussed earlier (eq. 1.13). Particular care was taken to ensure that the forces were obtained at mechanical and adsorption equilibrium. In Subramanian's experiments, the interaction energy decreased with increasing surfactant concentration up to a specific $C_{12}TAB$ concentration (1.4 mmol/kg). At greater concentrations, the trend reversed up to the *cmc* of the surfactant (not shown here). Changes in adsorption were calculated according to eq. 1.23.

$$\Gamma_i(s) - \Gamma_i(\infty) = -\frac{1}{2} \left(\frac{\partial E_a}{\partial \mu_i} \right)_{T,p,s,\mu_j} \quad (1.23)$$

Fig. 3.2 shows that E_a becomes more negative as the concentration increases (chemical potential becomes more positive). From eq. 1.23 $\Delta\Gamma > 0$, meaning that the surfactant adsorbs as the surfaces approach each other. As the surfactant concentration is raised above 1.4 mmol/kg, the trend in E_a with concentration reverses (the interaction becomes more repulsive with increased concentration). At these higher concentrations, from eq. 1.23, $\Delta\Gamma < 0$. Thus, as the surfaces approach one another at these higher concentrations, the surfactant leaves the surfaces. This is shown in Fig. 3.3.

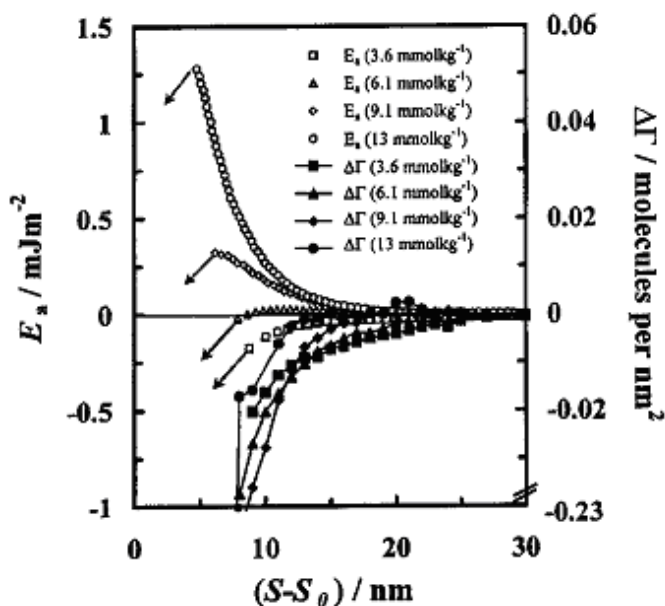


Figure 3.3 Interaction energies and changes in surface excess for $C_{12}TAB$ as a function of separation between two silica-like substrates. At these $C_{12}TAB$ concentrations the surfactant desorbs with decreasing separation. Reprinted with permission from Subramanian, V.; Ducker, W. J. *Phys. Chem. B* **2001**, *105* 1389-1402. Copyright 2001 American Chemical Society.

The behavior of the surfactant in Figs. 3.2–3.3 is explained by the regulation of the electrostatic double-layer interaction. At low concentrations, the surface charge is negative and the surfactant can adsorb to lower the net charge in the Stern layer. At

higher concentrations, the surface charge has been overcompensated and the surfactant desorbs to regulate the electrostatic potential generated by its head-group in a second surfactant layer. Notice in Fig. 3.3 that the range of $\Delta\Gamma$ with separation decreases with increasing concentration. This is because the Debye-length is controlled in part by the surfactant concentration rather than solely by the excess electrolyte.

The absence of a fixed counter-ion concentration poses a slight problem that was discussed by the authors. When surfactant is added to solution, the chemical potential of the surfactant ion and the counter-ion change simultaneously. Following the theory of electrolyte solutions, the authors defined $\mu_{\pm} = \frac{\mu_+ + \mu_-}{2}$ and considered only μ_{\pm} , therefore measuring $\Gamma_{\pm} = \Gamma_+ + \Gamma_-$. To obtain Γ_+ specifically, additional information is required. This means that the Maxwell relation cannot be used explicitly for the surfactant, but rather only for the surfactant-counter-ion couple. If the surfactant and counter-ion adsorb together then eq. 1.26 must be used.

$$\Gamma_{\pm}(s) - \Gamma_{\pm}(\infty) = -\frac{1}{4} \left(\frac{\partial E_a}{\partial \mu_{\pm}} \right)_{T,p,s,\mu_j} \quad (1.26)$$

Eq. 1.26 shows that the magnitude of the proximal adsorption could be half of what is calculated by assuming that the counter-ion effect is negligible (eq. 1.23).

This chapter will build upon the work of Subramanian by again examining forces for $C_{12}TAB$, but in an excess of monovalent electrolyte, KBr . The goals are two-fold. First, with excess electrolyte the concentration of the counter-ion will be essentially constant, allowing explicit determination of $\Delta\Gamma_{C_{12}TA^+}$. Secondly, addition of electrolyte will severely decrease the Debye-length. Comparison to Subramanian's data reveals the effect of the Debye-length.

3.2 Experiments in Electrolyte Solution

3.2.1 Bubble Effects

As mentioned in chapter 1, bubbles can often cause discontinuities in force measurements. In addition, salt has been reported to affect bubble coalescence.² Subramanian¹ and Carambassis et al³ have noted discontinuities in high salt, which they

attribute to bubble formation. Since bubbles are most stable on hydrophobic surfaces, the interaction energies in the presence of varying concentrations of KBr will be examined near the maximum attractive force, which will be shown later to be near the maximum hydrophobicity. Fig. 3.4 shows that raising the KBr concentration up to 30 mM leads to discontinuities in the attractive force profile. As a consequence, a concentration of 20 mM KBr is used in order to avoid such complications. Furthermore, such a concentration will reduce the Debye-length to 2.1 nm.

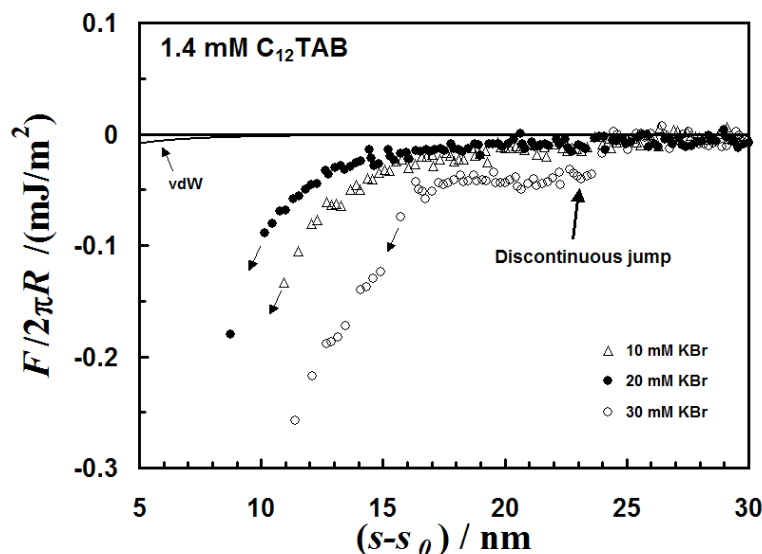


Figure 3.4 $F/2\pi R$ between a spherical particle and a flat sheet in 1.4 mM $C_{12}TAB$ in various KBr solutions. The arrows represent the onset of mechanical instabilities, where the particle jumps to the solid. Both curves for 10 mM and 20 mM KBr are continuous up to the 'jump-in'. Only in 30 mM KBr does the force show an additional jump (at $(s-s_0) = 24$ nm).

3.2.2 Chemical Potential Measurements

Eq. 1.23 requires knowledge of the chemical potential of the surfactant. An electrode selective to the $C_{12}TA^+$ ion was constructed as described by Cutler et al.⁴ Surfactant-selective electrode measurements were used to determine the chemical potential of the surfactant ion. Measurements were carried out at 25 ± 0.2 °C with a silver / silver chloride reference electrode (Orion, Beverly, MA) to complete the circuit. The plot of electrode potential versus surfactant concentration is shown in Fig. 3.5. Deviations from linearity are indicative of aggregation. The *cmc* is found by taking the intersection of the

two branches of the potential. The *cmc* of $C_{12}TAB$ in 20 mM KBr is determined to be 7.9 mM.

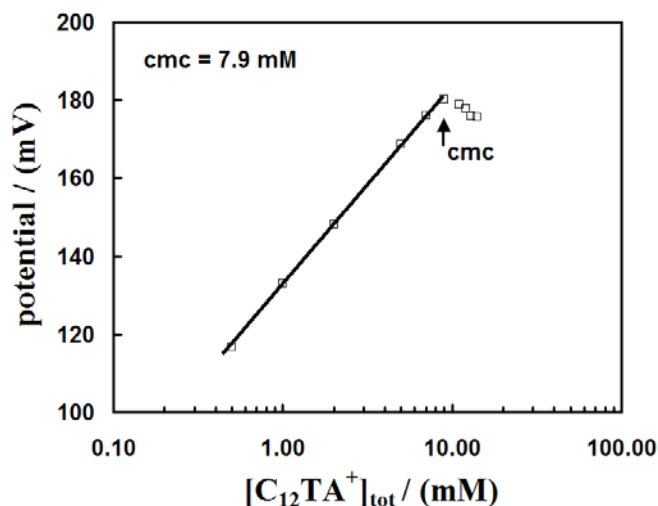


Figure 3.5 Potential from an electrode selective for $C_{12}TA^+$ versus total concentration of $C_{12}TA^+$. The maximum occurs at the *cmc* (7.9 mM). The potential drops above the *cmc* as the surfactant monomer concentration drops due to encapsulation in micelles.

3.2.3 Surface Forces

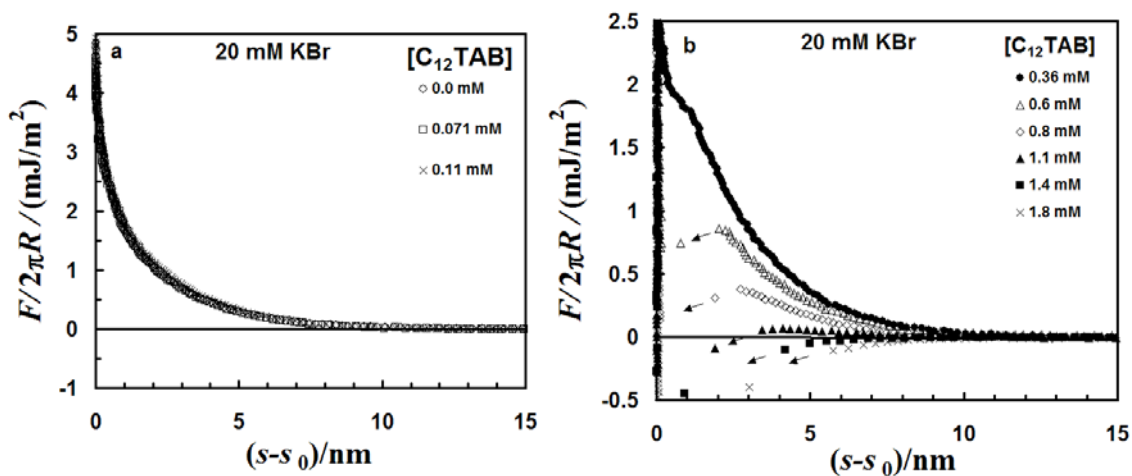


Figure 3.6 $F/2\pi R$ between a spherical particle and a flat sheet at low concentrations of $C_{12}TAB$ in a 20 mM KBr solution. **a)** There is no significant dependence of the force on the $C_{12}TA^+$ concentration. **b)** The force decreases monotonically with $C_{12}TA^+$ concentration. (Reproduced with permission from Lokar, W.J.; Ducker, W.A. *Langmuir* 2002,18, 3167-3175)

Figs. 3.6 and 3.7 show plots of $F/2\pi R$ versus separation for various $C_{12}TAB$ concentrations in the presence of 20 mM KBr. Fig. 3.6a shows that the force is not a function of $C_{12}TA^+$ concentration in the range 0–0.11 mM, whereas Fig. 3.6b shows that the force decreases upon addition of $C_{12}TA^+$ in the range 0.36–1.8 mM for all measurable separations. A mechanical instability, as described in chapter 2, occurs when $[C_{12}TA^+] > 0.6$ mM. This instability is found at larger separations for higher concentrations, up to 1.8 mM. Data obtained during a mechanical instability are not at equilibrium, and therefore were not analyzed using eqs. 1.22–1.26. Likewise, the Derjaguin approximation is not valid for non-equilibrium measurements.

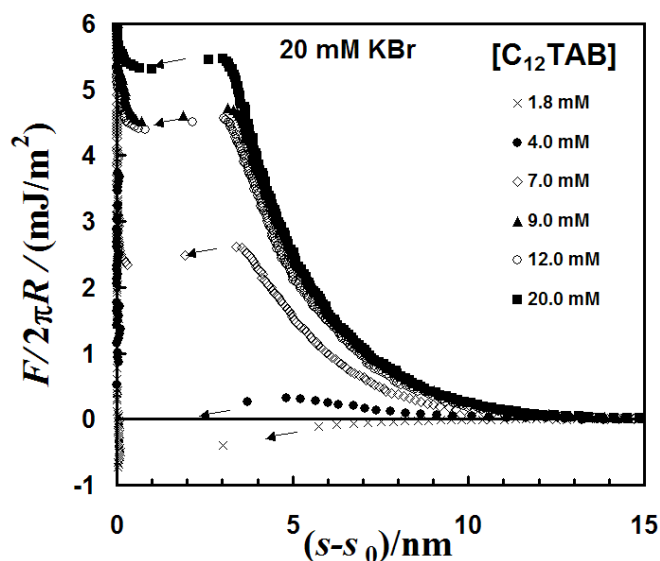


Figure 3.7 $F/2\pi R$ between a spherical particle and a flat sheet at higher concentrations of $C_{12}TAB$ in 20 mM KBr solution. The force increases monotonically with $C_{12}TA^+$ concentration until the cmc (7.9 mM). Above the cmc the force is constant with concentration for $(s-s_0) > 5$ nm and increases at smaller separations. (Reproduced with permission from Lokar, W.J.; Ducker, W.A. *Langmuir* **2002**,18, 3167-3175)

Fig. 3.7 shows the force in more concentrated $C_{12}TAB$ solutions (1.8–20 mM). The force increases with concentration above 1.8 mM. This suggests that the *ccp* is near 1.8 mM $C_{12}TA^+$ in 20 mM KBr. In fact, zeta potential measurements on the glass particles show that the potential drops to zero at approximately 4 mM (Fig. 3.8). The potential on the silica plate is unknown, however, the lack of co-incidence between the minimum force

and the zero zeta potential suggests that the plate and particle have slightly different surface charges. Above the *cmc*, the force curves change little with concentration. The zeta potential shows that the potential created by the surfactant adsorption does not change much in this region and the double-layer repulsion should be the same since the ionic strength does not change much above the *cmc*. The main effect of a concentration change from the *cmc* to $2.5 \times cmc$ is an increase in the final barrier height.

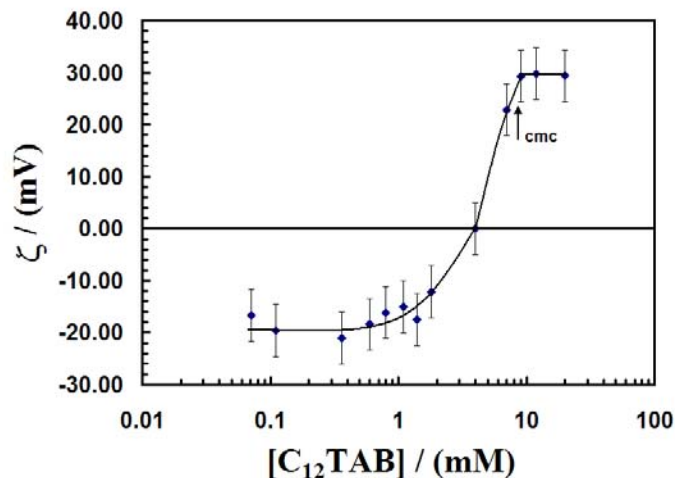


Figure 3.8 Zeta potential of glass spheres (Polysciences) as a function of C_{12TAB} concentration in 20 mM KBr. The *ccp* occurs at 4 mM. The potential plateaus above the *cmc*. The solid line is merely a guide for the eye rather than a fit.

After each approach, the surfaces were separated. For concentrations less than 0.36 mM, the forces on approach and separation were the same. For $[C_{12}TA^+] > 0.36$ mM, there was a mechanical instability when the surfaces were separated. At these concentrations an additional pulling force was required to separate the surfaces: the surfaces experience adhesion once in contact. The resulting load (negative force) required to separate the surfaces is plotted in Fig. 3.9. The magnitude of the negative load increases up to 4 mM, then decreases up to the *cmc*. The maximum adhesion corresponds to the *ccp* of the particles found by zeta potential measurements (Fig. 3.8)

The adhesion forces were more variable than approach forces. Even when the approach curve is highly reproducible, the magnitude of the adhesion varied from

experiment to experiment. Trends in adhesion, however, were the same from experiment to experiment.

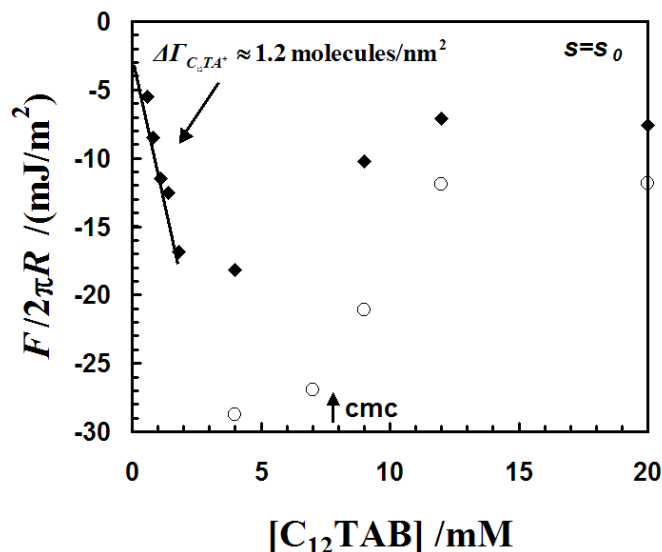


Figure 3.9 $F/2\pi R$ required to separate the spherical particle and the flat sheet from $s=s_0$ in $C_{12}TAB/20$ mM KBr solutions. There is a maximum in adhesion (minimum energy) at 1.8–4 mM. The open circles and closed diamonds represent two experiments, which produced different magnitudes but the same trend in force. (Reproduced with permission from Lokar, W.J.; Ducker, W.A. *Langmuir* **2002**,18, 3167-3175)

3.2.4 DLVO Analysis

Here, the interest is how the data compares to theories of colloidal stability. The force data is compared to calculated interactions between two flat surfaces using DLVO theory as discussed in chapter 1. In the calculation of DLVO forces, a simple model of the charged interface is used, in which the surface charge includes charge arising from both covalently-bound ions ($Si-O^-$) and from ions adsorbed directly to the surface (i.e. the Stern layer-charge). The van der Waals forces should be modeled to account for at least a five-layer system, consisting of silica/surfactant/water/surfactant/silica. The surfactant layer is also inhomogeneous because the head, tail, and ion groups have different dielectric properties. To simplify the calculation, the calculated van der Waals forces for silica/water/silica ($A= 0.8 \times 10^{-20}$ J) are used.⁵ This simplification is partly a necessity due to incomplete knowledge of the state of the surfactant layer. Furthermore,

the Hamaker constants for hydrocarbon and silica across water are similar and small ($A_{\text{dodecane-water-dodecane}} = 0.5 \times 10^{-20} \text{ J}$),⁵ thus a small error is expected by approximating A as that of the silica/water/silica system. The small magnitude of the van der Waals force means that it is often obscured by double-layer or hydration forces. The omission of the surfactant from the van der Waals calculation means that regulation of the van der Waals force is not accounted for during the surface–surface interaction. Van der Waals regulation only becomes significant at separations smaller than where the ‘jump-in’ occurs in the force data and therefore, is not of consequence in our analysis using eq. 1.23.

At large separations ($s-s_0 > \kappa^{-1}$), the force is independent of the boundary condition for surface charging, so both the surface potential and the Debye-length were fit in this region (Table 3.1). For surfactant concentrations greater than 1.8 mM, the measured force was greater than the force calculated at infinite potential when the plane of charge was at s_0 . From the force curves, there is a steep repulsive force at about 3.5 nm, which is consistent with a layer of surfactant on the surface. Earlier work has shown the existence of micelles on the surface of silica above the cmc in the absence of salt.¹ The contour length of the C_{12}TA^+ ion suggests that these micelles will be at least 2.4 nm in diameter, and thus the plane of charge should be shifted away from s_0 . Such an analysis was also performed by Subramanian and Ducker¹ and also by Parker and Rutland.⁶ For 7.0 and 9.0 mM solutions, a semi-arbitrary shift of 4.2 nm was chosen to achieve a physically realistic surface charge. The shift of 4.2 nm is in agreement with small-angle neutron scattering experiments, which suggest a bulk micellar diameter of 4.2 nm.⁷ Therefore, it is assumed in this fit that half a micelle exists on each surface.

At $s-s_0 < \kappa^{-1}$, the calculated force depends on how the surface charge responds to the approach of another particle (charge regulation). It is common to assign two limits to the charge regulation: an upper limit of constant charge and a lower limit of constant potential. These are plotted in Fig. 3.10. At small separations, there is an instability in the measured force at about the same separation at which the constant charge and constant potential calculations deviate from each other. The measured distance of the instability means that the force is becoming less repulsive and therefore, it is less repulsive than the constant potential condition. This deviation to less repulsive forces has

been used to signal the presence of an additional attractive force (the long-range hydrophobic interaction⁸), but the discrepancy can also be explained by adopting a more realistic boundary condition for the electrostatic force.

Table 3.1. Fitted DLVO Parameters for C₁₂TAB Experiments

[C ₁₂ TAB] /(mM)	ψ_0^* /(mV)	κ^{-1} /(nm)	Shift dist. /(nm)	σ_0^* /(e/nm ²)
0	-88	2.2	0	-0.277
0.11	-95	2.15	0	-0.328
0.36	-100	2.2	0	-0.356
0.6	-85	2.1	0	-0.267
0.8	-61	2.1	0	-0.157
4.0	+55	2.0	2.6	+0.146
7.0	+190/+77 ^a	1.9	2.5/4.2	+2.465/+0.261 ^a
9.0	+250/+130 ^a	1.85	3.5/4.2	+8.246/+0.753 ^a

*The sign of the potential and charge is inferred from the trend in forces and the zeta potential. ^aThe first value is the minimum shift of the plane of charge that allows a fit to the double-layer forces. This shift produces a surface charge that is unrealistically high. The second value was obtained using a semi-arbitrary shift of 4.2 nm for the plane of the surface charge. (Reproduced with permission from Lokar, W.J.; Ducker, W.A. *Langmuir* **2002**,18, 3167-3175)

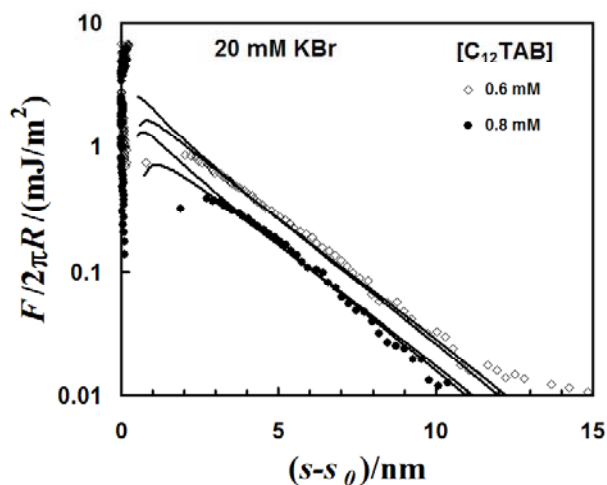


Figure 3.10 DLVO fits at 0.6 mM and 0.8 mM C₁₂TAB. Both constant charge (upper solid line) and constant potential (lower solid line) boundary conditions are plotted for each concentration. The fitted potentials are -85 and -61 mV respectively for 0.6 mM and 0.8 mM and the fitted Debye-length is 2.15 nm. The calculated $\kappa^{-1} = 2.09$ nm. Note that the measured force lies below the calculated force at constant ψ for $(s-s_0) < 2.3$ nm. (Reproduced with permission from Lokar, W.J.; Ducker, W.A. *Langmuir* **2002**,18, 3167-3175)

3.3 Equation of State

A general boundary condition should be devised for the double-layer interaction. In previous derivations of the Poisson-Boltzmann equation, two limits are considered: constant charge and constant potential.^{9,10} In these derivations, however, it has been assumed that the *chemical* interaction promoting adsorption is independent of adsorbed density or that the adsorption isotherm for potential determining ions does not change with the separation between two solids.¹⁰ If surfactant tails interact at the surface, condition one is not valid. Furthermore, from the measurements presented here, the adsorption of surfactant clearly changes with separation.

The obvious condition to use in the SFA and AFM experiments is constant chemical potential of all dissociable species, which is maintained by the large reservoir of bulk ions in equilibrium with the surface. It is well-known that surfactant adsorption to an isolated surface can cause a reduction and even a reversal of surface potential, as was shown in the zeta potential data in Fig. 3.8. The origin of this behavior is attributed to the short-range hydrophobic interaction between the alkyl chains of the surfactant. Adsorption of surfactant to an isolated surface has been well studied, and the adsorption to two interacting surfaces should be consistent with the adsorption to an isolated surface. Knowing this, it is necessary to write an expression for the chemical potential of the adsorbed surfactant ions that includes short-range interactions. Although the exact density dependence is unknown, a simple linear response to surface density (the Frumkin Isotherm¹¹) is a good starting point. The Frumkin isotherm should then be modified to allow for the effect of the surface potential, ψ .⁷

$$\mu_{ads} = \mu_{ads}^0 + RT \ln\left(\frac{\theta}{1-\theta}\right) + zF_A \psi(s) + RTA(\theta) \quad (3.1)$$

Here θ is the fraction of surface sites occupied by the adsorbate, zF_A is the charge per mole of the adsorbate, $\psi(s)$ is the separation-dependent surface potential, and $A(\theta)$ is a density dependent interaction parameter that incorporates interactions between adjacent molecules. Except for the last term, this is the form traditionally used to describe charge regulation during surface-surface interactions. Since the last term contains all density dependent chemical-specific short-range interactions, the functional form is difficult to write down. Prosser and Franses describe the Frumkin treatment, where $A(\theta)$ is negative

and linear and is used to account for attractive interactions between the alkyl chains (the hydrophobic effect). As will be shown in chapter 5, calculations of $A(\theta)$ from experimental data suggest that this is a reasonable assumption up to the charge neutralization point but that $\frac{\partial A(\theta)}{\partial \theta}$ can vary at higher surface densities. This is reasonable as the surfactant forms complex and perhaps even layered shapes at solid-liquid interfaces (micelles, bilayers etc.) and the extent of chain-chain interactions should not be the same at all concentrations. Furthermore, the existence of micelles on the surface suggests that there should also be repulsive terms in $A(\theta)$ that are important at high surface densities. In all cases presented here, $A(\theta) < 0$.

The effect of $A(\theta)$ is to reduce the chemical potential of the adsorbate and thus promote adsorption, even against an electrical potential. Unfortunately, the inclusion of the $RTA(\theta)$ term makes solution of the Poisson-Boltzmann equation very difficult. In particular, the density can become a two-valued function of concentration (corresponding to phase separation). The important qualitative points are (1) that constant electrical potential should not be assumed for surfactant adsorption (adsorption can exceed this limit) and (2) that the addition of an θ -dependent term means that adsorption can lead to further adsorption and thus to adsorption instabilities. Therefore, a small increase in adsorption caused by a long-range electrostatic interaction can lead to disproportionate adsorption of surfactant, or to an unstable adsorption regime and thus phase separation. As described by Pethica¹² and also by Podgornik and Parsegian¹³, phase separation can lead to unstable separation regimes. The sudden rise in adsorption induced by another surface is analogous to the sudden rise in adsorption induced by raising the concentration in an adsorption isotherm. In principle, additional adsorption could occur at long range via an electrostatic force or at molecular range via short-range hydrophobic interactions. Phase separation will be explored theoretically in chapters 8 and 9.

3.4 Adsorption Analysis

To determine how C_{12TA^+} responds on the surface when a second surface approaches, $\Delta\Gamma_{C_{12TA^+}}$ can be calculated from eq. 1.23. To do so, μ_i must be kept constant

for species other than $C_{12}TA^+$. The extent to which these experiments approximate this situation will now be discussed.

The experimental set-up has a very small surface area to volume ratio, so to a good approximation, changes in adsorption do not affect the total concentration or the chemical potential of any species. Constant chemical potential of Br^- is a good approximation when the concentration of added $C_{12}TAB$ is much less than the background 20 mM KBr. For example, in the range 1.8 mM to 4 mM $C_{12}TAB$, the chemical potential of Br^- changes by less than 3%. At higher concentrations of $C_{12}TAB$, this approximation obviously deteriorates. When there is a lot of $C_{12}TAB$ at the surface and in solution, one would expect to encounter a regime when $C_{12}TA^+$ and Br^- are the only two ions adsorbing in large amounts. From the electroneutrality condition, $\Delta\Gamma_{C_{12}TA^+} = \Delta\Gamma_{Br^-}$, and eq. 1.25 can be used. It is not obvious when this limit is reached in practice, but it will be used as a guide for determining the changes in adsorption at higher concentrations of $C_{12}TAB$.

The aqueous solutions are relatively dilute, so the change in chemical potential of other species (H^+ , OH^- , K^+) on addition of $C_{12}TAB$ is the result of small changes in the activity coefficient and can be calculated from Debye-Hückel theory. These changes scale approximately with $-0.5c^{-0.5}$, which at mM concentrations are much smaller than $d\mu_{C_{12}TAB}$, which changes as c^{-1} . For these experiments, $d\mu_j$ (Debye-Hückel) $\sim d\mu_{C_{12}TA^+}/10$. Thus, as long as the surface excess of any of these species (H^+ , OH^- , K^+) is not much bigger than the surface excess of $C_{12}TA^+$, these species can be ignored in eq. 1.21.

The force was measured as a function of separation at a variety of chemical potentials and interpolated to obtain E_a as a function of the same set of separations for all chemical potentials. The data are spaced at 0.2 nm intervals.

Fig. 3.11 shows plots of the interaction energy and its derivative versus the chemical potential of the surfactant monomer at $s-s_0 = 5$ nm. Positive values for $\left(\frac{\partial E_a}{\partial \mu_{C_{12}TA^+}}\right)_{p,T,\mu_j,s}$ in

Fig. 3.11 correspond to negative values of $\Delta\Gamma_{C_{12}TA^+}$ (desorption). When the surfaces

approach at $s-s_0 = 5$ nm, the surfactant desorbs at low concentration, adsorbs at intermediate concentrations and desorbs again at high concentrations.

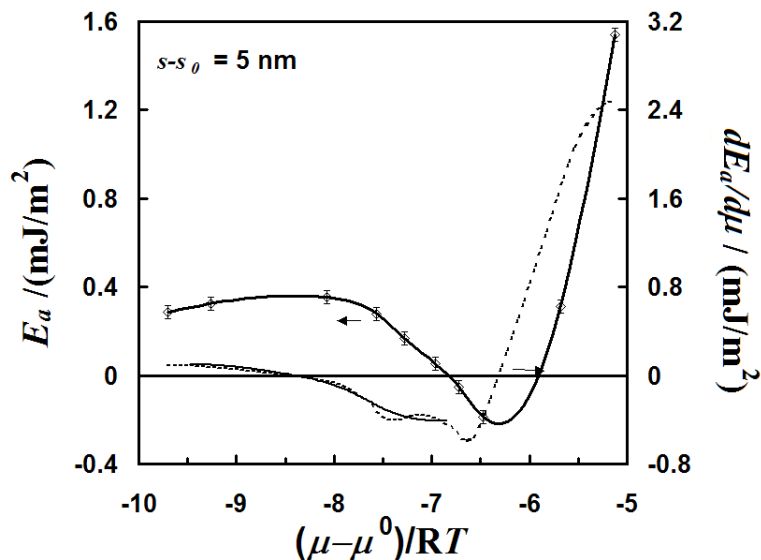


Figure 3.11 Experimental data for E_a (—) and derived values of $\left(\frac{\partial E_a}{\partial \mu_i}\right)_{p,T,\mu_j,s}$ (----) at a

separation of 5nm. The small minimum in $\mu-\mu^0/RT \approx -7.5$ is not experimentally significant. If a binomial smoothing (—) is applied to the data the derivative does not have a minimum at this concentration, but the fit at higher concentrations is worse. (Reproduced with permission from Lokar, W.J.; Ducker, W.A. *Langmuir* **2002**,18, 3167-3175)

3.5 Proximal Adsorption

3.5.1 $[C_{12}TAB] < 0.36$ mM

Fig. 3.12 shows the change in adsorption calculated using eq. 1.23 and the data from Fig. 3.6. Below 0.36 mM $C_{12}TAB$, the addition of surfactant has a minimal effect on the surface forces, and we conclude that surfactant adsorption at infinite separation is very small. H^+ , K^+ and $C_{12}TA^+$ all compete for surface sites on the negatively charged and hydrophilic silica. Comparing these three species, the H^+ forms a strong bond with the surface $Si-O^-$ group that includes some covalent character, and the K^+ exists in great excess, so these two species dominate adsorption. Furthermore, $C_{12}TA^+$ is in small

concentrations and should behave as a simple electrolyte. The forces are a function of concentration in the absence of KBr.¹ Therefore, the KBr clearly contributes to the lack of $C_{12}TA^+$ adsorption in 20 mM KBr. The addition of electrolyte is known to suppress surfactant adsorption to higher concentrations.¹⁴ $C_{12}TA^+$ only becomes competitive at higher chemical potentials.

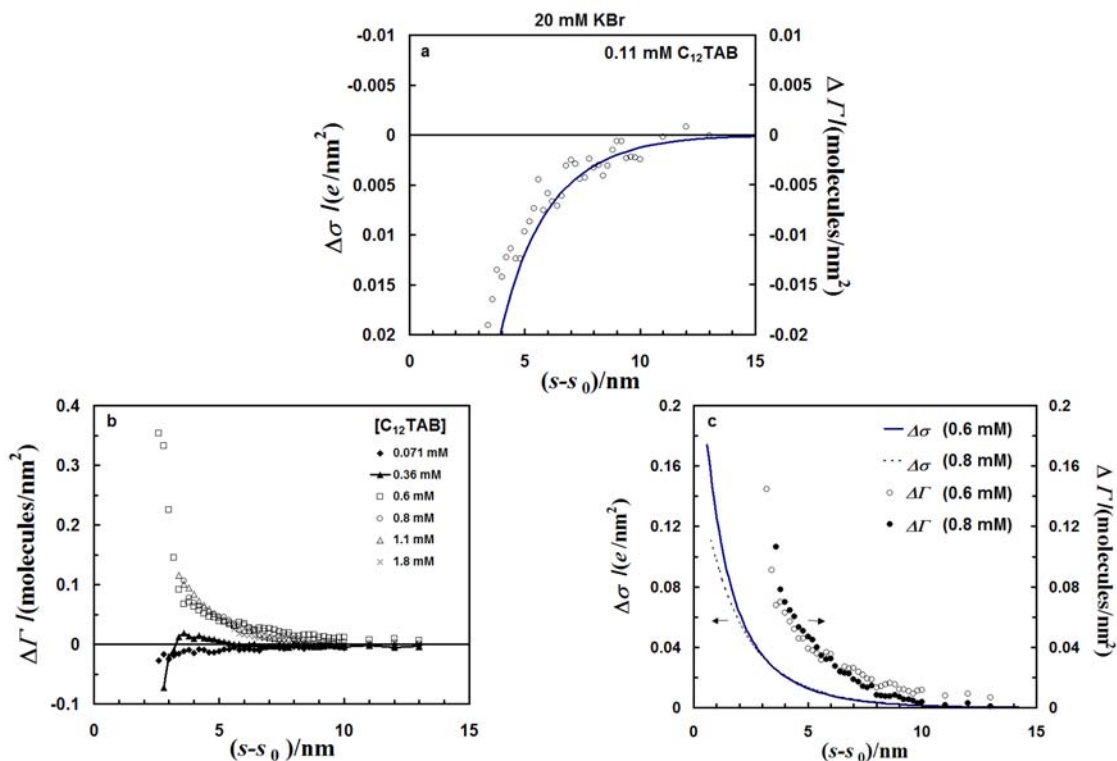


Figure 3.12 a) (\circ) $\Delta\Gamma$ of $C_{12}TA^+$ in 0.11 mM $C_{12}TAB$ and (—) change in charge required to maintain a constant surface potential of -95 mV. $\sigma_0 = -0.328$ e/ nm^2 . Note that the left-hand axis has been reversed for convenience. b) $\Delta\Gamma$ as a function of separation at low-medium concentrations. The change in adsorption is approximately constant with concentration between 0.6 and 1.8 mM. c) $\Delta\Gamma$ of the surfactant monomer and the change in charge required to maintain a constant surface potential in 0.6 mM and 0.8 mM $C_{12}TAB$. For both concentrations, the proximal adsorption is much greater than that required to achieve constant electrical potential. $\sigma_0(0.6) = -0.267$ e/ nm^2 , $\sigma_0(0.8) = -0.157$ e/ nm^2 , $\psi_0(0.6) = -85$ mV, and $\psi_0(0.8) = -61$ mV. (Reproduced with permission from Lokar, W.J.; Ducker, W.A. *Langmuir* 2002,18, 3167-3175)

Experiments showed a consistent (though small) increase in force as the concentration of $C_{12}TA^+$ increased from zero to 0.36 mM. This corresponds to desorption of surfactant as the surfaces approach (Fig. 3.12a). It is intriguing that the *cationic* surfactant *desorbs* when the negative surfaces approach because this action alone would raise the double-layer energy. The increase in force is too large to be assigned to a decrease in van der Waals force, so it is assigned to a change in double-layer force, following DLVO theory. Table 3.1 shows that the fitted negative surface charge at infinite separation increases in magnitude when surfactant is added. Furthermore, Fig. 3.8 shows an increase in the zeta potential at low concentrations. Note that this effect is distinct from the increase in generation of Si-O⁻ sites that has been observed when cationic surfactants are added to solution.¹⁵ Intuitively, one would expect that the addition of cationic surfactant would decrease the surface charge, but the data shows that desorption of surfactant is accompanied by the generation of two positive charges in the surface layer. For an unknown reason, adsorption of $C_{12}TA^+$ is either accompanied by adsorption of more than one anion, or it hinders the adsorption of more than one other cation (H⁺ and or K⁺).

Fig. 3.12a, compares $\Delta\Gamma_{C_{12}TA^+}$ (obtained with eq. 1.23 and our data) to $\Delta\sigma$ predicted by Poisson-Boltzmann theory (constant potential) given the fitted surface potentials in Table 3.1. The two are in reasonable agreement, meaning that the loss of $C_{12}TA^+$ during interaction of the two silica surfaces is consistent with a constant potential interaction similar to those obtained experimentally.

3.5.2 0.36 mM < [C₁₂TAB] < 1.8 mM

Fig. 3.12b shows that the surfactant surface excess remains constant up to about $s-s_0 = 6$ nm, rises slightly, then falls at $s-s_0 < 4$ nm. Again, this is entirely consistent with the charging behavior at infinite separation: the DLVO fits show that the surface potential and the surface charge peak at 0.36 mM (Table 3.1).

When the surfactant concentration is increased in this range, the force decreases at all measurable separations. The fitted potential and charge also decrease in magnitude. This regime can be compared to the concentration range 0.014–0.11 mmol/kg in the absence of salt,¹ where the force also decreased rapidly. Very similar changes in adsorption with

separation are observed even though the bulk concentration and surface charge are quite different.

A decrease in surface potential at infinite separation, as the chemical potential is increased, is most likely caused by adsorption of $C_{12}TA^+$ with the head-group binding to the negative sites on the silica surface. Approach of the two surfaces at constant charge would cause an increase in the surface potential and a concomitant increase in double-layer energy. Adsorption of cations can be used to relieve this buildup of potential (charge regulation). Fig. 3.12c shows the extent of charge adsorption that was obtained by using Poisson-Boltzmann theory and the fitted potentials in Table 3.1 (i.e. not with eq. 3.1). The much larger adsorption of $C_{12}TA^+$ from eq. 1.23 is shown on the same figure. Note that the $C_{12}TA^+$ adsorption data is model independent. The disagreement between the charge and adsorption data at all separations indicates that either (1) other ions are adsorbing or (2) that the calculation of the double-layer force contains a misleading assumption. Here, the lack of a tail-tail interaction in the surfactant chemical potential is discussed. The expected tail-tail interaction would lead to increased $C_{12}TA^+$ adsorption. The data shows that the surfactant adsorption is about twice as large as required to maintain constant potential. This means that the interaction will lie significantly below that of constant potential or adsorption of $C_{12}TA^+$ must be accompanied by co-adsorption of an anion (e.g. Br^-) or desorption of a cation (H^+ or K^+) for constant electrical potential to hold.

Fig. 3.12b shows the interesting feature that the change in adsorption with separation is the same in the range 0.6–1.1 mM. The force is linearly dependent upon chemical potential. This same feature was observed in the absence of salt. It is not obvious why this feature should extend over all separations, but it clearly shows the effect of non-electrostatic forces. Over this chemical potential range, the surface electrical potential at infinite separation drops from -85 mV down to values too small to measure, yet the approach of another surface drives the same change in adsorption. This shows that the proximal adsorption is not just a function of surface potential, it also responds to another effect, for example, an increase in the density of hydrocarbon chains on the surface. The force at $s=s_0$ (Fig. 3.9) also shows a linear dependence with chemical potential in this regime. The slope corresponds to $\Delta\Gamma_{C_{12}TA^+} = 1.2$ molecules/nm² as the surfaces are

brought into “contact”. In other words, a lot of surfactant is adsorbing (condensing) as the surfaces are brought into “contact”. This calculation should be taken as a rough estimate because (1) adsorption equilibrium may not be achieved in the thin film during the rapid change in surface separation and (2) the absolute surface separation at $s=s_0$ may not be the same at each concentration (as required by eq.1.23).

Rationalization of the large adsorption at small separations is fairly easy. When the surface separation drops down to molecular distances, molecules in the thin film are near surfactant from both surfaces. In other words, the density of hydrocarbon increases greatly even without further surfactant molecules moving to each surface. The free energy for adsorbed water molecules should be much higher in these circumstances, which favors their displacement by more surfactant molecules. This is the same effect as occurs at the hemi-micelle concentration for isolated surfaces, and should encourage the adsorption of more surfactant.¹⁶

3.5.3 $ccp < [C_{12}TAB] < cmc$

When the surfactant concentration is increased above 1.8 mM, the force increases and the surface potential becomes large and positive. Surfactant adsorption has overcompensated the silica surface charge because of attractive tail-tail interactions. Above the cmc , the force at $s-s_0 > 5$ nm is roughly constant. Adsorption to the isolated surface changes little because the chemical potential changes little. The final barrier height does increase, which would provide an increase in colloidal stability above the cmc . The behavior above the cmc is qualitatively very similar to that obtained in the absence of electrolyte¹ and will not be discussed in detail here. The similarity in this region arises from the fact that the ionic strengths are similar in the salt and no-salt case so the Debye-lengths and the chemical potentials are also similar.

In this regime it is no longer safe to assume that only the chemical potential of $C_{12}TA^+$ is changing and eq. 1.23 can no longer be used to determine the extent of adsorption as the surfaces approach. As a rough guide, the analyses using eqs. 1.23 and 1.26 (which differ only by a factor of 2) are shown for 4.0 and 7.0 mM $C_{12}TA^+$ (Fig. 3.13). As the positively charged surfaces approach, $C_{12}TA^+$ desorbs to reduce the electrostatic repulsion.

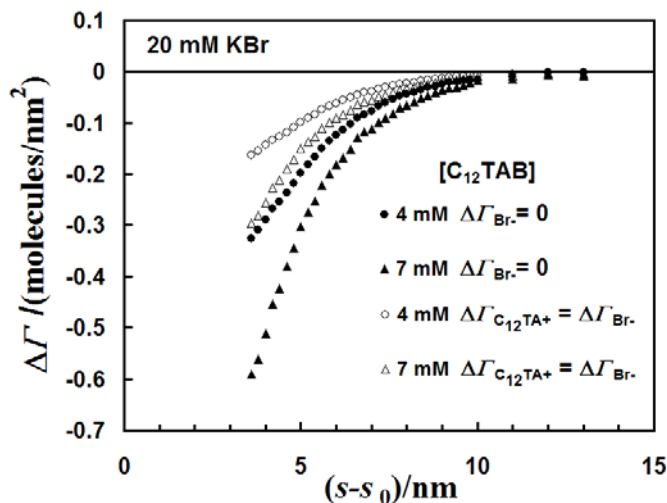


Figure 3.13 Comparison of $\Delta\Gamma_{C_{12}TA^+}$ vs. separation for cases where the counter-ion adsorption is neglected (\bullet, \blacktriangle) and where the counter-ion adsorption is equal to the surfactant monomer adsorption (\circ, \triangle). Both concentrations are in the regime between the charge compensation point and the critical micelle concentration. It is likely that the actual values for $\Delta\Gamma_{C_{12}TA^+}$ fall between the two curves at the same surfactant concentration. (Reproduced with permission from Lokar, W.J.; Ducker, W.A. *Langmuir* **2002**, *18*, 3167-3175)

3.6 Comparison of Forces in No-Added-Salt and 20 mM KBr

Compared to the data collected previously in the absence of added salt,¹ all forces in 20 mM KBr have a smaller range. All forces in 20 mM KBr only have significant gradients at separations less than about 10 nm, which is about 5 Debye-lengths. A necessary consequence of eq. 1.23 is that the changes in adsorption with separation are only significant at the same small separations. This provides new insight into the long-range forces/adsorption in the absence of salt. Either (1) the particular surface features generating the long-range forces in the absence of salt are no longer present in salt (at any surfactant concentration), or (2) the long-range forces in no added salt are screened by the electrolyte. Concerning case (1), it is likely that the addition of salt alters the structure of interfacial surfactant aggregates at some concentrations.¹⁷ However, it is unlikely that the addition of a moderate amount of salt should completely banish structures that generate non-screenable forces from the rather broad concentration regimes that have been

examined. Therefore, explanation (2), that the long-range forces in the absence of salt can be screened by electrolyte, is preferred.

Fig. 3.14a compares the data at 1.8 mM C₁₂TAB in 20 mM salt to the predicted van der Waals force between silica surfaces. The measured force is much greater than the van der Waals force and also has the wrong distance dependence for a van der Waals force. Empirically, the best fit is to a power law as $(s-s_0)^{-4}$, or to an exponential function with a decay length of 2.0 nm, which is a bit higher than those reported in the literature (1.0-1.4 nm, c.g. ch 1). The theoretical solution Debye-length is also 2.0 nm.

Fig. 3.14b shows two exponential fits to the 1.8 mM data. The data was first fit to a model developed by Kékicheff and Spalla,¹⁸ which assumes an overall neutral surface with positively and negatively-charged domains. The following functional form is expected:

$$F/R = \frac{-A \exp(-2\kappa(s-s_0))}{(\kappa(s-s_0))} \quad (3.2)$$

Kékicheff and Spalla¹⁸ found a good fit to this force law in C₁₆TAB solutions, but the fit to our data is not good. A better fit is obtained using a simple exponential with the theoretical solution Debye-length. The $1/s$ dependence does little to change the fit; the critical effect is the factor of two inside the exponential, which produces the incorrect slope in Fig. 3.14b. The better fit provided by a simple exponential is consistent with a simple electrostatic origin for this force, and may indicate that the two surfaces have slightly different charges at this concentration. This is consistent with the zeta potentials of the particles in Fig. 3.8. The particles have a *ccp* of 4 mM, but the maximum attractive force occurs at [C₁₂TAB] = 1.8 mM. Thus, the best explanation of the long-range attractive forces appear to be slightly different charge compensation points for the two solids.

The other major effect of the addition of salt is that a greater concentration of surfactant is required to obtain any effect on the surface forces. The most attractive forces are delayed by a factor of 10 in concentration so, as mentioned previously, K⁺ clearly retards the adsorption of C₁₂TA⁺ at low concentrations.

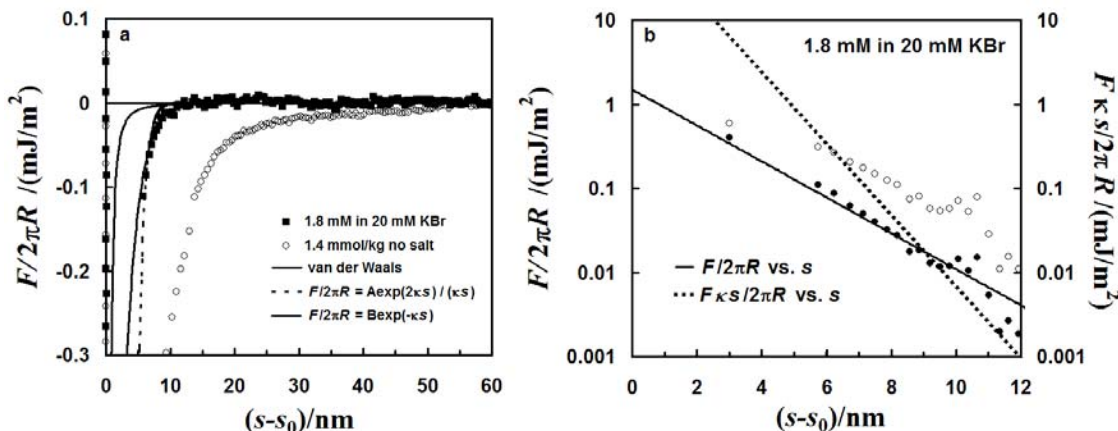


Figure 3.14 a) Force at 1.8 mM $C_{12}TAB$ and 20 mM KBr compared to: (1) a van der Waals force using a Hamaker constant of 0.8×10^{-20} J (silica), (2) to a charge patch model (Kékicheff, P.; Spalla, O. *Phys. Rev. Lett.* 1995, 75, 1851-1854), and (3) to a simple exponential. The most attractive curve in the absence of KBr ($[C_{12}TAB] = 1.4$ mmol/kg) is shown for comparison. (Subramanian, V.; Ducker, W. J. *Phys.Chem. B* 2001, 105, 1389-1402). b) $\frac{F}{2\pi R}$ and $\frac{F\kappa s}{2\pi R}$ plotted against the separation on a logarithmic scale. The circles represent the experimental data and the lines represent the theoretical fits. The simple exponential with $\kappa^{-1} = 2.0$ nm shows a much better fit to the experimental data. (Reproduced with permission from Lokar, W.J.; Ducker, W.A. *Langmuir* 2002,18, 3167-3175)

3.7 Conclusions

In $C_{12}TAB$ solutions that also contain 20 mM KBr, the forces between a silica plate and a glass sphere are all short-ranged, even the attractive forces. This suggests that all the long-range forces measured in the absence of salt have an electrostatic origin. However, because $C_{12}TA^+$ contains both a charged and a hydrophobic segment, adsorption of $C_{12}TA^+$ leads to changes in the local environment at the surface. The hydrophobic segment ensures that when the surface density of $C_{12}TA^+$ is sufficient for short-range interactions to become important (the hemi-micelle density), the adsorption of surfactant will provide a coupling between long-range electrostatic forces and short-range ‘hydrophobic effects’. The coupling between long and short-range forces may appear to produce ‘new’ long-range forces but are more likely a failure to account for

short-range interactions in equations for the chemical potential of surface species. These effects are made more obvious through measurement of proximal adsorption, which shows that, as two surfaces approach, surfactant molecules will adsorb in excess of purely electrostatic requirements. The approach of two surfaces sometimes leads to the same proximal adsorption even when the electrical potential varies greatly. The addition of a simple salt retards the adsorption of surfactant at concentrations below the charge compensation point. As described previously, this is because of competition for charged surface sites.

3.8 Cited Literature

- (1) Subramanian, V.; Ducker, W. *J. Phys. Chem. B* **2001**, *105*, 1389.
- (2) Craig, V. S. J.; Ninham, B. W.; Pashley, R. M. *J. Phys. Chem.* **1993**, *97*, 10192.
- (3) Carambassis, A.; Jonker, L. C.; Attard, P.; Rutland, M. W. *Phys. Rev. Lett.* **1998**, *80*, 5357.
- (4) Cutler, S. G.; Meares, P.; Hall, D. G. *J. Electroanal. Chem.* **1977**, *85*, 145.
- (5) Hough, D. B.; White, L. R. *Adv. Colloid Interface Sci.* **1980**, *14*, 3.
- (6) Rutland, M. W.; Parker, J. L. *Langmuir* **1994**, *10*, 1110.
- (7) Hayter, J. B. In *Physics of Amphiphiles: Micelles, Vesicles and Microemulsions*; North-Holland: Amsterdam, The Netherlands, 1985; pp 80.
- (8) Israelachvili, J. N.; Pashley, R. M. *J. Colloid Interface Sci.* **1984**, *98*, 500.
- (9) Verwey, E. J.; Overbeek, J. T. G. *Theory of the Stability of Lyophobic Colloids*; Elsevier: Amsterdam, 1948.
- (10) Chan, D. Y. C.; Mitchell, D. J. *J. Colloid Interface Sci.* **1983**, *95*, 193.
- (11) Prosser, A. J.; Franses, E. I. *Colloids and Surfaces A* **2001**, *178*, 1.
- (12) Pethica, B. A. *Colloids and Surfaces A* **1986**, *20*, 151.
- (13) Podgornik, R.; Parsegian, V. A. *J. Phys. Chem.* **1995**, *99*, 9491.
- (14) Goloub, T. P.; Koopal, L. K. *Langmuir* **1997**, *13*, 673.
- (15) Goloub, T. P.; Koopal, L. K.; Bijsterbosch, B. H.; Sidorova, M. P. *Langmuir* **1996**, *12*, 3188.
- (16) Somasundaran, P.; Fuerstenau, D. W. *J. Phys. Chem.* **1966**, *70*, 90.
- (17) Lamont, R. E.; Ducker, W. A. *J. Am. Chem. Soc.* **1998**, *120*, 7602.
- (18) Kékicheff, P.; Spalla, O. *Phys. Rev. Lett.* **1995**, *75*, 1851.

Chapter 4

Effects of Ionic Strength, pH, and Chain-length on Proximal Adsorption

4.1 Introduction

In the previous chapter, the proximal adsorption of C₁₂TAB was explicitly determined in electrolyte solutions by eq. 1.23.

$$\Gamma_i(s) - \Gamma_i(\infty) = -\frac{1}{2} \left(\frac{\partial E_a}{\partial \mu_i} \right)_{T,p,s,\mu_j} \quad (1.23)$$

In 20 mM KBr, the forces were shorter ranged, consistent with a smaller double-layer, and the surfactant proximal adsorption was in excess of simply regulating the surface charge at constant electrical potential.

In this chapter, experiments are carried out at different ionic strengths, pH, and for different chain length surfactants. The experiments at different ionic strengths and pH conditions are designed to gain further insight into the double-layer contribution to proximal adsorption, whereas experiments with different alkyl chain-lengths are used to understand the importance of chain-chain interactions. The surfactants used here are cetylpyridinium chloride (CPC) and dodecylpyridinium chloride (DPC) because the existence of a UV chromophore lends itself to future work with UV spectroscopy.

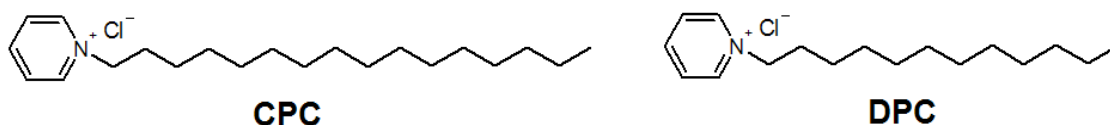


Figure 4.1 Cetylpyridinium chloride (CPC) and dodecylpyridinium chloride (DPC).

Forces between silica surfaces in CPC were previously measured by Pashley et al¹ in the presence of 0.1 M NaCl. They reported the presence of long-range (up to 40 nm) attractive forces. In chapter 3, step-like features were observed in force–separation data for surfactant solutions at concentrations of salt greater than 20 mM. These steps may be associated with the presence of small bubbles on the surface of the surfactant-coated silica. Therefore, measurements in this chapter are done in more dilute salt solutions, where there is more confidence that bubbles are not present.

The adsorption of CPC and DPC to suspensions of silica particles has been studied by Koopal and coworkers.²⁻⁴ They found that the functional form of the adsorption depends on the electrolyte concentration. At low salt concentrations (1 mM), the adsorption shows two plateaus, whereas at high concentrations (100 mM) the adsorption shows a steep rise. The first plateau occurs due to repulsions between adjacent surfactant head-groups at the surface as the *ccp* is approached. The higher salt concentration allows for more effective screening and therefore, reduction and eventual elimination of this first plateau. The second plateau stems from the *cmc*, above which the surfactant chemical potential does not vary much with concentration. At low surfactant concentrations, salt hinders the adsorption by screening the surface charge and competing with the surfactant for adsorption sites. At high surfactant concentrations the salt screens the repulsive interactions between surfactant molecules, leading to more surfactant adsorption at higher salt concentrations. These effects lead to a common intersection point (*cip*) in the adsorption isotherms when the net surface charge (silica plus adsorbates) is close to zero. The sessile contact angle is also a maximum at this point, indicating a maximum hydrophobicity for the surface.

4.2 Additional Experimental

4.2.1 Solid Substrates

AFM experiments in chapter 3 were between a soda-lime glass particle and a silica plate.^{5,6} Here, a borosilicate glass sphere (Duke Scientific, Palo Alto, CA) and a borosilicate glass plate (Fischer Sci., Pittsburgh, PA) are used in order to achieve a more symmetric system. The substrates were cleaned as stated in chapter 2. The plates were completely wet by water after the cleaning procedure.

4.2.2 Chemical Potential Measurements

Fig. 4.2 shows the electrical potential for CP⁺ and DP⁺-selective electrodes as a function of surfactant concentration. The change in slope reveals the *cmc* of the surfactants, which are summarized in Table 4.1 for different salt concentrations.

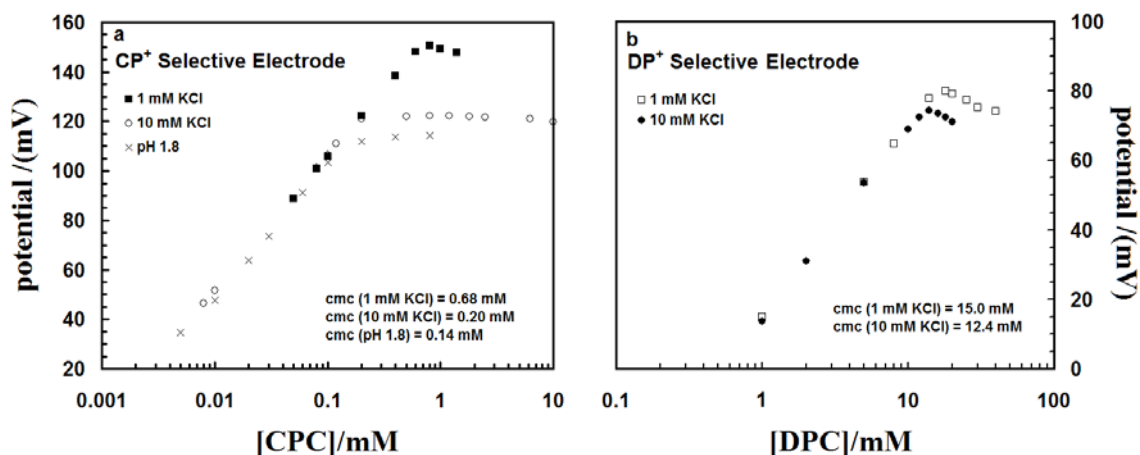


Figure 4.2 Electrical potential of surfactant-selective electrodes versus surfactant concentration. *a)* cetylpyridinium-selective electrode vs a silver/ silver chloride reference electrode. \times pH 1.8, \blacksquare pH 6 and 1 mM KCl, and \circ pH 6 and 10 mM KCl. *b)* dodecylpyridinium-selective electrode vs a silver/ silver chloride reference electrode. \square pH 6 and 1 mM KCl and \bullet pH 6 and 10 mM KCl.

Table 4.1. Cmc values for CPC and DPC at various solution conditions

Surfactant	Conditions	cmc / mM
CPC	1 mM KCl, pH 6	0.68
CPC	10 mM KCl, pH 6	0.20
CPC	pH 1.8	0.14
DPC	1 mM KCl, pH 6	15.0
DPC	10 mM KCl, pH 6	12.4

4.2.3 Zeta potential

The same batch of glass spheres was used for both the zeta potential and AFM experiments, but the treatments were slightly different. The substantially higher volume fraction of particles in the zeta potential measurements (8×10^{-7} %) compared to AFM measurements (7×10^{-12} %) means that one must consider pH changes when protons adsorb or desorb from the particles. For the zeta-potential measurements, the glass spheres were placed in water, then titrated to pH 6 using HCl. Measurements were conducted with a Zeta Meter 3.0+ (Zeta-Meter Inc., Staunton, VA). Approximately 0.01 g of particles were added to 50 ml solutions of surfactant and KCl and equilibrated

for 48 hours. The electrophoretic mobility, u , was measured in both forward and reverse directions and averaged over several particles. The zeta potential was then calculated from the Hemholtz-Smoluchowski equation:⁷

$$\zeta = \frac{\eta u}{\varepsilon_r \varepsilon_0} \quad (4.1)$$

where η is the viscosity of the solution, ε_r is the relative permittivity of the solution, and ε_0 is the permittivity of a vacuum. Eq. 4.1 assumes that the particle size is much greater than κ^{-1} . This assumption is valid here, where the borosilicate particles have a diameter of 5 μm and the largest Debye-length is 9.5 nm.

4.3 Surface Forces

4.3.1 CPC / 10 mM KCl Solutions

Fig. 4.3 shows the force as a function of CPC concentration in 10 mM KCl (Debye-length, $\kappa^{-1} = 3.0$ nm). The forces at all measurable concentrations follow a very simple form. There is no crossing of curves for different concentrations. At concentrations less than 0.005 mM, the force changes little with concentration aside from a small increase in force with the initial addition of surfactant. From 0.005 to 0.01 mM, the force decreases with concentration, and from 0.01 mM to the *cmc*, the force increases with concentration.

In general, these trends are consistent with the zeta potential measurements shown in Fig. 4.4. Since both surfaces are very similar, the force should be greater when the absolute surface potential is greater. Note, however, that the minimum in force (0.01 mM) is not exactly at the zero of zeta potential (0.02 mM). This is consistent with the observations in C_{12}TAB solutions. At the attractive minimum, the force is much greater in magnitude than the van der Waals force between two silica surfaces. Above the *cmc*, there is little change because the chemical potential of surfactant is relatively insensitive to changes in concentration, as can be seen from the electrode data in Fig. 4.2a.

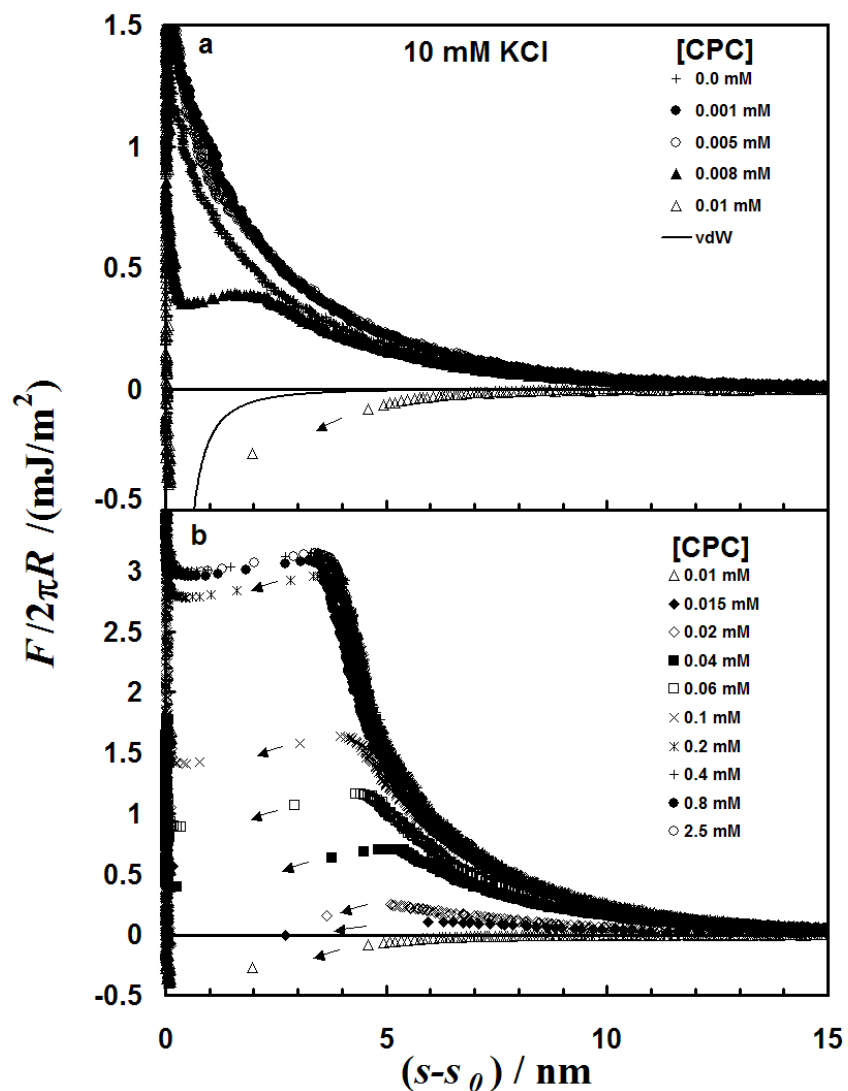


Figure 4.3 Forces between glass surfaces in 10 mM KCl as a function of CPC concentration. The Debye-length is $\kappa^{-1} = 3.0$ nm. **a)** Low concentrations. The force in 0.001 mM and 0.005 mM are the same within experimental error, and are slightly greater than in 0 mM CPC. From 0.008 mM to 0.01 mM CPC the force decreases as the concentration increases. The van der Waals force, shown for comparison, was calculated using the Hamaker constant for silica-water-silica of 0.8×10^{-20} J (Hough, D. B.; White, L. R. *Adv. Colloid Interface Sci.* **1980**, *14*, 3-41). **b)** Forces increase with increasing CPC concentration up to the cmc.

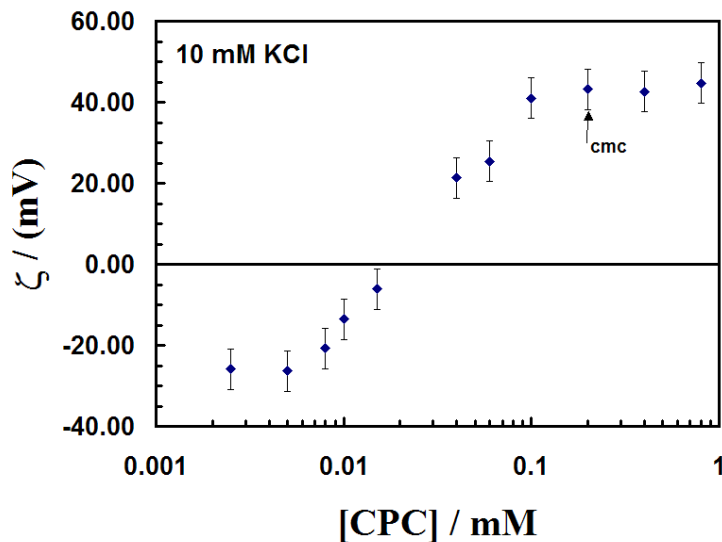


Figure 4.4. Zeta-potential of borosilicate glass spheres as a function of CPC concentration in 10 mM KCl at $\text{pH} = 6 \pm 0.2$. The zeta potential is zero at approximately 0.02 mM CPC, indicating that the surface charge on the silica plus the charge from adsorbed Cl^- is compensated by adsorption of CP^+ and K^+ ions from solution. (Reproduced with permission from Lokar, W.J.; Ducker, W.A. *Langmuir* **2004**, *20*, 378-388)

4.3.2 CPC / 1 mM KCl Solutions

The size of the double-layer increases by decreasing the ionic strength, which leads to a longer ranged double-layer force. The forces in 1 mM KCl (Fig. 4.5) are similar to those in 10 mM KCl, except that they are longer ranged, as expected ($\kappa^{-1}=9.5$ nm). The forces also change with concentration at these larger separations. Therefore, by eq. 1.23, the proximal adsorption occurs at larger separations at lower ionic strengths.

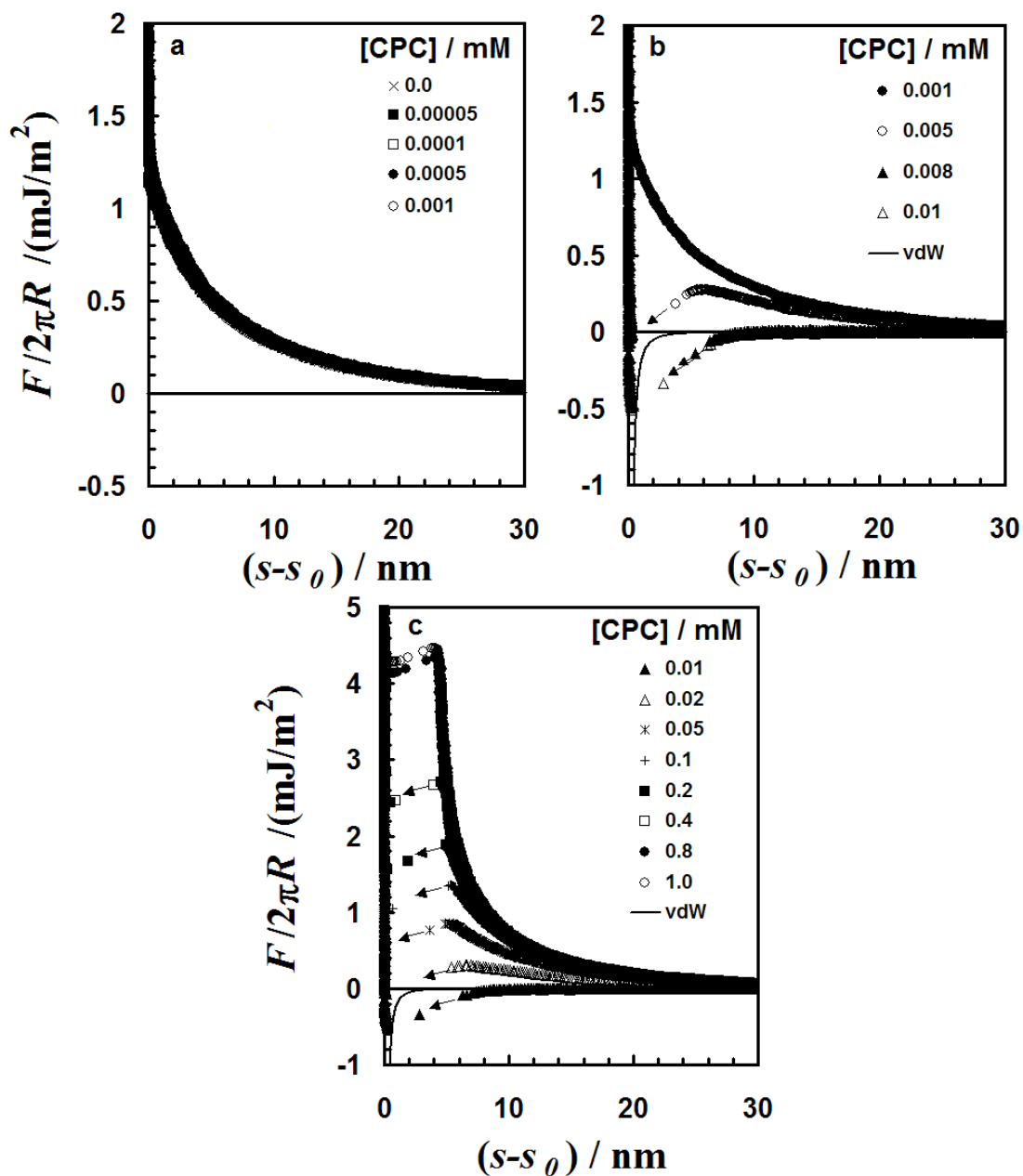


Figure 4.5 Forces between glass surfaces in 1 mM KCl as a function of CPC concentration. The van der Waals force shown is the same as in Fig. 4.3. **a)** Forces do not vary within experimental error for non-zero surfactant concentrations below 0.005 mM. The Debye-length is $\kappa^{-1} = 9.5$ nm. **b)** The force decreases from 0.005 mM to 0.01 mM CPC. The Debye-length is $\kappa^{-1} = 9.5$ nm. **c)** Above 0.01 mM CPC the force increases as the surfaces are brought together. The force is relatively constant above the cmc (0.68 mM). The Debye-length varies as the surfactant concentration approaches the KCl concentration.

The minimum in force occurs at the same CPC concentration for both salt concentrations, however, the force begins to become more attractive with concentration (implying proximal adsorption) at a lower surfactant concentration than in 10 mM KCl. This is because the steps in the adsorption isotherms occur at lower concentrations in more dilute salt solutions.⁴ In addition, the isotherms tend to intersect at the charge compensation point (*ccp*), which has been shown to be independent of salt.⁴ This should be in the vicinity of the most attractive forces.

4.3.3 CPC Solutions at pH 1.8

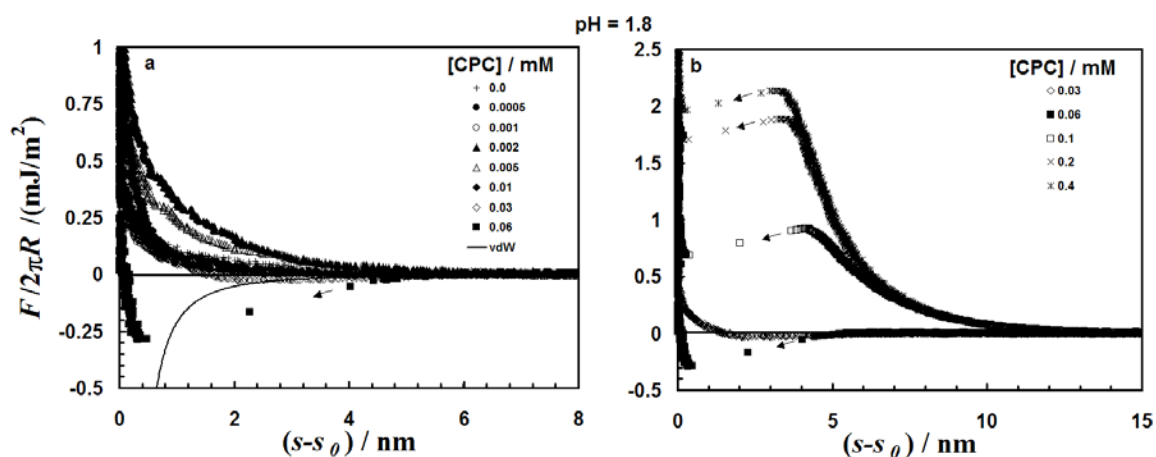


Figure 4.6. Forces between glass surfaces in as a function of CPC concentration at pH 1.8. The Debye-length is $\kappa^{-1} = 2.4$ nm. The van der Waals force shown is the same as in Fig. 4.3. **a)** Forces are virtually unchanged for CPC concentrations below 0.002 mM. Between 0.001 and 0.002 mM CPC the force increases slightly. The force then decreases as the concentration of CPC is increased. **b)** Forces increase with increasing CPC concentration above 0.06 mM.

Forces were also measured at pH = 1.8 (Fig. 4.6). At this pH, glass-like surfaces are known to have only a small charge.² In the absence of CPC, the force is weak and short-ranged, which is expected when the surface potential is small and the decay length is short ($\kappa^{-1} = 2.4$ nm). The forces increase slightly with concentration at low surfactant concentrations. This small increase in repulsive force at low surfactant concentrations is more pronounced at pH = 1.8 than at pH 6. The only significant changes in force as a function of surfactant concentration occur at very small separations, even smaller than 10

mM KCl, which has a similar Debye-length ($\kappa^{-1} = 3.0$ nm). The surfactant can, however, exert a strong influence on the force. At higher concentrations (Fig. 4.6b), the overall behavior is similar to that observed in 10 mM KCl: as the surfactant concentration is increased, the force increases.

4.3.4 DPC / 10 mM KCl

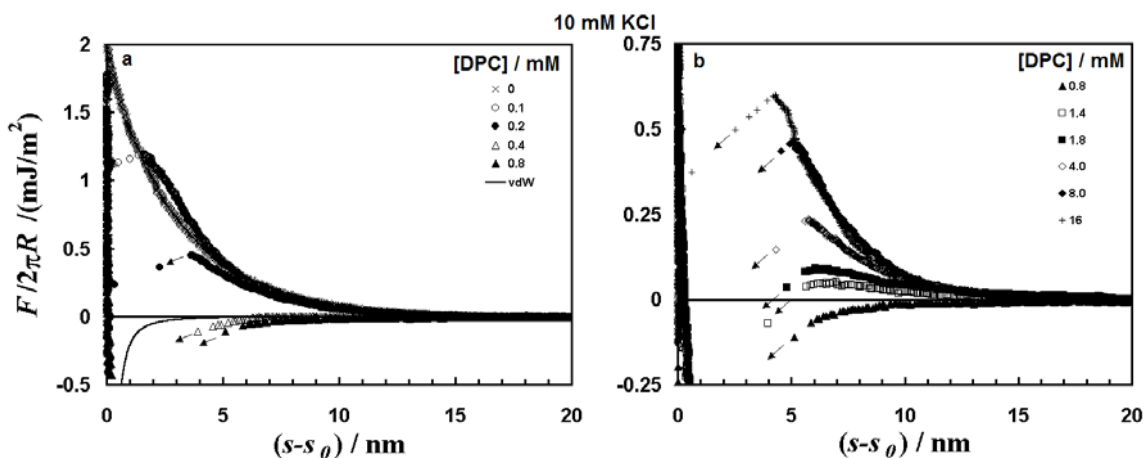


Figure 4.7 Forces between glass surfaces in 10 mM KCl as a function of DPC concentration. The arrows on the data show the force at which the cantilever spring constant equals the gradient in force. At this point the sphere undergoes non-equilibrium motion until $s = s_0$. The van der Waals force shown is the same as in Fig. 4.3. **a)** The force in 0.1 mM is slightly greater than in 0 mM DPC. From 0.1 mM to 0.8 mM DPC the force decreases as the concentration increases. The Debye-length is $\kappa^{-1} = 3.0$ nm. **b)** Forces increase with increasing DPC concentration up to the cmc. Note that the Debye-length is not constant for this data.

The force data presented in the previous sections gives a good representation of the effect of reducing the size of the double-layer and eliminating it at low pH. In this section force data in 10 mM KCl is presented for DPC, the 12-carbon analogue of CPC. Fig. 4.7 shows the forces as a function of DPC concentration. The forces are again very similar to those observed in CPC, but shifted to higher surfactant concentrations because of the greater surfactant solubility. As a consequence, the Debye-length varies as the cmc is approached, because the surfactant begins to contribute significantly to the ionic

strength. This is shown by the decrease in surfactant chemical potential above the *cmc* in Fig. 4.2b.

Above the *cmc*, the repulsive force in DPC is much smaller than in CPC, leading to the prediction that CPC would be much better at stabilizing negatively charged colloidal silica particles. The reason for this will be discussed in detail in the next chapter. Furthermore, the force goes from purely repulsive to attractive in Fig. 4.7a over a slightly larger range of concentrations. By eq. 1.23 the amount of proximal adsorption will be smaller in magnitude for the smaller chain length. The same phenomenon occurs in Fig. 4.7b, but in the opposite direction, as less proximal desorption occurs for DPC. A further analysis will be given later.

4.3.5 DPC / 1 mM KCl

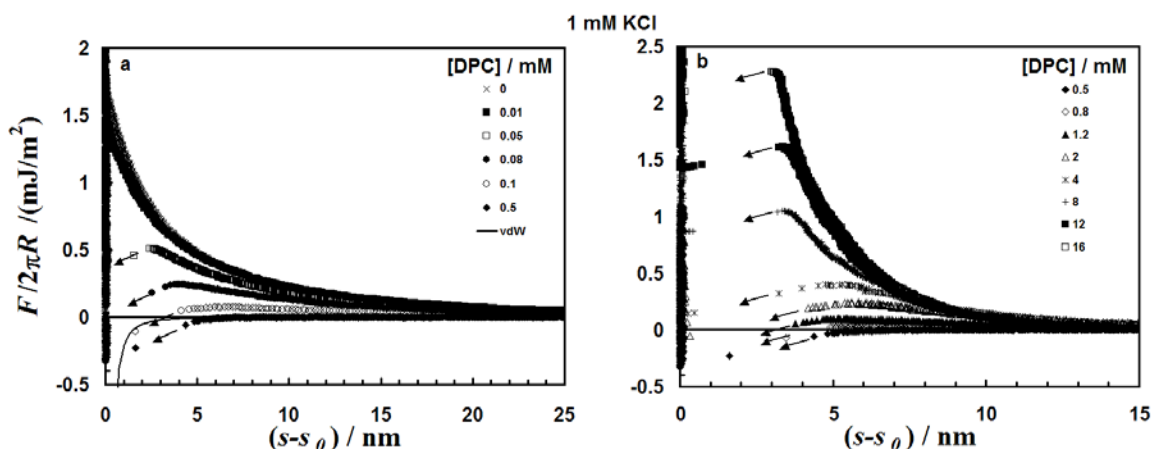


Figure 4.8 Forces between glass surfaces in 1 mM KCl as a function of DPC concentration. The arrows on the data show the force at which the cantilever spring constant equals the gradient in force. At this point the sphere undergoes non-equilibrium motion until $s = s_0$. The Debye-length varies with surfactant concentration. The van der Waals force shown is the same as in Fig. 4.3. **a)** From 0.01 mM to 0.5 mM DPC the force decreases as the concentration increases. **b)** Forces increase with increasing DPC concentration up to the *cmc*.

By measuring forces between glass surfaces in DPC / 1 mM KCl solutions, the electrolyte dependence for different chain lengths can be compared to confirm previous observations. The forces in 1 mM KCl (Fig. 4.8) are, once again, similar to those in 10

mM KCl, except that they are longer ranged. Due to the lower ionic strength, however, the Debye-length will vary even more at lower surfactant concentrations than in the 10 mM KCl case. The minimum in force occurs at a similar DPC concentration for both salt concentrations. This is similar to CPC. In addition, the force once again begins to become more attractive with concentration at a lower surfactant concentration than in 10 mM KCl, just as in CPC. The concentration range over which the force changes, is again larger than for CPC, suggesting less proximal adsorption and desorption of DP^+ by eq. 1.23.

4.3.6 Adhesion Data

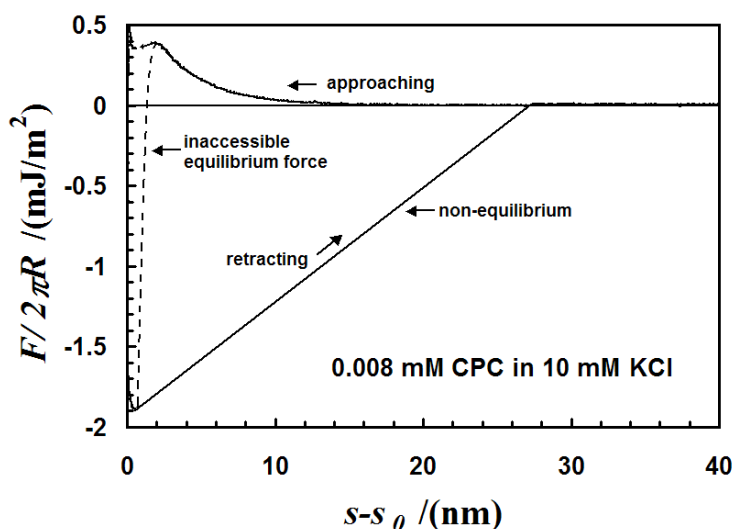


Figure 4.9 Comparison of forces upon approach and retraction of glass surfaces. This data is for $[CPC] = 0.008 \text{ mM}$ and $[KCl] = 10 \text{ mM}$. The approach force shows a repulsion until small separations, whereas upon retraction, the force is strongly attractive until the sphere jumps off of the surface. The dashed line shows an interpolated equilibrium force that is inaccessible by the AFM measurements.

The interaction forces between the surfaces in the previous sections were obtained as the surfaces approach in solution. This behavior is reversible down to the ‘jump-in’ point and the force upon retraction is the same. Once the surface jumps into ‘contact’, the retracting force curve is different from that on approach. As mentioned in chapter 2, this is because there is an adhesive force present between the surfaces. Fig. 4.9 shows an

example of the difference between the measured forces upon approach and retraction. Due to the mechanical instability of the cantilever that occurs, the equilibrium force curve is inaccessible during this instability. The interaction shows a strong attractive contribution as the surfaces are pulled apart. Once the spring constant of the cantilever is exceeded by the gradient of the pull-off force, the tip undergoes a non-equilibrium movement back to its equilibrium position. In Fig. 4.9 the dotted line corresponds to what the actual equilibrium force may look like.

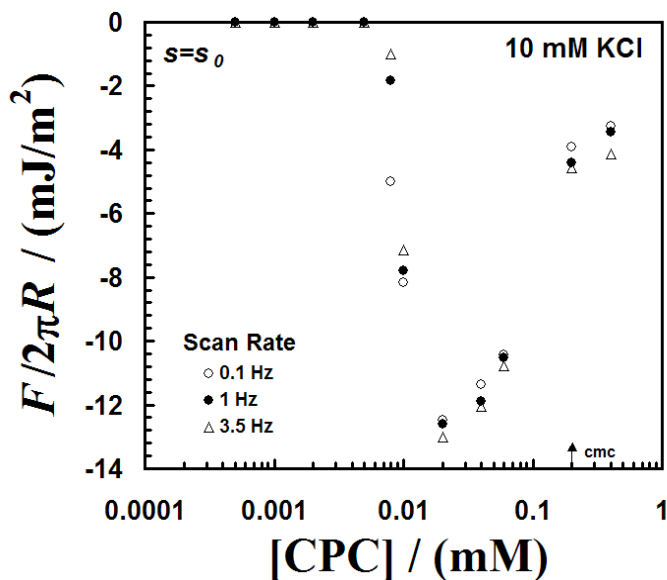


Figure 4.10 Adhesion vs. CPC concentration at various scan rates. This data is for CPC in 10 mM KCl. The adhesion is greatest (most attractive) at slow scan rates below $[CPC] = 0.2$ mM. Above $[CPC] = 0.2$ mM, faster scan rates produce a smaller adhesion.

The adhesion is sensitive to the speed of approach and retraction as a result of their non-equilibrium nature. Parker and Rutland⁸ have shown that the time that the surfaces are in contact will affect the adhesion considerably. The nature of the Digital Instruments AFM does not lend itself to maintaining contact for long periods of time. The effect of changing the continuous rate of approach then retraction can, however, be easily measured. Fig. 4.10 shows an example of the speed-dependence of adhesion. The largest speed-dependence appears to be near where the adhesion begins to change as a function

of surfactant concentration. As will be discussed later, there is a large amount of surfactant condensing between the surfaces in this concentration-separation regime, and sufficient time is required to allow this condensation to occur. This will be discussed in greater detail in the next chapter.

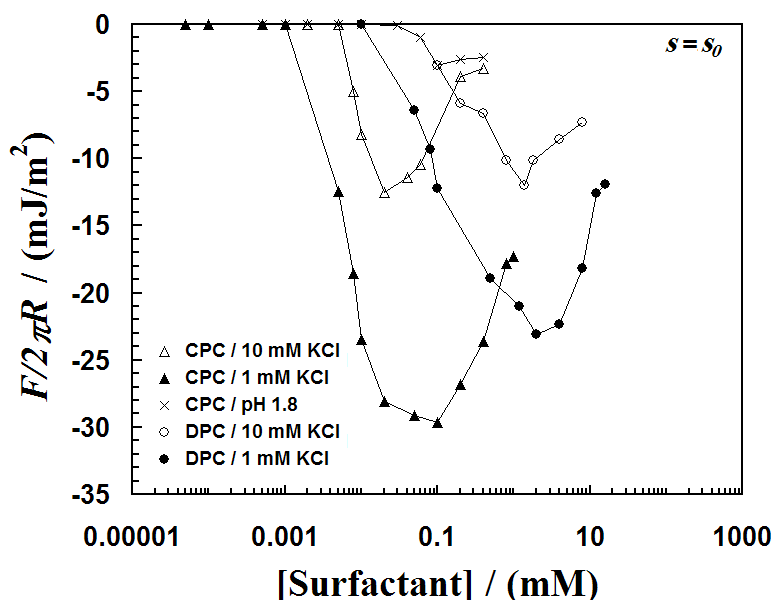


Figure 4.11 Adhesion vs. surfactant concentration at various solution conditions. The adhesion is greatest (most attractive) at lower salt concentrations for a particular surfactant. At a given ionic strength the adhesion is greater for the longer chained surfactant. The adhesion is small for CPC at pH 1.8.

Simultaneously, with the approaching force measurements, the adhesion was also measured for each of the surfactant/salt combinations shown in the preceding sections. In Fig. 4.11 the average adhesion at each concentration is plotted as a function of surfactant concentration. The adhesion shows roughly a parabolic shape, consistent with the work of Parker and Rutland.⁹ In the adhesion data, we see similar trends as with the force data upon approach. The slope of the force with log of the concentration is greater for CPC than for DPC, implying more proximal adsorption. In addition, the slopes are greater for CPC than DPC at similar ionic strength. Furthermore, both ionic strengths for a given surfactant show the minimum in force at similar surfactant concentrations. The breadth of the minimum is wider at lower ionic strengths, consistent with a wider first plateau in

the adsorption isotherm at lower ionic strengths.⁴ Eliminating the double-layer by decreasing the pH to 1.8 reduces the adhesion dramatically. This is consistent with the findings of Yaminsky,¹⁰ and suggests that the adhesion is strongly dependent upon the surface charge. This may be evidence that a strong charge–charge correlation between the surfaces exists at very small separations.

4.4 Proximal Adsorption

4.4.1 Analysis

In this section, eq. 1.23 is applied to the force data presented in section 4.3 in order to gain quantitative information about how the adsorption of CP⁺ and DP⁺ are changing as the glass surfaces interact.

The experimental forces were converted to E_a using Derjaguin's approximation (eq. 1.13). Values of E_a at a given surfactant chemical potential were converted to $\Delta\Gamma$ using eq. 1.23. For solutions below the *cmc*, μ_{CP^+} and μ_{DP^+} were obtained from Debye-Hückel theory, and for solutions above the *cmc*, μ_{CP^+} and μ_{DP^+} were determined from the electrochemical measurements presented in Fig. 4.2. The activity–potential relationship above the *cmc* was determined by calibrating the measured potential below the *cmc* with Debye-Hückel theory.

$$\mu_i = \mu_i^0 + RT \ln \gamma_i c_i \quad (4.2)$$

$$\gamma_i = \frac{-0.509\sqrt{I}}{1 + \sqrt{I}} \quad (4.3)$$

where γ_i is the activity coefficient, c_i is the concentration of i , and I is the ionic strength.

Eq. 1.23 requires a constant chemical potential of all species except the surfactant. An excess of KCl has been used to maintain μ_{Cl^-} constant. Therefore, eq. 1.23 can be applied specifically to the adsorption behavior of the surfactant cation. This approximation becomes worse when the concentration of surfactant approaches the concentration of added salt (for concentrated DPC and for concentrated CPC in 1 mM KCl).

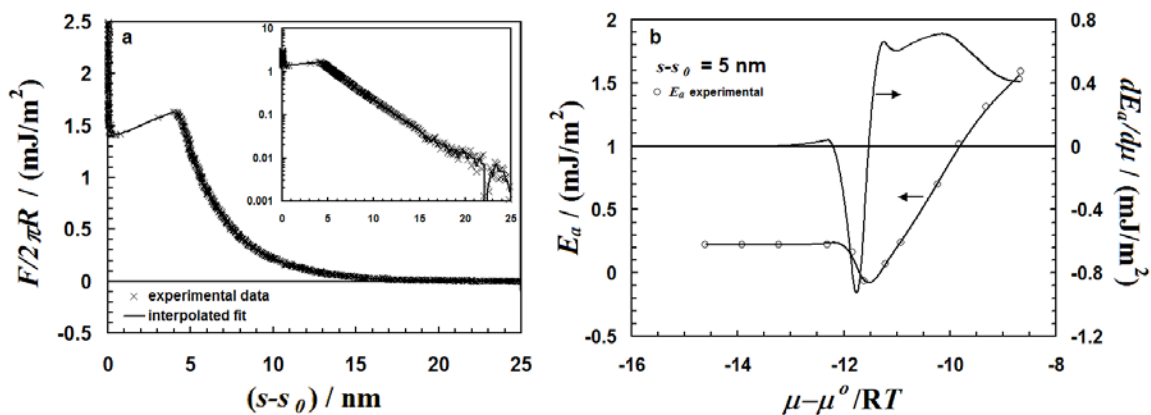


Figure 4.12 Interpolations of experimental data. **a)** Linear interpolation of force data. The data shown is for 0.1 mM CPC in 10 mM KCl. The solid line is the interpolated curve. The inset shows the same data on a log-lin scale. **b)** The interpolation of the interaction energy vs. the surfactant chemical potential is shown on the left axis for CPC in 10 mM KCl at $(s-s_0) = 5$ nm. The right axis shows the calculated derivative of the interpolated data used to determine the proximal adsorption.

Utilization of eq. 1.23 requires measurement of forces at a variety of concentrations, but at the same separation. Because of thermal drift in the AFM, the separation $(s-s_0)$ is only known after s_0 is established from the measurement. So measurements must be interpolated to obtain a data set at a constant separation. The data has been interpolated at 0.2 nm intervals using a linear interpolation. The derivatives in eq. 1.23 were determined from interpolated curves of E_a versus chemical potential. We used either a cubic or smoothing spline, whichever most accurately represented the experimental data. Fig. 4.12 shows an example of the interpolated data.

4.4.2 Results

The changes in surface excess as a function of separation at various surfactant concentrations and solution conditions are presented in Figs. 4.13–4.17. It is difficult to determine the exact concentration at which the minimum in force occurs, so there is a relatively large error in determining the concentration at which there is no proximal adsorption in this particular regime.

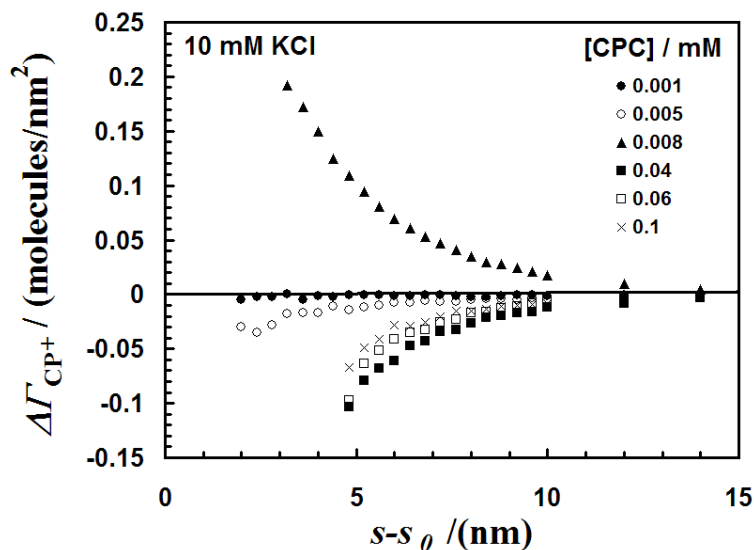


Figure 4.13 Changes in surface excess for CP^+ as a function of separation in 10 mM KCl. At $[CPC] \leq 0.005$ mM, the surfactant shows little change in adsorption. At 0.008 mM the surfactant adsorbs as the separations decreases. At higher surfactant concentrations, the surfactant desorbs as the separation decreases. The Debye-length is $\kappa^{-1} = 3.0$ nm.

While a detailed discussion of forces and proximal adsorption is reserved for the next chapter, where the mechanism of proximal adsorption will be discussed, a brief explanation of Figs 4.13–4.17 will be given. In all solutions, there are three basic regions to consider. Region (1) occurs at low concentrations, where the surfactant does not affect the surface forces. In this regime the surfactant adsorption is unaffected by the approach of a second surface. Region (2) is where the surface forces decrease as a function of surfactant concentration. Here, the surfactant adsorbs as the surfaces approach. The second and third regions are divided by a concentration at which the force is a minimum as a function of concentration. Here the adsorption is once again unaffected by the approach of two surfactant coated surfaces as $\left(\frac{\partial E_a}{\partial \mu_{\text{surfactant}}} \right) = 0$. In region (3), the force increases as the surfactant concentration increases and the surfactant desorbs as the surfaces approach.

In the first region, the force remains approximately the same as in the absence of surfactant. There is a small increase in force in this region, the reason for which is still unresolved. The increase in force is larger at higher ionic strengths and is largest at low pH, when there is a large amount of other cations present in solution. This suggests that the increase in force may be the result of an exchange between surfactant and other cations at the surface. This would explain why the strongly binding protons have the largest effect.

The transition between region (1) and region (2) shifts to higher surfactant concentrations in higher ionic strength solutions. This is consistent for both CPC and DPC and is the result of a shift in the hemi-micelle concentration to higher surfactant concentrations as the result of additional screening of the surface charge by the inert electrolyte.

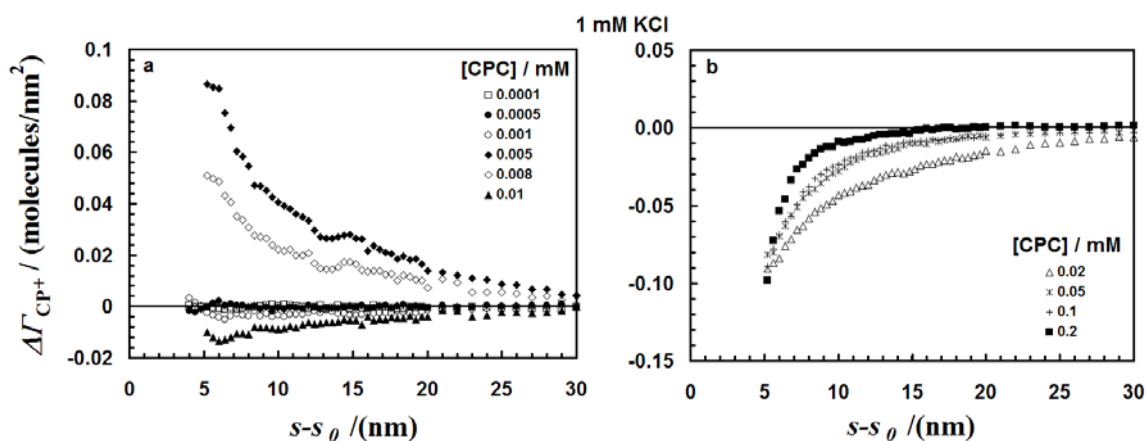


Figure 4.14 Changes in surface excess for CP^+ as a function of separation in 10 mM KCl. **a)** Low concentrations (below the pzc) of CPC in 1 mM KCl. The Debye-length is $\kappa^{-1} = 9.5$ nm. CP^+ does not adsorb for $[CPC] < 0.005$ mM. At 0.005 mM $\leq [CPC] < 0.01$ mM, c adsorbs as the surface approach. **b)** For 0.01 mM $< [CPC] < cmc$, the surfactant desorbs as the surfaces approach. The Debye-length varies.

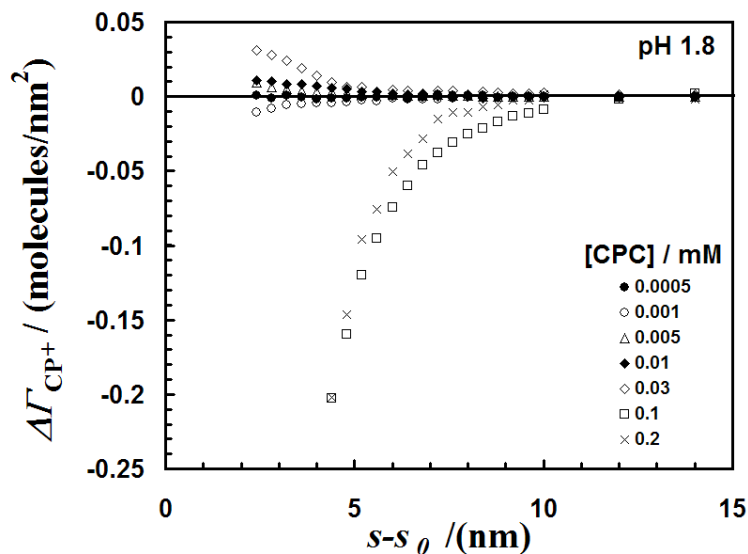


Figure 4.15 Changes in surface excess for CP^+ as a function of separation for various concentrations of CPC at pH 1.8. No significant adsorption as a function of separation occurs for $s-s_0 > 5$ nm. At higher concentrations the surfactant desorbs as the surfaces approach. The Debye-length is $\kappa^{-1} = 2.4$ nm.

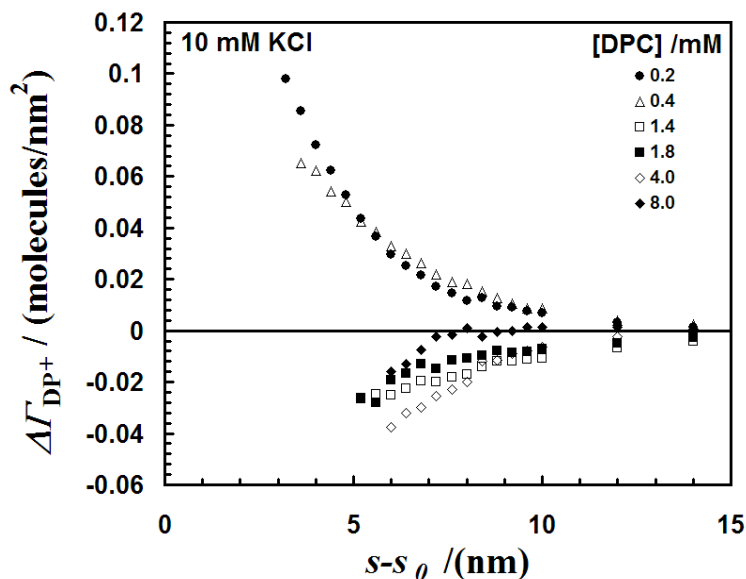


Figure 4.16 Changes in surface excess for DP^+ as a function of separation for various concentrations of DPC in 10 mM KCl. DP^+ adsorbs with decreasing separation for 0.2 and 0.4 mM DPC, but desorbs for 1.4, 1.8, and 4.0 mM DPC. The Debye-length varies according to surfactant concentration.

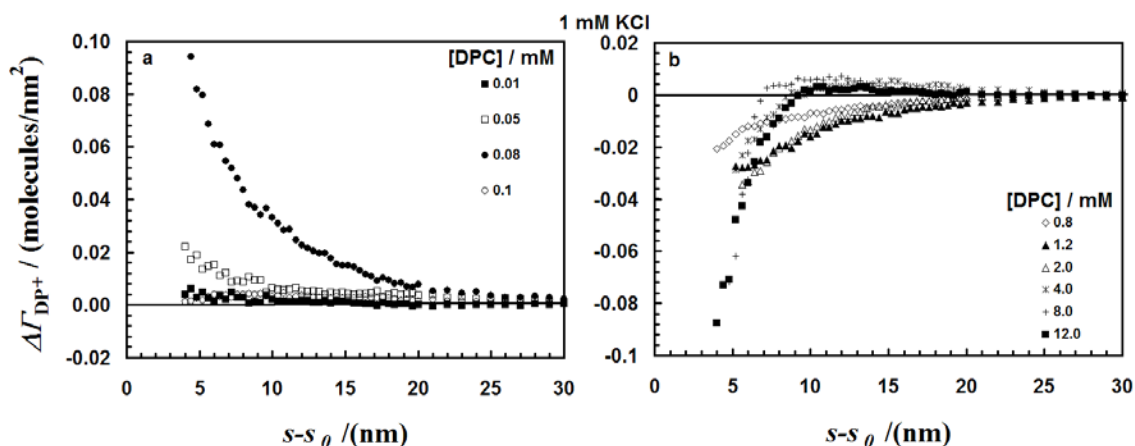


Figure 4.17 Changes in surface excess for DP^+ as a function of separation for various concentrations of DPC in 1 mM KCl. The Debye-length varies according to surfactant concentration. **a)** DP^+ adsorbs with decreasing separation for $0.01 \text{ mM} < [DPC] < 0.1 \text{ mM}$. **b)** DP^+ desorbs with decreasing separation. As the cmc is approached the proximal desorption becomes more short-ranged.

In region (2), the proximal adsorption is longer ranged in 1 mM KCl as a result of the increased Debye-length. This shows the strong influence of the double-layer upon proximal adsorption. Furthermore, eliminating the double-layer by reducing the pH to near the point of zero charge, eliminates all proximal adsorption except that at very small separations, showing that electrostatics are the dominant forces in proximal adsorption. If the behavior is compared as a function of chain-length, the proximal adsorption is greater for CPC at both ionic strengths. This shows that there is a distinct contribution of the surfactant chain to the magnitude of the proximal adsorption. The maximum attractive force occurs at the same surfactant concentration for CPC in both salt solutions, while there is only a small difference between salt solutions for DPC. At pH 1.8, the minimum force is shifted to higher CPC concentrations as a result of the strong neutralization of the surface charge by the potential determining protons.

In region (3), the surfactant desorbs as the surfactant concentration increases. Once again the range of the proximal desorption is longer in 1 mM KCl and the proximal desorption is larger for the longer chain CP^+ . At high surfactant concentrations near the cmc , the proximal desorption is often smaller than at slightly lower concentrations. This

is because there are two effects that are contributing. First, as the surfactant concentration increases, the ionic strength can begin to change. This means that the Debye-length is changing and eq. 1.23 may no longer be applicable. This occurs in the DPC measurements and for CPC in 1 mM KCl. The other effect is the loss of depletion. Since the surface is positively charged in this region, the Boltzmann equation tells us that positive species will be excluded from regions near the surface. Loss of depletion is therefore seen as additional adsorption. This effect is small as only small decreases in the desorption of CP^+ occur in 10 mM KCl and at pH 1.8. The changing Debye-length is most dominant in the DPC measurements and can be easily seen by the changing range of the proximal desorption in Figs. 4.16 and 4.17.

One of the most intriguing features in region (3) is that the proximal desorption of CP^+ is similar in 10 mM KCl and at pH 1.8 despite the fact that the adsorption behavior in region (2) is drastically different. The reason for this behavior stems from the adsorption mechanism. The surfactant is adsorbing to an already adsorbed surfactant layer rather than the glass surface, where the proton is also a potential determining ion. At these concentrations, the potential determining ions are the surfactant ions alone and not the protons. Therefore, the key effect of the pH is to control the ionic strength. This is why the behavior is similar to the 10 mM KCl, which had a similar Debye-length.

Eq. 1.23 can also be applied to the adhesion data to get an idea of how the surfactant behaves as the surfaces are brought into ‘contact’. It should be noted that the AFM convention of using the region of constant compliance as the zero of separation may mean that the glass surfaces are not necessarily in contact but rather the ‘contact’ is between two rigid condensed phases of adsorbed surfactant. Therefore, there may be error in using eq. 1.23, stemming from a change in the absolute separation if a condensed surfactant layer varies in thickness with concentration. In addition, unlike the approach data, which showed no scan rate dependence, the adhesion data may not be at adsorption equilibrium. There may not be sufficient time for large amounts of surfactant to adsorb and desorb as the surface cycle between zero and finite separations. This further complicates analysis with eq. 1.23, however, it can still provide a general idea of the behavior as the surfaces come into very close proximity.

Fig. 4.18 shows that at low chemical potentials in region (1), the surfactant surface excess does not change upon ‘contact’ by a second surface, following from the fact that there is no adhesion in Fig. 4.11. In region (2), the adhesion becomes prominent and the surfactant condenses between the surfaces. Despite, the ‘jump-in’ in the approach force data, the surfactant is *not* removed from the surface. In region (3), the surfactant is excluded from the surface to some extent. In both region (2) and (3), the amount of condensation and exclusion is greater at lower ionic strengths and greatly reduced when the surface charge is very low (pH 1.8).

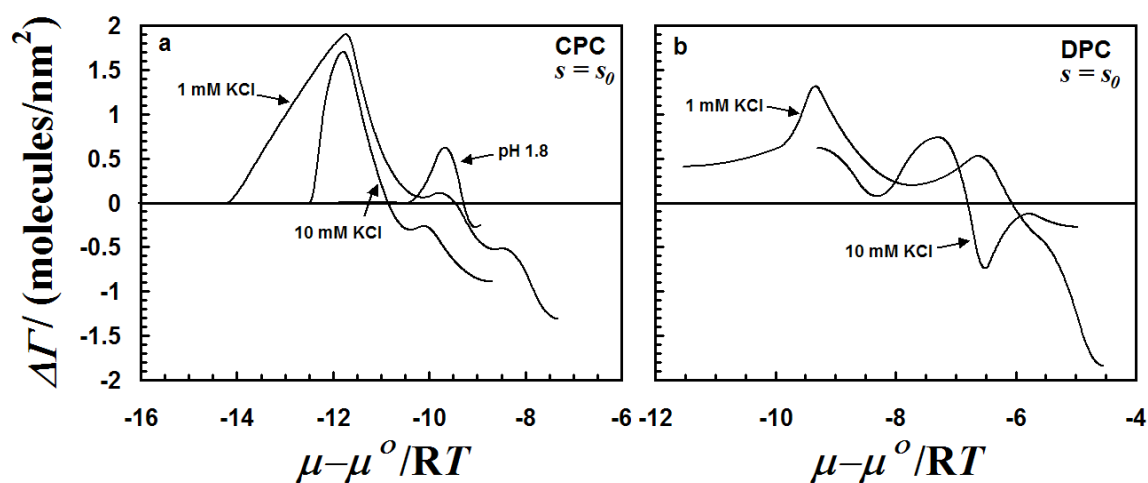


Figure 4.18 Changes in surfactant surface excess vs. surfactant chemical potential at $s=s_0$. **a)** Results for CPC. The surfactant condenses between the surfaces at low chemical potentials and is excluded from the surface at higher chemical potentials. Both condensation and exclusion are greater in 1 mM KCl and much smaller at pH 1.8. **b)** Results for DPC. The surfactant once again condenses between the surfaces at low chemical potentials and is excluded from the surface at higher chemical potentials. Both condensation and exclusion are greater in 1 mM KCl.

4.5 Conclusions

In 1 mM or 10 mM KCl solutions, the force between glass surfaces decreases at all finite separations when the concentration of surfactant is progressively increased to 0.01 mM CPC, and then increases as further surfactant is added up to the *cmc*. The largest net attractive forces measured are much larger than van der Waals forces, and are measurable

up to about 7 nm separation between the surfaces. Analysis using eq. 1.23 shows that, when the separation between the glass surfaces is decreased, the CP⁺ adsorbs below 0.01 mM, and desorbs above 0.01 mM, while the dividing concentration in DPC is ≈ 0.5 mM. The cationic surfactant adsorbs with decreasing separation when the surfaces have a negative potential and a significant concentration has been reached and desorbs when the surfaces have a positive potential resulting from the charge of the surfactant. The range in the proximal sorption changes with the changing Debye-length and proximal adsorption (at $s > s_0$) of surfactant is very low when the surface charge is low. The magnitude of the proximal adsorption depends on the chain length of the surfactant and therefore on the short-range (contact) interactions between surfactant molecules. When two surfaces come into contact ($s \sim s_0$), the close proximity of the surfaces causes a dramatic increase in surfactant adsorption in region (2) and a dramatic decrease in region (3) *relative to an isolated surface*. The range and magnitude of proximal adsorption depend on both κ^{-1} and the chain length (i.e. the double-layer and the short-range hydrophobic effect)

4.6 Cited Literature

- (1) Craig, V. S. J.; Ninham, B. W.; Pashley, R. M. *Langmuir* **1998**, *14*, 3326.
- (2) Goloub, T. P.; Koopal, L. K.; Bijsterbosch, B. H.; Sidorova, M. P. *Langmuir* **1996**, *12*, 3188.
- (3) Koopal, L. K.; Goloub, T. P.; de Keizer, A.; Sidorova, M. P. *Colloids and Surfaces A* **1999**, *151*, 15.
- (4) Goloub, T. P.; Koopal, L. K. *Langmuir* **1997**, *13*, 673.
- (5) Lokar, W. J.; Ducker, W. A. *Langmuir* **2002**, *18*, 3167.
- (6) Subramanian, V.; Ducker, W. *J. Phys. Chem. B* **2001**, *105*, 1389.
- (7) Evans, D. F.; Wennerström, H. *The Colloidal Domain: Where Physics, Chemistry, Biology, and Technology Meet*, 2nd ed.; Wiley-VCH: New York, 1999.
- (8) Parker, J. L.; Rutland, M. W. *Langmuir* **1993**, *9*, 1965.
- (9) Rutland, M. W.; Parker, J. L. *Langmuir* **1994**, *10*, 1110.
- (10) Yaminsky, V. V. *Langmuir* **1994**, *10*, 2710.

Chapter 5

Deducing Double-Layer and Chain Contributions to Proximal Adsorption

5.1 Introduction

In chapter 4, the forces between glass surfaces were presented for both CPC and DPC in 1 and 10 mM KCl. Furthermore, CPC measurements were conducted at pH 1.8 to show the effects of eliminating the double-layer. Eq. 1.23 was applied to the data in order to calculate the changes in surfactant adsorption as a function of the approach of a second, surfactant coated surface. In this chapter, the analysis in the previous chapter will be extended to give a more detailed discussion of the adsorption mechanism for cationic surfactants between approaching glass surfaces.

In particular, the focus will be on how the surfactant can regulate the interaction between the surfaces. It is well known that when like-charged surfaces interact in electrolyte solution, there will be a repulsive force between the surfaces as a result of the decrease in entropy when the two double-layers (one from each surface) overlap.^{1,2} The magnitude of the repulsive force depends on the way in which the ions adsorb and desorb in response to the overlap of the double-layers. This sorption alters the charge on the surface that contributes to the electric potential. This is known as charge regulation.³

The regulation produced by simple ions can be easily modeled by Poisson-Boltzmann theory, where the main energetic difference between bulk and adsorbed states as a function of separation is the surface potential. For surfactants, however, the hydrocarbon chain adds the possibility of additional energetic contributions due to its preferential exclusion from the aqueous environment. In chapter 3, an equation of state that included the Frumkin isotherm⁴ was proposed for the surfactant at the surface.

$$\mu_{ads} = \mu_{ads}^0 + RT \ln\left(\frac{\theta}{1-\theta}\right) + zF_A \psi(s) + RTA(\theta) \quad (3.1)$$

This equation has been used to describe adsorption at a single isolated surface. It therefore, would seem reasonable to use it as an initial starting point for discussion adsorption as a function of separation. In this chapter, the proximal adsorption from the previous chapter is discussed in the context of eq. 3.1. Several additional analyses are performed in order to further deduce the adsorption mechanisms that occur between

interacting surfaces. In addition, experimental data will be used to obtain values for $A(\theta)$. The overall goal is to eventually incorporate $A(\theta)$ into the charge regulation model to calculate double-layer forces. The hope is that this will provide a better fit to experimental data in surfactant solutions.

As a supplement to the force data and zeta potential measurements in chapter 4, additional experiments were performed to help characterize the systems. In particular, the adsorption to isolated glass particles and contact angles on our borosilicate glass plates provide useful information. The adsorption of cationic surfactants to silica in the presence of surfactant has been studied previously.⁵⁻¹² There is, however, often considerable variation between results obtained for different particles, so the adsorption was measured on the same particles as used for the force measurements.

5.2 Additional Experimental

5.2.1 Adsorption to 'Isolated' Particles

The same batch of glass spheres was used for adsorption as was used for AFM and zeta potential measurements. The treatment is the same as for the zeta potential measurements except that the spheres were dried for the adsorption isotherms so that the exact mass of particles was known. The surface area of the particles was determined to be 3.85 ± 0.20 m²/g by BET analysis. Adsorption to suspensions of particles was measured by the solution depletion method. An accurately known mass of approximately 20 mg of particles was added to 4 ml of a known concentration of surfactant and salt solution and allowed to equilibrate for 48 hours. During the equilibration the solutions were shaken and sonicated periodically to redisperse the particles. At the end of this period, the pH was measured. In all cases it was in the range 6.0 ± 0.2 so no further adjustments of the pH were made. Finally, the particles were removed by sedimentation and the solution was analyzed by a UV spectrometer (Ocean Optics Inc., Dunedin, FL) at 260 nm. The final concentrations were determined by reference to a calibration plot of absorbance versus known concentration.

5.2.2 Contact Angles

Contact angles were measured using a First Ten Angstroms model FT125 (Portsmouth, VA). The plates were treated as for AFM experiments, then a solution droplet was placed on the surface for ~ 10 min prior to measuring the receding angle.

5.3 Adsorption and Contact Angles

Fig. 5.1 shows the adsorption of CP^+ on the glass spheres as a function of surfactant concentration in the presence of 10 mM KCl. Adsorption rises slowly at low concentrations as expected, and shows a steep rise before leveling off near the cmc. The isotherm shows similar behavior to isotherms for CPC on silica at 10 mM salt and similar pH.^{8,13}

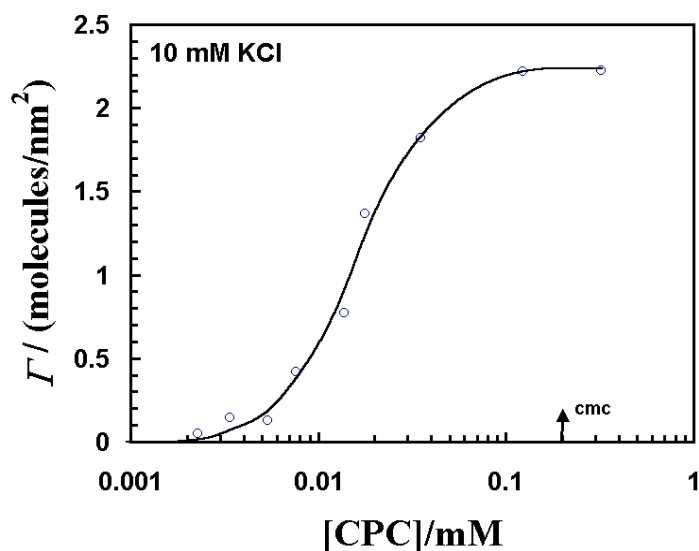


Figure 5.1 Adsorption of CPC to borosilicate glass particles in the presence of 10 mM KCl at $pH = 6 \pm 0.2$. The plateau adsorption occurs at a value of 2.2 molecules/nm².

Fig. 5.2 shows the *receding* contact angle of aqueous solutions of CPC on the same glass material that was used for the force measurements. As is typical for surfactant solutions on hydrophilic surfaces, the contact angle passes through a maximum.¹¹ The initial rise in contact angle is usually interpreted as being a result of surfactant adsorption with the alkyl chains facing the solution and the decline in contact angle at higher

concentrations is usually interpreted as being the result of adsorption with the head groups facing the solution. In our results, the addition of KCl is seen to increase the slope in the contact angle below the maximum. This is consistent with a smaller first plateau in the adsorption isotherms in higher salt, caused by screening of the electrostatic interaction between the surfactant head-groups and competition of other cations for adsorption sites on the silica surface.⁸ At concentrations greater than the maximum contact angle, the salt decreases the contact angle because it allows enhanced adsorption of surfactant, thereby making the surface more hydrophilic as the surfactant head-groups now face the bulk solution.

The addition of HCl causes a reduction in the maximum contact angle, which is consistent with less adsorption of surfactant. The proton is known to have a higher affinity for silica than K^+ .¹⁶

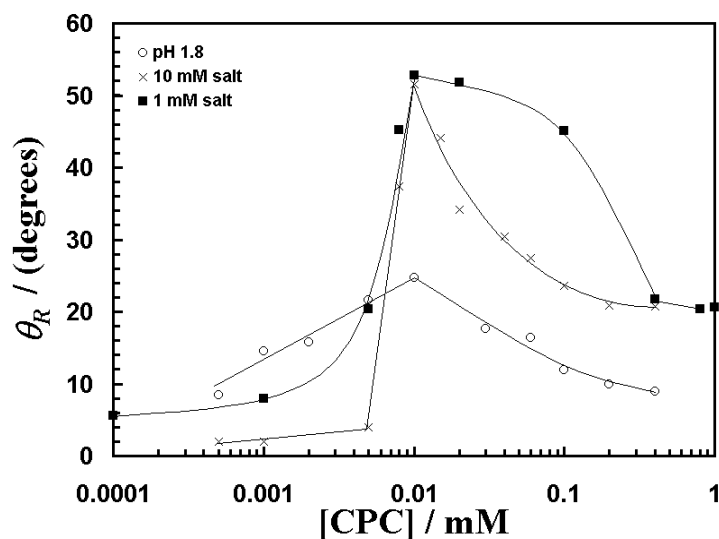


Figure 5.2 Receding contact angles for CPC solution droplets on a borosilicate glass plate at $pH = 6 \pm 0.2$. The lines are merely aids to enhance discrimination of data sets.

5.4 Proximal Adsorption

5.4.1 Double-Layer Effects

In the previous chapter, the range of the proximal adsorption appeared to scale with the range of the force. In lower electrolyte solutions, where the Debye-length is longer,

the proximal adsorption extended to larger separations. Furthermore, the plots of $\Delta\Gamma$ vs. $(s-s_0)$ in chapter 4 appear at first glance to decay exponentially. In Fig. 5.3 we have plotted a selection of proximal adsorption data on a log-lin scale to show that the curves do indeed decay exponentially.

At low surface potentials, the double-layer force also decays exponentially. Furthermore, experimental Debye-lengths are often determined by fitting a simple exponential to force data at large separations ($> \kappa^{-1}$). Therefore, by fitting an exponential curve to the proximal adsorption data the decay length of the proximal adsorption can be determined and compared to the theoretical Debye-length in solution. Such a comparison is given in Fig. 5.4. The decay lengths of the proximal adsorption correspond quite well to the Debye-lengths. This means that the proximal adsorption decays in a similar manner to the electrostatic double-layer force. Therefore, there is a very strong double-layer component to proximal adsorption of cationic surfactants on negatively charged surfaces. Fig. 5.4 includes data from many experiments including those conducted at pH = 1.8. Therefore, even though adsorption of H^+ reduces the magnitude of the proximal adsorption of surfactant, it does not appear to have changed the mechanism.

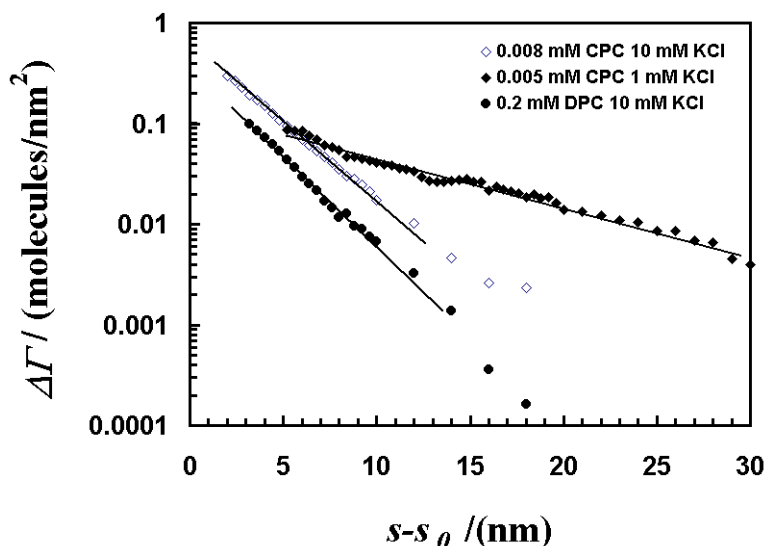


Figure 5.3 Examples of changes in surface excess displayed on a semi-logarithmic scale. The proximal adsorption is exponential with respect to separation.

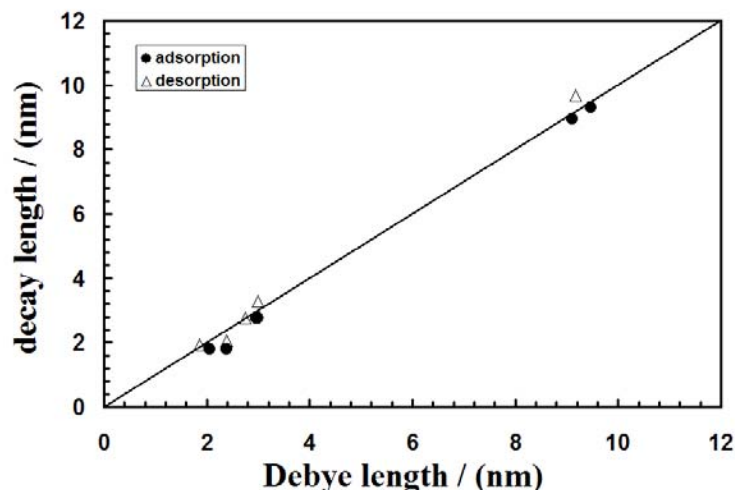


Figure 5.4 Decay length for proximal adsorption (●) and desorption (Δ) plotted versus the solution Debye-length. The solid line has a slope of one. The decay lengths correlate well with the Debye-length. The proximal adsorption and desorption used for the fits correspond to regions where the proximal sorption is a maximum.

If the double-layer contributes strongly to proximal desorption, does ΔF for the surfactant agree with Poisson-Boltzmann theory for simple ions? Similar to in chapter 3, the data is fit to DLVO theory using an exact numerical solution to the Poisson-Boltzmann equation and a Hamaker constant of 0.8×10^{-20} J (silica/water/silica).¹⁴ This will provide a useful comparison of our surfactant behavior to that predicted by DLVO for simple ions. Poisson-Boltzmann theory assumes that the charge on the surface is smeared out (mean-field) over a smooth plane. For small ions it is usually assumed that the plane simply corresponds to the solid-liquid interface. When surfactant adsorbs to the surface, it is reasonable that this ‘effective’ charge should move into solution. In other words, the thickness of the Stern layer increases. This is depicted in Fig. 5.5. Using the charge plane as the solid-liquid interface is a reasonable assumption when little surfactant is adsorbed or when the chain density does not significantly affect the local dielectric permittivity. When a second layer of surfactant adsorbs, Fig. 5.5 clearly shows the necessity in shifting the plane of charge away from the solid-liquid interface.

The potentials were fit at large separation, where the effect of adsorption changes is small. At concentrations, where the force increases with surfactant concentration, the

forces were too large to fit to DLVO theory if the plane of charge were placed at s_0 , as discussed in chapter 3 and by Rutland and Parker.¹⁵ Results from neutron reflectivity,¹⁶ as well as our contact angle measurements, suggest that there are head-groups facing solution. The steep rise in the force curve at about 5 nm also suggests that the surfactant film is at least 2.5 nm thick on each surface (at the *cmc*). Therefore, the plane of charge has been shifted to $s > s_0$. The plane of charge may move under an applied force as will be shown theoretically in chapters 8 and 9, but such additional freedom has not been incorporated into this fit. The adsorption of surfactant may also change the van der Waals force. The Hamaker constant for alkane/water/alkane, however, is similar to that of silica/water/silica¹⁴ so we made an approximate calculation of the van der Waals force by simply moving the zero of the van der Waals force to the same position as the zero for charge.

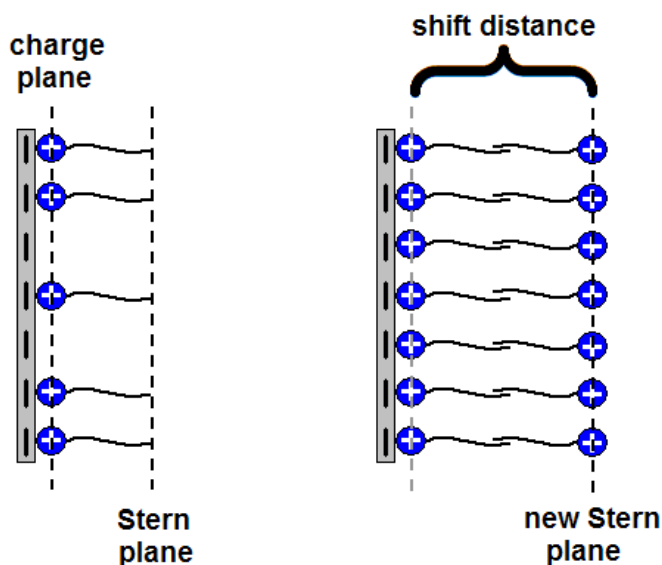


Figure 5.5 Representation of the shift in charge plane. At low adsorbed amounts, the charge plane is very close to the solid-liquid interface. When a second layer of surfactant is present, the plane of charge is shifted away from the solid-liquid interface.

The DLVO forces shown in Fig. 5.6 were calculated using a constant potential boundary condition, which in this case *fits* the data quite well down to small separations in 10 mM salt. In 1 mM salt the measured force is less repulsive than the fitted force for $s-s_0 < 3$ nm. Three examples of fits are shown in Fig. 5.6 for different surfactants and different ionic strengths. Tables 5.1 and 5.2 summarize the DLVO parameters, including

the shift distance, for all the force data in 1 and 10 mM KCl. The fitted potentials are plotted versus surfactant concentration in Fig. 5.7 to better aid comparison. The general form of the curves is very similar to the zeta-potential data presented in the previous chapter.

The potentials fit to double-layer theory are consistently greater than the zeta potentials measured on the particles (Fig. 4.4) under identical conditions. This is the opposite trend to that observed by Scales et al.¹⁷ The zeta-potential is the potential measured at the plane of shear, so one would expect a lower zeta-potential when the Debye-length is only 3 nm. If a plane of shear is chosen at $s-s_0 = 3$ nm, the zeta potential fits well to the fitted surface potential at all concentrations.

At higher surfactant concentrations, the shift required to fit DLVO theory begins to decrease at higher surface potentials. This could mean that the effective thickness of the charged layer decreases at small separations. As mentioned, this will be explored in the self-consistent field calculations in chapters 8 and 9.

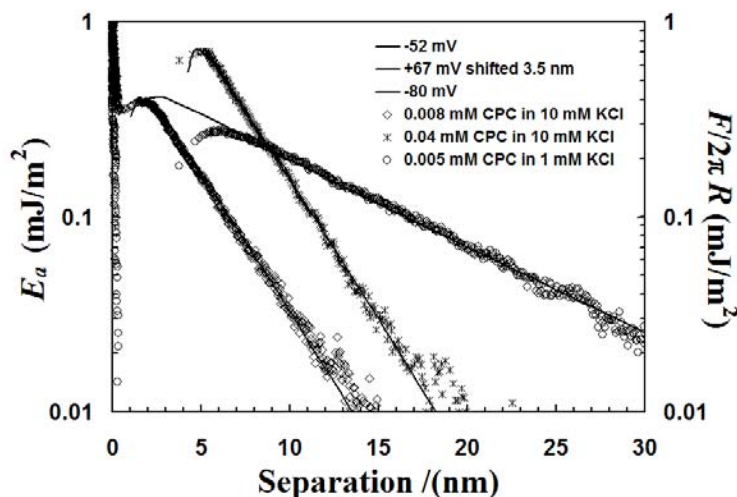


Figure 5.6 Interaction energy, E_a , measured by AFM compared to the energy calculated using DLVO theory at constant electrical potential. The experimental forces are at 0.008 mM and 0.04 mM CPC in 10 mM KCl and 0.005 mM CPC in 1 mM KCl. The DLVO fits shown are for $-52 \text{ mV} / \kappa^{-1} = 2.9 \text{ nm}$ and $+67 \text{ mV} / \kappa^{-1} = 2.9 \text{ nm}$, and $-80 \text{ mV} / \kappa^{-1} = 9.45 \text{ nm}$. The plane of charge for $+67 \text{ mV}$ has been shifted 3.5 nm toward the bulk solution.

Table 5.1. Fitted DLVO Parameters for CPC Experiments

[Surf.] / (mM)	ψ_0^a / (mV)	κ^{-1} / (nm)	Shift dist. / (nm)	σ_0^a / (e / nm^2)
CPC in 10 mM KCl				
0	-58	2.9	0	-0.10816
0.0005	-60	2.9	0	-0.11317
0.001	-60	2.9	0	-0.11317
0.002	-60	3.0	0	-0.10969
0.005	-62	2.9	0	-0.11893
0.008	-52	2.9	0	-0.09321
0.02	+45	2.9	2.7	+0.07740
0.04	+67	2.9	3.5	+0.13349
0.06	+79	2.75	3.4	+0.18342
0.1	+93	2.9	3.3	+0.23361
0.2	+118	2.9	2.8	+0.38830
0.4	+123	3.0	2.7	+0.41486
0.8	+120	2.85	2.5	+0.41126
CPC in 1 mM KCl				
0	-92	9.45	0	-0.07022
0.0001	-97	9.45	0	-0.07786
0.0005	-102	9.45	0	-0.08625
0.001	-102	9.45	0	-0.08625
0.005	-80	9.45	0	-0.05453
0.02	+73	9.6	3.0	+0.04611
0.05	+106	9.3	3.3	+0.09507
0.1	+125	9.1	3.8	+0.14234
0.2	+138	8.9	3.9	+0.18850
0.4	+154	8.0	3.6	+0.28785
0.8	+174	7.2	3.0	+0.47457
1.0	+176	7.4	2.6	+0.48031

^aThe sign of the potentials and charges are inferred from both the trends in the force data and the zeta potential measurements.

Table 5.2. Fitted DLVO Parameters for DPC Experiments

[Surf.] / (mM)	ψ_0^a / (mV)	κ^{-1} / (nm)	Shift dist. / (nm)	σ_0^a / (e / nm^2)
DPC in 10 mM KCl				
0	-85	3.1	0	-0.18489
0.1	-95	2.8	0	-0.25216
0.2	-75	3.0	0	-0.15418
4.0	+40	2.6	3.8	+0.07475
8.0	+52	2.2	3.6	+0.12287
12.0	+56	2.1	3.6	+0.14227
16.0	+56	2.1	3.6	+0.14227
DPC in 1 mM KCl				
0	-82	9.3	0	-0.05783
0.01	-80	9.45	0	-0.06065
0.05	-74	9.45	0	-0.04684
0.08	-61	9.1	0	-0.03703
0.1	-40	9.0	0	-0.02160
0.8	+22	6.5	2.0	+0.01533
1.2	+36	6.3	2.0	+0.02725
2.0	+53	5.5	2.5	+0.05041
4.0	+60	4.1	3.0	+0.08026
8.0	+79	2.9	2.2	+0.17393
12.0	+89	2.5	2.3	+0.24935
16.0	+98	2.3	2.3	+0.32652

^aThe sign of the potentials and charges are inferred from the trends in the force data.

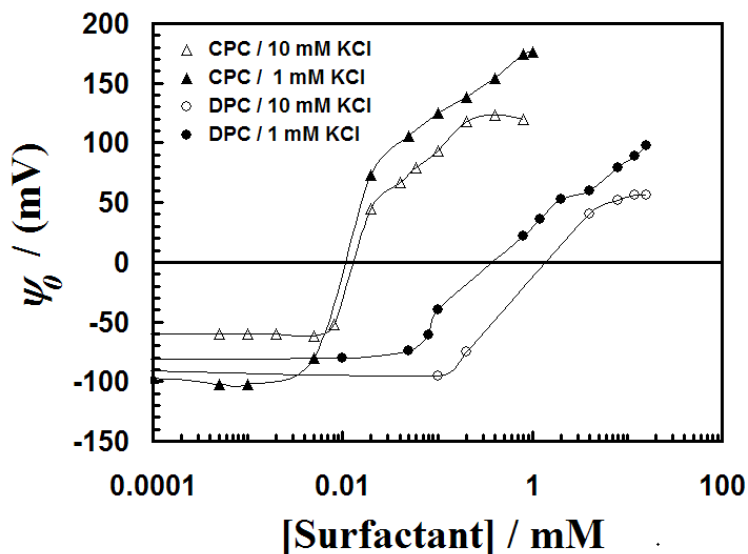


Figure 5.7 Fitted DLVO potentials versus surfactant concentration. The potentials are negative at low surfactant concentration and then pass through zero as the concentration is raised. The potential levels out at the cmc in each data set. The solid lines are merely guides, not theoretical fits to the data.

5.4.2 Chain Effects

If the surfactant ions behave like simple electrolytes as the surfaces interact, then Poisson-Boltzmann theory should provide a fairly accurate description of the regulation by the surfactant. In other words, our proximal adsorption should be consistent with the changes in charge predicted by the DLVO fits in the previous section. As was shown in chapter 3 for $C_{12}TA^+$, this is not the case. The surfactant adsorption changes in excess of that required to maintain constant electrical potential. Data for CPC and DPC are similar: surfactant proximal adsorption exceeds the amount required to regulate the charge. Fig. 5.8 shows the change in charge predicted by the fitted data in Tables 5.1 and 5.2 compared to $\Delta\Gamma$ calculated from eq. 1.23 using the force data in chapter 4. For both CP^+ and DP^+ , the deviation from Poisson-Boltzmann theory extends to larger separations at lower ionic strengths. Furthermore, the surfactant adsorbs more than required to maintain a constant potential interaction.

Other ions, however, must be considered. From Poisson-Boltzmann theory for simple ions, all positively charged ions should be adsorbing and negative ions should be desorbing in response to the overlap of double-layers as the negatively charged surfaces

approach. If this occurred to a significant extent, then the surfactant adsorption would be *less than* required to regulate the charge. In fact, the opposite occurs. Therefore, the excess adsorption of surfactant either (1) causes an even lower bound than constant potential for the double-layer interaction, (2) causes the behavior of one or more of the other ions to reverse, or (3) a combination of the two effects. This behavior will be discussed in more detail in the theoretical calculations in chapter 9. For now, emphasis is placed upon the magnitude of the enhanced surfactant adsorption.

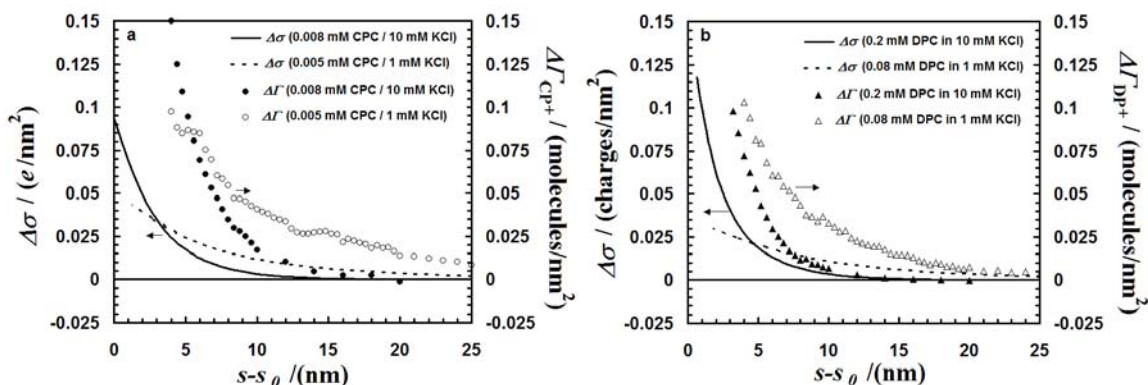


Figure 5.8 Change in surface excess of surfactant monomers and the change in charge required to maintain a constant surface potential in CPC and DPC solutions. Each curve represents the concentration where $\Delta\Gamma$ is a maximum in Figs. 4.14-4.17. The charge data is obtained from DLVO fits using the parameters in Table 5.1 and 5.2 **a)** Data in CPC solutions. $\Delta\Gamma$ exceeds $\Delta\sigma$ at all measured separations. **b)** Data in DPC solutions. $\Delta\Gamma$ exceeds $\Delta\sigma$ at all measured separations.

In order to deduce the effect of the surfactant chain, the deviations from Poisson-Boltzmann are plotted for different conditions. In Fig. 5.9 the difference between the changing surfactant surface excess and the predicted change in charge from Poisson-Boltzmann theory ($\Delta\Gamma - \Delta\sigma$) is shown.

Fig. 5.9 shows that at a lower salt concentrations, the deviation extends to greater separations. The deviation is so large at this long Debye-length that it is not possible to even fit the surface forces at small separation. (Fig. 5.6) When the measured force is much more attractive than calculated using DLVO theory, there is a temptation to

conclude that there is an additional long-range attractive force. This is how the ‘hydrophobic’ force was discovered.¹⁸ The proximal adsorption analysis shows us that the actual surfactant adsorption is much greater than that required to maintain constant electrical potential. Unless this discrepancy is made up by adsorption of Cl^- or desorption of K^+ , the surface charge is smaller than required by the fit to constant electrical potential, and the double-layer force is weaker than was predicted by conventional charge regulation models. The need to invoke an additional long-range force is replaced by a need to more accurately model the regulation of surfactant adsorption at constant chemical potential.

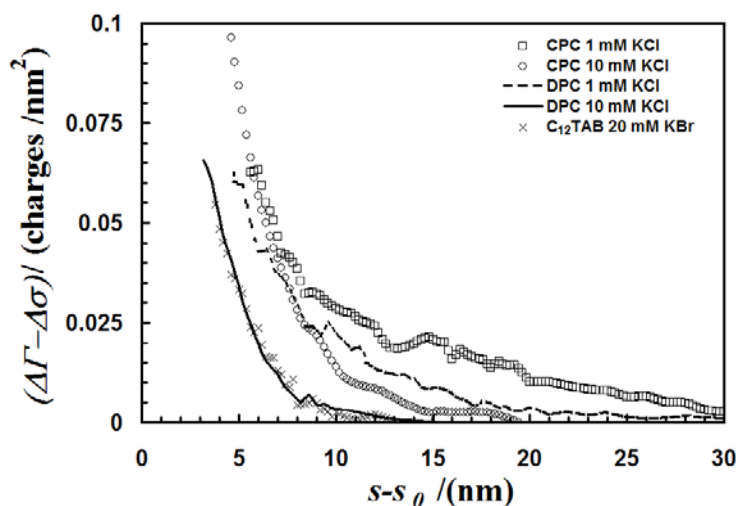


Figure 5.9 Differences between the proximal adsorption ($\Delta\Gamma$) calculated from $E_a(\mu)$ using equation 4 and the change in the number of charges ($\Delta\sigma/e$) obtained by fitting solutions to the Poisson–Boltzmann equation at constant electrical potential to $E_a(s-s_0)$. (\circ) 0.008 mM CPC in 10 mM KCl, (\square) 0.005 mM CPC in 1 mM KCl, (---) 0.08 mM DPC in 1 mM KCl, (—) 0.2 mM DPC in 10 mM KCl, and (\times) 0.8 mM C_{12}TABr in 20 mM KBr. The curves for the surfactants with a 12-carbon chain (DPC and C_{12}TAB) are considerably smaller in magnitude than those for the 16-carbon chain (CPC). The data for C_{12}TAB was taken from chapter 3.

In addition to the range of the deviations scaling inversely with ionic strength, the deviations are much greater for the 16-carbon CP^+ than the 12-carbon DP^+ . The chain-

chain interaction between surfactants is known to be important in adsorption of surfactants to isolated surfaces.¹⁹ Here, Fig. 5.9 shows a clear chain-length dependence upon the deviation from Poisson-Boltzmann theory. In addition, for similar ionic strengths, the curves for DP⁺ (10 mM KCl) and C₁₂TA⁺ (20 mM KBr) are nearly identical, despite the different head-group and the slightly different glass surfaces (borosilicate versus soda-lime glass). This shows that the deviation is strongly chain dependent with the minor differences in head-group-surface interaction playing a negligible role.

5.5 The Equation of State

Section 5.4 showed the importance of both the double-layer interaction and the short-range hydrophobic effect on the adsorption of surfactant between two interacting surfaces. In this section the experimental results in CPC and DPC solutions are summarized in the context of the proposed equation of state. In addition, experimental data is used to back out a reasonable form for the interaction term $A(\theta)$.

$$\mu_{ads} = \mu_{ads}^0 + RT \ln\left(\frac{\theta}{1-\theta}\right) + zF_A \psi(s) + RTA(\theta) \quad (3.1)$$

To aid this discussion, it is helpful to have the actual adsorption isotherms as a function of separation. In Fig. 5.10, the proximal adsorption calculated from eq. 1.23 (Fig. 4.13) is added to the isolated adsorption isotherm in Fig. 5.1 to obtain isotherms at various separations between our glass surfaces. The same three basic regions are present as mentioned in chapter 4. At low concentrations, the isotherms are unaffected by separation. Once the hemi-micelle concentration is reached, the isotherm begins to rise and the surfactant adsorbs as the separation is decreased. At $[CPC] > 0.1$ mM, the surfactant desorbs as the surfaces approach. Due to this switch over from proximal *adsorption* to proximal *desorption*, the isotherms as a function of separation show a common intersection, where the force as a function of concentration is a minimum. Bringing the surfaces into ‘contact’ leads to a large condensation of surfactant once the hemi-micelle concentration is reached. Furthermore, ‘contact’ between the surfaces causes the common intersection to be lost and the condensation occurs to the level of adsorption found near the *ccp* of the particles (Fig. 4.4). Parker and Rutland observed

condensation at concentrations below the hemi-micelle concentration if the surfaces were left in contact rather than cycled.^{15,20} Such behavior is observed in our theoretical calculations and will be mentioned later.

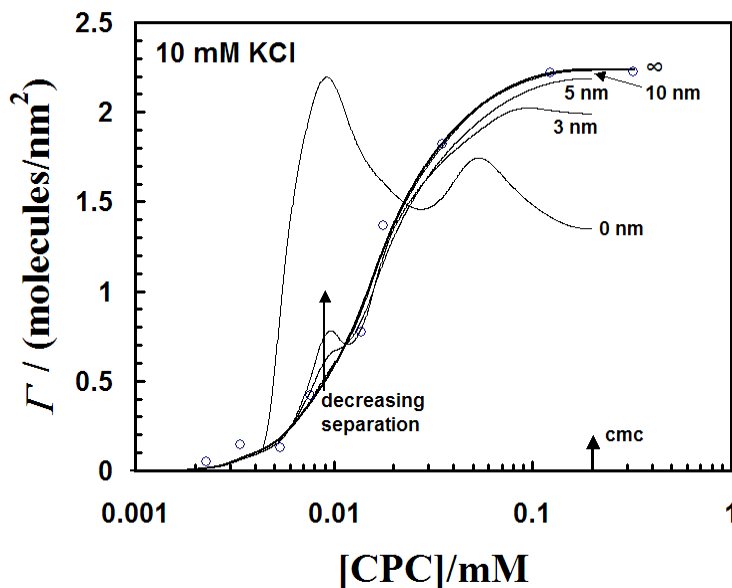


Figure 5.10 Adsorption as a function of concentration for various separations. The isotherm at infinite separation is for particles only, and the adsorption at other separations was obtained by adding the proximal adsorption for the particle–plate interaction. The plateau decreases with decreasing separation. The height of the peak below $[CPC] = 0.01$ mM increases as the separation decreases.

The results can be interpreted in terms of the chemical potential of the surfactant at the surface. In these experiments, the surfactant at the glass–aqueous solution interface is in equilibrium with a much larger amount of surfactant in bulk solution so the limit of a constant chemical potential of surfactant during changes in separation between the particles is discussed.

Because the last term in eq. 3.1 contains all density dependent chemical-specific short-range interactions, the functional form is difficult to write down. In chapter 3, the treatment of Prosser and Franses⁴ was followed, whereby $A(\theta)$ is negative and linear and is used to account for attractive interactions between the alkyl chains in aqueous solutions (the hydrophobic effect).

$A(\theta)$ is plotted versus θ , within the context of eq. 3.1 by using surface potential data and the measured adsorption isotherm. θ is determined from the isotherm as $\frac{\Gamma}{\Gamma_{cmc}}$.

Considering eq. 3.1 along with eq. 5.1, $A(\theta)$ can be calculated by equating the chemical potentials in the bulk and at the surface. Here, the bulk chemical potential is given by eq. 5.1. The activity of the ions is approximated here by the concentration. c^0 is the standard state concentration.

$$\mu_{bulk} = \mu_{bulk}^0 + RT \ln\left(\frac{c}{c^0}\right) \quad (5.1)$$

$$A(\theta) = \left(\frac{\mu_{bulk} - \mu_{ads}^0}{RT}\right) + \ln\left(\frac{c}{c^0}\right) - \ln\left(\frac{\theta}{1-\theta}\right) - \frac{zF_A\psi(s)}{RT} \quad (5.2)$$

Eq. 5.2 shows that the final two terms possess all the coverage dependence. The first term is a constant and is fit by assuming that $A(\theta)$ is approximately zero when $\theta=0$. The concentrations can be determined as a function of θ from the adsorption isotherm in Fig. 5.1. There are essentially two choices for the potentials. Either the fitted surface potentials from DLVO theory in Table 5.1 or the measured zeta potentials in Fig. 4.4 can be used.

Fig. 5.11 provides a comparison of $A(\theta)$ calculated from each set of potentials. Both show similar trends, however, the different magnitude in the potentials leads to some differences in $A(\theta)$ and $\left(\frac{\mu_{bulk} - \mu_{ads}^0}{RT}\right)$. For the data calculated from the measured zeta potentials, $A(\theta)$ is linear for $0.1 < \theta < 0.9$. The deviation at low coverage is probably due to larger experimental error in θ . At high coverages, surfactants are known to form surface aggregates, leading to a large cooperative effect. For the DLVO fitted data, there are deviations from linearity at intermediate coverages. This lack of linearity could be caused by two effects. First, the potentials required a semi-arbitrary shift of the plane of charge at high surfactant concentrations (Table 5.1). Possible error in this shift could contribute to error in the calculated $A(\theta)$.

Furthermore, the experimental measurements used here have different sensitivities to surface heterogeneity. The depletion isotherm measurements and zeta potential

measurements, require a large number of individual spheres, therefore, transitions can often be blurred by surface heterogeneity between particles. Therefore, the step in the isotherm marking the transition from monolayer to bilayer coverages can be blurred. The AFM measurements, on the other hand, use only two surfaces so steps may be more easily seen. Both possibilities are consistent with the fact that the change in slope for $A(\theta)$ calculated from the DLVO surface potentials occurs near the ccp , where the monolayer to bilayer transition begins. Furthermore, the correspondence between the change in slope of $A(\theta)$ and the change in slope of the DLVO fitted potentials can easily be seen in Fig. 5.11.

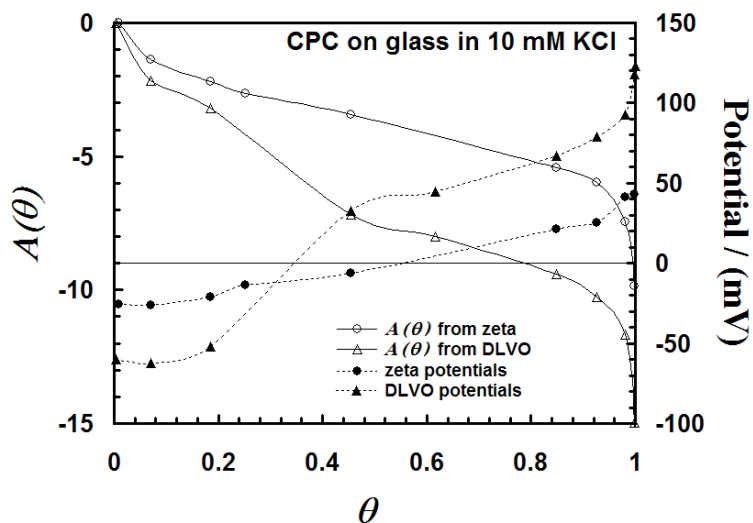


Figure 5.11 $A(\theta)$ and potentials vs θ for CPC in 10 mM KCl. The values for $A(\theta)$ are represented by the open symbols and the corresponding potentials from which they were calculated are shown with the solid symbols.

As a starting point, a straight line is fit to each $A(\theta)$ data set and the corresponding adsorption isotherms are calculated. In addition, a piece-wise function of two lines is also shown for comparison. It is reasonable to assume that the interaction parameter may be different in each region above and below the ccp due to some interactions of the surfactant with either the glass surface or a hydrocarbon layer (above the ccp). The calculated isotherms are shown in Fig. 5.12. For a linear fit (Fig. 5.12a and b), the calculated isotherm from eq. 3.1 is in excellent agreement for the zeta potential data. The

DLVO data provides a reasonable fit, however, the isotherms differ most drastically, where the linear fit and $A(\theta)$ deviate.

For the piece-wise combination of two lines, the calculated isotherms are in even better agreement. This process, however, produces a discontinuity in the adsorption isotherm. Other functional forms for $A(\theta)$ have been explored, however, focus is placed on the linear form because of both its simplicity and the fact that it can be expected that energies related to interactions between molecules should be scaled by the number of interactions.

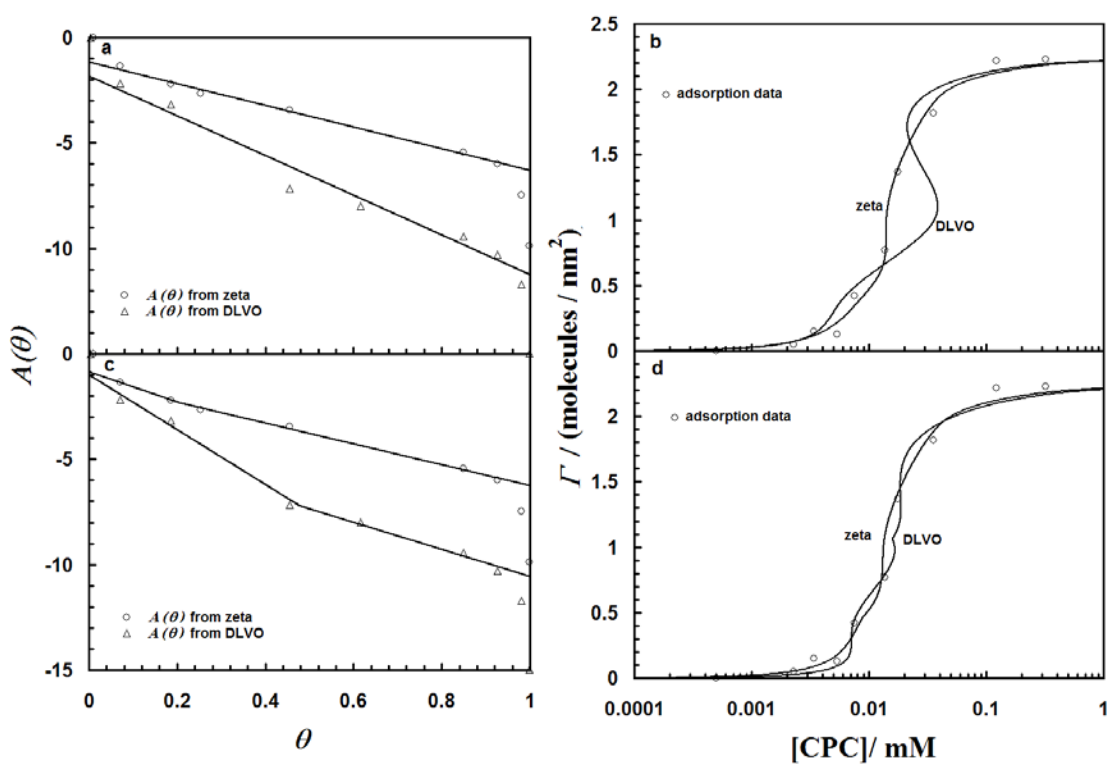


Figure 5.12 Fitted $A(\theta)$ (a and c) and corresponding isotherms (b and d). **a)** both $A(\theta)$ data sets are fit with a straight line. **b)** the corresponding isotherms are presented. The isotherm from the zeta potential shows very good agreement. The isotherm for the DLVO fit shows a condensation loop. **c)** both $A(\theta)$ data sets are fit with a two straight lines. **d)** The isotherm show better agreement with experimental data. Discontinuities occurs in the isotherms as the result of the discontinuous $A(\theta)$.

5.6 The Mechanism of Proximal Adsorption

5.6.1 Below the Hemi-Micelle Concentration

In this section the results of the previous work are discussed in terms of the modified Frumkin equation of state. At separations greater than where mechanical instabilities of the AFM cantilever are observed, the electrostatic potential term in the equation of state provides the driving force for changes in adsorption. All other terms respond merely as a result of the changing potential. For materials with larger Hamaker constants, the van der Waals force may play a role in changing adsorption.

At low surfactant concentrations, where there is little surfactant adsorbed and the force does not change as surfactant is added, the adsorption does not change as the surfaces approach each other. This is easily explained because the surfactant density is so low that the last term in eq. 3.1 is negligible. This is confirmed by the data in Fig. 5.11. During the approach of another surface, the charge on both surfaces can be regulated by adsorption of the much more numerous K^+ ions and the Poisson-Boltzmann equation should be acceptable. This is depicted in Fig. 5.13

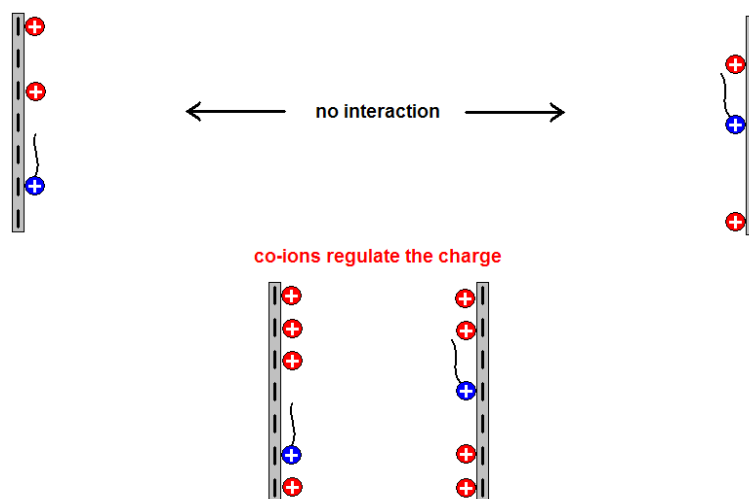


Figure 5.13 Depiction of regulation below the hemi-micelle concentration. The excess cations in solution regulate the charge.

5.6.2 $hmc < [Surfactant] < ccp$

At higher surfactant concentrations, the steep rise in the adsorption isotherm, as well as the receding contact angles (Figs. 5.1 and 5.2), indicate that $A(\theta)$ is now significant. In

Fig. 5.10, at the same surface excess where the density is very responsive to chemical potential, the density is also responsive to the approach of another surface. In 10 mM KCl, the adsorption of CP^+ increases by about 50% as the surfaces approach down to $(s-s_0) = 3$ nm in 0.008 mM CPC.

Despite being able to reasonably fit the force data to a double-layer force calculated at constant potential with no $A(\theta)$ term, the actual adsorption of CP^+ and DP^+ is much greater than is suggested by the good fit to the constant potential boundary condition. This deviation was shown to scale with the surfactant chain length and occurred out to separations that were dictated by the ionic strength. As the surfaces are brought together in electrolyte solutions, the overlap of the double-layers occurs at larger separations at lower ionic strengths. From eq. 3.1, this would lead to an increase in the potential at separations dictated by the Debye-length. An increase in the magnitude of ψ , leads to a reduction in the surface chemical potential. In an effort to maintain equilibrium with the bulk, the surface coverage of the oppositely charged surfactant increases. The process would cease here for a simple ion, however, raising the surface coverage causes a further reduction of the chemical potential by the $A(\theta)$ term. Therefore, the coverage of surfactant must again increase until all terms balance. The magnitude of this compensatory adsorption is determined by the magnitude of $A(\theta)$, whose value depends upon the chain length of the surfactant. This is shown in Fig. 5.14.

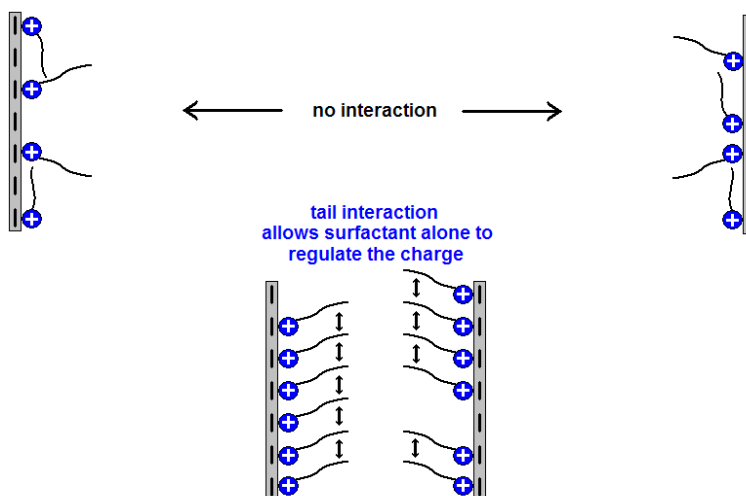


Figure 5.14 Depiction of regulation for $hmc < [\text{surfactant}] < ccp$. The excess tail interactions allow for adsorption in excess of charge regulation.

Reducing the double-layer by lowering the pH leads to a change in behavior based on the electrostatic term in eq. 3.1. The potential is now almost zero, therefore there is minimal double-layer overlap as the surface approach. Consequently, there is no driving force for the chemical potential to change with separation.

When the surface charge is near zero (at pH 1.8 or at the *ccp*), there will be no double-layer overlap as the surfaces approach and also no driving force for adsorption changes with decreasing separation by eq. 3.1. At this point, $\left(\frac{\partial E_a}{\partial \mu}\right)$ is zero and $\Delta\Gamma = 0$.

5.6.3 $ccp < [Surfactant] < cmc$

As the surfactant concentration is increased beyond the force minimum, the potential becomes positive and approach of a second, surfactant-coated surface leads to an increase in the potential once again. This time, however, the potential and the surfactant charge have the same sign. Therefore, overlap of the potential profiles causes an increase in the surface chemical potential of the surfactant leading to desorption of the surfactant to maintain equilibrium with the bulk. The fact that the desorption of surfactant is less for a shorter chain surfactant may at first seem counter-intuitive, however, it follows from the equation of state similarly to the case below the *ccp*.

The potential overlap increases the surfactant chemical potential and causes desorption to satisfy the entropic term. Lowering the coverage reduces the magnitude of the final term. Since this term is negative, a smaller negative term contributes to an increase in chemical potential and further desorption of surfactant. An increased value of A will lead to a larger reduction of $A\theta$ for a given change in θ . Therefore, more additional *desorption* for a larger value of A (longer chain). This is shown in Fig. 5.15.

Since the magnitude to the initial adsorption at large separations is dependent upon A , a larger A will contribute to more initial adsorption and a higher surface potential on the isolated surface above the *ccp*. This can be noticed by comparing the positive potentials between Tables 5.1 and 5.2. A larger potential will lead to a larger overlap and a larger initial driving force for desorption, as in the case of the longer surfactant.

Changing the pH has little effect at higher surfactant concentrations, because the surfactants are the potential determining ions and the pH does not affect the double-layer

other than to control the ionic strength. In systems where the surfactant head-group has dissociable protons such as carboxylic acids or amines, the pH is expected to affect proximal desorption.

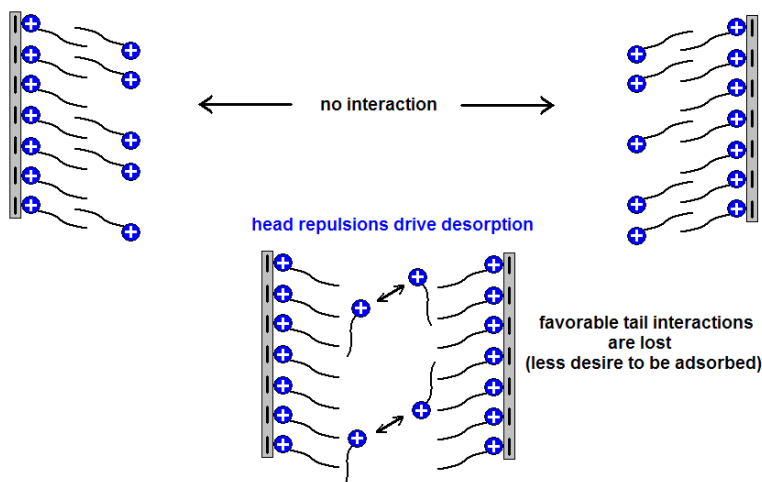


Figure 5.15 Depiction of regulation for $ccp < [surfactant] < cmc$. Head-group repulsions drive desorption, while the loss of favorable tail interactions allows for further desorption.

In general, the approach of a second surface is a bit like changing the pH for an isolated surface. The second surface changes the local potential, causing adsorption or desorption of the charged surfactant. This effect is large just below the ccp , where the dense alkyl chains and the negative potential conspire to enhance adsorption.

5.6.4 Proximal Sorption in ‘Contact’

Even greater adsorption occurs at \sim zero separation, where the alkyl chains from the two surfaces can overlap. The ‘contact’ data above the ccp suggests that all the surfactant is not removed from the surface. Details of the adsorption at zero separation, however, must be viewed with some skepticism because (1) it is more difficult to achieve equilibrium in a thin film, (2) the adhesion measurement is necessarily dynamic, and (3) the steep forces introduces large errors. These, factors are apparent in Fig. 4.10, where we looked at the effect of approach rate. Furthermore, Rutland and Parker have showed that at low concentrations keeping the surfaces in contact for longer periods of time leads to enhanced adsorption and a larger adhesion.²⁰ From the isotherm in Fig. 5.10, there is

strong adsorption as the surfaces are brought into ‘contact’ at low concentrations. In addition, the adsorption seems to form a plateau at a value where the isolated *particle* has zero charge. This will be discussed more in the context of the calculations in chapter 9.

The adsorption behavior at ‘contact’ can be used to explain the trend in the adhesion with increasing scan rate. Bringing the surfaces together more slowly, allows time for the surfactant to condense in the gap between the surfaces and also increases the contact time slightly. This is consistent with the results of Rutland and Parker.²⁰ At concentrations above where the strongest adhesion occurs, the trend with scan rate reverses and the speed dependence appears to be much smaller. This is likely due to the fact that there is more time for the surfactant to re-adsorb as the surfaces are separated and therefore, the forces can be more easily separated if more time is given to reach equilibrium.

In the context of eq. 3.1, the behavior at ‘contact’ is similar to other separations, except that the final interaction term should likely double as the surface layers from opposite surfaces merge. This is due to the fact that the surfactants have access to interactions with twice as many other surfactants once the layers merge.

5.7 Conclusions

Proximal adsorption of cationic surfactants to glass surfaces shows a strong dependence upon both electrostatic double-layer forces and the length of the hydrocarbon chain. The decay-length of $\Delta\Gamma$ versus separation shows good agreement with the solution Debye-length. Furthermore, eliminating the double-layer eliminates proximal adsorption at separations larger than about 5 nm. The amount of proximal adsorption scales with the surfactant chain length. Furthermore, deviations in the surfactant adsorption compared to predicted changes in ionic adsorption for simple ions shows a clear dependence upon chain-length. The use of an equation of state for the surfactant following from the Frumkin isotherm, provides reasonable fits to the adsorption isotherm for an isolated surface using a simple linear dependence of the chain interaction term on the surface coverage of surfactant. Such an equation of state allows for a qualitative description of the adsorption as a function of separation between glass surfaces, and therefore a qualitative description of the force as a function of separation. A functional form of $A(\theta)$,

which can be used in future work to obtain a more realistic regulation model for surfactant adsorption has been obtained.

5.8 Cited Literature

- (1) Derjaguin, B. V.; Landau, L. D. *Acta Phys.-Chim URSS* **1941**, *14*, 633.
- (2) Verwey, E. J.; Overbeek, J. T. G. *Theory of the Stability of Lyophobic Colloids*; Elsevier: Amsterdam, 1948.
- (3) Ninham, B. W.; Parsegian, V. A. *J. Theor. Biol.* **1971**, *31*, 405.
- (4) Prosser, A. J.; Franses, E. I. *Colloids and Surfaces A* **2001**, *178*, 1.
- (5) Wängnerud, P.; Olofsson, G. *J. Colloid Interface Sci.* **1992**, *153*, 392.
- (6) Goloub, T. P.; Koopal, L. K.; Bijsterbosch, B. H.; Sidorova, M. P. *Langmuir* **1996**, *12*, 3188.
- (7) Esumi, K.; Matoba, M.; Yamanaka, Y. *Langmuir* **1996**, *12*, 2130.
- (8) Goloub, T. P.; Koopal, L. K. *Langmuir* **1997**, *13*, 673.
- (9) Favoriti, P.; Treiner, C. *Langmuir* **1998**, *14*, 7493.
- (10) Pashley, R. M.; Karaman, M. E.; Craig, V. S. J.; Kohonen, M. M. *Colloids and Surfaces A* **1998**, *144*, 1.
- (11) Koopal, L. K.; Goloub, T. P.; de Keizer, A.; Sidorova, M. P. *Colloids and Surfaces A* **1999**, *151*, 15.
- (12) Fleming, B. D.; Biggs, S.; Wanless, E. J. *J. Phys. Chem. B* **2001**, *105*, 9537.
- (13) Favoriti, P.; Mannebach, M. H.; Treiner, C. *Langmuir* **1996**, *12*, 4691.
- (14) Hough, D. B.; White, L. R. *Adv. Colloid Interface Sci.* **1980**, *14*, 3.
- (15) Rutland, M. W.; Parker, J. L. *Langmuir* **1994**, *10*, 1110.
- (16) Fragneto, G.; Thomas, R. K.; Rennie, A. R.; Penfold, J. *Langmuir* **1996**, *12*, 6036.
- (17) Johnson, S. B.; Drummond, C. J.; Scales, P. J.; Nishimura, S. *Langmuir* **1995**, *11*, 2367.
- (18) Israelachvili, J.; Pashley, R. *Nature* **1982**, *300*, 341.
- (19) Somasundaran, P.; Fuerstenau, D. W. *J. Phys. Chem.* **1966**, *70*, 90.
- (20) Parker, J. L.; Rutland, M. W. *Langmuir* **1993**, *9*, 1965.

Chapter 6

Proximal Adsorption in Mixed Cationic-Zwitterionic Surfactants

6.1 Introduction

In chapters 3-5, it was proposed that an accurate description of the proximal adsorption of cationic surfactant requires a term in the chemical potential, $RTA(\theta)$ to account for the net-attractive interactions between the surfactant molecules (particularly the alkyl chains) in water:^{1,2}

$$\mu_{ads} = \mu_{ads}^0 + RT \ln\left(\frac{\theta}{1-\theta}\right) + zF_A\psi(s) + RTA(\theta) \quad (3.1)$$

In particular, the electrostatic interaction of the surfactant with the surface initiates proximal adsorption, but the chain length ultimately governs the magnitude of the adsorption changes. Here forces and adsorption are examined in aqueous solutions containing both a net-uncharged zwitterionic surfactant (N-dodecyl-N,N-dimethyl-3-ammonio-1-propanesulfonate or DDAPS) and a cationic surfactant (dodecylpyridinium chloride or DPC). The aim is to examine how forces and adsorption are affected by interactions between alkyl chains on different types of surfactants, one which can regulate the charge (DPC) and one, which can not (DDAPS). The structures of these surfactants are shown in Fig. 6.1.

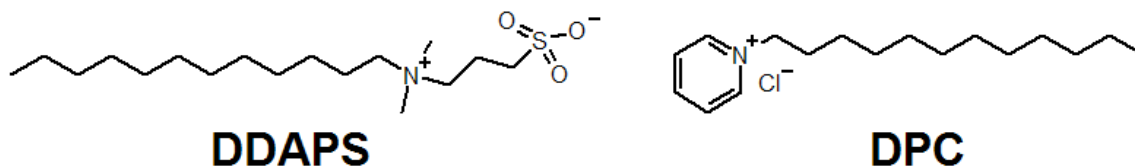


Figure 6.1 *N-dodecyl-N,N-dimethyl-3-ammonio-1-propanesulfonate (DDAPS) and dodecylpyridinium chloride (DPC).*

Eq. 3.1 assumes that $A(\theta)$ and the entropy of mixing depend only upon the surface density of a single adsorbate. This equation is reasonable when one adsorbate dominates adsorption, such as for a cationic surfactant above the hemi-micelle concentration. If there are two species that dominate adsorption, then eq. 3.1 should be rederived for more than one adsorbate. Since in this chapter adsorption of two different surfactant molecules

is monitored simultaneously, a version of eq. 3.1 will be derived for two adsorbing species.

Consider a lattice on the surface with N surface sites. Three different types of molecules can be distributed on this lattice, a solvent molecule (1), and two adsorbing molecules (2 and 3). The Gibb's free energy of this incompressible lattice is written as

$$G = G^0 + n_2\mu_2^0 + n_3\mu_3^0 - TS + x_1n_1\frac{w_{11}}{2} + x_2n_2\frac{w_{22}}{2} + x_3n_3\frac{w_{33}}{2} + (n_1x_2 + n_2x_1)\frac{w_{12}}{4} + (n_1x_3 + n_3x_1)\frac{w_{13}}{4} + (n_2x_3 + n_3x_2)\frac{w_{23}}{4} \quad (6.1)$$

where G^0 is the standard state Gibb's free energy of the solvent. μ_2^0 and μ_3^0 are the standard state chemical potentials of each surfactant (molecules 2 and 3). Therefore, the second and third terms account for the change in G brought about by adding n_2 molecules of type 2 and n_3 molecules of type 3 to the surface. The fourth term accounts for the entropic contribution brought about by adding adsorbates 2 and 3. Terms 5–7 account for homomolecular interactions and terms 8–10 account for heteromolecular interactions, where x_i is the mole fraction of i and w_{ij} is the pair-wise interaction energy (per molecule) of i with j . The interactions are weighted by the number of molecules, n_i of a species multiplied by the probability (volume fraction) that an adjacent site will be occupied by molecule j .

Eq. 6.1 can be rewritten as

$$G = G^0 + n_2\mu_2^0 + n_3\mu_3^0 - TS + \frac{n_1^2w_{11}}{2N} + \frac{n_2^2w_{22}}{2N} + \frac{n_3^2w_{33}}{2N} + \frac{n_1n_2w_{12}}{2N} + \frac{n_1n_3w_{13}}{2N} + \frac{n_2n_3w_{23}}{2N} \quad (6.2)$$

The entropy of this surface lattice is simply given by

$$S = k_B \ln \Omega \quad (6.3)$$

where k_B is Boltzmann's constant and Ω is the number of possible configurations of the system. Ω is determined as follows. For the solvent molecules, there are N free sites to begin with and n_1 solvent molecules. The number of possible configurations is

$\frac{N!}{n_1!(N-n_1)!}$. There are now $(N-n_1)$ sites on which to place n_2 molecules of type 2.

There are now $\frac{(N-n_1)!}{n_2!(N-n_1-n_2)!}$ possible ways of arranging these molecules. Next,

molecules of type 3 are added, however, there is only one remaining possibility, which is to fill all remaining sites with molecule 3. Therefore, the overall number of configurations for this 3-molecule system is given as,

$$\Omega = \frac{N!}{n_1!(N-n_1)!} \frac{(N-n_1)!}{n_2!(N-n_1-n_2)!} = \frac{N!}{n_1!n_2!n_3!} \quad (6.4)$$

S can now be evaluated.

$$S = k_B \ln \left(\frac{N!}{n_1!n_2!n_3!} \right) \quad (6.5)$$

$$S = k_B [\ln N! - \ln n_1! - \ln n_2! - \ln n_3!] \quad (6.6)$$

Sterling's approximation is used to convert eq. 6.6 to a more manageable form.

$$\text{For large } N, \quad \ln N! \approx N \ln N - N \quad (6.7)$$

Now,

$$S = k_B [N \ln N - N - \{n_1 \ln n_1 - n_1 + n_2 \ln n_2 - n_2 + n_3 \ln n_2 - n_3\}] \quad (6.8)$$

$$S = k_B [N \ln N - n_1 \ln n_1 - n_2 \ln n_2 - n_3 \ln n_3] \quad (6.9)$$

If the system is considered on a per mole basis, k_B becomes R , and recognizing that

$$\frac{n_i}{N} = x_i,$$

$$S = -R [n_1 \ln x_1 + n_2 \ln x_2 + n_3 \ln x_3] \quad (6.10)$$

So now,

$$G = G^0 + n_2 \mu_2^0 + n_3 \mu_3^0 + RT [n_1 \ln x_1 + n_2 \ln x_2 + n_3 \ln x_3] \\ + \frac{n_1^2 W_{11}}{2N} + \frac{n_2^2 W_{22}}{2N} + \frac{n_3^2 W_{33}}{2N} + \frac{n_1 n_2 W_{12}}{2N} + \frac{n_1 n_3 W_{13}}{2N} + \frac{n_2 n_3 W_{23}}{2N} \quad (6.11)$$

where W is the pair-wise interaction per mole. Eq. 6.11 is now rewritten in terms of the surfactant molecules.

$$G = G^0 + n_2 \mu_2^0 + n_3 \mu_3^0 + RT [(N - n_2 - n_3) \ln(1 - x_2 - x_3) + n_2 \ln x_2 + n_3 \ln x_3] \\ + \frac{(N - n_2 - n_3)^2 W_{11}}{2N} + \frac{n_2^2 W_{22}}{2N} + \frac{n_3^2 W_{33}}{2N} + \frac{(N - n_2 - n_3) n_2 W_{12}}{2N} \\ + \frac{(N - n_2 - n_3) n_3 W_{13}}{2N} + \frac{n_2 n_3 W_{23}}{2N} \quad (6.12)$$

The chemical potential is the partial molar Gibb's free energy. However, in an incompressible system of fixed size, the amount of one type of molecule cannot be

changed without either changing the amount of at least one other molecule. Therefore, the constraint of constant n_j will be relaxed such that infinitesimal changes in the surfactant amount only alter the amount of solvent. This is consistent with the Langmuir equation in the limit of two different, non-interacting molecules.

$$\mu_i = \left(\frac{\partial G}{\partial n_i} \right)_{p,T,N,n_{j \neq \text{solvent}}} \quad (6.13)$$

$$\begin{aligned} \mu_2 = \mu_2^0 + RT[\ln x_2 - \ln(1 - x_2 - x_3)] + (W_{11} + W_{22} - W_{12})x_2 \\ + \left(W_{11} + \frac{W_{23} - W_{22} - W_{13}}{2} \right)x_3 + \left(\frac{W_{12}}{2} - W_{11} \right) \end{aligned} \quad (6.14)$$

The mole fractions can be written as fractional coverages, θ , and the interaction terms can be summed into one term.

$$\mu_2 = \mu_2^0 + RT \ln \left(\frac{\theta_2}{1 - \theta_2 - \theta_3} \right) + RTB(\theta_2, \theta_3) \quad (6.15)$$

Eq. 6.15 gives the chemical potential in the absence of any electrical fields. In the experiments in this thesis, the charged surfaces generate a potential, $\psi(s)$. The chemical potential for a charged adsorbing species is simply given as,

$$\mu_2 = \mu_2^0 + RT \ln \left(\frac{\theta_2}{1 - \theta_2 - \theta_3} \right) + RTB(\theta_2, \theta_3) + z_2 F_A \psi(s) \quad (6.16)$$

where z_2 is the unit charge on species 2 and F_A is Faraday's constant.

From eq. 6.16 the surface coverage of one species is inherently linked to the adsorption of the other species through the pair-wise interaction terms. Therefore, it is reasonable to assume that the proximal adsorption of one species will be coupled to the other species. In this chapter such a phenomenon is explored.

6.2 Additional Experimental

6.2.1 Reagents

D₂O (99.9%, Cambridge Isotope Laboratory) used for ATR-IR experiments was distilled before use.

6.2.2 Adsorption to 'Isolated' Surfaces

Adsorption to 'isolated' surfaces was measured using Attenuated Total Reflectance Infrared (ATR-IR) spectroscopy at 25°C as described previously.³ The spectra were recorded using a Nicolet Nexus 670 Fourier transform infrared spectrometer (Madison, WI). The conditions for these measurements were not the same as for the AFM measurements. All isotherms were measured in D₂O rather than in H₂O, so as to avoid the overlap between OH and CH absorption bands. Furthermore, the solid substrate was a silicon internal reflection element (Wilmad, Buena, NJ) with a native layer of silicon oxide, rather than the glass surfaces used in the AFM experiments. The silicon IRE was prepared by rinsing with a large volume of ethanol (100%, Aaper, Shelbyville, KY) and a large volume of water until the water wet the surface. The crystal was dried with a stream of nitrogen and each side of the crystal was exposed to UV light from a UV Pen Ray lamp (UVP, Upland, CA) for 30 min.

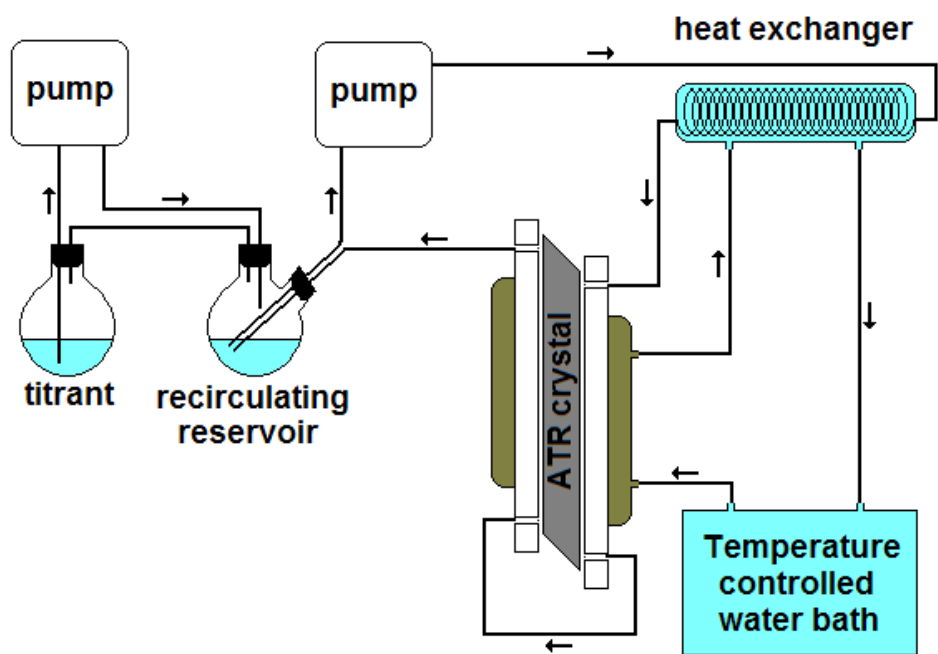


Figure 6.2 Schematic of the ATR-IR experimental setup.

The isotherms were measured by sequential addition of a stock surfactant solution to a recirculating reservoir. Each concentration was permitted to equilibrate for 45 minutes in a temperature controlled ATR cell before spectra were measured. Each spectrum

consisted of 256 scans with 2 cm^{-1} resolution at 25°C . When there was only one surfactant present, the adsorption was obtained from integration of aliphatic CH stretch in the range $3000\text{--}2800 \text{ cm}^{-1}$. A schematic of the experimental setup is shown in Fig. 6.2.

Fig. 6.3 shows sample spectra for adsorption from a surfactant mixture. In a mixture of surfactants, the adsorption of DPC was calculated from integration of the pyridinium CH stretch in the range $3160\text{--}3035 \text{ cm}^{-1}$. The known adsorption of DPC was used to calculate the DPC contribution to the aliphatic CH stretch. The remainder of the aliphatic CH stretch absorption was then attributed to DDAPS, and used to calculate the DDAPS adsorption.

Quantization of the area of the weak pyridinium CH stretch was complicated by absorption by a trace amount of H_2O . This absorption was accounted for with measurements in the absence of surfactant, and in DPC-only solutions.

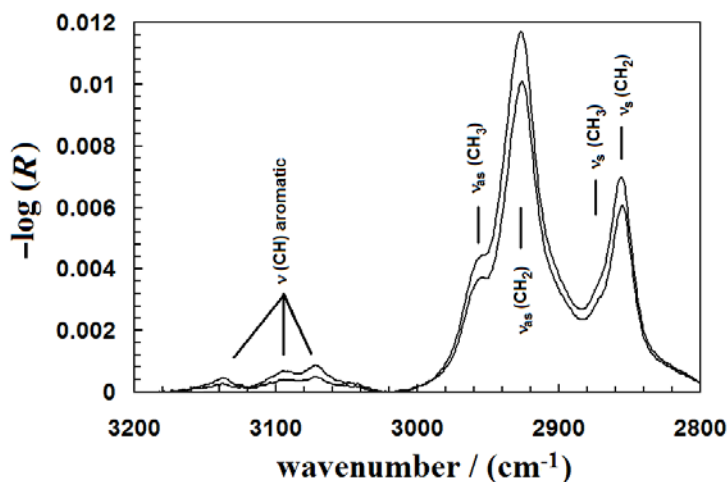


Figure 6.3 Sample ATR-IR Spectra in D_2O on an oxidized silicon crystal in the presence of 0.75 mM DDAPS, 1 mM KCl, and 16.0 mM DPC (upper curve) or 6.0 mM DPC (lower curve). The absorption bands at $3160\text{--}3025 \text{ cm}^{-1}$ are the CH stretching bands for the pyridinium ring. The bands in the range $3000\text{--}2800 \text{ cm}^{-1}$ are the symmetric (ν_s) or asymmetric (ν_{as}) CH stretching bands for the methyl and methylene groups in the hydrocarbon chain. (Reproduced with permission from Lokar, W.J.; Ducker, W.A. *Langmuir* **2004**,*20*, 4553-4558)

The surface excess, Γ , is determined from eq. 6.17.

$$-\log(R) = N\varepsilon C_{bulk} b_{eff} + N\varepsilon \frac{b_{eff}}{d} \Gamma \quad (6.17)$$

where $-\log(R)$ is the integrated absorbance, N is the number of internal reflections, ε is the integrated transmission extinction coefficient, C_{bulk} is the bulk concentration of absorbing species, b_{eff} is the effective path length, and d is the penetration depth. The integrated transmission molar extinction coefficients were calculated from bulk measurements of the integrated absorbance versus concentration and are shown in Table 6.1 along with the calculated values for d and b_{eff} . Details of the evaluation of b_{eff} and d are described in detail elsewhere.³⁻⁸ To obtain a surface excess of surfactant from the absorption, it is necessary to subtract the absorption that would occur if the bulk concentration of surfactant continued right up to the solid. This absorption is in the first term on the right hand side of eq. 6.17. This subtraction was made using the measured molar absorption coefficient of the surfactant and b_{eff} obtained from the calculated profile of electrical field magnitude as a function of depth into the solution, z . The decay of this electric field is about 200 nm. Because the electric field decays as a function of distance into the solution, the absorption due to the surface excess depends in principle on the density of surfactant as a function of z . Here it is assumed that the surface excess is concentrated in the region immediately adjacent to the solid ($z \ll 200$ nm) and the magnitude of the electric field at the interface ($z = 0$) is used.

Table 6.1 Extinction coefficients and penetration depths for ATR-IR spectra

	DDAPS	DPC
ε (aliphatic CH) ($M^{-1}m^{-2}$)	2.64×10^9	2.47×10^9
ε (pyridinium CH) ($M^{-1}m^{-2}$)	-	1.51×10^8
d (nm)		119
b_{eff} (nm)		207

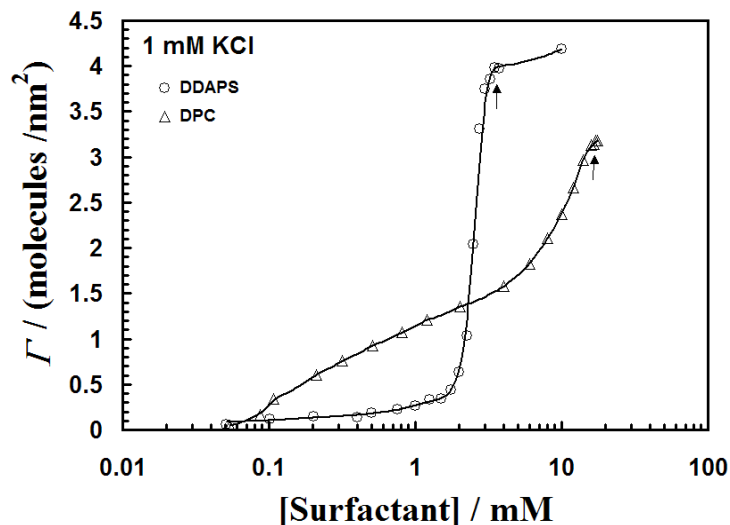


Figure 6.4 Adsorption of DDAPS and DPC to an oxidized silicon ATR crystal as a function of surfactant concentration in D_2O and 1 mM KCl. The plateau adsorption values are 4.1 molecules/nm² for DDAPS and 3.1 molecules/nm² for DPC. Arrows indicate the cmc of each surfactant in 1 mM KCl. (Reproduced with permission from Lokar, W.J.; Ducker, W.A. *Langmuir* **2004**,20, 4553-4558)

Fig. 6.4 shows the adsorption to the oxidized surface of a silicon ATR element from D_2O solutions for DDAPS only and DPC only. All solutions also contain 1 mM KCl.

DPC and DDAPS have the same alkyl chain length (C_{12}), so differences in adsorption can be attributed to the surfactant head-groups. The adsorption of DPC begins at much lower concentrations because of the attractive force between the positively charged surfactant and the negatively charged surface. For example, a surface excess of 0.5 molecules/nm² occurs in 0.1 mM DPC and in 2 mM DDAPS. The slope of the adsorption–concentration graph is much less for the DPC at a surface excess greater than 0.5 molecules/nm² because electrostatic repulsion between the charged head-groups of DPC hinders further adsorption once the net surface charge is positive.⁹ The adsorption of DDAPS is consistent with other studies under similar conditions.¹⁰

6.3 Interactions in DDAPS Solutions

Figs. 6.5 and 6.6 show the forces between glass substrates as function of their separation at various DDAPS concentrations in the presence of 1 mM KCl. The force is

normalized by the radius so that it is equal to the energy per unit area for one flat surface interacting with another infinite flat surface. The separation axis is the distance minus the zero distance. The zero distance was defined by the region of constant compliance, using the usual AFM convention as mentioned in chapter 2.

At low DDAPS concentrations ($[DDAPS] < 2.0$ mM), the forces are not a function of DDAPS concentration, with the exception of a small ‘jump-in’ below $s-s_0 = 2$ nm for $[DDAPS] = 2.0$ mM. This is not surprising, as the adsorption isotherm shows little surfactant adsorbed to the surface. From eq. 1.23, the invariance of the force means that the surfactant adsorption is not changing as a function of s .

$$\Gamma_i(s) - \Gamma_i(\infty) = -\frac{1}{2} \left(\frac{\partial E_a}{\partial \mu_i} \right)_{T,p,s,\mu_j} \quad (1.23)$$

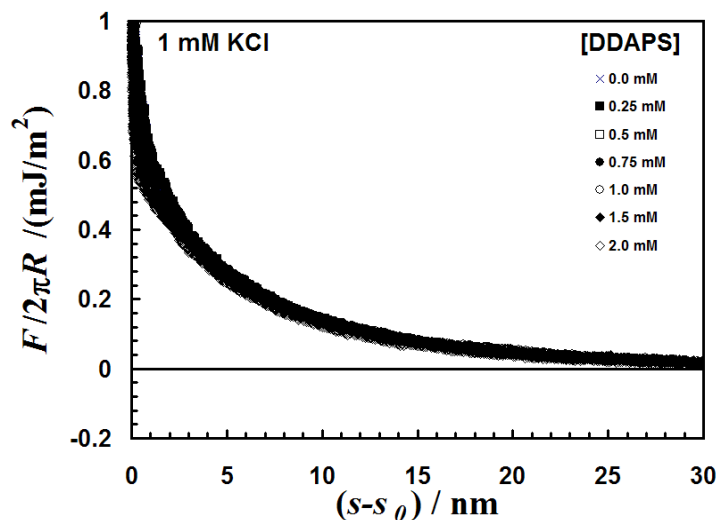


Figure 6.5 Forces between borosilicate glass surfaces as a function of separation in 1 mM KCl for a series of DDAPS concentrations < 2 mM. The forces are invariant with concentration with the exception of a small ‘jump-in’ at $s-s_0 = 1.5$ nm for $[DDAPS] = 2.0$ mM. The Debye-length is $\kappa^{-1} = 9.5$ nm. (Reproduced with permission from Lokar, W.J.; Ducker, W.A. *Langmuir* **2004**, *20*, 4553-4558)

The absence of proximal adsorption is consistent with the weak dependence of adsorption on the chemical potential in this range (Fig. 6.4) and the weak influence of the approaching surface on the zwitterionic surfactant. Furthermore, eq. 3.1 suggests that the chemical potential of DDAPS at the surface should be unaffected by the approach of a

second charged surface because the net-charge on the zwitterion is zero. This is additional confirmation of the hypothesis developed in chapter 4 that an electrostatic mechanism initially drives proximal adsorption. When the surface charge was removed by lowering the pH, the proximal adsorption was essentially zero. Now by removing the charge on the surfactant the proximal adsorption goes to zero.

Fig. 6.6 shows that the force gradually increases in the range $2.0 \text{ mM} < [\text{DDAPS}] < c_{mc}$. From eq. 1.23, this means that DDAPS desorbs as the surfaces approach. The force is also larger at separations up to 10 nm, which may be because the adsorption of a dense layer of (zwitterionic) dipoles moves the plane of net charge further into solution.

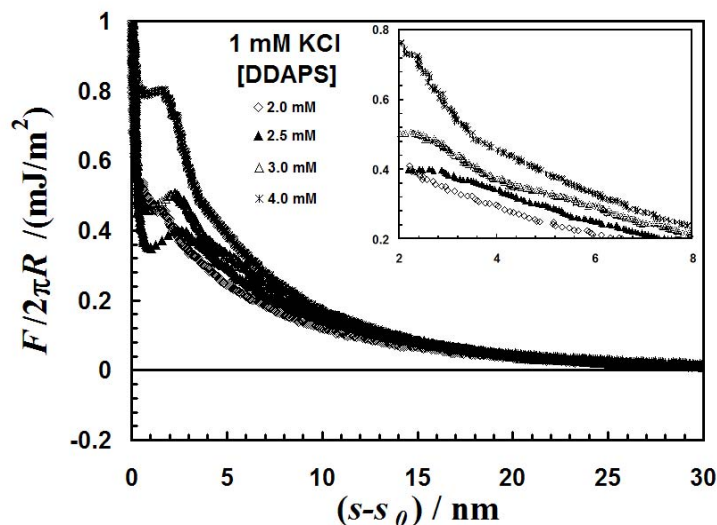


Figure 6.6 Forces between borosilicate glass surfaces as a function of separation in 1 mM KCl for a series of DDAPS concentrations $> 2 \text{ mM}$. The forces increase with concentration at $s-s_0 < 15 \text{ nm}$. A mechanical instability occurs at $1.5 < s-s_0 < 2.5 \text{ nm}$ depending upon concentration. The inset shows more clearly that for $s-s_0 > 2 \text{ nm}$ the force increases with increasing surfactant concentration. The Debye-length is $\kappa^{-1} = 9.5 \text{ nm}$ (Reproduced with permission from Lokar, W.J.; Ducker, W.A. *Langmuir* **2004**, *20*, 4553-4558).

6.4 Interactions in Mixed DDAPS/DPC Solutions

6.4.1 Constant DPC Concentration

In earlier chapters it was shown that the behavior for a cationic surfactant is quite different from the behavior of DDAPS. Fig. 6.7 shows that at low DPC concentrations in 1 mM KCl, the force decreases as the surfactant concentration increases. This means the surfactant adsorbs as the glass surfaces approach each other. The changes in adsorption for DP^+ in 1 mM KCl were shown in Fig. 4.17. Adsorption of the cationic surfactant reduces the magnitude of the long-range repulsive double-layer force between the surfaces and provides a hydrocarbon environment near its tail.

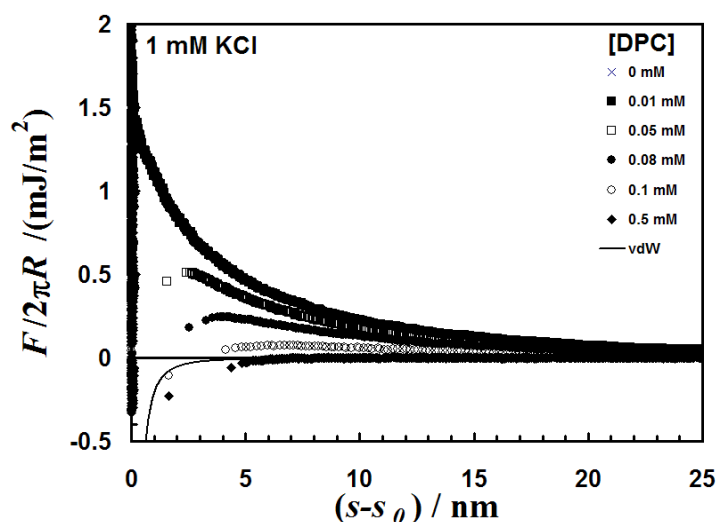


Figure 6.7 Forces between borosilicate glass surfaces as a function of separation in 1 mM KCl for a series of DPC concentrations. The forces decrease with concentration at $s-s_0 < 25$ nm. A mechanical instability occurs at $2 < s-s_0 < 4$ nm depending upon the concentration. The van der Waals force, shown for comparison, was calculated using the Hamaker constant for silica-water-silica of 0.8×10^{-20} J (Hough, D. B.; White, L. R. *Adv. Colloid Interface Sci.* **1980**, *14*, 3-41). The Debye-length is $\kappa^{-1} = 9.5$ nm. (Reproduced with permission from Lokar, W.J.; Ducker, W.A. *Langmuir* **2004**, *20*, 4553-4558)

Furthermore, in Fig. 6.4 DP^+ adsorbs to the silicon oxide on the ATR crystal at much lower surfactant concentrations due to the attractive electrostatic interaction of the surfactant head with the negative surface. In eq. 6.16 the surface chemical potentials of

two adsorbing species will be linked because of cross terms that depend on the surface density. Therefore, if DPC is added to solutions of DDAPS, a cooperative effect should likely be observed.

In Fig. 6.8 the adsorption of DDAPS and DP^+ are shown simultaneously in a solution of changing DDAPS concentration and 0.05 mM DPC. This DPC concentration was chosen because it is the lowest concentration at which a change in the force as a function of concentration was observed (Fig. 6.7).

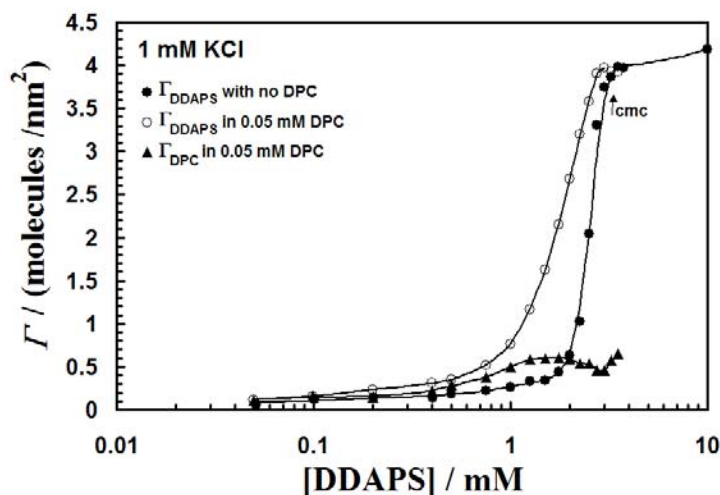


Figure 6.8 Adsorption of DDAPS and DPC to an oxidized silicon ATR crystal as a function of DDAPS concentration in D_2O , 0.05 mM DPC, and 1 mM KCl. The isotherm of DDAPS in the absence of DPC is given for comparison. The adsorption of DDAPS is greater in the presence of DPC and the step shifts to lower DDAPS concentrations. The adsorption of DP^+ increases near the step in the DDAPS isotherm and then decreases again near the cmc (2.8 mM). The decrease in adsorption of DP^+ above the cmc is probably because of solubilization of the DPC in the micelles in bulk. (Reproduced with permission from Lokar, W.J.; Ducker, W.A. *Langmuir* **2004**,20, 4553-4558)

The addition of 0.05 mM DPC to a DDAPS solutions causes a shift in the plateau surface excess to a slightly lower concentration (2.8 mM vs. 3.2 mM) and therefore the cmc is decreased to the same extent. The DDAPS adsorption is greater at all concentrations below the plateau, which is explained by the existence of a surface that is

more hydrophobic in the presence of adsorbed DP^+ . The addition of DDAPS causes an increase in the adsorption of DP^+ by the same mechanism.

In summary, net-attractive interactions between the alkyl chains in water promotes adsorption of each surfactant in the presence of the other surfactant. This is consistent with the inclusion the interaction term, B , which is a function of the surface density of both surfactants (eq. 6.16). Thus, the charge regulation when two surfaces interact should be dependent on the concentration of both DDAPS and DPC.

The consequences of adding DPC to DDAPS solutions will now be explored in terms of the surface forces. Fig. 6.9a shows the forces in a variety of DDAPS concentrations in the presence of 0.05 mM DPC and 1 mM KCl. The addition of just a small amount of DPC ($cmc/300$) makes the force very sensitive to the DDAPS concentration. At low DDAPS concentrations, the force decreases as the DDAPS concentration increases. The surface potential is now a strong function of the DDAPS concentration. The surface potentials and surface charges (at infinite separation) obtained from fitting DLVO theory (as in previous chapters) are shown in Table 6.2. The experimental data deviates below the constant potential boundary at separations below about 10 nm.

**Table 6.2 Fitted Surface Potential and Charge for DDAPS in
0.05 mM DPC/ 1 mM KCl**

[DDAPS] (mM)	ψ_0 (mV)	σ_0 (e/nm ²)
0 (1 mM KCl only)	-85	-0.06588
0 (DPC and KCl)	-78	-0.05740
0.1	-73	-0.05147
0.2	-66	-0.04452
0.5	-58	-0.03690
0.75	-46	-0.02714
1	-30	-0.01642
1.5	-25	-0.01344

Surface potentials and surface charges were obtained by fitting DLVO theory at $(s-s_0) > \kappa^{-1}$ to force curves in Fig. 6.9a. The Hamaker constant used was taken as that for silica/water/silica (0.8×10^{-20} J).¹¹

The mechanism for the discharging of the surface through the addition of a net-neutral surfactant can be understood with the aid of eq. 6.16 and the adsorption isotherms in Fig. 6.8. When DDAPS adsorbs to an isolated surface, DP^+ adsorbs despite the fact

that its bulk chemical potential is pinned by its bulk concentration. It is this adsorption of DP^+ that allows the surface potential to change.

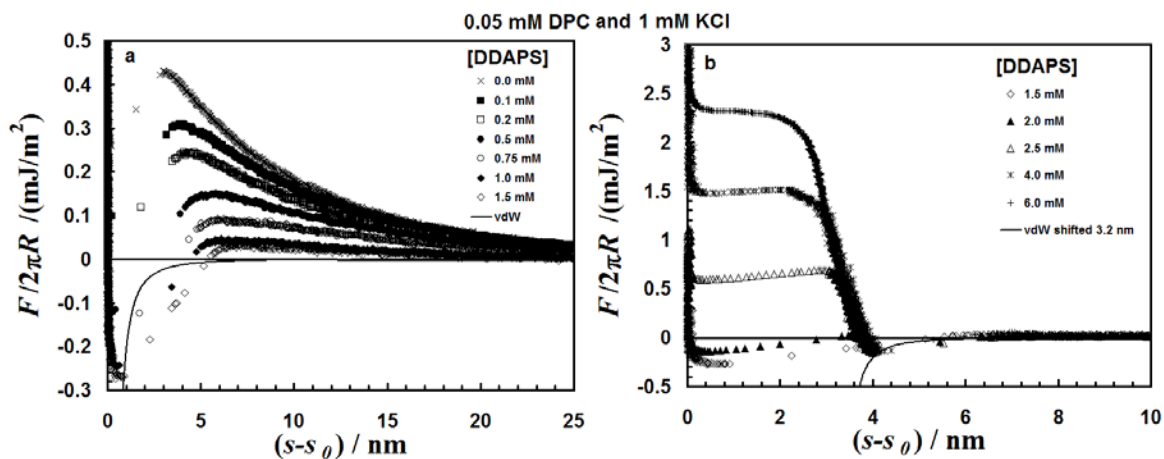


Figure 6.9 Forces between borosilicate glass surfaces as a function of separation in 0.05 mM DPC and 1 mM KCl and a series of $DDAPS$ concentrations. **a)** $[DDAPS] < 1.5 \text{ mM}$ The forces decrease with concentration at $s-s_0 < 25 \text{ nm}$. The van der Waals force, shown for comparison, is the same as in Fig. 6.7. **b)** $[DDAPS] > 1.5 \text{ mM}$. The forces are approximately constant for $s-s_0 > 4 \text{ nm}$ and the force barrier increases with concentration above $[DDAPS] = 1.5 \text{ mM}$. The Hamaker constant for the van der Waals force is taken for hydrocarbon-water-hydrocarbon, $0.5 \times 10^{-20} \text{ J}$ (Hough, D. B.; White, L. R. *Adv. Colloid Interface Sci.* **1980**, *14*, 3-41). Furthermore, it has been shifted 3.2 nm into solution to simulate attraction by a surfactant layer. The Debye-length is $\kappa^{-1} = 9.3 \text{ nm}$. (Reproduced with permission from Lokar, W.J.; Ducker, W.A. *Langmuir* **2004**, *20*, 4553-4558)

The discharging behavior for the isolated surface gives insight into the behavior as the separation is decreased. $DDAPS$ does not have a net-charge, so it should not, in general, feel the approach of the other charged solid. DP^+ , on the other hand, does have a charge, so it does feel the approach of another surface, and it responds by adsorbing. The chemical potentials of DP^+ and $DDAPS$ on the surface, however, are coupled (eq. 6.16). The adsorption of DP^+ lowers the chemical potential of adsorbed $DDAPS$, which causes $DDAPS$ adsorption in order to maintain the surface chemical potential equal to that in the

bulk. This, in turn, lowers the chemical potential of adsorbed DP^+ causing further adsorption of DP^+ . In other words, DDAPS amplifies the adsorption of DP^+ . This effect will be shown momentarily.

The changes in adsorption are largest at $[DDAPS] = 0.75$ mM, where the isotherm in Fig. 6.8 begins to rise. This is consistent with the hydrophobic effect being a strong contributor since the surfactant chains begin to interact at the hemi-micelle concentration (where the isotherm begins to rise steeply).¹² Furthermore, the adsorption changes extend out to $s-s_0 \approx 3\kappa^{-1}$. Therefore, despite the absence of a net charge on DDAPS, proximal adsorption of DDAPS occurs over the same range as the electric double-layer force.

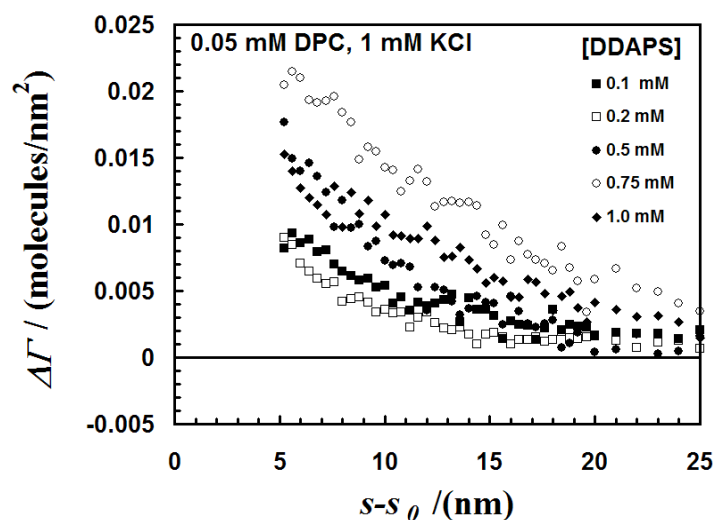


Figure 6.10 Changes in surface excess for DDAPS as a function of separation in 0.05 mM DPC and 1 mM KCl. DDAPS adsorbs with decreasing separation. The Debye-length is $\kappa^{-1} = 9.3$ nm. The calculation of $\Delta\Gamma_{DDAPS}$ requires the assumption that μ_{DPC} is constant when the concentration of DDAPS is varied. This assumption was verified (within experimental error) by measurement of μ_{DPC} using a surfactant selective electrode. (Reproduced with permission from Lokar, W.J.; Ducker, W.A. *Langmuir* **2004**, *20*, 4553-4558)

Fig. 6.9b shows the effect of adding 0.05 mM DPC on the forces at higher DDAPS concentrations (2.0 mM $< [DDAPS] < 2 \times cmc$). The forces are predicted reasonably well by the van der Waals force for a hydrocarbon-water-hydrocarbon interaction if the

surface is moved 3.2 nm into solution (i.e. a surfactant layer 1.6 nm thick on each surface provides the force). Secondly, the force barrier increases with increasing surfactant concentration. Fig. 6.11 shows forces with and without 0.05 mM DPC for easy comparison. At high DDAPS concentrations ($> \frac{2}{3}cmc$), the double-layer can be eliminated by addition of $\frac{1}{10}$ the amount of DPC necessary to eliminate the double-layer in the absence of DDAPS. Furthermore, in the presence of 2.0 mM DDAPS, the addition of 0.05 mM DPC reduces the force greatly at $(s-s_0) > 4$ nm, whereas without DDAPS the change in force was small (compare Figs. 6.7 and 6.11). This is due to the increased hydrophobic environment at the surface. Furthermore, without affecting the force at large separations, the force barrier in this mixed surfactant system can be adjusted to a desired level by addition of the appropriate amount of DDAPS. The force barrier in the mixed system is also much steeper, meaning that the adsorbed layer is much more incompressible. The previous two points are extremely important for colloidal processing.

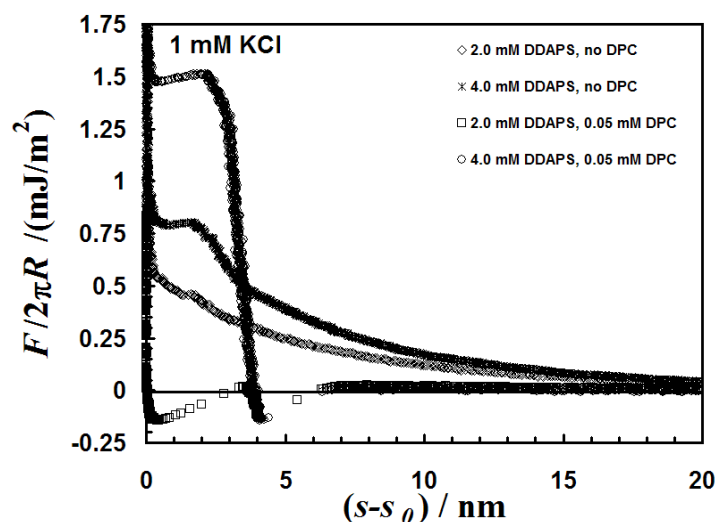


Figure 6.11 Forces between borosilicate glass surfaces reproduced from Figs. 6.7 and 6.9b. Addition of 0.05 mM DPC reduces the force at large separations, but increases the slope of the force barrier. (Reproduced with permission from Lokar, W.J.; Ducker, W.A. *Langmuir* 2004,20, 4553-4558)

6.4.2 Constant DDAPS Concentration

Eq. 1.23 is very useful to determine changes in adsorption. The restriction of maintaining other chemical potentials constant, however, precludes the extraction of the behavior of DP^+ from the previous experiments. Experiments specifically designed to determine the proximal adsorption of DP^+ in this particular system are now presented. To do so, the chemical potential of DDAPS must be held constant while the DPC concentration is varied. Since the maximum proximal adsorption and step in the mixed isotherm occur at 0.75 mM, a fixed DDAPS concentration of 0.75 mM will be used and it is assumed that the chemical potential of the DDAPS is unaffected by changes in DPC concentration, which should be a reasonable approximation since we are well below the *cmc*. Fig. 6.12 shows the forces measured in DPC solutions in 1 mM KCl with a constant DDAPS concentration of 0.75 mM.

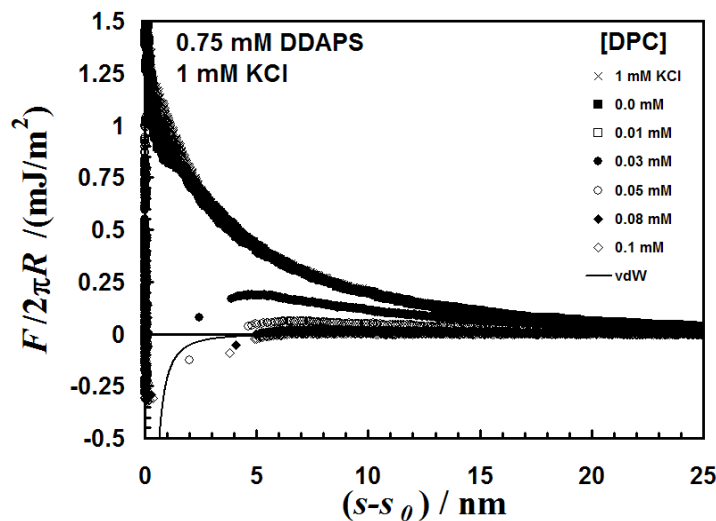


Figure 6.12 Forces between borosilicate glass surfaces as a function of separation in 1 mM KCl and 0.75 mM DDAPS for a series of DPC concentrations. The forces decrease with concentration at $s-s_0 < 25$ nm. A mechanical instability occurs at $2 < s-s_0 < 5$ nm depending upon concentration. The van der Waals force, shown for comparison, is the same as in Fig. 6.8. The Debye-length varies slightly with concentration. (Reproduced with permission from Lokar, W.J.; Ducker, W.A. *Langmuir* **2004**, *20*, 4553-4558)

Comparison with Fig. 6.7 reveals two effects. First, DPC changes the force at a lower concentration in the presence of DDAPS. In addition, the interaction goes from purely repulsive to attractive over a narrower concentration regime. Accordingly, the numerator in eq. 1.23 is greater while the denominator is about the same. Therefore, with DDAPS present, more DPC adsorbs during a collision.

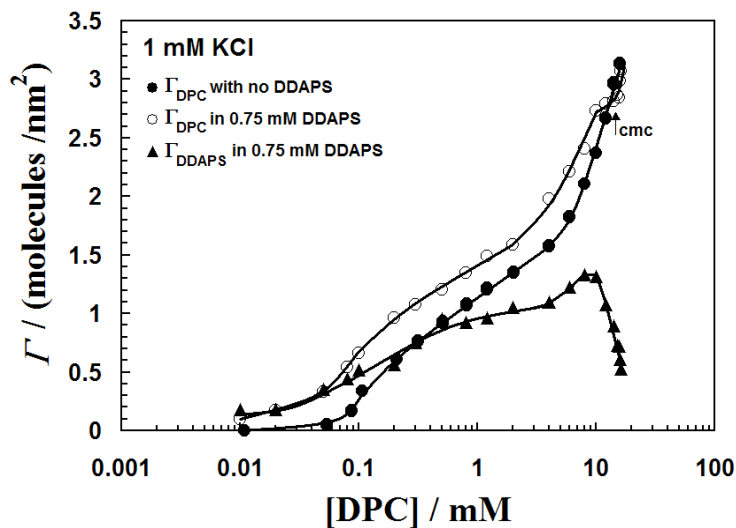


Figure 6.13 Adsorption of DPC and DDAPS to an oxidized silicon ATR crystal as a function of DPC concentration in D_2O , 0.75 mM DDAPS, and 1 mM KCl. The isotherm of DPC in the absence of DDAPS is given for comparison. The adsorption of DPC is greater in the presence of DDAPS and the step shifts to lower DPC concentrations. The adsorption of DDAPS increases with increasing DPC adsorption then decreases above the cmc (15.5 mM), probably because of solubilization of DDAPS in bulk micelles. (Reproduced with permission from Lokar, W.J.; Ducker, W.A. *Langmuir* **2004**, *20*, 4553-4558)

The same effect occurs for a single (isolated) surface. Fig. 6.13 shows the adsorption of DPC in the presence of 0.75 mM DDAPS measured with ATR-IR. The DDAPS increases the surface excess of DPC and shifts the step in the isotherm to lower concentrations. In Fig. 6.14 the proximal adsorption analysis of the force data reveals that the maximum changes in surface excess occur at $[DPC] = 0.03$ mM, whereas in the absence of DDAPS, the maximum occurred at $[DPC] = 0.08$ mM. This shift in proximal

adsorption mirrors the shift in the adsorption to the isolated surface (Fig. 6.13). The similar adsorption behavior between isolated and interacting surfaces suggests that the same form of the surface chemical potential should be used.

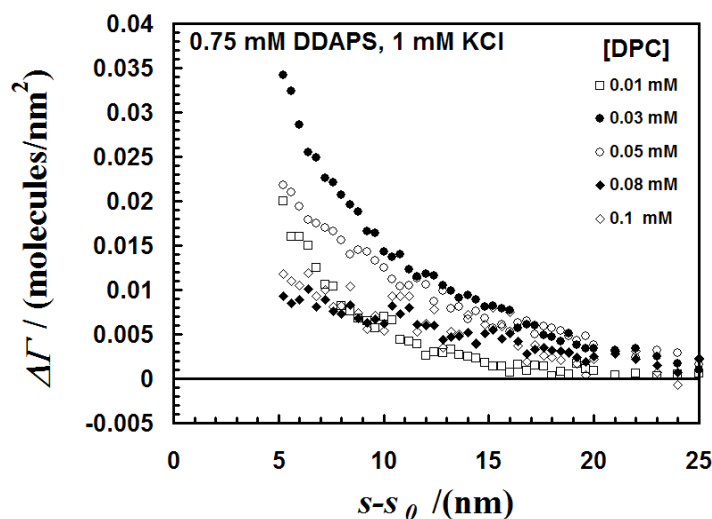


Figure 6.14 Changes in surface excess for DPC as a function of separation in 0.75 mM DDAPS and 1 mM KCl. DPC adsorbs with decreasing separation. The Debye-length varies slightly with concentration. (Reproduced with permission from Lokar, W.J.; Ducker, W.A. *Langmuir* **2004**, *20*, 4553-4558)

6.5 Total Proximal Adsorption for DDAPS/ DPC/ KCl

The magnitudes of the proximal adsorption can be compared for the two surfactants at a given solution composition: 0.75 mM DDAPS, 0.05 mM DPC, and 1 mM KCl. Fig. 6.15 shows that (a) $\Delta\Gamma$ of each surfactant is greater in the mixed system; (b) $\Delta\Gamma$ of surfactant in the mixed surfactant system greatly exceeds $\Delta\Gamma$ for each of the single surfactant systems; (c) the proximal adsorptions of DDAPS and DPC are the same within experimental error. The similarity of the two adsorptions probably arises because the surface charge is small (Fig. 6.12 shows a small force) and thus proximal adsorption is relatively unaffected by the head-group charge.

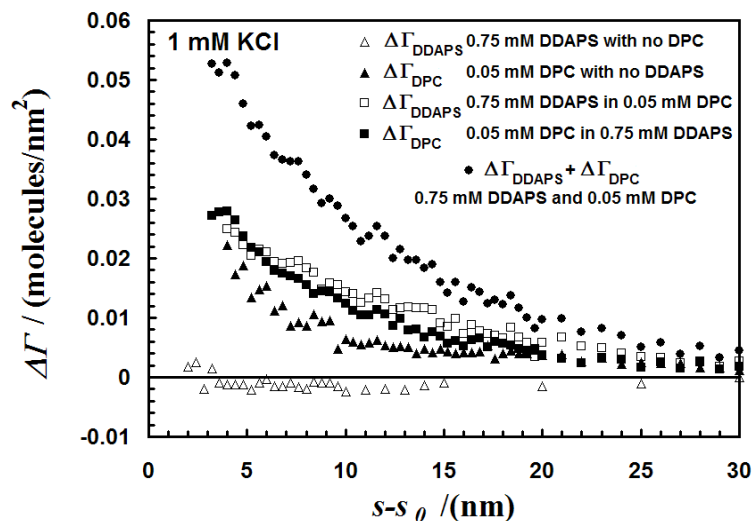


Figure 6.15 Comparison of the changes in surface excess for DPC and DDAPS as a function of separation in 1 mM KCl. Proximal adsorption of DPC is greater in the presence of 0.75 mM DDAPS at $[DPC] = 0.05$ mM, and the total proximal adsorption is much larger in the presence of DDAPS.

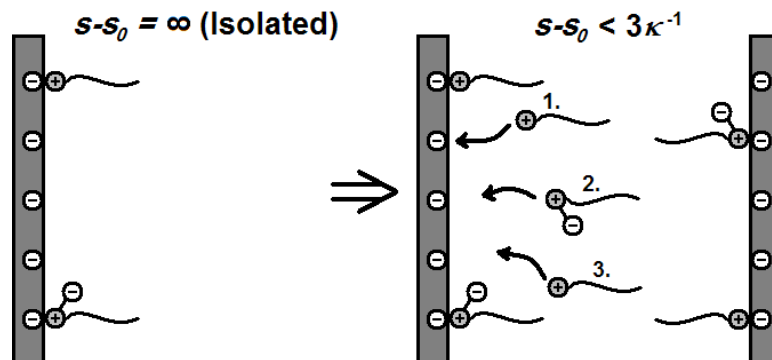


Figure 6.16 Schematic of proximal adsorption in a mixed surfactant system. On the left, a mixture of cationic and zwitterionic surfactants is adsorbed to an isolated surface (infinite separation). Bringing a second surface into close proximity (within 3 Debye-lengths), increases the magnitude of the negative electrostatic potential and drives further adsorption of the cationic surfactant (1). This increases the surface hydrophobicity and drives further adsorption of the zwitterionic surfactant (2). This adsorption of the cationic surfactant is greater than in the absence of the zwitterionic surfactant (3) because the zwitterionic surfactant also increases the surface hydrophobicity. (Reproduced with permission from Lokar, W.J.; Ducker, W.A. *Langmuir* 2004,20, 4553-4558)

6.6 Conclusions

Only a small amount of zwitterionic surfactant adsorbs to silica-like surfaces at concentrations less than 2.0 mM. Furthermore, at these concentrations, the zwitterionic surfactant is not useful for changing the surface forces, and therefore is not sensitive to the separation between the particles.

The addition of a small amount of cationic surfactant makes the zwitterionic surfactant much more sensitive to perturbations in conditions. The zwitterionic surfactant adsorbs at lower concentrations and can now be used to control the surface forces. The effect of the zwitterionic surfactant on the surface forces stems from behavior similar to that which occurs on isolated surface.

The approach of another surface causes the cationic surfactant to adsorb to reduce the magnitude of the surface charge. Because the chemical potential of the surfactants on the surface is linked through the net-attractive short-range hydrophobic effect, the adsorption of the cationic surfactant promotes further adsorption of the zwitterionic surfactant. Likewise, the coupling between the chemical potentials makes adsorption of the cationic surfactant greater during a particle collision in the presence of the zwitterionic surfactant. An example is shown in which the total proximal adsorption of surfactant is about three times larger in the presence of a zwitterionic surfactant than it is in a solution of cationic surfactant alone.

Coupling between the long-range electrostatic force and the short-range (contact) hydrophobic effect can produce interesting changes in surface forces. This coupling can either be homogeneous, when the alkyl chain is covalently bound to the charge, or heterogeneous, when the alkyl chain is on another molecule.

Furthermore, ATR-IR is a useful tool to measure isotherms of mixed surfactant systems by utilizing different chromophores.

6.7 Cited Literature

- (1) Lokar, W. J.; Ducker, W. A. *Langmuir* **2002**, *18*, 3167.
- (2) Lokar, W. J.; Ducker, W. A. *Langmuir* **2004**, *20*, 378.
- (3) Clark, S.; Ducker, W. A. *J. Phys. Chem. B* **2003**, *107*, 9011.
- (4) Sperline, R. P.; Jeon, J. S.; Raghavan, S. R. *Appl. Spectrosc.* **1992**, *46*, 1644.
- (5) Sperline, R. P.; Freiser, H. *Langmuir* **1990**, *6*, 344.
- (6) Sperline, R. P.; Song, Y.; Freiser, H. *Langmuir* **1994**, *10*, 37.
- (7) Hansen, W. N.; Kuwana, T.; Osteryoung, R. A. *Anal. Chem.* **1966**, *38*, 1810.

- (8) Thompkins, H. G. *Appl. Spectrosc.* **1974**, 28, 335.
- (9) Goloub, T. P.; Koopal, L. K.; Bijsterbosch, B. H.; Sidorova, M. P. *Langmuir* **1996**, 12, 3188.
- (10) Zajac, J.; Chorro, C.; Lindheimer, M.; Partyka, S. *Langmuir* **1997**, 13, 1486.
- (11) Hough, D. B.; White, L. R. *Adv. Colloid Interface Sci.* **1980**, 14, 3.
- (12) Somasundaran, P.; Fuerstenau, D. W. *J. Phys. Chem.* **1966**, 70, 90.

Chapter 7

Self-Consistent Field Theory: Methods and Applications to Surfactants in Bulk Solution

7.1 Introduction

In chapters 3-6, experimental studies of surfactant adsorption between interacting colloidal surfaces were discussed. There are several properties of these interacting systems that are a bit more difficult to explore experimentally. The experimental methods in this thesis allow only the total changes in adsorption to be determined. No explicit structural information is available from the experimental data presented in the previous chapters. Furthermore, the behavior of the simple electrolyte ions cannot be obtained from eq. 1.23 due to the coupling of chemical potentials.

In this chapter, self-consistent field theory (SCF) will be used to calculate behavior in surfactants systems. The advantage of SCF is that the distributions of all components in the system can be calculated. Structural information can be calculated by obtaining the distribution of molecules normal to the surface. Furthermore, agreement is sought between experiment and theory, such that SCF calculations can be used to provide a useful means of predicting behavior in systems that are more time consuming to study experimentally.

In chapters 8 and 9, SCF will be used to calculate adsorption between surfaces as a function of the separation between them and comparisons will be made to experimental findings. As a prelude, the theory will be outlined and the modelled bulk behavior discussed.

Until now, adsorption of surfactants as a function of solid-solid separation (proximal adsorption) has not been studied thoroughly from a theoretical standpoint. For systems involving chain molecules such as surfactants and polymers, 'exact' theories become extremely complicated and very expensive in terms of computer power and time.

Here we will use a relatively inexpensive theory originally developed by Scheutjens and Fleer^{1,2} for studies of polymer adsorption to solid surfaces and self-association of surfactants. Studies have been routinely conducted using the Scheutjens-Fleer (SF) method to model lipid bilayer membranes,³⁻⁵ self-assembly of surfactants in solution and

at interfaces,⁶⁻¹¹ polyelectrolyte adsorption,^{12,13} polymer brushes,^{14,15} wettability,¹⁶ colloidal stability,¹⁷ and liquid chromatography.¹⁸

7.2 The Theory

The self-consistent field theory for adsorption and association (SCFA) is based on lattice and mean-field approximations. The particular lattice geometry selected, dictates the geometry of any aggregates formed (whether surface or in the bulk). For bulk studies we can compare spherical, cylindrical, and flat structures and determine the most stable structure by the lowest energy. In the next section, such a comparison is shown. In chapters 8 and 9, where adsorption onto solid surfaces is examined, a system of two flat homogeneous surfaces is studied some separation, H apart.

Fig. 7.1 shows a schematic of the general flat lattice model with $M = 8$ lattice layers. In this work a simplified one-dimensional theory is used, where field fluctuations are permitted in only one coordinate. This is depicted in Fig. 7.1. Density fluctuations are ignored (mean-field) in the xy plane and permitted perpendicular to it (z -direction). The one-dimensional model allows the calculations to be simplified, but does have serious limitations in that it cannot describe heterogeneous surfaces (i.e. sparse coverages and adsorbed micelles). This is due to the mean-field in the xy plane. The one-dimensional model is most reasonable for monolayer or bilayer coverages and will allow for a good first approximation of the behavior of interacting colloidal systems.

7.2.1 Lattice

In SCFA theory, all molecular species are represented as a segment or sequence of connected segments. These segments are arranged on a lattice to enable conformational probabilities to be calculated. All lattice sites are filled with a segment of a molecule, ion, or solvent. Therefore, the volume fractions of all segments A , ϕ_A , will always sum to unity (the incompressibility approximation).

$$\sum_A \phi_A(z) = 1 \quad \forall z \in 1, \dots, M \quad (7.1)$$

Before delving into the mathematics, there are two basic lattice parameters that should be discussed. These parameters greatly affect the calculations. The first

parameter is the lattice site size and the second is the step probability between adjacent sites.

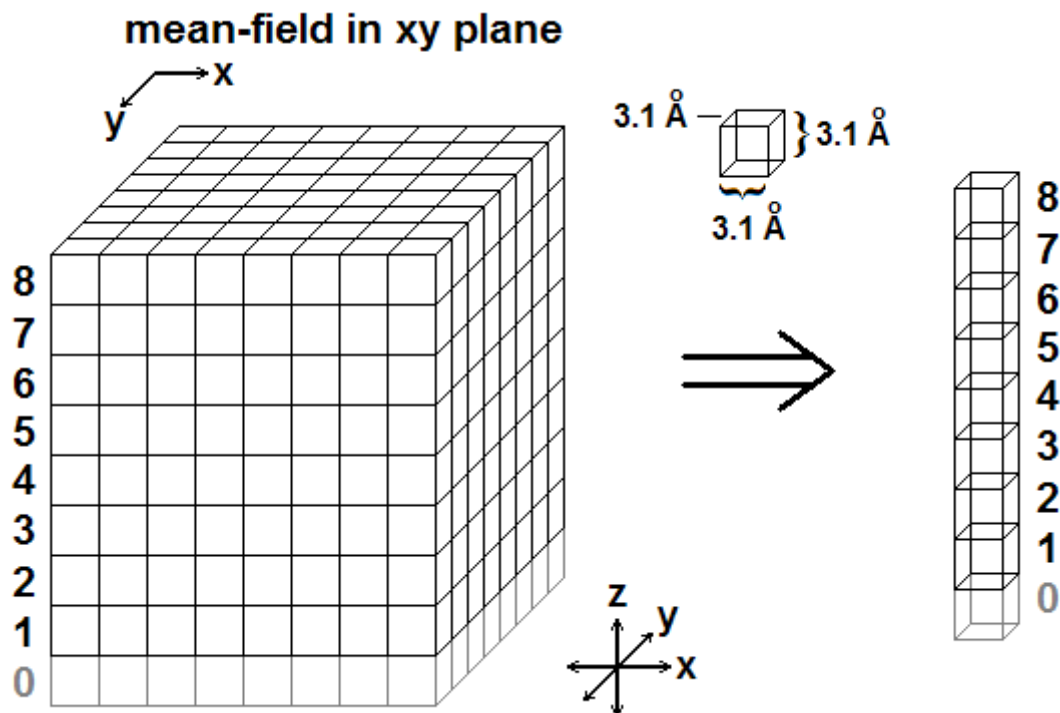


Figure 7.1 Schematic of the one-dimensional flat SCFA lattice containing $M=8$ layers. A mean-field is taken in the xy plane so the lattice reduces to that shown on the right with each layer containing the mean-field properties of each plane on the left. The zeroeth layer is essentially a virtual layer and is the lower-bound of the system. Surface segments will be placed in the zeroeth layer for calculations in chapter 8.

The lattice site cross-section is chosen to be 0.31 nm so that, when the lattice is fully occupied by water, a concentration of 55.5 moles per liter is obtained as found experimentally. This imparts an approximation that all other segments will have the same volume as a water molecule. Therefore, size differences between salt ions are not accounted for. Furthermore, since the hydrocarbon chain will be modeled as a sequence of C segments (sec. 7.2.3), the cube of the lattice cross-section should be compared to the volume of a CH_2 unit. From density data for liquid hydrocarbons at 25°C , the volume of a CH_2 unit is determined to be 0.027 nm^3 ,¹⁹ whereas the cube of the lattice cross-section is 0.030 nm^3 . Therefore, the volume of each methylene unit is over-estimated by about

10%. These effects will be secondary compared to the Markov approximation used to calculate the chain conformations (sec. 7.2.3).

In the case of the flat lattice, the fraction of contacts that one site has with sites in a previous or following layer (λ_{-l} and λ_l) is naturally independent of z , however, for the spherical and cylindrical cases the fraction of contacts is a function of z . Details for the spherical and cylindrical cases are given elsewhere.²⁰ The fraction of contacts in an adjacent layer (λ_l), and within the same layer (λ_0), is governed by the type of lattice chosen for the calculations. For this particular study, the step probabilities of a face-centered cubic lattice in which $\lambda_{-l} = \lambda_0 = \lambda_l = 1/3$ are used. Such a choice has been found to minimize lattice artifacts in the calculations.²¹

7.2.2 Potential Energy

The physical details of the calculations will now be presented. A dimensionless density $\phi_A(z)$, is defined as the volume fraction of segments of type A (not molecules) in layer z . For bulk volume fractions, $\phi_A(z)$ is no longer a function of z and now the notation becomes ϕ_A^b . From the Boltzmann expression, the density of segments at a particular distance from the surface can be calculated using a Boltzmann factor, G_A .

$$G_A(z) = \exp\left[\frac{-u_A(z)}{k_B T}\right] \quad (7.2)$$

$$\phi_A(z) = G_A(z)\phi_A^b \quad (7.3)$$

where $u_A(z)$ is the mean potential energy (Gibbs energy per segment) difference required to move a segment A from the bulk to layer z . $u_A(z)$ is defined as,

$$u_A(z) = u'(z) + k_B T \sum_B (\langle \phi_B(z) \rangle - \phi_B^b) \chi_{AB} + v_A e \psi(z) - \frac{1}{2}(\epsilon_A - \epsilon_0) E(z)^2 \quad (7.4)$$

The first term represents the volume work, $u'(z)$, needed to insert a segment at position z . If the coordinate z tends to be overcrowded, then $u'(z)$ will be positive (segments would like to avoid this region). On the other hand, when $u'(z) < 0$, the segments are attracted to coordinate z . It is independent of the segment type (all

segments have the same size) and is adjusted only such that the incompressibility constraint (eq. 7.1) holds.

The second term accounts for contact interactions between segments in adjacent layers. Nearest neighbour contact energies are accounted for through the well-known Flory-Huggins interaction parameters χ_{AB} .²² There is one χ_{AB} for each pair of contacts between unlike segments A and B . $\chi_{AB} > 0$ for repulsion and $\chi_{AB} < 0$ for attraction. The other contribution to pair interaction term, $\langle \phi_B(z) \rangle - \phi_B^b$ accounts for differences in the contacts felt at layer z with respect to that in the bulk. Here a Bragg-Williams approximation is used, which estimates the contacts based upon the volume fractions.¹ Realizing that a segment of type A at layer z can interact with segments of type B in adjacent layers $z'=z-1, z, z+1$, an average is taken over three layers. Such an average is represented by the angular brackets:

$$\langle \phi(z) \rangle = \lambda_{-1}\phi(z-1) + \lambda_0\phi(z) + \lambda_1\phi(z+1) \quad (7.5)$$

where, as previously mentioned, λ_{-1}, λ_0 , and λ_1 represent the fraction of contacts in the previous, same, and following layers respectively. In these calculations all values of lambda are 1/3.

The third term represents the classical electrostatic work needed to bring an ionic species to layer z . $\psi(z)$ is the electrostatic potential, e is the elementary charge, and v_A is the valence of segment A .

The final contribution to the segment potential is the free energy change (per segment) upon bringing a segment from the bulk, where the electric field, $E(z) = -\frac{\partial \psi(z)}{\partial z}$, is zero to coordinate z with a finite electric field. The segments will become polarized in a finite electric field. This polarization is proportional to the difference between the segment dielectric permittivity, ϵ_A , and that of a vacuum, ϵ_0 , and is proportional to the field strength. The energy gain is again proportional to the polarizability and E , leading to $(\epsilon_A - \epsilon_0)E(z)^2$. The factor of $1/2$ in eq. 7.4 originates from the fact that induction of a dipole in the segment has an entropic effect as well. It can be shown that this unfavourable contribution reduces the energetic gain by $1/2$.²¹

The third and fourth terms in eq. 7.4 are rather straightforward, however, $\psi(z)$ and $E(z)$ must be determined within each layer. These quantities follow from solving a discretized version of the Poisson equation to obtain the local charge density $\sigma(z)$.

$$-\sigma(z) = \frac{\partial \varepsilon(z) \partial \psi(z)}{\partial z^2} \quad (7.6)$$

The electrostatic potentials are calculated from a model similar to considering multiple Stern layers. According to eq. 7.6, the net charge and the capacitance of each layer are required. The local charge density is calculated from the local volume fractions per segment type.

$$\sigma(z) = \sum_A v_A e \phi_A(z) \quad (7.7)$$

The charge is considered to lie at the midpoint of each layer, and the permittivity of each layer is given by a volume fraction weighted average of the permittivity of each species.

$$\varepsilon(z) = \sum_A \varepsilon_A \phi_A(z) \quad (7.8)$$

Additional details of evaluating $\psi(z)$ can be found elsewhere.²⁰ The boundary conditions for eq. 7.6 in these systems are

$$\begin{aligned} \left. \frac{\partial \psi(z)}{\partial z} \right|_{z=0} &= -\frac{\sigma_0}{\varepsilon(0)} \\ \left. \frac{\partial \psi(z)}{\partial z} \right|_{z=H+1} &= -\frac{\sigma_0}{\varepsilon(H+1)} \end{aligned} \quad (7.9)$$

where H is the separation between the solids and $\varepsilon(0) = \varepsilon(H+1)$ is the dielectric permittivity of the solid phase.

For flat solid surfaces, the above equations amount to an extension of Gouy-Chapman theory to include finite size effects, segment–segment interactions and polarization effects.

7.2.3 Extension to Chain Molecules

Up until now, a theory has been described, which can adequately deal with simple molecules. When dealing with chain molecules, such as surfactants, it is important to account for the chain conformations in a reasonable manner. Surfactants are short chain molecules that are composed of a string of segments that occupy several consecutive sites

consequence, chain flexibility will be over-estimated. For example, this contributes to an underestimate of surfactant layer thicknesses. It should be noted that in a self-consistent field theory intermolecular excluded volume interactions are treated approximate as well.

In these calculations, the goal is to find a self-consistent set of potentials (eq. 7.4) and volume fractions. For chain molecules, the volume fraction profile of segment s of molecule i , $\phi_i(z, s)$ is calculated from the so-called composition law:

$$\phi_i(z, s) = C_i \langle G_i(z, s-1 | 1) \rangle G_i(z, s) \langle G_i(z, s+1 | N) \rangle \quad (7.10)$$

Here, C_i is a normalisation constant to be specified below. Furthermore, there are two complementary end point distribution functions $G_i(z, s-1 | 1)$ and $G_i(z, s+1 | N)$, which are generated by propagator-like equations starting from end $s = 1$ or $s = N$ respectively. The propagator procedure will be given below. The other factor in eq. 7.10 is the generalized Boltzmann weight for segment s , of type i in layer s :

$$G_i(z, s) = \sum_A \delta_{s,i}^A G_A(z) \quad (7.11)$$

Eq. 7.11 specifies the proper segmental Boltzmann weight for each segment along the chain. The physical interpretation of eq. 7.10 is that the concentration of segment s in coordinate z is found by the combined statistical weight of all possible walks from $s' = 1$ to $s' = s-1$, multiplied by the statistical weight of all possible walks from $s' = N$ to $s' = s+1$, and then connected to the central segment $s' = s$, for which the ‘detached’ statistical weight of eq. 7.11 is introduced. The angular brackets in eq. 7.10 give a three-layer average similar to eq. 7.5 and physically provide all possible ways segment $s-1$ connects to s and $s+1$ to s respectively. Finally, the forward and backward propagators are given by

$$G_i(z, s | 1) = G_i(z, s) \langle G_i(z, s-1 | 1) \rangle \quad (7.12a)$$

$$G_i(z, s | N) = G_i(z, s) \langle G_i(z, s+1 | N) \rangle \quad (7.12b)$$

relating the end point distribution of a chain fragment $s-1$ segments long (i.e. $s'=1, \dots, s-1$) to one which is one segment longer $s'=1, \dots, s$ (eq. 7.12a), and similarly for the backward propagator from $s'=N, \dots, s+1$ to $s'=N, \dots, s$ (eq. 7.12b). The propagators are started at the

first and last segment respectively, for which $G_i(z,1|1) = G_i(z,1)$ and $G_i(z,N|N) = G_i(z,N)$ respectively.

Using eq. 7.12, it is easily seen that the composition law of eq. 7.10 may also be expressed as:

$$\phi_i(z,s) = C_i \frac{G_i(z,s|1)G_i(z,s|N)}{G_i(z,s)} \quad (7.13)$$

The free segment distribution function in the denominator is present because the potential field experienced by segment s is included in both end point distribution functions in the numerator. For the surfactants we typically work in a canonical ensemble for which the total number of surfactant molecules per unit area is fixed. The normalisation constant C_i is chosen such that the specified amount is indeed present.

When $n_i = \sum_z \phi_i(z)$ is an input quantity, it follows that $C_i = \frac{n_i}{\sum_z G_i(z,1|N)}$. Here

$\sum_z G_i(z,1|N)$ may be identified by the single chain partition function (it gives the total statistical weight to find molecule i in the system. The segment distributions of all tail segments or all head-group segments follow from summation over the appropriate ranking numbers, or more generally:

$$\phi_A(z) = \sum_i \sum_s \phi_i(z,s) \delta_{s,i}^A \quad (7.14)$$

A simplified example of this propagator method will now be given by considering the generic block copolymer A_4B_4 in Fig. 7.3. The overall statistical weights of conformations I and II are shown in eq. 7.15. Where G_A and G_B are determined from eq. 7.2.

$$G^I = G_A(1,1)\lambda_1 G_A(2,2)\lambda_1 G_A(3,3)\lambda_1 G_A(3,4)\lambda_0 G_B(3,5)\lambda_1 G_B(4,6)\lambda_0 G_B(4,7)\lambda_1 G_B(5,8) \quad (7.15a)$$

$$G^{II} = G_A(1,1)\lambda_1 G_A(2,2)\lambda_0 G_A(2,3)\lambda_1 G_A(3,4)\lambda_0 G_B(3,5)\lambda_1 G_B(4,6)\lambda_1 G_B(5,7)\lambda_1 G_B(6,8) \quad (7.15b)$$

In conformation I , segment $s = 1$ is in layer $z = 1$ and has weight $G_A(1,1)$. It is bonded into the next layer (λ_1) to segment $s = 2$ in layer $z = 2$ with weight $G_A(2,2)$ and so on to the end of the chain. We can determine the volume fraction of each segment type as follows:

$$\phi_A(z) = \sum_I G^I r_A^I(z) \quad (7.16a)$$

$$\phi_B(z) = \sum_I G^I r_B^I(z) \quad (7.16b)$$

$r_A^I(z)$ is the number of segments of type A in layer z for conformation I . From this generalized method the volume fraction profile of each segment type in a chain molecule can be determined.

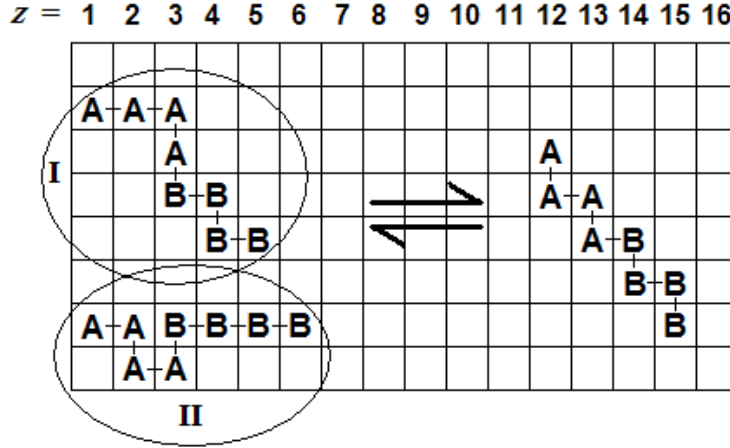


Figure 7.3 Schematic of two possible conformations (I and II) of A_4B_4 in equilibrium with the average bulk conformation.

The density profiles quite naturally blend in with the SCF scheme sketched above. A set of equations now exists that will allow the evaluation of the segment densities (eq. 7.3) and the potentials (eq. 7.4). Both of these quantities, however, are mutually dependent. Therefore, an iterative process can be carried out by adjusting the potentials and volume fractions until a self-consistent set of potentials and volume fractions is obtained.

Once the SCF solution is available one can compute the grand potential $\gamma = \gamma([\phi, u])$, which is defined as

$$\gamma = F - \sum_i \mu_i n_i \quad (7.17)$$

where F is the Helmholtz energy of the incompressible system at constant T , μ_i is the chemical potential of segment i , and n_i is the number of segments of i in the system. The

grand potential is, in this sense, the surface free energy. The grand potential as a function of separation between two surfaces, H , follows from a summation over the grand potential density, Π .

$$\gamma(H) = -\sum_{z=1}^H \Pi(z) \quad (7.18)$$

The grand potential density is a function of the segment densities and the segment potentials, including the electrostatic contributions and the short-range interactions. The grand potential density is given as

$$\begin{aligned} \Pi(z) = & k_B T \sum_i \frac{(\phi_i(z) - \phi_i^b)}{N_i} + \sum_A u_A(z) \phi_A(z) - \frac{1}{2} \sigma(z) \psi(z) \\ & - \frac{1}{2} k_B T \sum_A \sum_B \chi_{AB} [\phi_A(z)(\phi_B(z) - \phi_B^b) - \phi_B^b(z)(\phi_B(z) - \phi_B^b(z))] \end{aligned} \quad (7.19)$$

The free energy of interaction, $F_{\text{int}}(H)$, at a solid-solid separation, H , is given by the difference between the grand potential at separation, H , and that at infinity.

$$F_{\text{int}}(H) = \gamma(H) - \gamma(\infty) \quad (7.20)$$

In this work values for the adsorption of a particular species are presented. This value is calculated by summing the excess volume fraction of the segments, of a particular species, i , over all layers and dividing by the number of segments that comprise a single molecule, N_i , and the square of the lattice site dimension.

$$\Gamma_i = \frac{\sum (\phi_i(z) - \phi_i^b)}{a^2 N_i} \quad (7.21)$$

Within the framework of these calculations the chemical potential is given as

$$\mu_i = \mu_i^0 + k_B T (\ln \phi_i^b + 1) - k_B T N_i \sum_j \frac{\phi_j^b}{N_j} + \frac{k_B T N_i}{2} \sum_A \sum_B \chi_{AB} (1 - \phi_A^b)(\phi_B^b - 1) \quad (7.22)$$

7.3 Bulk Surfactant Behavior

7.3.1 Cmc Determination

In this section the parameters used to calculate bulk properties of the model surfactant are discussed. The first item to discuss is how SCFA is used to calculate the critical micelle concentration for surfactants. This is done by plotting the grand potential and the chemical potential versus the calculated excess surfactant in the system (eq. 7.23). Fig. 7.4 shows such a plot. The maximum in grand potential and minimum in chemical potential correspond to the most stable aggregate. The bulk concentration at which this value of the chemical potential is obtained is the theoretical *cmc*.

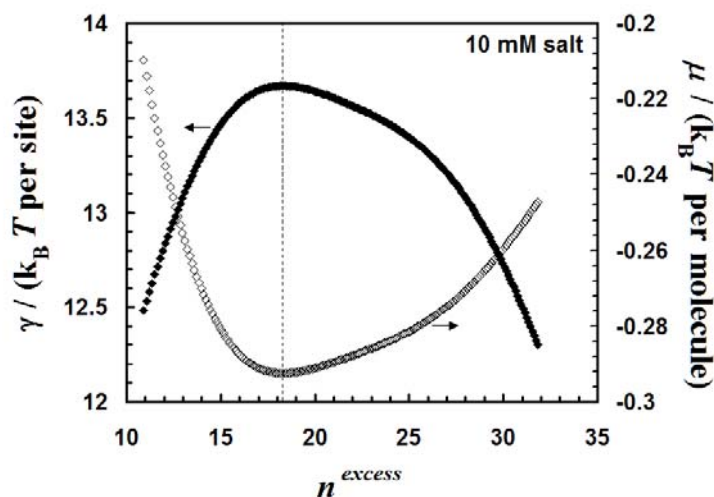


Figure 7.4 Chemical potential and grand potential versus excess number of molecules of surfactant in 10 mM monovalent salt (spherical micelles). The *cmc* is denoted by the dotted line. The concentration where the minimum chemical potential is reached is the *cmc* (1.43 mM).

In Fig. 7.4, the *x*-axis is the excess number of molecules in the system, in other words, those in excess of the bulk. This quantity is related to the aggregation number less any depletion that occurs in the vicinity of the micelle due to charge–charge repulsion. The excess number of molecules is calculated simply as

$$n_i^{excess} = \frac{\sum_z L(z)(\phi_i(z) - \phi_i^b)}{N_i} \quad (7.23)$$

where $L(z)$ is the number of lattice sites per lattice layer. This quantity is important for spherical and cylindrical lattices, however, is simply equal to one for flat lattices. In

addition, we should note that for flat bilayer or cylindrical micelles determining the *cmc* is slightly different due to the fact that the translational entropy is negligible. In these cases, the *cmc* is determined by taking the x -intercept of the grand potential function.

7.3.2 Parameters

The results of the SCFA analysis depend strongly upon the choice of several molecule and system specific parameters. First, the parameter choices for the surfactant are discussed (shown in Table 7.1). The cationic surfactant is modeled as a sequence of segments of two different types. One segment is given aliphatic characteristics (C), and the other more hydrophilic characteristics (P). The surfactant is modeled as 16 C units attached to 3 P units, $C_{16}P_3$. The P units each have a charge equal to $+1/3$, bringing the total net charge to $+1$ for the surfactant as was shown in Fig. 7.2. Such a head-group has been used previously to model cationic surfactants with this theory.⁹ In addition, the system is comprised of two other molecules that introduce 3 other segments: a solvent segment, (W), and two segments, (K) and (B), which represent salt ions. K possesses a valence of $+1$ and B a valence of -1 . Segments K and B are independent of each other (strong electrolyte). In addition, the permittivity must be chosen for each segment. The permittivity for the solvent and aliphatic segments is set to $80\epsilon_0$ and $2\epsilon_0$ respectively. The permittivity for segments K, B, and P is set at $40\epsilon_0$. Due to the dilute nature of these segments in the system, this choice has little effect on the bulk *cmc* over a range of $10\epsilon_0$ to $80\epsilon_0$. Therefore, a value in the middle was chosen.

As stated earlier, the short-range contact interactions between segments are given by the Flory-Huggins chi parameters, χ_{AB} . The chi parameters for segments A' ($A' = K, B,$ and P) with respect to the solvent segment W are all set to 0: $\chi_{A'W} = 0$. Therefore, no preferential interaction is given for these segments with water. Furthermore, the chi parameters for A' with respect to the aliphatic C segments are set to 2: $\chi_{A'C} = 2$. This means that there is a repulsion between the aliphatic chain segments and the more hydrophilic salt and head-group segments.

Table 7.1. Bulk Chi parameters

Segments	C		P		W		K, B
	420	031	420	031	420	031	420 and 031
C (tails)	-	-	2	2	1.9	1.9	2
P (heads)	2	2	-	-	0	0	0
W (water)	1.9	1.9	0	0	-	-	0

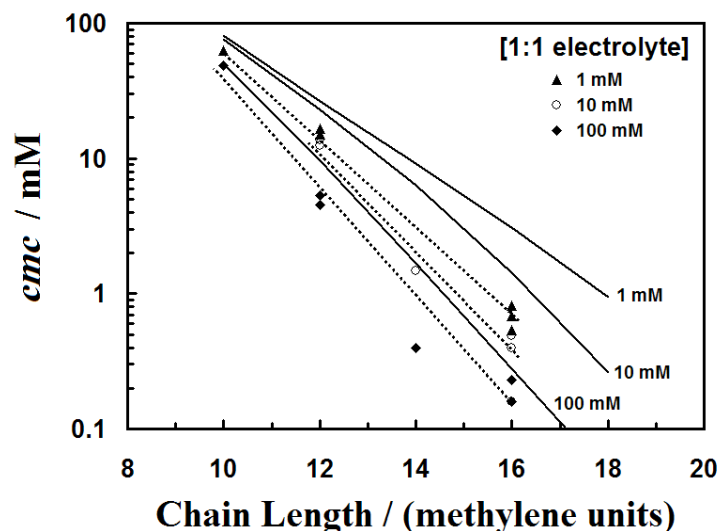


Figure 7.5 Critical micelle concentration (*cmc*) versus surfactant chain length at various 1:1 electrolyte concentrations. The symbols represent experimental values taken from references 24–27 for alkyl trimethylammonium and pyridinium surfactants. The dotted lines are merely guides for elucidation of the data sets. The solid lines represent the calculated values for $C_nP_3^+$ surfactants obtained with the SCFA Theory. (Reproduced with permission from Lokar, W. J.; Koopal, L. K.; Leermakers, F. A. M.; Ducker, W. A. J. *Phys. Chem. B* **2004**, 108, 3633-3643)

Perhaps the most crucial parameter selection for surfactants is the choice for χ_{CW} . The selection of this parameter should ensure reasonable behavior of the surfactant with respect to experimental conditions, such as the effect of chain length or ionic strength on the critical micelle concentration (*cmc*). A value of between 1.9 and 2 yields the most accurate behavior with respect to the chain length dependence of the *cmc*. This value is slightly lower than the value of 2.3 suggested by Tanford.²³ In addition, the use of the value 2 or higher results in lattice artifacts that arise as the result of the sharpness of the

aliphatic–water interface being the same order as the lattice size. Therefore, a value of 1.9 is chosen to avoid such complications.

Fig. 7.5 shows several experimental values for the *cmc* of various alkyl trimethylammonium and pyridinium surfactants²⁴⁻²⁷ compared to the calculated values. Here the concern is that the slopes and trends with ionic strength are reasonable despite the fact that the quantitative agreement is not exact. The lack of quantitative agreement can result from several factors including the modeling of the ω -methyl group, the head group, or the counter-ion. Studies have shown that the counter-ion can have a significant effect upon the *cmc* of ionic surfactants.²⁸ Agreement of the change in the *cmc* with chain length means that the short-range hydrophobic effect is reasonably modeled by $\chi_{CW} = 1.9$. This is critical for studies of adsorption and surfactant association.

The aim of the next two chapters is to examine surfactant adsorption on solid surfaces as a function of the separation between the two solids. As a prelude, a brief discussion of the modeled bulk properties is given in order to show that the model parameters yield reasonable results compared to experimental literature. In addition, the structural and electrical properties of the modeled bulk aggregates are also discussed.

Fig. 7.6 shows the equilibrium chemical potential for the surfactant at different salt concentrations for spherical, cylindrical and flat bilayer micelles. Surfactants forming spherical micelles have a lower chemical potential than cylindrical or bilayer micelles. Therefore, at a given concentration, spherical micelles will be more stable than the other two structures. This is consistent with experimental findings for ionic surfactants of similar chain length.²⁹⁻³² Therefore, all *cmc* values presented are for calculations with spherical micelles. The *cmc* values calculated for $C_{16}P_3^+$ with the parameter selections in Table 7.1 are presented in Table 7.2.

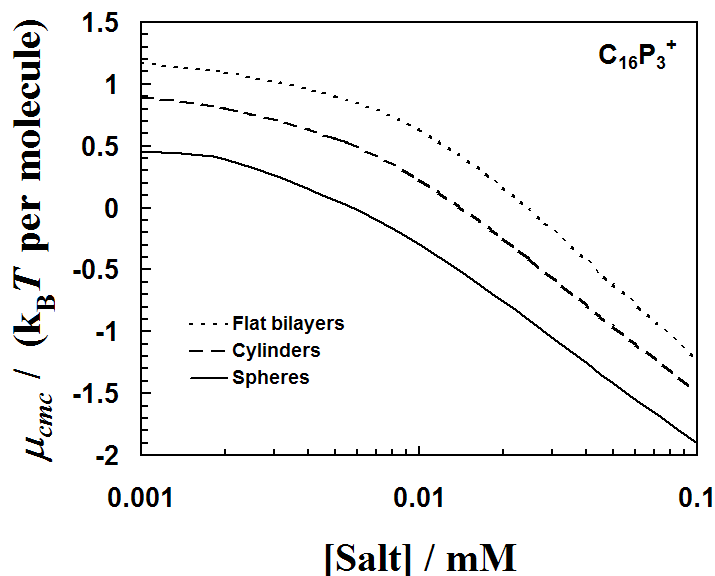


Figure 7.6 Chemical potential of surfactant versus salt concentration for $C_{16}P_3^+$ forming micelles of various shapes. The chemical potential is lower for spherical micelles at all ionic strengths calculated here.

Table 7.2. Cmc of $C_{16}P_3^+$ from SCFA at various monovalent salt concentrations

salt] / mM	cmc / mM
1	3.08
5	2.05
10	1.43
20	0.895
50	0.456
100	0.279
200	0.176
500	0.104

Since the double-layer force is central in this work, and this force is dictated by the ionic strength in solution, the discussion of bulk properties will center around ionic strength effects.

In Fig. 7.7 the distribution of segments in a micelle is given both for the tails and head-groups in the presence of 10 and 100 mM monovalent salt. It is easy to see from Fig. 7.7 that the tail groups occupy the center of the micelle (center of mass is $z = 0$). The head groups are situated with a distribution over a couple of layers with a peak at about 6

or 7 lattice layers from the center of the micelle, depending upon ionic strength. This means that the micelles have diameters of about 3.7-4.3 nm. This micellar size, as well as the thicknesses of adsorbed layers discussed later, are underestimated by the current model due to the extra flexibility of the aliphatic tail imparted by the Markov approximation to calculate chain conformations.

An increase in the ionic strength causes the chain distribution to extend to higher z . Therefore, there are more trans conformations and the aggregation number is greater at higher ionic strengths. Furthermore, the additional screening of surfactant head-groups allows for a tighter packing of molecules in the micelle (notice narrower head-group peak in Fig. 7.7) and thus a higher aggregation number.

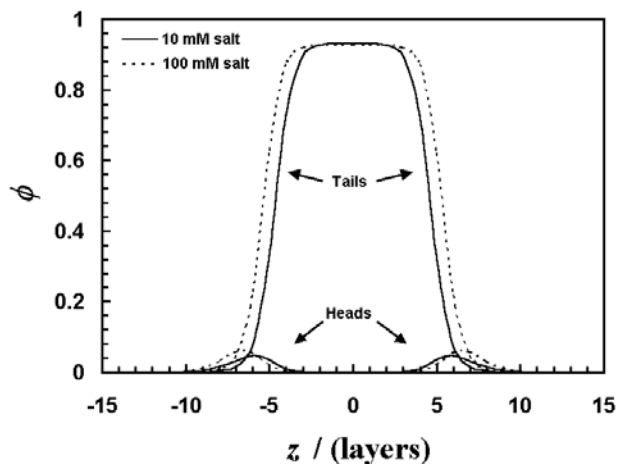


Figure 7.7 Radial segment distribution for $C_{16}P_3^+$ surfactants in a spherical micelle at salt concentrations of 10 and 100 mM. $z = 0$ is the center of mass of the micelle. Both the tail and head group distributions extend to higher z as the ionic strength increases. $\chi_{AW} = 0$, $\chi_{AC} = 2$, $\chi_{CW} = 1.9$. (Reproduced with permission from Lokar, W. J.; Koopal, L. K.; Leermakers, F. A. M.; Ducker, W. A. J. *Phys. Chem. B* **2004**, 108, 3633-3643)

The electric potential profile around a $C_{16}P_3^+$ micelle is presented in Fig. 7.8 for 10 and 100 mM monovalent salt. The peaks in the potential correspond with the maximum volume fraction of head-groups. The calculated potential in solution decays exponentially at large z as the inverse square of the ionic strength (I) as is predicted by Poisson-Boltzmann theory.

$$\kappa^{-1} = \frac{0.97 \text{ layers}}{\sqrt{I/M}} = \frac{0.30 \text{ nm}}{\sqrt{I/M}} \quad (7.24)$$

The coefficient of 0.30 nm is in agreement with Poisson-Boltzmann theory for 1:1 electrolytes at 298 K.³³

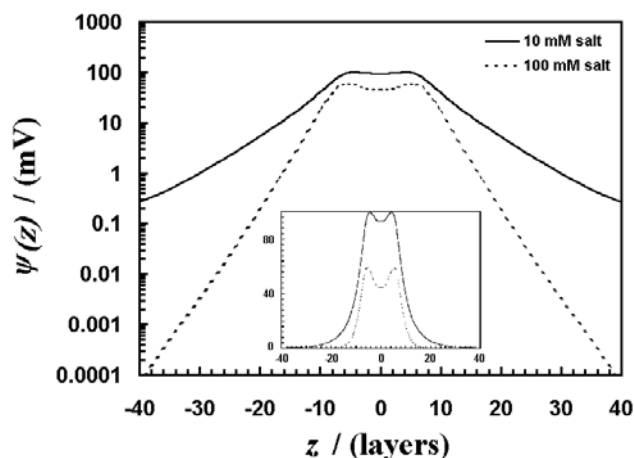


Figure 7.8 Electrical potential around a spherical micelle of $C_{16}P_3^+$ in 10 and 100 mM salt solutions. The y-axis is on a log scale so the different decay lengths can easily be discerned. The inset shows the same data on a linear scale. The magnitude and range of the potential decreases with increased electrolyte concentration. The parameters are the same as in Fig. 7.7. (Reproduced with permission from Lokar, W. J.; Koopal, L. K.; Leermakers, F. A. M.; Ducker, W. A. J. *Phys. Chem. B* **2004**, 108, 3633-3643)

Within the micelle, the decay length is much longer because the dielectric permittivity and electrolyte concentration within the micelle is much lower. Furthermore, the potential (at the maximum head group density) is lower at higher ionic strengths. This decrease in micelle electrical potential is non-Nernstian with salt concentration. In this case the slope is only -40 mV per decade of salt concentration. This is because the potential determining ions are not the salt ions but rather the surfactant ions, whose characteristic concentration is the *cmc*. The ionic strength affects the potential by changing the value of the *cmc*. The micelle potential scales with the ionic strength dependent *cmc*, $cmc(I)$, in a Nernstian fashion.

$$\frac{\partial \psi_{micelle}}{\partial \log[cmc(I)]} = 58 \text{ mV} \quad (7.25)$$

7.4 Conclusions

Aggregation of surfactants in bulk solution can be reasonably modeled using SCFA. In addition, the calculated electric double-layer potentials around aggregates decay as expected from Poisson-Boltzmann theory. The choice of parameters yields the same shape of bulk micelles as for surfactants similar to those used in the experimental portion of this thesis. Furthermore, the hydrophobic effect is modeled reasonably well by the parameter selections in that the theoretical *cmc* scales with the chain length in a similar fashion to experimental results.

7.5 Cited Literature

- (1) Scheutjens, J. M. H. M.; Fleer, G. J. *J. Phys. Chem.* **1979**, *83*, 1619.
- (2) Scheutjens, J. M. H. M.; Fleer, G. J. *J. Phys. Chem.* **1980**, *84*, 178.
- (3) Meijer, L. A.; Leermakers, F. A. M.; Lyklema, J. *J. Chem. Phys.* **1999**, *110*, 6560.
- (4) Oversteegen, S. M. *Phys. Rev. E: Stat., Nonlinear, Soft Matter Phys.* **2000**, *62*, 8453.
- (5) Leermakers, F. A. M.; Scheutjens, J. M. H. M.; Lyklema, J. *Biophys. Chem.* **1983**, *18*, 353.
- (6) Böhmer, M. R.; Koopal, L. K. *Langmuir* **1992**, *8*, 2660.
- (7) Böhmer, M. R.; Koopal, L. K.; Lyklema, J. *J. Phys. Chem.* **1991**, *95*, 9569.
- (8) Koopal, L. K.; Lee, E. M.; Böhmer, M. R. *J. Colloid Interface Sci.* **1995**, *170*, 85.
- (9) Goloub, T. P.; Koopal, L. K. *Langmuir* **1997**, *13*, 673.
- (10) Böhmer, M. R.; Koopal, L. K. *Langmuir* **1992**, *8*, 2649.
- (11) Jódar-Reyes, A. B.; Ortega-Vinuesa, J. L.; Martín-Rodríguez, A.; Leermakers, F. A. M. *Langmuir* **2003**, *19*, 878.
- (12) Vermeer, A. W. P.; Leermakers, F. A. M.; Koopal, L. K. *Langmuir* **1997**, *13*, 4413.
- (13) Wolterink, J. K.; Leermakers, F. A. M.; Fleer, G. J.; Koopal, L. K.; Zhulina, E. B.; Borisov, O. V. *Macromolecules* **1999**, *32*, 2365.
- (14) Wijmans, C. M.; Scheutjens, J. M. H. M.; Zhulina, E. B. *Macromolecules* **1992**, *25*, 2657.
- (15) Israëls, R.; Leermakers, F. A. M.; Fleer, G. J. *Macromolecules* **1994**, *27*, 3087.
- (16) Sader, J. E.; Chan, D. Y. C. *Langmuir* **2000**, *16*, 324.
- (17) Wijmans, C. M.; Leermakers, F. A. M.; Fleer, G. J. *J. Colloid Interface Sci.* **1994**, *167*, 124.
- (18) Böhmer, M. R.; Koopal, L. K.; Tijssen, R. *J. Phys. Chem.* **1991**, *95*, 6285.
- (19) Riesco, N.; Villa, S.; González, J. A.; Fuente, I. G. d. l.; Cobos, J. C. *Fluid Phase Equilibria* **2002**, *202*, 345.

- (20) Böhmer, M. R. Adsorption and Micellization of Surfactants. Ph.D. Thesis, Wageningen Agricultural University, 1991.
- (21) van Male, J. Self-consistent-field theory for chain molecules: extensions, computational aspects, and applications. Ph.D. Thesis, Wageningen University, 2003.
- (22) Flory, P. *Principles of Polymer Chemistry*; Cornell University Press: Ithica, New York, 1953.
- (23) Tanford, C. *The Hydrophobic Effect*; Wiley Interscience: New York, 1980.
- (24) van Os, N. M.; Haak, J. R.; Rupert, L. A. M. *Physico-Chemical Properties of Selected Anionic, Cationic, and Nonionic Surfactants*; Elsevier: Amsterdam, 1993.
- (25) Lokar, W. J.; Ducker, W. A. *Langmuir* **2004**, *20*, 378.
- (26) Mehrian, T.; de Keizer, A.; Korteweg, A. J.; Lyklema, J. *Colloids and Surfaces* **1993**, *71*, 255.
- (27) Goloub, T. P.; Koopal, L. K.; Bijsterbosch, B. H.; Sidorova, M. P. *Langmuir* **1996**, *12*, 3188.
- (28) Berr, S.; Jones, R. R. M.; Johnsson, J. S., Jr. *J. Phys. Chem.* **1992**, *96*, 5611.
- (29) Pisarcik, M.; Devinsky, F.; Svajdlenka, E. *Colloids and Surfaces A* **1996**, *119*, 115.
- (30) Ozeki, S.; Ikeda, S. *Bull. Chem. Soc. Japan* **1981**, *54*, 552.
- (31) Imae, T.; Kamiya, R.; Ikeda, S. *J. Colloid Interface Sci.* **1985**, *108*, 215.
- (32) Fujio, K. *Bull. Chem. Soc. Japan* **1998**, *71*, 83.
- (33) Israelachvili, J. N. *Intermolecular and surface forces*, 2nd ed.; Academic Press London: London, 1991.

Chapter 8

SCFA Calculations of Adsorption between Neutral Surfaces

8.1 Introduction

In the previous chapter, SCFA results were presented for surfactant aggregation in the bulk. In this thesis the primary concern is surfactant aggregation at solid surfaces and, in particular, what happens when these solid surfaces interact in solution. As demonstrated in chapters 3–6, accounting for the hydrophobic effect is critical to accurately describe surfactant behavior between interacting solid surfaces. In chapter 7, non-electrostatic interactions were modeled with Flory-Huggins interaction parameters. In particular, a selection of $\chi_{CW} = 1.9$, predicts the appropriate slope of the *cmc* with chain length. In other words, the hydrophobic effect is reasonably modeled.

In this chapter adsorption to a solid surface is modeled using SCFA, which includes non-electrostatic interactions such as those proposed experimentally in chapters 3-6. Here, the effects of changing the separation between the solids, H , is calculated while maintaining equilibrium with a bulk reservoir. In this chapter uncharged solids are studied. The goal here is to see what happens when ionic surfactants adsorb to neutral surfaces and how the interactions between these surfaces are affected by the surfactant and *vice versa*. In chapter 9, the case where the surfaces possess a constant charge will be examined.

8.2 Additional Theoretical Detail

The ionic surfactant modeled here is the same as discussed in chapter 7. The separation between the solid surfaces is varied by changing the number of lattice units, M , while maintaining an equilibrium with a bulk reservoir. In these calculations a mirror boundary condition is applied between the M^{th} and $(M+1)^{\text{th}}$ layers. Therefore, the system will be completely symmetric about the mid-plane between the surfaces. The surfaces can be thought of as being at the zeroeth and $(2M+1)^{\text{th}}$ layers with the separation given as $H = 2M$. This is illustrated in Fig. 8.1

For the neutral surfaces presented here, two cases with slightly different surface parameters are discussed in order to illustrate the effect of some of the surface parameters.

The first model surface has a somewhat hydrophobic character. The surface segments, S, are given a permittivity of $80\epsilon_0$ (the same as water). The χ parameters are chosen with respect to the other segments such that the head-group segments are given a preferential attraction to the surface by selecting $\chi_{PS} = -4$. In addition, the carbon-like segments are given a slight attraction for the surface, $\chi_{CS} = -2$. All other segments in solution are given a non-preferential interaction with the surface by selecting the χ values to be zero. This particular surface will be hence referred to as the (420) surface. This notation illustrates the negative χ parameters with respect to the surface for the head group, aliphatic chain, and water respectively.

The second model surface has the same parameters with respect to the electrolyte, but the χ values with respect to the head group, aliphatic segments, and water are different. In this case $\chi_{PS} = 0$, $\chi_{CS} = -3$, and $\chi_{WS} = -1$. Here the preferential head-group attraction to the surface has been removed, the aliphatic attraction is increased slightly, and water is given a bit of attraction for the surface. This second surface will be given the index (031).

In order to compare these two surfaces, a displacement chi parameter is defined for each segment A.

$$\chi_{d,A} = \chi_{AS} + \chi_{WW} - \chi_{WS} - \chi_{AW} \quad (8.1)$$

This quantity represents the standard Gibbs energy of adsorption, i.e. the energy to exchange a water segment (W) on the surface with a segment A from bulk solution. Despite the differences in surface parameters for the (420) and (031) surfaces, the displacement chi parameter with respect to the aliphatic segments is the same in both cases ($\chi_{d,C} = -3.9$). This means that both surfaces have the same hydrophobicity. Note that this displacement chi value amounts to about $1.3 k_B T$ of energy per C segment. This is just slightly greater than the value of $1.0 k_B T$ per CH_2 for cationic surfactant adsorption on silica-like substrates near the *ccp*.¹ Therefore, despite some hydrophobicity these surfaces can still give a good estimate of the behavior for some more polar surfaces. The

Table 8.1 Chi parameters for the (420) and (031) surfaces.

Segments	S	
	420	031
C (tails)	-2	-3
P (heads)	-4	0
S (surface)	-	-
W (water)	0	-1
K, B (salt ions)	0	0

8.3 Adsorption at Large Separations

8.3.1 (420) Surface

SCFA isotherms and segment profiles for isolated surfaces are not new to the literature,³⁻⁷ however, they provide an appropriate initial discussion for this study. First, adsorption isotherms are calculated as a function of ionic strength in solution for the (420) surface. The isotherms presented in Fig. 8.2 show the basic features associated with adsorption on a solid, uncharged surface. At low surfactant concentrations the slope of the adsorption is small. The hydrophobic tails are attracted to the surface, but there is a repulsive interaction between the charged head-groups of neighboring surfactants on the surface. This is clearly shown at lower salt concentrations by the smaller slope in the adsorption isotherm due to longer range head-group repulsions (longer Debye-length). Once the tails reach a given density on the surface (0.1–0.2 molecules/nm²), the adsorption begins to rise steeply due to a loss of unfavorable C-W interactions. As the surfactant concentration approaches the *cmc*, the electrostatic repulsion between head-groups causes a decrease in the slope of the isotherm.

In addition, the isotherms in Fig. 8.2 show the expected increase in the adsorption plateau at higher ionic strengths due to the increased screening of head-group repulsions. This screening also shifts the step in the isotherm to lower surfactant concentrations because there is a smaller repulsive force between the head-groups and adsorption can be achieved at lower chemical potentials.

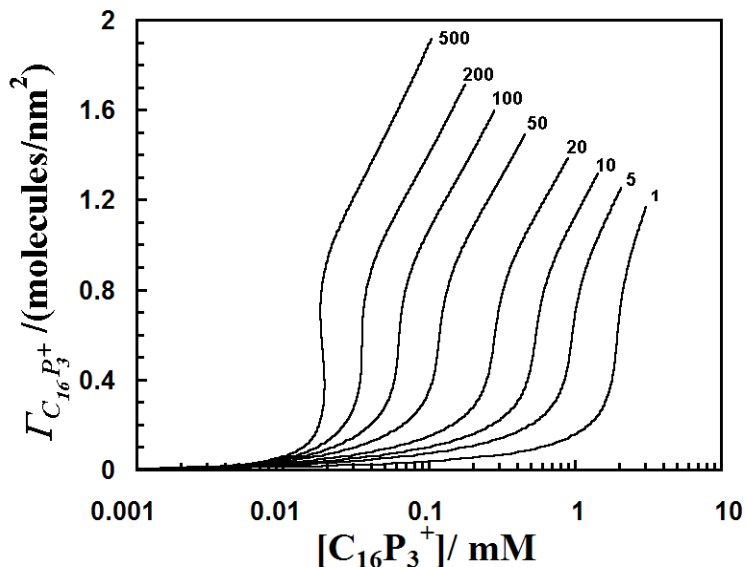


Figure 8.2 Adsorption as a function of $C_{16}P_3^+$ concentration at various electrolyte concentrations on an isolated, neutral surface (420). Each curve is labeled with the electrolyte concentration in units of mM. Adsorption increases as the salt concentration is raised. $\chi_{AW} = 0$, $\chi_{AC} = 2$, $\chi_{CW} = 1.9$, $\chi_{CS} = -2$, and $\chi_{PS} = -4$.

The average orientation of the surfactant with respect to the surface can be deduced from the density profile. Fig. 8.3 shows examples in 10 mM electrolyte solution. At low surfactant concentrations, the head group is attracted to the surface along with the tails and the surfactant adsorbs relatively flat on the surface. At high concentrations, closer to the *cmc* (Fig. 8.3b), the number of tail-tail interactions is larger and the surfactant is primarily oriented with its charged head toward the solution. Over the isotherm a transition occurs whereby the surfactant goes from lying down on the surface to a more extended “monolayer”-type structure.

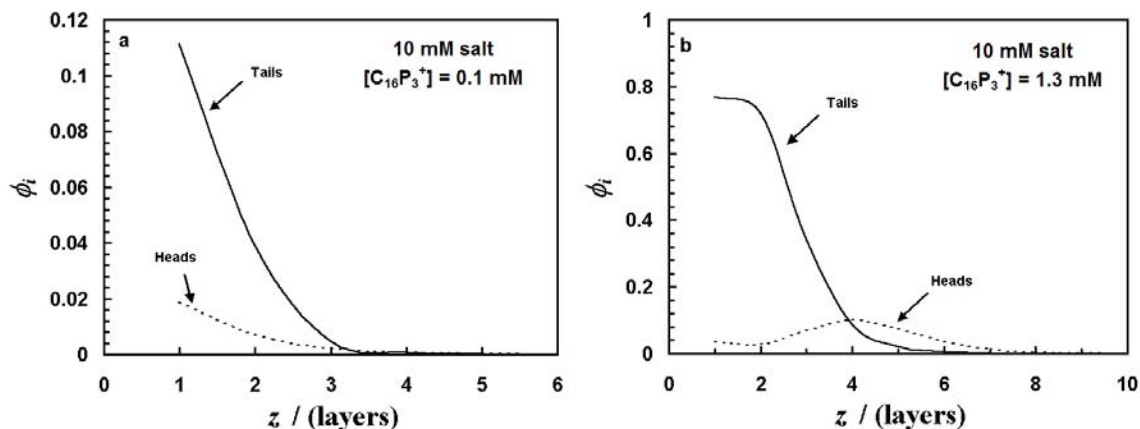


Figure 8.3 Segment distributions for two $C_{16}P_3^+$ concentrations near an isolated, neutral (420) surface. a) At low concentrations the surfactant lies almost flat on the surface with both the head groups and tails in the first 2 layers. Note: there are 16 tails groups for every 3 head groups. b) At higher concentrations, the ratio of tails to heads is greater in the first layer. The surfaces are separated by $H = 70$ lattice layers.

8.3.2 (031) Surface

For the (031) surface, a very different shape to the isotherm is observed. The isotherms have a discontinuous step (s-shaped loop). Such loops in the isotherms have been discussed previously in SCFA calculations.^{3,7,8} Along this loop there are multiple values of the surface excess for a single surfactant concentration (Fig. 8.4). The two points where the slope in the isotherm changes sign are the spinodal points. They dictate the boundaries of an unstable portion of the isotherm in between. Using an equal area argument ($\int \mu d\Gamma$), the location of the binodal point can be determined. At this point (concentration) there are two stable values for the surface excess. The system can phase separate into regions of low surfactant density and high surfactant density. Between the spinodal points and the stable surface excess values at the binodal concentration, there is a meta-stable regime.

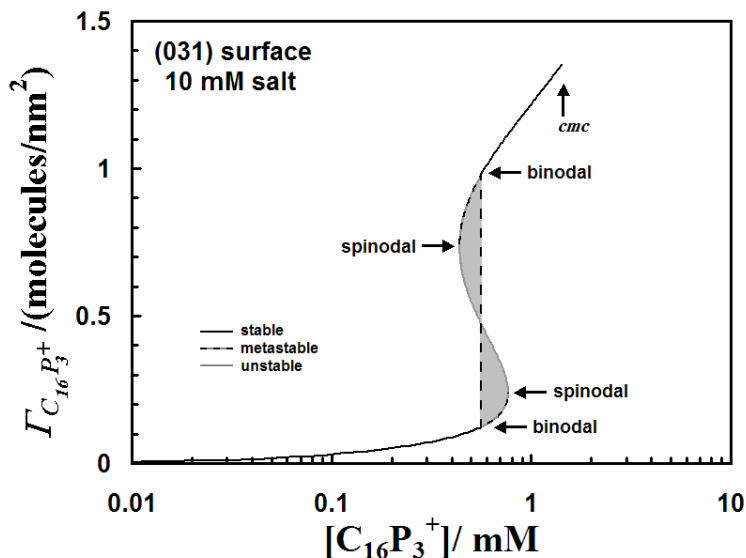


Figure 8.4 Adsorption isotherm for $C_{16}P_3^+$ on an isolated, neutral surface (031) in 10 mM electrolyte. The binodal and spinodal points are highlighted. The shaded areas are used in the equal area construction to determine the concentration at which the binodal points occur. The dashed line through the binodal connects the two stable branches of the isotherm. Metastable and unstable regions of the isotherm occur along the s-shaped loop.

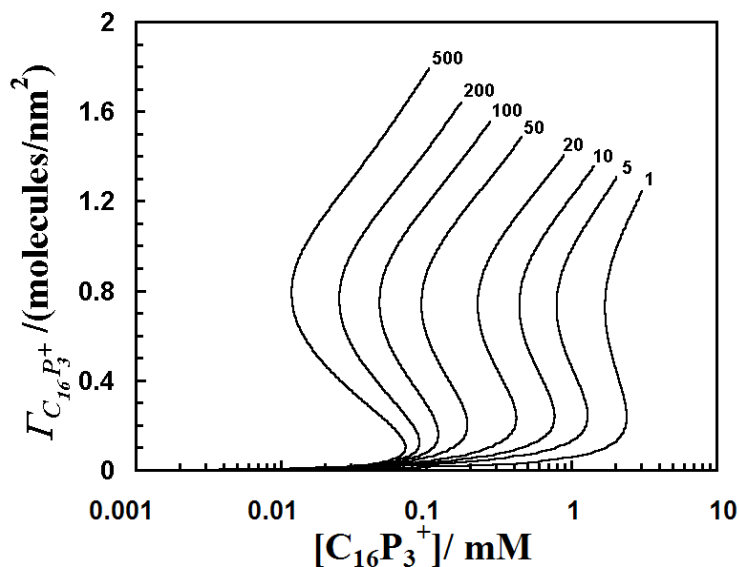


Figure 8.5 Adsorption isotherms for $C_{16}P_3^+$ on an isolated, neutral surface (031) as a function of electrolyte concentration. Each curve is labeled with the electrolyte concentration in units of mM. Adsorption increases as the salt concentration is raised.

In Fig. 8.5, it is easy to see that the size of the loop increases with increased salt concentration. This was also the case for the (420) surface, with a small loop appearing at 500 mM salt. In Fig. 8.6 isotherms are compared for each type of surface at 1, 10, and 100 mM salt. Compared to the (420) surface, the adsorption for (031) is suppressed until higher surfactant concentrations. The surfactant chemical potential in the bulk must be much higher to force the surfactant to adsorb and displace the water. Furthermore, the steps in the isotherms occur at similar surfactant concentrations at a given ionic strength. The discontinuous steps in the (031) isotherms occur near the top (higher concentration side) of the step in the corresponding (420) isotherm. Above the step, the phase transition allows for more C-C interactions initially leading to more adsorption for the (031) surface.

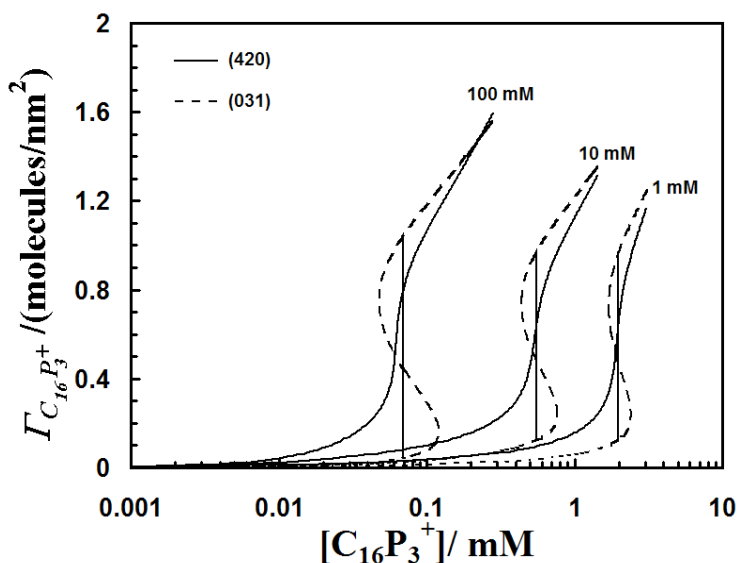


Figure 8.6 Comparison of isotherms for (420) and (031) surfaces at different ionic strengths. The vertical lines represent the $[C_{16}P_3^+]$ of the phase transition for each of the (031) isotherms.

8.4 Adsorption between Confined Surfaces

8.4.1 (420) Surfaces

Now the size of the lattice will be decreased, and thus the effect of decreased separation between the solid surfaces can be calculated. Fig. 8.7 shows a series of adsorption isotherms calculated at different solid-solid separations for the (420) surface at a constant monovalent salt concentration of 10 mM.

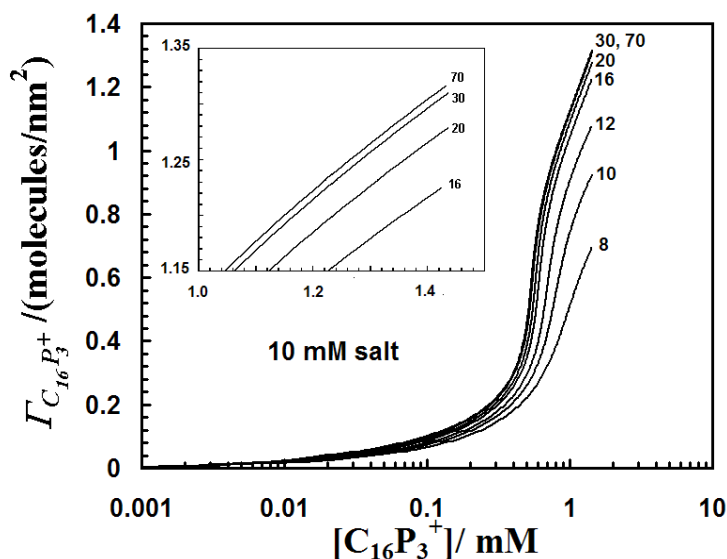


Figure 8.7 Adsorption as a function of $C_{16}P_3^+$ concentration at various solid-solid separations on a neutral (420) surface in 10 mM salt. The separation is listed next to the respective curve in units of lattice layers. The amount adsorbed decreases as the separation is made sufficiently small. The inset shows the data for separations 16, 20, 30 and 70. The adsorption is essentially constant (to within 1%) until the separation falls below about 30 layers $\sim (3\kappa^{-1})$.

Fig. 8.7 shows that the adsorption has the same general shape at smaller separations, however, the magnitude in the adsorption changes considerably. Changes in adsorption become significant when the separation between the solids is less than about $3\kappa^{-1}$ (when the electric double-layers begin to overlap). The largest absolute changes in adsorption with separation occur at surfactant concentrations at or above the step in the isotherm. For example, at 0.6 mM $C_{16}P_3^+$, the absolute adsorption changes from 0.77

molecules/nm² at $H = 70$ layers to 0.39 molecules/nm² at $H = 12$ layers. A drastic change in adsorption occurs when the step in the isotherm is very steep, as will be most apparent for the (031) surfaces.

Increasing the electrolyte concentration, yields isotherms with the same general shape (Fig. 8.8), however, since at larger separations the regulating force is the double-layer force, one should expect that the deviation is smaller if the double-layer force is shorter-ranged. At the *cmc* in 10 mM salt (1.43 mM), the change in adsorbed amount was 1% going from a separation of 70 to 30 layers, however, at the *cmc* in 100 mM salt (0.279 mM), the change is now less than 0.1% over the same separations.

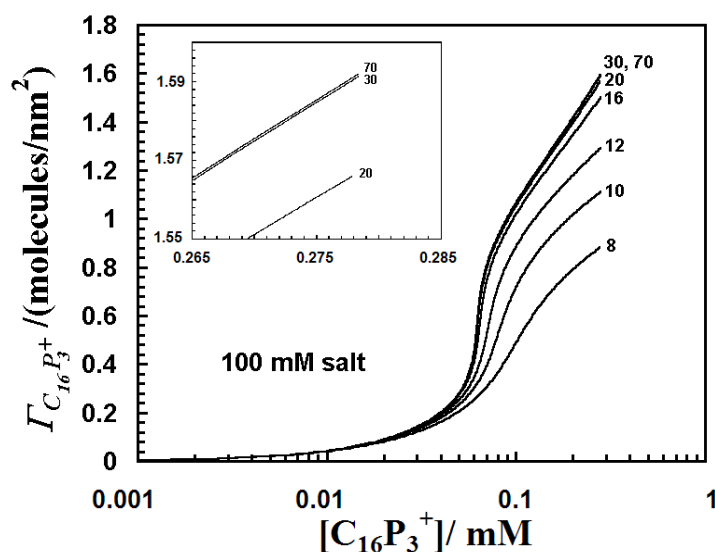


Figure 8.8 Adsorption as a function of $C_{16}P_3^+$ concentration at various solid-solid separations on a neutral (420) surface in 100 mM salt. The separation is listed next to the respective curve in units of lattice layers. A smaller separation is required to cause desorption in 100 mM versus 10 mM salt.

8.4.2 (031) Surfaces

For (031) isotherms the confinement by another surface also decreases the plateau adsorption and shifts the adsorption curve to higher concentrations. Above and below the step in the isotherm, the trends are the same as for the (420) surface. Below the step, however, both the interaction energy and change in adsorption are less in magnitude at a

given concentration for (031) than for (420). This results from the fact that the surface excess is lower in this region due to the increased affinity of water for the surface. The lower amount of adsorbed surfactant leads to a lower positive potential between the surfaces and thus a decreased interaction energy. This leads to a decreased driving force for proximal desorption for most concentrations compared to the (420) surface.

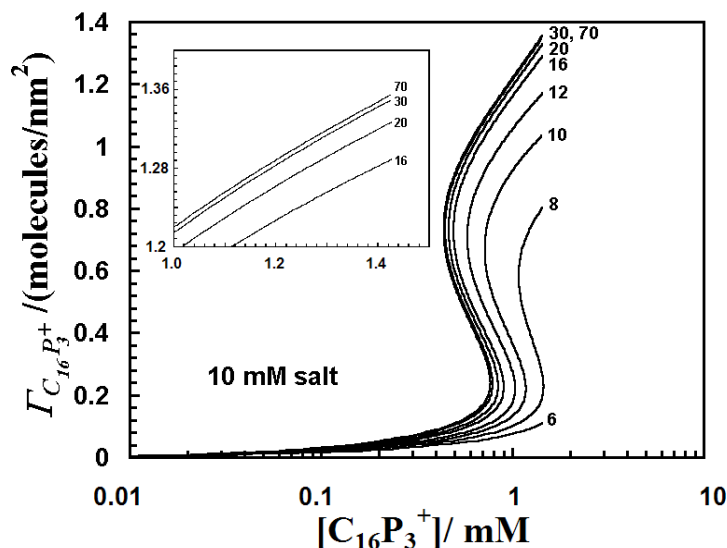


Figure 8.9 Adsorption isotherms as a function of solid-solid separation on a neutral (031) surface in 10 mM salt. The separation is listed next to the respective curve in units of lattice layers. The amount adsorbed decreases as the separation is made sufficiently small. The inset shows the data for separations 16, 20, 30 and 70. At 30 layers the adsorption is a bit lower than for 70 layers.

Once again, there is interesting behavior near the step in the isotherm. Due to the discontinuous nature of the step, an analysis near the step, such as that shown for the (420) surface, is much more complicated. As the separation is decreased, the step in the isotherm shifts to higher surfactant concentrations as shown in Fig. 8.9. Therefore, as the separation is decreased at a constant concentration, the adsorption can either traverse a metastable branch of the new isotherm (smaller separation) or jump to a much lower equilibrium value. If the adsorption follows the metastable regimes upon compression and separation of the surfaces, a hysteresis develops in both the adsorption versus

separation as well as the interaction energy versus separation. Otherwise, at equilibrium, the adsorption jumps between two different, but stable surface excess values. This can lead to large proximal desorption at concentrations in the vicinity of the discontinuous step in the isotherm.

8.5 Interactions between Surfaces

8.5.1 (420) Surfaces

In the previous section, adsorption isotherms were presented at varied separations between two solids. If the surfactant concentration is held constant, the interaction energy between the solids can be calculated as the separation decreases. Fig. 8.10 shows the interaction energy as a function of solid–solid separation, H . The interaction energy is repulsive (positive) for $H > 6-8$ layers. Furthermore, at larger separations, the interaction becomes more repulsive as the surfactant concentration increases. This results from a greater electric potential due to the presence of a higher density of charged surfactant on the surfaces.

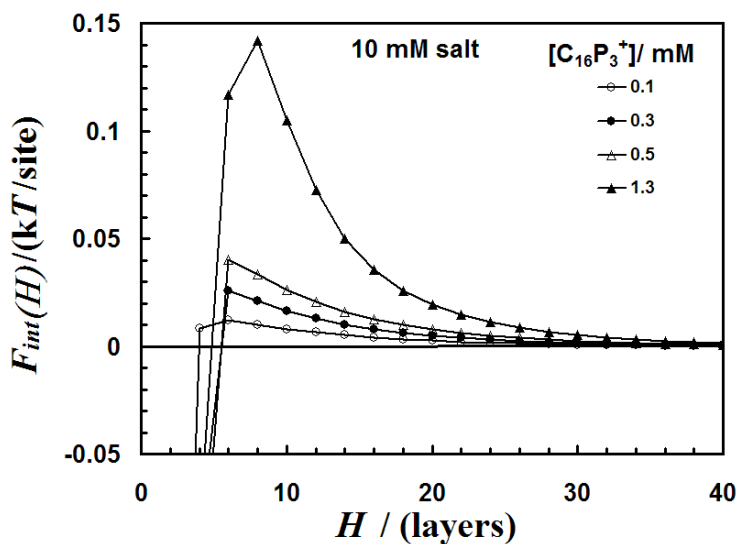


Figure 8.10 The interaction energy is plotted as a function of separation for neutral (420) surfaces in 10 mM salt. As the concentration of surfactant increases, the interaction energy also increases.

The peak in the interaction energy at small separations is particularly interesting. The decrease in energy from the maximum means that the force goes from repulsive to attractive. Such an attractive contribution to the overall force was apparent in experimental measurements in surfactant solutions in chapters 3-6. In these calculations, however, there is no van der Waals force. Therefore, such an attractive contribution can be attributed to other mechanisms.

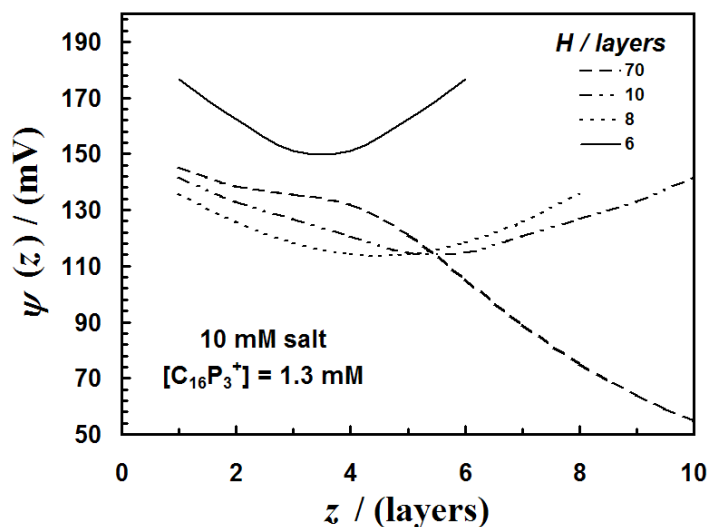


Figure 8.11 The electrical potential as a function of distance from the solid for various separations between the two solids (70, 10, 8 and 6 layers). $[C_{16}P_3^+] = 1.3 \text{ mM}$ and $[\text{salt}] = 10 \text{ mM}$.

Table 8.2 Electric Potentials at the Mid-Plane Between Two Flat, Uncharged (420) Surfaces. ($[C_{16}P_3^+] = 1.3 \text{ mM}$)

H / layers	$\psi\left(\frac{H}{2}\right) / \text{mV}$
70	3.84
30	41.3
20	70.7
16	88.5
12	108
10	115
8	114
6	151

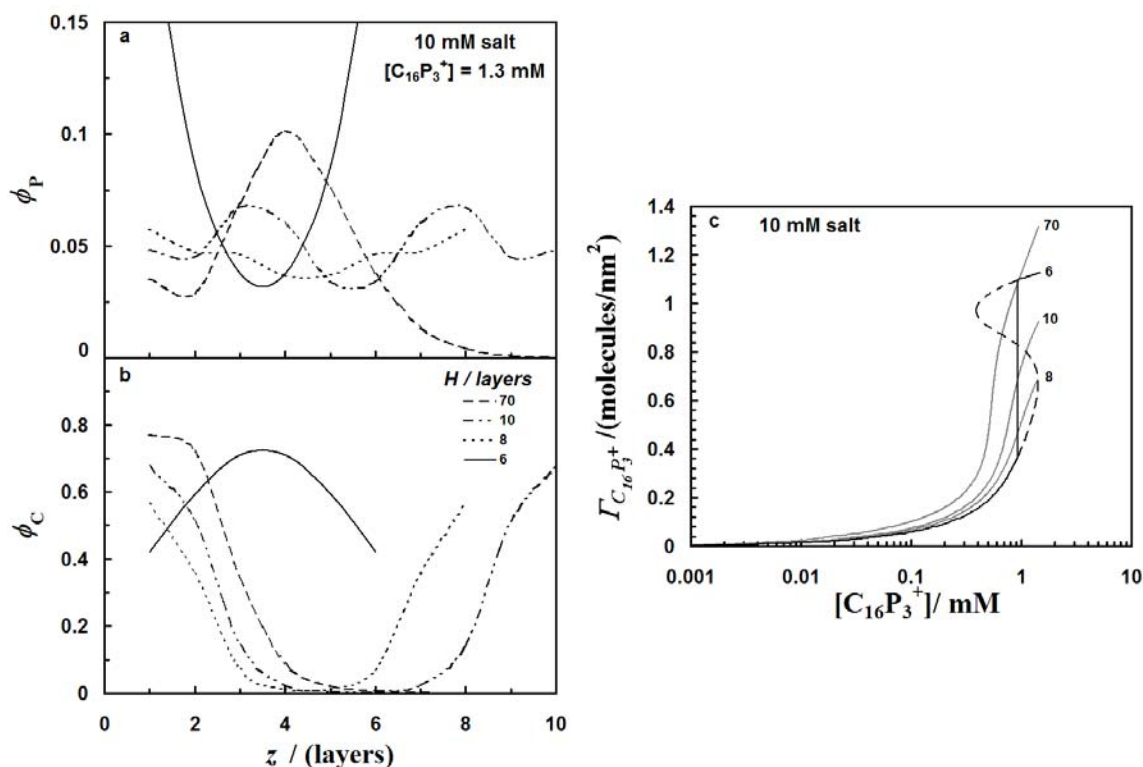


Figure 8.12 a and b) Density profiles of head group segments (P) and tail segments (C) in the vicinity of a (420) surface is shown as a function solid-solid separation. The separation is listed in the figure in units of lattice layers. All curves shown are for $[C_{16}P_3^+] = 1.3$ mM in the presence of 10 mM salt. **c)** Adsorption isotherms are presented for $H = 70, 10, 8,$ and 6 layers. The isotherms in gray were shown in Fig. 8.7. At $H = 6$, a phase transition occurs similar to those shown in Figs. 8.4-8.6.

In order to understand the maximum in the interaction better, the behavior in 1.3 mM $C_{16}P_3^+$ is examined more closely. In Fig. 8.11, the electric potential profiles are shown for $[C_{16}P_3^+] = 1.3$ mM. This concentration is $0.9 \times \text{cmc}$, but still results in a large absolute adsorption. In general, the potential at the mid-plane between the solids, $\psi\left(\frac{H}{2}\right)$, increases as the surfaces approach. There is a slight change in behavior for $6 < H < 10$ layers. The mid-plane potential is actually lower at a separation of $H = 8$ than $H = 10$ layers. The values for the mid-plane potentials are given in Table 8.2. Such a local

maximum in the electric potential results from a change in the shape of the potential profile as the adsorbed layers on both surfaces begin to merge. More important is the drastic increase in potential at a separation of $H = 6$ layers. Such a large increase alone would increase the repulsion between the surfaces, however, the calculated interaction in Fig. 8.10 suggests that there is an attractive force present.

Near the maximum in the interaction, the calculated profiles for the head-group and tail segments are plotted as a function of separation (Fig. 8.12). Since the maximum in interaction energy occurs at $H = 8$ layers at this particular concentration, focus will be on differences between $H = 8$ and $H = 6$. For the head-group densities in Fig. 8.12a, the shape of the profile changes drastically between $H = 8$ and 6. At $H = 6$ the profile goes to a parabolic shape. Furthermore, the density increases drastically in layer $z = 1$. The tail group profile in Fig. 8.12b, on the other hand, shows a large increase in the density of tail groups at the mid-plane between the surfaces. The system has gone from two individual “monolayers” on each surface to a bilayer with reversed orientation between the surfaces. This is shown schematically in Fig. 8.13.

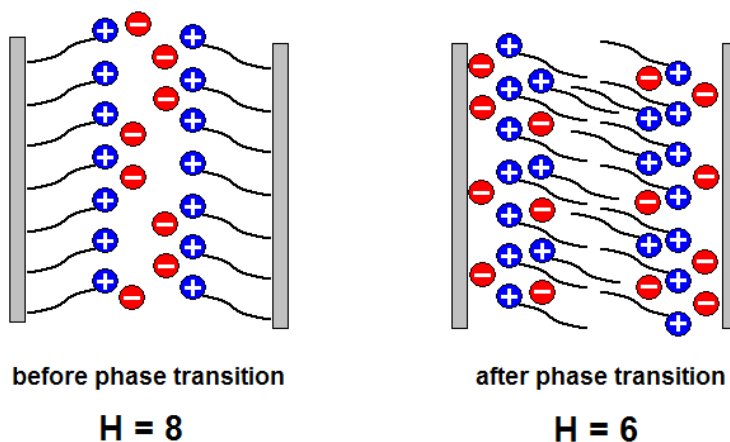


Figure 8.13 Schematic of a confinement-induced phase transition at $[C_{16}P_3^+] = 1.3$ mM. Orientation of surfactant reverses relative to the surface, with the head-groups nearer the surface after the transition.

The isotherms are compared in Fig. 8.12c. This time the separation is examined down to $H = 6$ layers. At small separations, a confinement-induced phase transition

occurs that leads to roughly a doubling of the amount of adsorbed surfactant. In Fig. 8.12b it is shown that in the vicinity of this phase transition the surfactant tails from opposite surfaces merge. This large increase in favorable C-C interactions initiates a large condensation of surfactant in the gap between the surfaces and subsequently contributes an attractive force. This is in agreement with the results in chapter 5. At smaller separations, the head-group density profile has become parabolic so the potential increases everywhere between the surfaces and now the surfactant will again desorb as the surfaces come closer together. In addition, the number of possible conformations for the surfactant in the film between the solids is decreased. The entropic cost of losing conformations can lead to a depletion of surfactant from the solid surface.

In Fig. 8.14 the change in adsorption as a function of solid-solid separation is plotted for the same four surfactant concentrations as in Fig. 8.10. Such a plot allows the quantitative differences in the adsorption as a function of separation between the two solids to be more easily viewed.

For $H > 10$ layers, the change in adsorption shows a maximum with respect to concentration around 0.6 mM. The magnitude of the adsorption regulation increases up to 0.6 mM and decreases thereafter. This is because at 0.6 mM the surfactant concentration is near a pseudo phase transition (the step in the isotherm, Fig. 8.7). At such a concentration, small deviations in confinement can lead to large changes in the adsorption behavior, just as small changes in concentration can cause large changes in adsorption for an isolated surface.

At smaller separations, the step in the isotherm occurs at higher concentrations (Fig. 8.2). According to our previous hypothesis, the desorption should be a maximum at higher concentrations. Indeed this is the case at $8 < H < 10$ layers, as is shown in Fig. 8.14. At the step in the isotherm, the electrostatic potential increases sharply due to surfactant adsorption, and it is the minimization of this potential that drives the adsorption changes upon confinement.

At small separations ($H < 8$ layers) the surfactant desorbs, adsorbs, and then desorbs again. This was explained by the confinement-induced phase transition. At lower concentrations this is seen at smaller separations because the chains do not extend as far from the surface (Fig. 8.3).

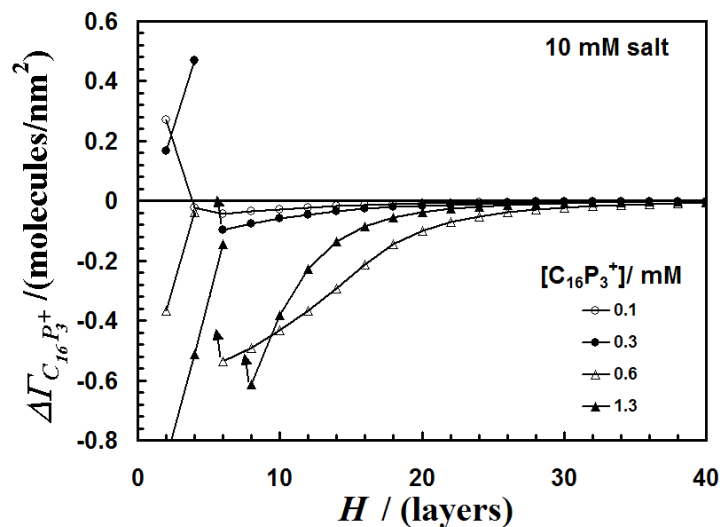


Figure 8.14 The change in surface excess for $C_{16}P_3^+$ is plotted versus separation for neutral (420) surfaces in 10 mM salt. The surfactant desorbs as the surfaces interact. The arrows indicate a phase transition between two different adsorbed amounts.

8.5.2 (031) Surfaces

Fig. 8.15 shows the interaction curves and the changes in adsorbed amount brought about by confinement of the (031) surfaces. Once again at the concentrations shown, the behavior is very similar to that shown for the (420) surface, however, the magnitude of surfactant that desorbs at $H < 8$ layers in 1.3 mM surfactant is greatly increased due to structural differences in the adsorbed layer brought about by the differences in head, tail, and water interaction with the (031) surface.

For the (031) surface there is the possibility for two types of phase transitions. One induced by a merging of the surfactant layers. This occurs at slightly smaller separations for the (031) surfaces. The other phase transition occurs as a consequence of the shifting of the step in the isotherm. Going from $H = 10$ to $H = 8$ at $[C_{16}P_3^+] = 1.0$ mM, the adsorption jumps from the upper branch of the isotherm to the lower branch (Fig. 8.9). In addition to the jump in adsorbed amount, the interaction energy shows a kink due to a reduction in the potential caused by decreasing the adsorbed amount of ionic surfactant.

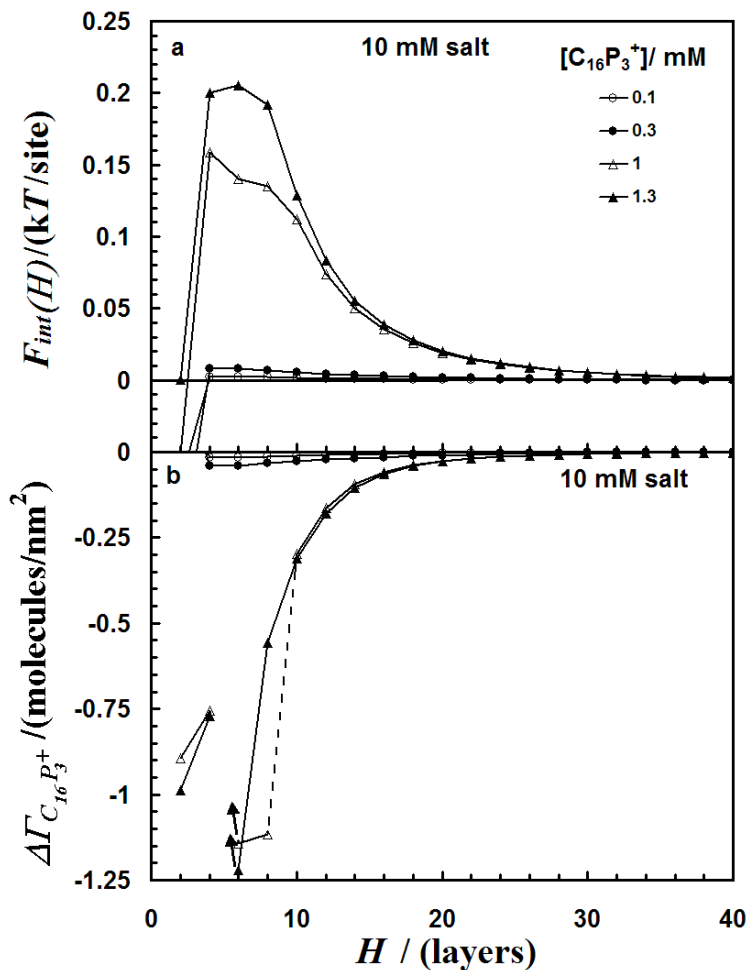


Figure 8.15 *a)* Interaction energy as a function of separation for neutral (031) surfaces in 10 mM salt. As the concentration of surfactant increases, the interaction energy also increases. *b)* The change in surface excess for $C_{16}P_3^+$ is plotted versus separation for neutral (031) surfaces in 10 mM salt. The surfactant desorbs as the surfaces interact. The arrows indicate a confinement-induced phase transition induced by a merging of surfactant layers. The dashed line indicates a phase transition induced by a small shift in the isotherm to higher concentrations.

8.6 Adsorbed Surfactant Layer Thickness

8.6.1 Analysis

In the previous analysis, the surfactant desorbed as the surfaces approached. Fig. 8.12a shows an interesting feature that has relevance to the analysis of experimental force measurements presented in chapters 3–6. Notice, that the peak in the head-group density moves closer to the solid surfaces as a second solid approaches. This means that the surfactant layer is being compressed as the interaction energy increases. If the thickness of the adsorbed surfactant layer, t , is defined as the number weighted average location of head-group segments, then the fractional thickness, $\Theta(H)$, of the surfactant layer can be calculated as the separation is decreased to H .

$$\Theta(H) = \frac{t(H)}{t(\infty)} \quad (8.2)$$

Fig. 8.16 shows the fractional thickness as a function of solid–solid separation. At the separation where the maximum interaction energy occurs ($H = 8$ layers), the surfactant layer has been compressed to about 60% of its original thickness. This has particular importance when trying to fit DLVO theory to experimental interaction energies in surfactant solutions. For simplicity, it is customary to fit the double-layer potential by assuming that there is a plane of charge at a fixed distance from the solid surface (i.e. constant adsorbed film thickness). In contrast, the calculations show that the adsorbed film thickness diminishes significantly during the interaction. The planes of charge therefore, approach each other to a smaller degree than the solid surfaces approach each other. *This is regulation of film thickness as well as charge density* (by the desorption of surfactant). At even smaller solid–solid separations, the segment densities (Fig. 8.14) show hydrocarbon density at all separations. The film profiles are highly distorted from those at $H = 70$ layers and it is not clear that adsorption should be treated as still occurring in two discrete layers: the surfactant layers have merged. An increase in ionic strength suppresses the film thinning until smaller separations, implying that electrostatic forces between the films on opposite surfaces promote film thinning. Remember, however, when interpreting these results that the chain flexibility is overestimated in these calculations.

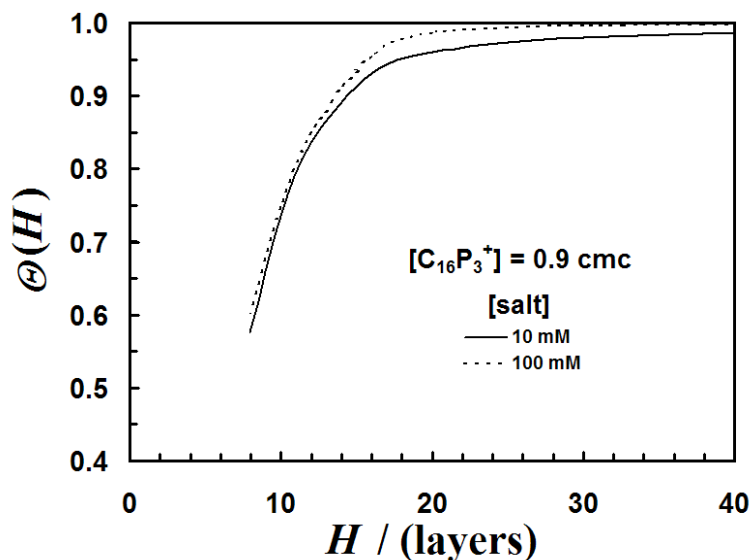


Figure 8.16 Fractional thickness of the surfactant layer as a function of solid-solid separation for the (420) surface at 0.9 cmc $C_{16}P_3^+$ (1.3 mM at $[salt] = 10$ mM and 0.25 mM at $[salt] = 100$ mM). The layer is compressed as the surfaces approach.

8.6.2 Experimental Consequences

The theoretical findings will now be related to the experimental practice of measuring surfactant layer thickness using atomic force microscopy (AFM) or the surface forces apparatus (SFA). It is common practice to use the separation at the onset of mechanical instability as an indication of the film thickness.⁹⁻¹⁴ The relationship between these parameters is complex. The mechanical instability occurs when the force gradient equals the spring constant of the AFM or SFA cantilever. This can occur for any attractive force (e.g. van der Waals) and does not require a surfactant layer. Here a different issue is explored – the extent of compression of the film thickness by an opposing solid surface at the maximum force. (Note the differences in geometry between AFM measurements and these calculations.) Assuming that the mechanical instability in force measurements occurs in the vicinity of the maximum interaction energy ($H = 8$ layers or 2.5 nm) in 1.3 mM $C_{16}P_3^+$, then equating this separation to twice the adsorbed film thickness, yields a surfactant film 4 lattice layers (1.25 nm) thick per surface. At this solid-solid separation, the film has been distorted and there is a high head-group density at all z . The film thickness of 4 lattice layers predicted from interaction energy maximum does, perhaps by

coincidence, correspond to the maximum in head group density at $H = \infty$. Furthermore, the ‘jump-in’ in AFM measurements is often interpreted as pushing off surfactant, but the confinement-induced phase transition shows that the initial attractive contribution coincides with an additional adsorption of surfactant, although further confinement does lead to desorption.

8.7 Electrolyte Adsorption/Desorption Behavior

All ions in solution contribute to the regulation of the solid–solid interaction. Here, the behavior of the inert salt ions in solution is calculated during the solid–solid interaction in order to deduce their contributions.

In Fig. 8.17a the desorption of B^- mirrors that of the surfactant, however to a smaller extent. This is because at infinite separation, the surface charge (charge from adsorbed surfactant) is largely compensated by adsorption of counter-ions and to a smaller extent by exclusion of co-ions.

As the separation between the solids is decreased, the surfactant desorbs and the co-ion exclusion (desorption) is less. This is seen as an adsorption of K^+ compared to infinite separation (Fig. 8.17). This gives a good indication of how the surfactant desorbs *without* its counter-ion, since the value of $\Delta\Gamma$ for the surfactant desorbing *without* a counter-ion is simply the negative of the change in adsorption for K^+ .

Furthermore, as the solid–solid separation decreases and the surfactant desorbs, the loss of co-ion exclusion plays a much larger role in the charge compensation because the surface potential is becoming less positive. This is expected from Poisson-Boltzmann

theory, where the ratio $\frac{\Gamma_{K^+}}{\Gamma_{B^-}}$ will go from zero at $\psi(0) = +\infty$ to unity at $\psi(0) = 0$.

Comparison of the magnitudes of the surfactant desorption with and without a counter-ion reveals an interesting phenomenon. As the surfactant desorbs, the potential becomes less positive close to the surface where the surfactant is adsorbed (see Fig. 8.11). Therefore, the surfactant counter-ion (anion) is less favored near the surface. Consequently, the counter-ion can leave more readily with the surfactant. Even though the number of surfactants that desorb *without* their counter-ion is increasing with

decreased separation, the fraction of those desorbing *without* a counter-ion actually decreases due to the increased desorption of B^- .

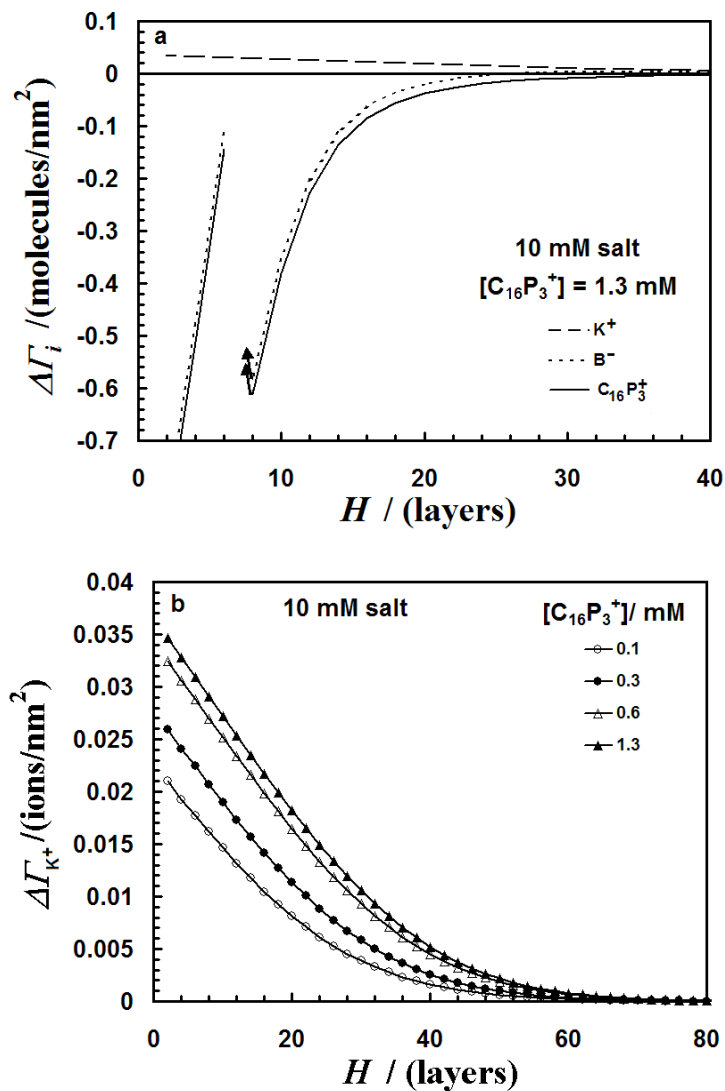


Figure 8.17 a) Change in surface excess for K^+ , B^- , and $C_{16}P_3^+$ versus solid-solid (420) separation in 10 mM salt at $[C_{16}P_3^+] = 1.3$ mM. The arrows indicate a confinement induced phase transition. b) Change in surface excess for K^+ versus solid-solid separation in 10 mM salt at different surfactant concentrations. K^+ adsorbs as the surfaces interact.

8.8 Conclusions

The adsorption of a model ionic surfactant on a neutral, slightly hydrophobic, flat surface has been studied as a function of the interaction with a second identical surface. A strong repulsive force is created by the presence of an adsorbed charged surfactant layer.

During the approach of the second solid, the adsorbed layer of surfactant responds so as to reduce the repulsive force that would otherwise occur. This response consists of desorption of surfactant and counter-ions, adsorption of co-ions, and a thinner layer of surfactant. Ultimately, the surfactant layers on the two solids begin to merge, causing a confinement-induced phase transition that leads to a large adsorption of surfactant in the gap between the surfaces.

The largest desorption of surfactant occurs at or above the surfactant concentration where there is a steep rise in the adsorption-concentration curve. Closer approach of the solids shifts the position of this steep rise to higher surfactant concentrations. The shift in this curve makes the adsorption very sensitive to the separation between the solids.

When the head-groups do not have an affinity for the solid ((031) surface), the adsorption shows an s-shaped isotherm, and is even more responsive to the approach of another solid near the step in the isotherm. A small change in separation can cause switching between branches of the adsorption curve and bring about large changes in adsorption.

The calculations show that ‘jumps’ in force measurements may be due to ‘chemical instabilities’ as well as measurement instabilities. Discontinuities in the adsorption as a function of separation will lead to discontinuities in the force. Furthermore, the confinement-induced phase transition that occurs when the surfactant layers on opposite surface merge, leads to a strong attractive force.

8.9 Cited Literature

- (1) Somasundaran, P.; Healy, T. W.; Fuerstenau, D. W. *J. Phys. Chem.* **1964**, *68*, 3562.
- (2) Grant, L. M.; Tiberg, F.; Ducker, W. A. *J. Phys. Chem. B* **1998**, *102*, 4288.
- (3) Jódar-Reyes, A. B.; Ortega-Vinuesa, J. L.; Martín-Rodríguez, A.; Leermakers, F. A. M. *Langmuir* **2003**, *19*, 878.

- (4) Böhmer, M. R.; Koopal, L. K.; Janssen, R.; Lee, E. M.; Thomas, R. K.; Rennie, A. R. *Langmuir* **1992**, *8*, 2228.
- (5) Scheutjens, J. M. H. M.; Fleer, G. J. *J. Phys. Chem.* **1979**, *83*, 1619.
- (6) Böhmer, M. R.; Koopal, L. K. *Langmuir* **1992**, *8*, 2649.
- (7) Goloub, T. P.; Koopal, L. K. *Langmuir* **1997**, *13*, 673.
- (8) Böhmer, M. R. Adsorption and Micellization of Surfactants. Ph.D. Thesis, Wageningen Agricultural University, 1991.
- (9) Pashley, R. M.; Israelachvili, J. N. *Colloids and Surfaces* **1981**, *2*, 169.
- (10) Wanless, E. J.; Ducker, W. A. *J. Phys. Chem.* **1996**, *100*, 3207.
- (11) Kékicheff, P.; Christenson, H. K.; Ninham, B. W. *Colloids and Surfaces* **1989**, *40*, 31.
- (12) Patrick, H. N.; Warr, G. G.; Manne, S.; Aksay, I. A. *Langmuir* **1999**, *15*, 1685.
- (13) Wanless, E. J.; Ducker, W. A. *Langmuir* **1997**, *13*, 1463.
- (14) Liu, J.-F.; Ducker, W. A. *J. Phys. Chem. B* **1999**, *103*, 8558.

Chapter 9

SCFA Calculations of Adsorption between Charged Surfaces

9.1 Introduction

In the previous chapter, results of SCFA calculations for ionic surfactant adsorption on uncharged solids were discussed, whereas the experiments in chapters 3–6, however, dealt with charged solids. In this chapter the behavior of ionic surfactants between two interacting charged solids is calculated with SCFA. In contrast, in the experimental measurements, the density of charged surface groups is a function of ionic strength and pH. By beginning the discussion of charged solids by adding a *fixed* surface charge while maintaining all other properties the same, the features resulting from the charge on the surface can easily be noted.

In addition, (420) surfaces in 10 mM salt are studied. The theoretical *cmc* of $C_{16}P_3^+$ is 1.43 mM at this ionic strength. The only difference in the solids presented here as opposed to the previous chapter is that that surface groups are given a fixed charge. The surface charge density, σ_0 , is determined by simply dividing the charge per surface segment by the square of the lattice site dimension.

9.2 Adsorption to Constant Charge Solids at Large Separation

Fig. 9.1 shows the calculated adsorption at large solid–solid separation as a function of the surface charge. If a constant charge (opposite to the surfactant charge) is added to the surface groups, then the shape of the adsorption isotherm changes due to a change in the adsorption mechanism (compare to $\sigma_0 = 0$ in Fig. 9.1). As the surface charge is increased, the amount of surfactant adsorbed to the surface increases due to the increased charge–charge attraction between the cationic surfactant and the negative surface charges. The first plateau is located where the adsorbed surfactant charge compensates the surface charge. This is similar to recent experimental observations on fixed charge self-assembled monolayers.¹ The total adsorption (at the *cmc*) also increases with the surface charge but the details are different to the experiments reported in reference 1.

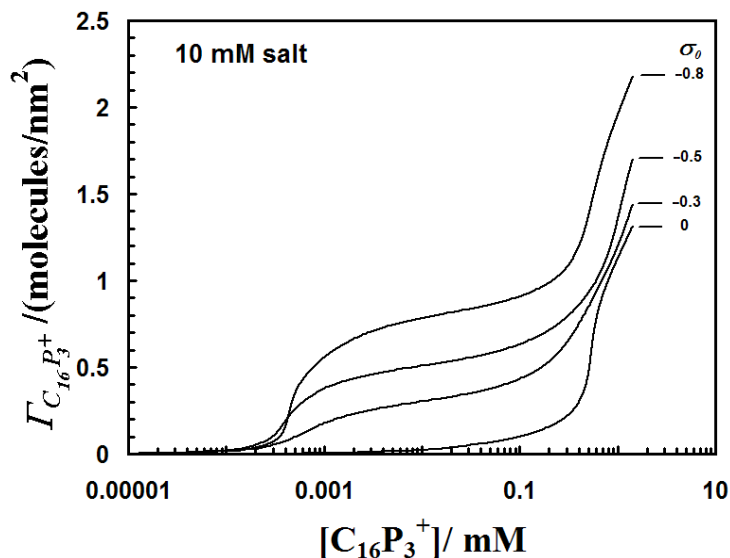


Figure 9.1 Surface excess of $C_{16}P_3^+$ as a function of $C_{16}P_3^+$ concentration on an isolated surface in 10 mM salt at various surface charges. Each curve is labeled with the surface charge of the solid in units of e / nm^2 . Adsorption increases as the surface charge is increased.

The calculated segment density profiles for the head-group and aliphatic tail segments are shown in Fig. 9.2 for concentrations below and above the charge compensation point (*ccp*). At low concentrations, the surfactant adsorbs with its head-group near to the solid (Fig. 9.2a). As the surfactant concentration surpasses the *ccp*, additional surfactant adsorbs with its head-group away from the solid. Above the *ccp* the tail density has a maximum between two concentrated head-groups regions (Fig. 9.2b). The second head-group peak occurs at $z = 6$ lattice layers, corresponding to a thickness of 1.9 nm. This is a bit thin for a C_{16} surfactant bilayer. As described in chapters 7 and 8, the extra flexibility of the aliphatic tail imparted by the Markov approximation to calculate chain conformations leads to this underestimate of the surfactant layer thickness.

Once the charge is compensated, the isotherms for the charged surfaces show similar behavior to the uncharged case. Even the segment distributions are very similar at 1.3 mM surfactant (compare with Fig. 8.3b) if the “first surfactant layer” adsorbing head down is ignored in Fig. 9.2b.

Further discussion of the adsorption of surfactants on isolated constant charge surfaces is provided by Böhmer and Koopal.² They give a more detailed account of the effects of ionic strength and chain length on the adsorption, including the electrostatic potential and charge distributions as a function of distance from the solid. Here the goal is studying the effects of the proximity of a second surface.

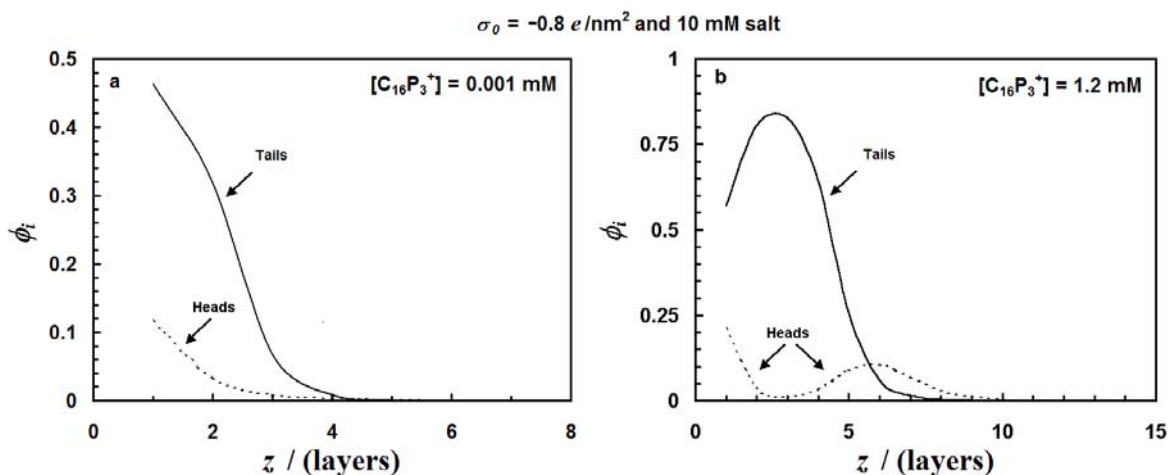


Figure. 9.2 Segment distributions near the solid for two $C_{16}P_3^+$ concentrations for an isolated ($H = 90$), constant charge surface. **a)** At low concentrations ($< c_{cp}$), the surfactant lays almost flat on the surface with both the head groups and tails in the first three layers. Note: there are 16 tails segments for every 3 head segments. **b)** At higher concentrations ($> c_{cp}$), the head-groups are concentrated in two distinct regions, and the tail density is a maximum at an intermediate distance.

9.3 Effect of Surface Charge on Solid-Solid Interactions

At constant bulk surfactant concentrations, the magnitude of the surface charge effects on the interaction energy of the solids as well as the adsorption of the surfactant is calculated. Fig. 9.3 shows the interaction free energies and changes in surface excess for the same two surfactant concentrations as in Fig. 9.2. For simplicity, only the portion of the curve at separations is shown. At smaller separations, a confinement-induced phase transition (as mentioned in chapter 8) occurs. These phase transitions will be discussed in the next section.

In general, the interaction energy increases (the force is more repulsive) at higher surface charge, but the relationship is complex. For example, the interaction energy for $-0.3 e/\text{nm}^2$ is slightly greater than for $-0.5 e/\text{nm}^2$. Table 9.1 shows the potential at various locations within the surfactant film. The trend in electrostatic potential at the outer edge of the surfactant film ($z = 4$) correlates better with the interaction energy than does the potential at $z = 1$. A similar trend is observed at other concentrations (described below).

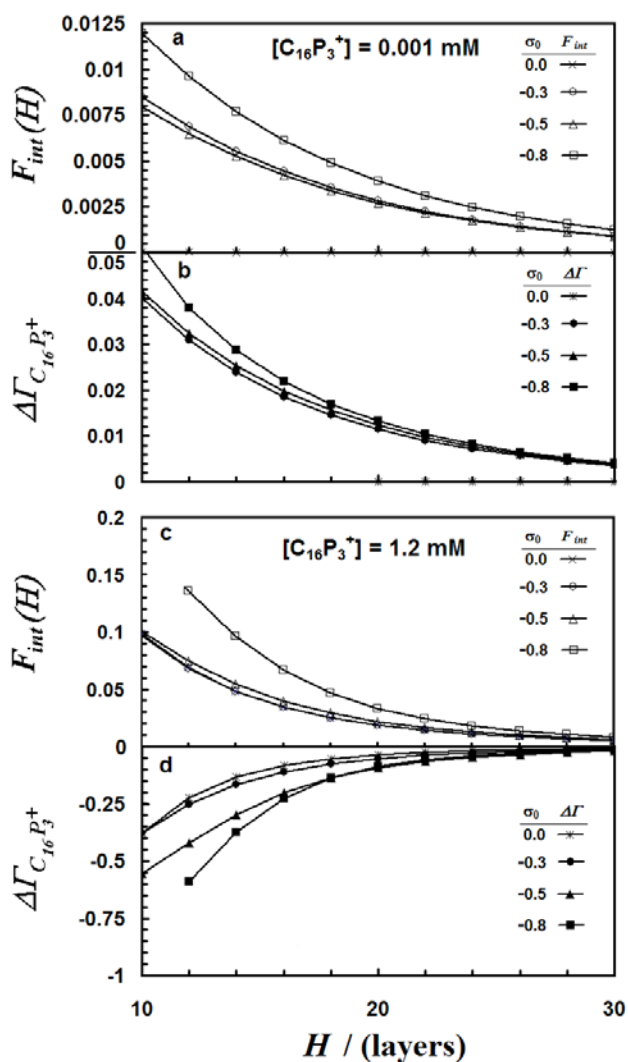


Figure 9.3 Interaction free energy (in units of $k_B T/\text{lattice site}$) and change in $C_{16}P_3^+$ adsorption (in units of molecules/ nm^2) as a function of solid-solid separation for a series of constant charge surfaces in 10 mM salt. **a) and b)** $[C_{16}P_3^+] = 0.001$ mM (below the ccp). The energy of interaction is greater for higher surface charge densities. The surfactant adsorbs as H decreases. **c and d)** $[C_{16}P_3^+] = 1.2$ mM (above the ccp). As the surface charge is increased, the interaction energy becomes more repulsive, and the magnitude of the proximal adsorption increases. The curve at $-0.8 e/\text{nm}^2$ is truncated at $H = 12$ layers because at this separation a phase transition occurs as seen in Fig. 9.5.

Below the *ccp*, the surfactant adsorbs as the solid surfaces approach. This adsorption decreases the electrostatic potential compared to no additional adsorption, thereby lowering the energy of the system.

At concentrations above the *ccp*, but below the *cmc*, the interaction energy is larger for greater surface charge densities (Fig. 9.3c). Again, the magnitude of the interaction energy roughly tracks the potential at the outer edge of the surfactant layer at infinite separation (See $\psi_z = 6$ in Table 9.1). Above the *ccp*, the potential at $z = 6$ is positive because of the high density of adsorbed surfactant, so a reduction in H leads to desorption of surfactant in order to reduce the electrostatic energy. The increase in potential above the *ccp* with surface charge arises from the following mechanism. The large surface charge increases the density of head segments in $z = 1$ and therefore the number of tail segments in the next few layers. Further adsorption is favored by the ability of the surfactant to have additional C-C interactions in layers $2 < z < 4$. Additional adsorption in excess of the *ccp*, thereby increases the potential at $z = 6$. This is shown in Fig. 9.4.

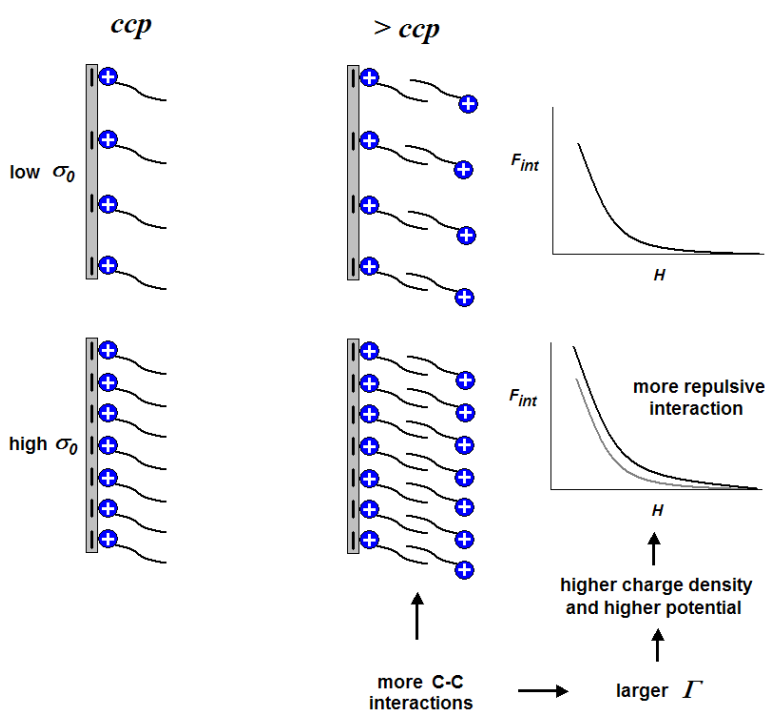


Figure. 9.4 Schematic depicting the effect of the surface charge (σ_0) on the adsorption and resulting interaction above the *ccp*.

Although the inhomogeneity of the charge density and dielectric constant *perpendicular* to the surface produce a complex profile of the potential through the surfactant layer, the trends in interaction energy follow the trends in potential at $z = 6$. This is consistent with the common experimental practice of using a zeta potential measurement to estimate the double-layer force contribution to colloidal stability at large separations, provided that the shear plane is not within the surfactant layer. Furthermore, the estimation of a ‘surface’ potential at the outer layer of the surfactant at infinite surface separation from experimental surface force measurements is consistent with the calculations presented here.

Table 9.1. Electrostatic potential at large H as a function of surface charge density.

	$\sigma_0 / (e/nm^2)$			
	0.0	-0.3	-0.5	-0.8
$[C_{16}P_3^+] = 0.001 \text{ mM}$				
$\psi_{z=1}/(\text{mV})$	+2.8	-75.2	-89.3	-130.3
$\psi_{z=4}/(\text{mV})$	+2.0	-43.3	-42.6	-53.0
$[C_{16}P_3^+] = 0.01 \text{ mM}^*$				
$\psi_{z=1}/(\text{mV})$	+58.7	-10.8	-30.5	-81.6
$\psi_{z=4}/(\text{mV})$	+41.8	+4.90	+6.53	-1.72
$\psi_{z=6}/(\text{mV})$	+32.0	+4.12	+5.85	+0.57
$[C_{16}P_3^+] = 1.2 \text{ mM}$				
$\psi_{z=1}/(\text{mV})$	+144.7	+106.4	+91.3	+98.0
$\psi_{\phi_{P \max}}/(\text{mV})^a$	+130.4	+128.1	+125.4	+131.7
$\psi_{z=6}/(\text{mV})$	+103.4	+104.2	+112.8	+131.7

Electrostatic potential values are given for layers $z = 1$ and $z = 4$ for $[C_{16}P_3^+] = 0.001 \text{ mM}$ and at $z = 1, 4$, and 6 for $[C_{16}P_3^+] = 0.01 \text{ mM}$. At $[C_{16}P_3^+] = 1.2 \text{ mM}$, electrostatic potentials are given for layers $z = 1$, the layer where the density of head-groups is a maximum, and layer $z = 6$. *concentration corresponding to the common intersection in Fig. 9.5a. ^a $\psi_{\phi_{P \max}}$ occurs at $z=4$ for $\sigma_0 = 0.0$, $z=4$ for $\sigma_0 = -0.3$, $z=5$ for $\sigma_0 = -0.5$ and $z=6$ for $\sigma_0 = -0.8 \text{ e/nm}^2$.

9.4 Adsorption and Phase Transitions in Confined Films

In this section all data is for a surface charge density of $-0.8 e/\text{nm}^2$. The calculated adsorption isotherms in 10 mM salt and a constant surface charge of $-0.8 e/\text{nm}^2$ are shown in Fig. 9.5 for various solid-solid separations, H . The isotherms for $H > 16$ lattice layers are shown in Fig. 9.5a. At surfactant concentrations less than about 1 mM, there is only a small amount of proximal adsorption, and the proximal adsorption is divided into two regimes by a concentration at which the adsorption is independent of separation (0.01 mM). At this concentration, the potential outside the surfactant layer is very small, so each surface has a weak influence on the other surface (the potentials are given in Table 9.1). At other concentrations, proximal adsorption occurs to reduce the double-layer potential. At lower surfactant concentrations, the potential on each isolated surface is negative, so the surfactant adsorbs as the surfaces approach. At $[\text{C}_{16}\text{P}_3^+] > 0.01$ mM, the surfactant desorbs as the separation decreases. The inset of Fig. 9.5a shows this trend more clearly. A common intersection of isotherms as a function of separation is also present according to experimental data (Fig. 5.10), where the interaction energy is a minimum with respect to concentration.

The isotherms for $H < 16$ layers are shown in Fig. 9.5b. Each of these isotherms has a phase transition that occurs at small separations, as a consequence of the loop in the isotherm ($H = 6$, the loop has been omitted for clarity at $H = 12, 10$, and 8 layers). For example, at $H = 6$ the dashed line represents meta-stable and unstable regions of the isotherms. The solid vertical line divides the calculated isotherm into two regions of equal area, $\int \mu d\Gamma$, and thus connects the stable branches of the isotherm. The phase transition is similar to the confinement-induced phase transitions shown in the previous chapter. Two different, but stable surface excess values occur at the binodal concentration (vertical step in the isotherm).

As drawn, the phase transition is seen to be transition from a low-density structure to a high-density structure when the bulk concentration is increased at constant separation between the solids. If bulk concentration is kept constant and the separation is changed (along the dotted vertical line in Fig. 9.5b), the phase transitions are induced at a critical separation (binodal separation). This phase transition is initiated when the surfactant layers on opposite surfaces come into contact and there is a possibility of a large number

of C-C contacts. In so far as the χ_{CW} is designed to model the hydrophobic effect, the phase transition is induced by the hydrophobic effect. The phase transition leads to a discontinuity in the gradient of the interaction energy at the binodal separation. At $H <$ binodal separation, an attractive contribution to the interaction occurs. This behavior has been noted previously in SCFA calculations involving polymer-coated surfaces, where an attraction is seen as the solvophobic chains on opposite surfaces merge.^{3,4} Such behavior is analogous to the experimentally observed lateral organization of surfactant into hemimicelles or micelles that occurs when alkyl chains reach a sufficient density.

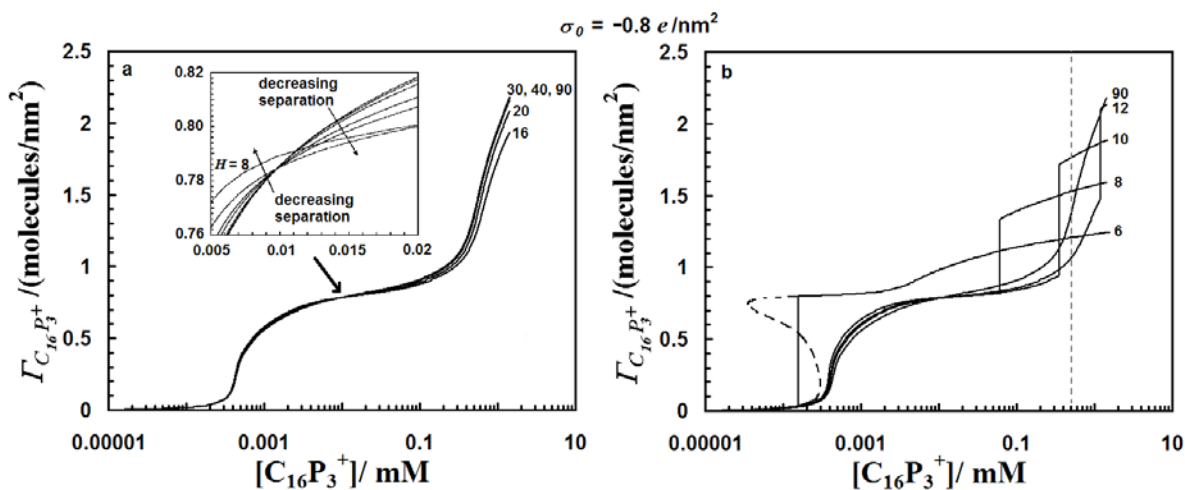
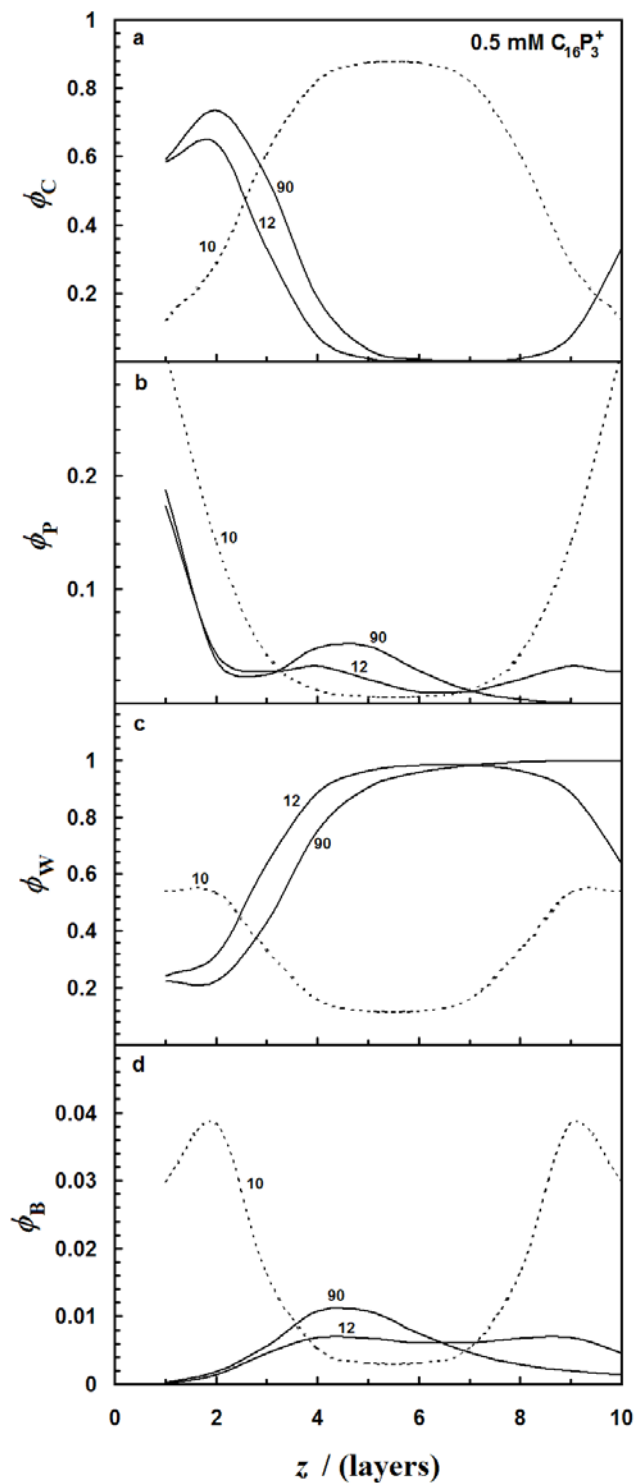


Figure. 9.5 Surface excess as a function of $C_{16}P_3^+$ concentration at various solid-solid separations on a constant charge ($-0.8 e / nm^2$) surface in 10 mM salt. The separation is listed next to the respective curve in units of lattice layers. **a)** Isotherms at larger separations. The cip is marked by the arrow. Below the cip, the amount adsorbed increases as the separation is made sufficiently small. Above the cip the surface excess decreases as the solid-solid separation is decreased. The inset shows the data around the cip. The inset also includes data at $H = 12, 10,$ and 8 layers. The adsorption is essentially constant (to within 1%) until the separation falls below about 30 layers $\sim (3\kappa^{-1})$. **b)** Isotherms at small confinements. Each isotherm shows a condensation loop as the result of a first-order phase transition. An example of such a loop is shown at $H = 6$ lattice layers. The dashed line represents meta-stable and unstable portions of the curve. The solid vertical lines connect the stable portions of each isotherm. The location of the phase-transition moves to lower concentrations upon further confinement. The dotted vertical line indicates the concentration that is explored in Fig. 9.6.

At higher concentrations the surfactant layers are thicker and the surfactant layers merge at larger solid–solid separations. Therefore, the phase transitions occur at larger separations (Fig. 9.5b). When the concentration is increased, the phase transitions once again go from low to high surface excess. As a function of separation, the phase transition also goes from a low to a high surface excess, but subsequent confinement reduces the surface excess again. The change in sign of the adsorption gradient as a function of separation is the result of competition between electrostatic forces, which are driving desorption of the surfactant and the replacement of C-W contacts with C-C contacts, which drives adsorption. Fig. 9.6 shows the calculated densities of all segments (except K, whose density is very small here) at 0.5 mM $C_{16}P_3^+$. From the isotherms in Fig. 9.5, the confinement–induced phase transition occurs between $H = 12$ and $H = 10$ layers. At this concentration, the surfactant layers go from a thinned bilayer on each surface with an aqueous phase in between to a more-dense bilayer between the surfaces with an aqueous region near each surface. The consequences of this adsorption behavior are shown in the calculated interaction energies in Fig. 9.7.

In Fig. 9.7 the interaction energies and changes in adsorption are plotted versus separation for the low concentration (a and c) and the high concentration (b and d) regions. Because the calculation uses space divided into a lattice, only discrete separations are accessible and the phase transitions often occur between these separations. The separation at which the phase transition occurs (binodal separation) depends upon the bulk concentration as shown in Fig. 9.5. At low surfactant concentrations ($< c_{cp}$), the phase transition occurs when H is reduced to 6 layers. The transition is from a low surface excess to a surface excess that is similar to the charge compensation point; i.e. the transition occurs so as to make the surfactant approximately neutralize the surface charge. These changes in surface excess are shown more clearly in Fig. 9.7c. Large adsorption of surfactant at sufficiently small separations has also been noted experimentally on hydrophilic surfaces in chapters 3–5 and in the literature.⁵⁻⁹ In addition, note that each time the surface excess jumps to a higher value as a result of a confinement–induced phase transition, the interaction shows a strong attraction similar to that observed in chapter 8 for neutral solids.



$H >$ binodal separation

$H <$ binodal separation

Figure 9.6 Density profiles and schematic of the behavior near the confinement induce phase transition for $0.5 \text{ mM } C_{16}P_3^+$. In a-d, each curve is label with the separation, H in lattice layers. At the phase-transition, individual layers on each solid merge to form a more-dense bilayer between the solids. Note also that the aqueous regime moves from between the surfactant layers to adjacent to the solids.

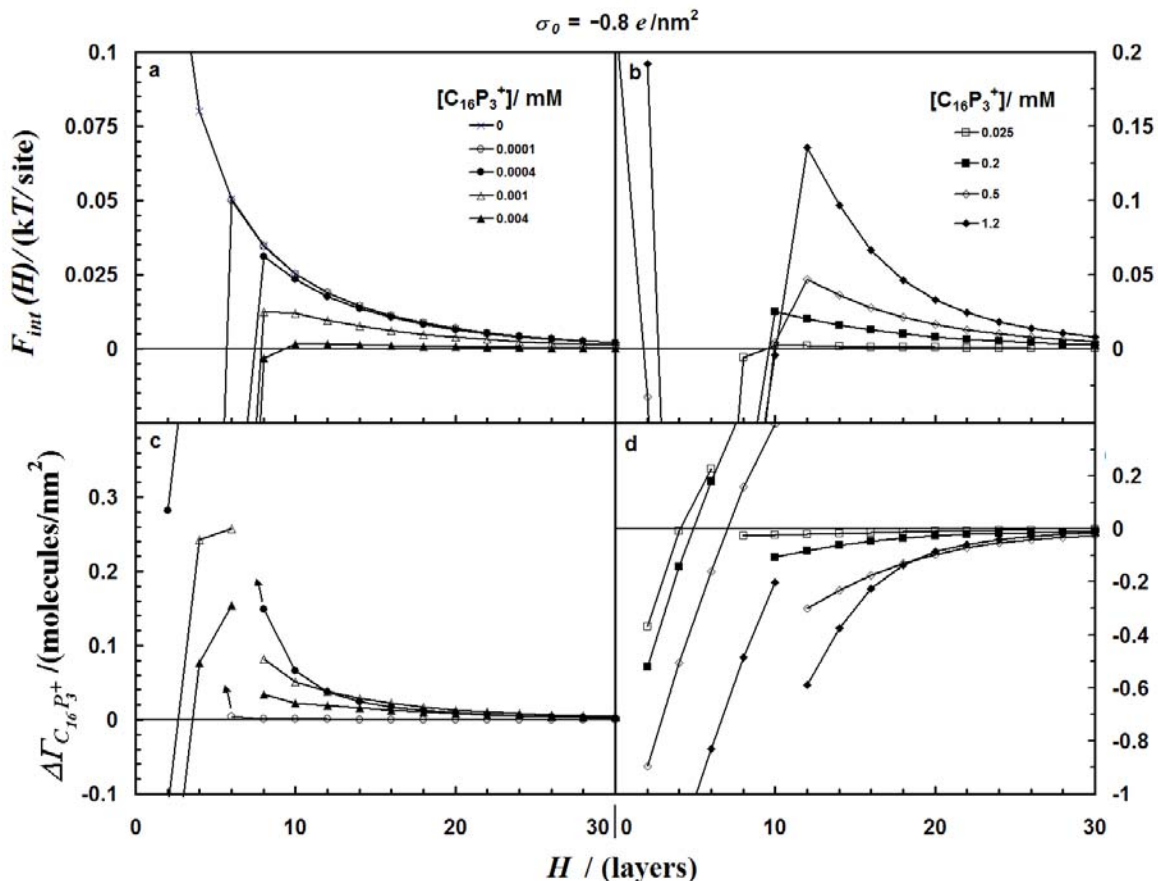


Figure 9.7 Interaction energies and changes in $C_{16}P_3^+$ adsorption as a function of solid-solid separation for a constant charge ($-0.8 e / nm^2$) surface in 10 mM salt. **a)** Interaction Energy, F_{int} , as a function of separation, H , and concentration below the ccp. The interaction becomes less repulsive with increased surfactant concentration and the phase transition shifts to larger separations. Due to the discretization of our system, the discontinuity in the slope is shown at integer values of H , when in fact the transition will lie between these two stable values. **b)** F_{int} above the ccp, the interaction becomes more repulsive with increasing surfactant concentration. **c)** Proximal adsorption, $\Delta\Gamma$, of surfactant below the ccp. The surfactant adsorbs with decreasing separation at $H > 6$ layers. The arrows indicate a large condensation off scale. **d)** $\Delta\Gamma$ above the ccp. The surfactant desorbs with decreasing separation at $H > 10$ layers. The discontinuities in the surface excess correspond to the discontinuity in the slope of the interaction energies in a and b. At the phase-transition there is a vertical step in the surface excess.

9.5 Electric Potential versus Separation

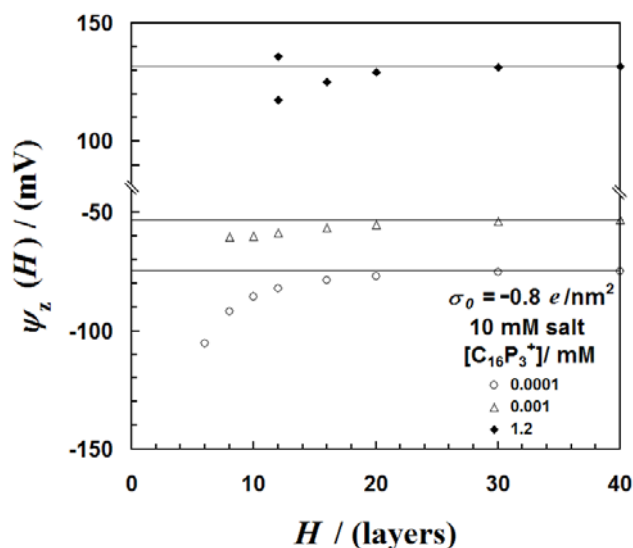


Figure 9.8 Electrostatic potential outside the surfactant layer in 10 mM salt vs solid-solid separation, H , at different concentrations. The charge on the solid is held constant at $-0.8 e/\text{nm}^2$. The solid lines represent the values at large H . For 0.0001 and 0.001 mM the values are at $z = 4$, whereas for 1.2 mM the values are at $z = 6$. The multiple values at $H = 12$ layers for 1.2 mM occur due to a surface induced phase transition. As H decreases the electrostatic potential decreases becomes more negative.

The SFA or AFM (using the colloidal probe technique) is often used to measure surface forces in surfactant solution.¹⁰ It is common practice to fit theoretical double-layer forces to measured double-layer forces at separations where the overlap of the double-layers drives changes in adsorption and surface charge (charge regulation).¹¹ This procedure is usually performed in order to infer the existence of additional forces. Very frequently, researchers assume that the lowest energy double-layer interaction occurs when the surface potential is held constant. Fig. 9.8 shows the electrostatic potential for both low and high surfactant concentrations. At low concentrations the potential at $z = 4$ (outside the adsorbed layer) increases in magnitude as H decreases. As the concentration nears the *ccp*, the interaction approaches constant potential. Above the *ccp*, the potential decreases in magnitude with the separation. As described above, the important value is at $z = 6$ because this determines the double-layer force. *The lowest energy interaction*

clearly occurs when the potential decreases as the separation decreases. This result clearly contradicts the ‘principle’ that constant potential is a lower bound for double-layer forces in the presence of surfactant.

Note that the bifurcation of the potential at $H = 12$ arises because of a phase transition: the potential is different in each phase. This model, however, does not allow for structure within each lattice layer (variation in structure parallel to the interface). Note that if patches of different potential are present on both surfaces, and if they are free to migrate, correlations will lead to attractive forces as described previously.¹² Also, breaking of symmetry through creation of different potential on each surface will also lead to a less repulsive force.

9.6 Regulation of the Surfactant Layer Thicknesses

It is quite common to use experimental force measurements to understand the structure of the adsorbed layer. If the adsorbed layer structure and amount is changing as a function of separation, one should be careful when relating measurements on a confined layer to conclusions about the isolated solid–liquid interface. Such behavior will now be discussed.

In the previous chapter it was shown that, on a neutral surface, the same forces that cause changes in the adsorption can also cause a thinning of the adsorbed surfactant layer. As before, a separation dependent thickness of the adsorbed layer, $t(H)$ is defined. Since the surfactant adsorbs head down in the first layer, below the *ccp*, $t(H)$ is defined as the number weighted average location of the tail segments.

Above the *ccp*, where there is also surfactant adsorbed with its head-group facing the solution, $t(H)$ is defined as the number weighted average head-group density of the head-group peak at larger z (Fig. 9.2b). Fig. 9.9 shows how the layers respond to a change in solid–solid separation for concentrations above and below the *ccp*. At $[C_{16}P_3^+] = 0.001$ mM, the surfactant layer becomes thicker as the solids come together. This is consistent with the extra absorption that occurs. The thickening also means that the surfactant layers come into contact at a greater solid–solid separation than would be predicted from the film thickness on an isolated surface.

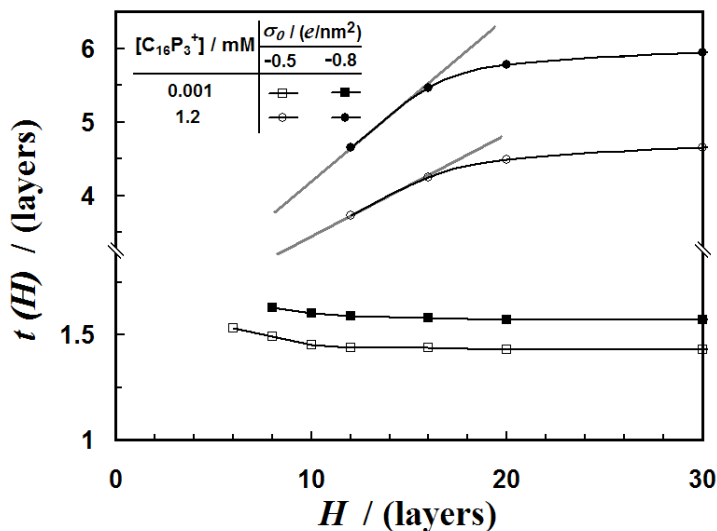


Figure 9.9 Thickness of surfactant layers adsorbed on the solid surface as a function of solid-solid separation, H in 10 mM salt. For $[C_{16}P_3^+] = 0.001$ mM, the layer thickness increases with decreasing H for both surface charges. For $[C_{16}P_3^+] = 1.2$ mM, the layer thicknesses decrease with decreasing H for both surface charges. All values shown here are at large enough separations that a surface-induced phase transition does not occur. The gray lines denote the gradient of thickness with separation. Note: the data scales are different above and below the axis split.

At $[C_{16}P_3^+] = 1.2$ mM, the surfactant layers become thinner as the solids come together. The thinning is consistent with the proximal desorption of the surfactant, which is driven by the electrostatic repulsion between head-groups on opposite solids. This is shown by the larger gradient of thinning for the higher potential $\sigma_0 = -0.8$ e/nm² surface. In addition, the behavior is similar to the neutral surfaces in the previous chapter, where the surfactant head-group repulsions also drive proximal desorption of $C_{16}P_3^+$.

9.7 Proximal Adsorption of Salt

As in chapter 8, the proximal adsorption of salt is calculated. Here, however, the behavior is complicated by the fact that the surfaces pass from negatively charged to positively charged as the surfactant adsorption neutralizes the surface and then recharges it as a result of the surfactant head-group charge. In dilute solution, when the surfactant

density is low, the surfactant behaves similarly to a simple electrolyte (like K and B). If, however, the tails can interact with each other and promote additional surfactant adsorption (i.e. at or above a step in the isotherm), it can be expected that this will have a profound effect on the balance of ions near the surface. In Fig. 9.10 the density of the cationic K segments, ϕ_K , near the surface is plotted when the potential near the surface is negative. Two cases are considered: when the surfactant concentration is below the first step in the isotherm, $[C_{16}P_3^+] = 0.0001$ mM (no tail association) and when it is above the first step in the isotherm, $[C_{16}P_3^+] = 0.001$ mM (significant tail association). At 0.0001 mM, K *adsorbs* as H decreases, relieving the overlap of electrical potential near the surface. At 0.001 mM, K *desorbs* with decreasing H , which would on its own increase the potential between the surfaces. The reason for this behavior is that the surfactant proximal adsorption is so large that it decreases the potential causing the cation to be less favored near the surface. In previous chapters, similar surfactant adsorption in excess of charge regulation has been observed experimentally above the step in the isotherm for cationic surfactants on glass.

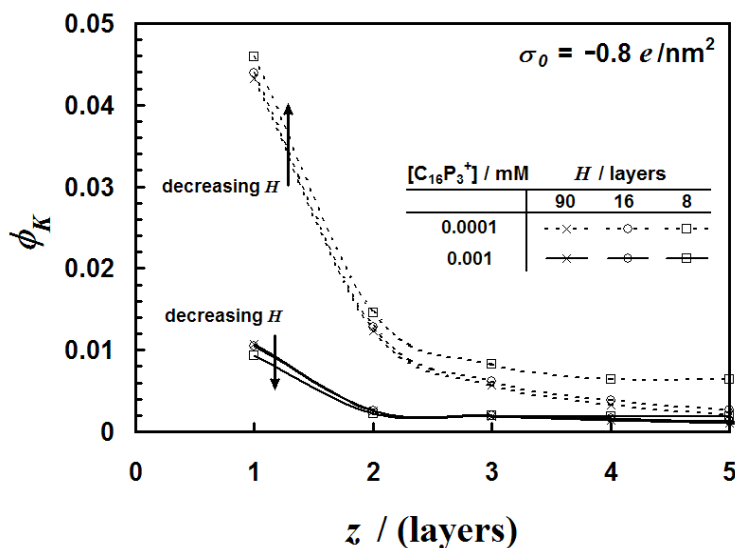


Figure 9.10 Density profile of K segments in the vicinity of the solid surface at various solid-solid separations for 0.0001 mM (dotted line) and 0.001 mM $C_{16}P_3^+$ (solid line) in 10 mM salt. At $[C_{16}P_3^+] = 0.0001$ mM, the density of K increases as H is decreased, whereas at $[C_{16}P_3^+] = 0.001$ mM, the density of K decreases as H is decreased.

9.8 Effect of Surfactant Chain Length

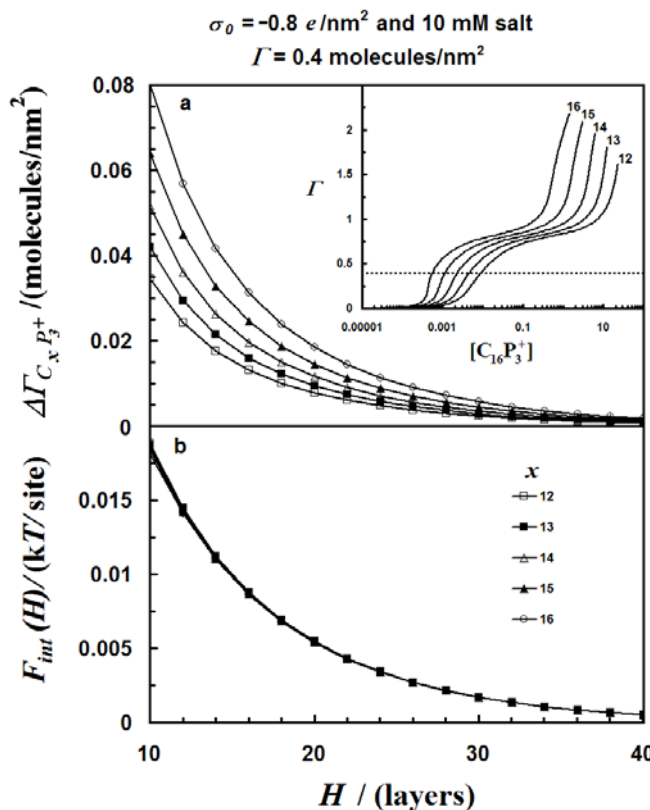


Figure 9.11 Changes in surfactant adsorption and interaction energies vs H for various surfactant chain lengths for a constant surface excess of $0.4 \text{ molecules/nm}^2$. The inset shows complete isotherms for different chain lengths, $x = 12-16$. The dotted line indicates the region, where the interaction and $\Delta\Gamma$ have been calculated. $\Delta\Gamma$ clearly scales with the chain length, however, the interaction energies are about the same.

Since the alkyl chain is the key difference between surfactants and simple ions, in this section the effect of changing the alkyl chain length of surfactant is briefly examined. The adsorbed amount at a given surfactant concentration is clearly a function of chain length (see inset to Fig. 9.11a) so there is a choice of different conditions that can be held constant when comparing different surfactant chain lengths. Here, the proximal adsorption of surfactants of different alkyl chain lengths are compared at the same surface excess at infinite separation ($0.4 \text{ molecules/nm}^2 \sim ccp/2$). The bulk concentration for each surfactant is adjusted to reach this surface density. Fig. 9.11a shows the proximal adsorption for chain lengths of 12–16 C units. The proximal adsorption clearly increases with chain length, which is consistent with the experimental measurements in chapters 4 and 5. The longer chain makes the surfactant adsorption more sensitive to changes in the local conditions at the interface. This effect is also apparent in the isolated adsorption

isotherm (inset to Fig. 9.11a), where the slope of the adsorption is greater for a longer chain length.

Fig. 9.11b shows the interaction energy as a function of separation for the same conditions as for the proximal adsorption data in Fig. 9.11a. Although the proximal adsorption of surfactant is a strong function of the chain length, the interaction energy is relatively independent of the chain length, *when comparing curves of identical surface excess at infinite separation*. The other ions (K and B) are adsorbing and desorbing such that the net force and charge regulation are almost independent of the chain length. By choosing the same adsorption of surfactant at infinite separation, most of the difference in chain length has been accounted for by changing the chemical potential in solution.

9.9 Conclusions

Increasing the charge on the solid leads to an increase in the surfactant adsorption at all concentrations. The interaction energy is governed by the potential at the outer (solution-side) boundary of the adsorbed layer and occurs below constant potential conditions above the *ccp*. Therefore, the proximal adsorption is also driven by the potentials at the outer (solution-side) boundary of the adsorbed layer.

During confinement, the adsorbed layer approaches the structure found at the *ccp*. *Below the ccp*, the surfactant adsorbs with decreasing separation between the solids. This added adsorption leads to a thickening of the surfactant layer. At sufficient confinement, additional C-C interactions contributed by merging surfactant layers adsorbed on opposite solids leads to a phase-transition, whereby the surface excess can jump from very low coverages to monolayer-like levels. *Above the ccp*, an increase in surfactant concentration leads to an increased interaction energy between the solids and desorption of the surfactant as H is decreased down to the binodal separation. In order to regulate the repulsive interaction, surfactant desorbs and the surfactant layer thins. As the hydrocarbon tails merge at these higher concentrations, a phase-transition occurs taking the surface excess toward bilayer coverages depending upon concentration and separation. At sufficient confinement, the increase in electrostatic repulsion in the gap between the surfaces leads to subsequent desorption of the newly adsorbed layer.

The merging of surfactant layers and subsequent phase-transitions account for the discontinuous slope in the interaction energy and the discontinuous adsorption profiles as a function of separation. Similar for the neutral solids, the calculations indicate that ‘jumps’ in force measurements may be due to ‘chemical instabilities’ as well as measurement instabilities. The confinement-induced phase transition that occurs when the surfactant layers on opposite surface merge, once again, leads to a strong attractive force.

Furthermore, below the first step in the isotherm, all ions adsorb with decreased separation (down to the binodal separation). At the first step in the isotherm, a critical density of surfactant is reached on the surface and the surfactant undergoes the largest proximal adsorption. In fact, the proximal adsorption of surfactant is so large that the co-ions now desorb. The magnitude of the potential increases slightly as the separation decreases. The proximal adsorption of surfactant scales with the surfactant chain length. Above the *ccp*, the surface charge and potential are created by the surfactant, and the potential at the edge of the surfactant film decreases in magnitude as the separation is decreased.

Finally, the effects of proximal adsorption and proximity-induced phase transitions should be considered when interpreting experiments involving significant forces between and confinement of colloidal surfaces.

9.10 Cited Literature

- (1) Tulpar, A.; Ducker, W. J. *Phys. Chem. B* **2004**, *108*, 1667.
- (2) Böhmer, M. R.; Koopal, L. K. *Langmuir* **1992**, *8*, 1594.
- (3) Singh, C.; Balazs, A. C. *J. Chem. Phys.* **1996**, *105*, 706.
- (4) Singh, C.; Pickett, G. T.; Zhulina, E.; Balazs, A. C. *J. Phys. Chem. B* **1997**, *101*, 10614.
- (5) Subramanian, V.; Ducker, W. J. *Phys. Chem. B* **2001**, *105*, 1389.
- (6) Lokar, W. J.; Ducker, W. A. *Langmuir* **2002**, *18*, 3167.
- (7) Lokar, W. J.; Ducker, W. A. *Langmuir* **2004**, *20*, 378.
- (8) Rutland, M. W.; Parker, J. L. *Langmuir* **1994**, *10*, 1110.
- (9) Yaminsky, V. V. *Langmuir* **1994**, *10*, 2710.
- (10) Kékicheff, P.; Christenson, H. K.; Ninham, B. W. *Colloids and Surfaces* **1989**, *40*, 31.
- (11) Ninham, B. W.; Parsegian, V. A. *J. Theor. Biol.* **1971**, *31*, 405.
- (12) Tsao, Y.-H.; Evans, D. F.; Wennerström, H. *Science* **1993**, *262*, 547.

Chapter 10

Summary and Future Work

10.1 Introduction

The adsorption of surfactant on solid surfaces depends on the distance between the two solids when they are in close proximity. This process is important because it affects the forces between the solids and the stability of colloidal suspensions of these solids. In this thesis, the adsorption of surfactants has been studied between two interacting silica-like surfaces. Atomic Force Microscopy (AFM) was used to measure interaction forces by the colloidal probe technique outlined in chapter 2. These interaction forces were measured as a function of surfactant concentration in various electrolyte solutions and at two different surfactant chain lengths. A Maxwell relation (eq. 1.22) was applied to the AFM data to gain quantitative information about how the surface excess of surfactant ions changes as two surfaces approach each other in aqueous solution. From that information, several key mechanistic features of our systems could be inferred. In addition, an equation of state that enables coupling of electric forces to the short-range hydrophobic effect was proposed.

In chapters 7-9, Self-Consistent Field (SCF) calculations were used to calculate behavior in surfactant systems. The calculations confirmed several experimental results as well as enabled the exploration of behavior that is not easily studied experimentally. In particular, the calculation of surfactant density profiles enabled structural information to be obtained as a function of solid–solid separation. In addition, the behavior of the electrolyte could be followed during the interactions. The ability to calculate density profiles allowed the behavior near the maximum interaction energy to be explored in detail, contributing to a new understanding of experimental force measurements.

In this chapter, the experimental and theoretical results will be tied together. In addition, avenues for future work in this area will be proposed.

10.2 Predicting Interactions from Adsorption Isotherms

From the work presented in this thesis, a general rule of thumb for determining interactions between colloidal particles in surfactant solutions can be developed from the

adsorption isotherm of an ionic surfactant on a solid surface. Fig. 10.1 shows a general adsorption isotherm divided into 4 regions. The first three regions are the same as discussed previously, and the fourth is above the *cmc*.

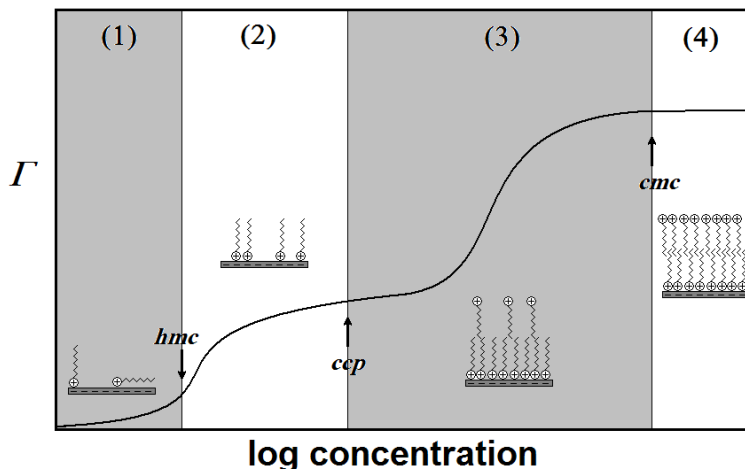


Figure 10.1 General isotherm for ionic surfactant adsorption onto an oppositely charged surface. The isotherm is broken into 4 regions. In region (1), surfactant is adsorbed sparsely on the surface. In region (2), surfactant tails can interact, however, the Stern layer charge is still negative. In region (3), the surfactant forms a partial second layer and the Stern layer charge is positive. In region (4), the adsorption changes little with concentration just above the *cmc*.

10.2.1 Region (1): $[\text{Surfactant}] < hmc$

In region (1), the density of surfactant is very low and charge regulation is dominated by the excess of cations in electrolyte solutions. The range of the interaction is governed by the ionic strength in solution. Furthermore, at lower ionic strengths, the upper concentration boundary of this region (*hmc*) shifts to lower concentrations. As two identical surfaces approach, the interaction becomes repulsive at a separation of approximately three Debye-lengths. The electrostatic interaction is monotonically repulsive down to contact and completely reversible upon retraction.

The work of Parker and Rutland,^{1,2} however, suggests that if the particles are able to remain in contact for large periods of time that a strong attraction could develop at very close solid-solid separations ($< 3 \text{ nm}$). In a colloidal suspension, it is unlikely that the

particles will come into contact as the activation barrier is on the order of $100 \text{ k}_B\text{T}$ per nm^2 of contact area.

10.2.2 Region (2): $hmc < [\text{Surfactant}] < ccp$

When the surfactants associate on the surface (above the hemi-micelle concentration), the surfactant can influence the interactions significantly. As the separation decreases, the interaction is repulsive and becomes significant around $3\kappa^{-1}$. The interaction becomes more repulsive with decreased separation until a critical separation that is on the order of twice the adsorbed layer thickness. This is not, however, twice the layer thickness for an isolated surface because the surfactant layer thickens as the surfaces approach due to increased adsorption. At this critical separation, a strong attractive component to the interaction is present and the surfaces collapse together. Upon separation, a strong attraction is present that must be overcome by a strong tensile force.

The magnitude of the repulsive interaction decreases with increased concentration up to the *ccp*, where the net charge on each interface is approximately zero. Furthermore, the critical separation where the strong attraction takes place shifts to larger separations in accordance with more adsorbed surfactant at higher surfactant concentrations. Raising the surfactant concentration up to the *ccp*, leads to an increase in the force required to separate the surfaces from ‘contact’.

At the *ccp*, SCFA calculations show that the force is short-ranged as expected: there is no net charge to communicate a long-ranged force. In addition, the mean-field approximation excludes the possibility of induced dipoles on the surface. Experiments, however, reveal strong attractive force in excess of the van der Waals attraction. This attraction occurs at concentrations within the first plateau in the isotherm. Therefore, at lower ionic strengths, when the plateau extends over a larger concentration range, these strong attractions also extend over the same larger concentration range. Furthermore, since the *ccp* does not shift due to ionic strength, region (2) extends over a larger concentration range at lower ionic strengths. This was especially apparent in the work of Subramanian and Ducker.³ The true mechanism of the strong attraction near the *ccp* remains controversial in colloidal science. In this thesis, these attractions show an exponential decay with distance, which is consistent with electrostatic forces, although

the attractions in 1 mM salt are of much shorter range than the Debye-length. Other work, however, does not show this behavior. The origin of the attractions in this thesis could be the existence of slightly different charge compensation points on the two approaching surfaces. The existence of phase-transitions in the SCFA calculations, suggests that this may be a possible mechanism, however, the phase-transitions in this work occur at much smaller separations.

10.2.3 Region (3): $ccp < [Surfactant] < cmc$

After the charge is compensated by the surfactant and the Stern charge becomes positive in region (3), a repulsive interaction occurs as the surface approach. Once again the interaction becomes more repulsive down to a critical separation, where a strong attraction is present that pulls the surfaces together. As the surfaces are separated, a strong tensile force is once again required to separate the surfaces.

Indeed, the behavior in region (2) and region (3) is very similar except for the concentration dependence. As the surfactant concentration increases in region (3), the positive potential increases and the repulsive interaction becomes stronger up to the *cmc*. Therefore, if the interaction is known in an unknown concentration of cationic surfactant, then to determine if the system lies in region (2) or region (3), either the sign of the Stern potential (or zeta potential) is required, or the system must be diluted slightly and the trend in interaction noted. If dilution by a small amount leads to a decrease in the interaction, then the original system lies in region (3).

10.2.4 Region (4): $[Surfactant] > cmc$

Just above the *cmc*, the interaction is strongly repulsive, with a strong attraction present at a critical separation of approximately twice the surfactant chain length. Here, the interaction does not change much with a change in concentration, because the adsorbed amount changes little and the chemical potential of the surfactant is relatively unaltered by small perturbations in the system. At concentrations far above the *cmc*, oscillatory forces have been measured by Subramanian and Ducker³ as bulk micelles are successively depleted from the interaction zone. Furthermore, the strong tensile force

required to separate the solids above the *cmc* is relatively unaffected by surfactant concentration just above the *cmc*.

10.3 Prediction of Adsorption between Confined Surfaces

The second half of this thesis is concerned with how the adsorption of species changes as two surfaces interact. Once again, the adsorption can be predicted in general from knowledge of the adsorption isotherm for an isolated surface. The same regions will be considered as in the previous section.

10.3.1 Region (1): $[Surfactant] < hmc$

At low surfactant concentrations in Region (1), the surfactant adsorption is low enough that chain interactions are not significant and the surfactant can be approximated as a simple electrolyte. SCF calculations suggest that in this region the surfactant and co-ion are both adsorbing as the separation decreases, while the counter-ions are desorbing. The co-ions dominate the adsorption changes due to their larger bulk concentration. The experimental studies, however, suggest that small amount of surfactant may be desorbing in this region. The reason for the discrepancy, suggests that there may be effects that are not accounted for with SCF.

At sufficiently small separations ($< 2\text{-}3$ nm), the SCF calculations suggest that at equilibrium, a large amount of surfactant can condense in the gap between the surfaces, such that the surface charge is compensated. This is not seen experimentally, however, Rutland and Parker suggest that this may occur if the surfaces are held in contact,^{1,2} which is the situation calculated in chapter 9. As mentioned in the previous section, the energy barrier is sufficient that this situation is unlikely to occur in a free suspension of colloidal particles.

10.3.2 Region (2): $hmc < [Surfactant] < ccp$

In region (2), both SCF and experiments confirm the adsorption of surfactant as the separation is decreased. In addition, the calculations in chapter 9 confirm that the proximal adsorption of surfactant does indeed scale with chain length as was shown experimentally. Furthermore, SCF shows that the co-ions desorb as the separation

decreases to compensate some for some of the excess surfactant adsorption. As the surfactant tails interact to promote additional adsorption on the surface, some of the cations on the surface are displaced.

As the surfactant adsorbs, the adsorbed layer becomes thicker. At sufficient confinement, the layers on opposite surface interact with each other and the SCF calculations suggest a confinement–induce phase transition occurs, which leads to a large adsorption of surfactant. In Region (2), the surfactant condenses to levels required to compensate the charge on the solid. This is consistent with the proximal isotherm in Fig. 5.9, where the condensation at ‘contact’ occurs up to the level where the particles are neutral according to zeta potential measurements.

The calculations suggest that this confinement–induced phase transition, may be the reason for the strong attraction that occurs at a critical separation in experimental force data.

10.3.3 Region (3): $ccp < [Surfactant] < cmc$

In region (3), the surfactant desorbs as the solid–solid separation decreases. The SCF calculations suggest that, small amounts of co-ion adsorb, while the counter-ion mirrors the behavior of the surfactant. The surfactant layer becomes thinner as the surfaces approach down to a critical separation. The SCF calculations show that the interaction occurs at decreasing potential, and suggest that constant potential should not be considered as the lower-bound for interactions in surfactant solutions.

When the surfactant layers interact a phase transition occurs as in region (2). The tails can interact to promote adsorption. This phase transition contributes a strong attraction whose onset is not necessarily indicative of twice the thickness of the surfactant layer as proposed by other researchers⁴⁻⁸ due to a thinning of the surfactant layers as the separation decreases. This suggests that the ‘jump-in’ in AFM force measurements should not necessarily be taken as an indication of the surfactant film thickness on an isolated surface.

10.4 Conclusions

For negatively charged silica-like surfaces, the presence of surfactant can have a significant effect on the surface forces provided it can affect the double-layer charge distribution. The range of interactions between charged surfaces in aqueous electrolyte solutions is governed by the Debye-length. The range of surfactant proximal adsorption is also governed by the Debye-length if there is a charge–charge attraction between surfactant and the surface. The magnitude of the adsorption changes scale with the chain length. Furthermore, the hydrophobic surfactant chain can allow surfactants with no strong attraction for the surface to proximally adsorb by coupling to other surfactants via the short-range (contact) hydrophobic effect. Changes in adsorbed amounts and the thickness of surfactant layers suggest that structural changes may occur during interactions. This should be considered when interpreting images of facile structures obtained with AFM. Furthermore, the practice of centrifuging colloidal suspensions to remove particles for depletion adsorption experiments complicates the experiments as the applied force could lead to changes in adsorption.

10.5 Future Work

In this thesis the necessity of an equation of state that accounts for chemical interactions between surfactant molecules is demonstrated. The use of this equation of state to develop a more rigorous means of fitting force data in surfactant solutions is the next likely step forward from the work presented in this thesis.

Other extensions of this work could include studies of systems near critical points such as mixed surfactant systems near phase transitions, or systems near the Kraft point. In addition, the construction of devices with the goal of specifically monitoring adsorption at various separations would provide the most significant advances. For instance, osmotic pressure measurements of colloidal suspensions with *in situ* spectroscopic monitoring of concentration could provide such information. Furthermore, surface spectroscopic techniques in the presence of a second surface with accurately controlled proximity may provide both adsorption as well as structural information if a polarized spectroscopy is used.

10.6 Cited Literature

- (1) Rutland, M. W.; Parker, J. L. *Langmuir* **1994**, *10*, 1110.
- (2) Parker, J. L.; Rutland, M. W. *Langmuir* **1993**, *9*, 1965.
- (3) Subramanian, V.; Ducker, W. *J. Phys. Chem. B* **2001**, *105*, 1389.
- (4) Pashley, R. M.; Israelachvili, J. N. *Colloids and Surfaces* **1981**, *2*, 169.
- (5) Kékicheff, P.; Christenson, H. K.; Ninham, B. W. *Colloids and Surfaces* **1989**, *40*, 31.
- (6) Patrick, H. N.; Warr, G. G.; Manne, S.; Aksay, I. A. *Langmuir* **1999**, *15*, 1685.
- (7) Wanless, E. J.; Ducker, W. A. *Langmuir* **1997**, *13*, 1463.
- (8) Wanless, E. J.; Ducker, W. A. *J. Phys. Chem.* **1996**, *100*, 3207.

VITA

William J. Lokar III was born on March 14, 1977 in Uniontown, Pennsylvania to parents William and Diana Lokar. He spent his entire childhood in Uniontown, where he graduated second in his high school class at Laurel Highlands Senior High School in 1995. He continued his education at Allegheny College in Meadville, Pennsylvania. During his studies at Allegheny, he was named a distinguished Alden and Doane Scholar multiple times. He graduated *magna cum laude* in 1999 with his B.S. in chemistry. He continued on to graduate school at Virginia Tech in Blacksburg, Virginia, where he received a Cunningham Fellowship and worked in the laboratory of William A. Ducker. During his stay in Blacksburg, he received the graduate research award in chemistry. In addition, he spent six months during his graduate studies working with Luuk K. Koopal and Frans A.M. Leermakers in the Laboratory of Physical Chemistry and Colloid Science at Wageningen University in Wageningen, The Netherlands. Upon finishing his Ph.D. in physical chemistry at Virginia Tech in July 2004, he joined the faculty at Lynchburg College in Lynchburg, Virginia.